Skyrmions and spirals in cubic chiral magnets

Bannenberg, Lars

DOI
10.4233/uuid:2b87c62b-6078-454d-939a-20966fefc464

Publication date
2019

Document Version
Final published version

Skyrmions and Spirals in Cubic Chiral Magnets

Lars Johannes Bannenberg

SKYRMIONS AND SPIRALS IN CUBIC CHIRAL MAGNETS

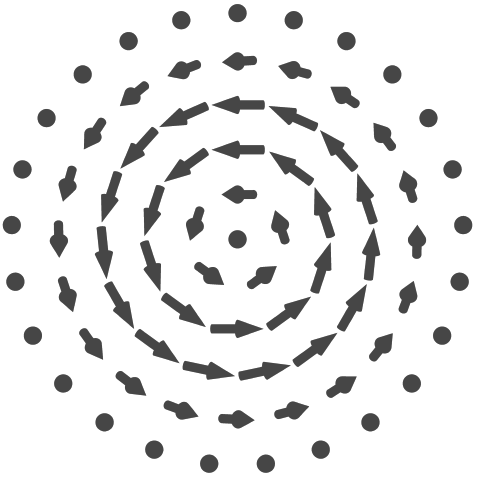

Lars Johannes Bannenberg

SKYRMIONS AND SPIRALS IN CUBIC CHIRAL MAGNETS

Proefschrift

ter verkrijging van de graad van doctor
aan de Technische Universiteit Delft,
op gezag van de Rector Magnificus prof. dr. ir. T.H.J.J. van der Hagen,
voorzitter van het College voor Promoties,
in het openbaar te verdedigen op maandag 29 april 2019 om 15:00 uur

door

Lars Johannes BANNENBERG

Master of Science in Applied Physics,
Technische Universiteit Delft, Delft, Nederland,
Master of Science in Financial Economics,
Erasmus Universiteit, Rotterdam, Nederland,
geboren te Apeldoorn, Nederland.

Dit proefschrift is goedgekeurd door de promotoren.

Samenstelling promotiecommissie bestaat uit:

Rector Magnificus	voorzitter
Prof. dr. C. Pappas	Technische Universiteit Delft, promotor
Dr. ir. A. A. van Well	Technische Universiteit Delft, copromotor
Onafhankelijke leden:	
Prof. dr. E. H. Brück	Technische Universiteit Delft
Prof. dr. M. V. Mostovoy	Rijksuniversiteit Groningen
Dr. F. Weber	Karlsruher Institut für Technologie
Dr. R. M. Dalgliesh	ISIS Neutron and Muon Source
Dr. N. Martin	Laboratoire Léon Brillouin
Prof. dr. ir. M. Wagemaker	Technische Universiteit Delft, reservelid

The work presented in this thesis is financially supported by NWO through NWO Groot Project 721.012.102 (Larmor). Other contributions made to this project are listed in the Appendix. Beamtime allocations by the ISIS Neutron and Muon source, Institut Laue-Langevin, Laboratoire Léon Brillouin and Oak Ridge National Laboratory are kindly acknowledged.

Keywords: Skyrmions, helimagnetism, cubic chiral magnets, neutron scattering, susceptibility and magnetization measurements

Printed by: Ipskamp Printing B.V.

Front & Back: Outside: Illustration of a Bloch skyrmion.
Inside: Small Angle Neutron Scattering (SANS) patterns of skyrmion lattices and spirals.

ISBN 978-94-028-1463-7

An electronic version of this dissertation is available at
http://repository.tudelft.nl/.

CONTENTS

1

INTRODUCTION

It was in the early 1960s when Tony Skyrme introduced a localized solution in fields of pion particles [1–3]. Since then, the concept of a skyrmion, being a non-singular localized and topologically stable field configuration, has been applied beyond the field of Nuclear Physics and found its way through many branches of (condensed matter) physics [4], including quantum Hall systems [5–8], liquid crystals [9–13], Bose-Einstein condensates [14, 15] and optics [16, 17].

In recent years, the concept of a skyrmion has probably been most often associated with magnetism. Figure 1.1(a) of Box 1 depicts the most frequently observed magnetic skyrmion - the Bloch skyrmion - (other types of skyrmions are discussed in Box 2 and 3). These skyrmions are reasonably small with dimensions in the order of several to hundreds of nanometers. They are two-dimensional non-trivial magnetic textures which are topologically protected, i.e. there exist no continuous transition in which one can transform a skyrmion into a topological trivial magnetic state as for example a ferromagnetic or helical state.[1]

The first theoretical prediction of the existence of these vortex-like magnetic textures in magnetic materials dates back to the late 1980s [18–21] when Bogdanov and his coworkers demonstrated theoretically that uniaxial anisotropy can stabilize vortex-like magnetic textures in non-centrosymmetric magnets. However, these magnetic textures where usually named vortices and it took until about ten years later before the term skyrmion was (presumably) first mentioned in this context [22]. Subsequently, Rössler et al. (2006) [23] showed that skyrmions may crystallize into skyrmion *lattices* in bulk materials without inversion symmetry, as well as in thin films and at the surfaces of magnetic materials.

The first experimental observation of magnetic skyrmions was indeed a skyrmion lattice, reported by Mühlbauer et al. in 2009 [24], and observed in the cubic chiral magnet MnSi by Small Angle Neutron Scattering (SANS). As further addressed in Box 1,

[1] In the field of Nuclear Physics, two-dimensional skyrmions are often referred to as 'baby-skyrmions' to distinguish them from their three-dimensional counter parts.

1

Box 1: Skyrmions and skyrmion lattices

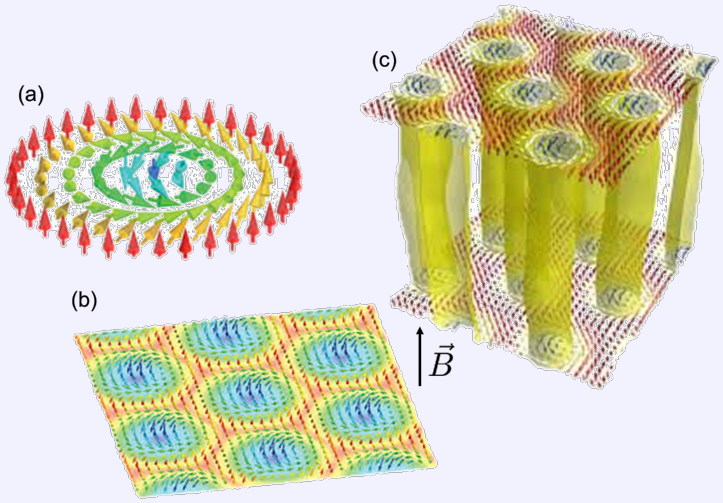

Figure 1.1: Magnetic textures of skyrmions and their lattices. (a) Single magnetic (Bloch) skyrmion. (b) 2D view of a hexagonal skyrmion lattice. (c) 3D view of a hexaganal skyrmion lattice. The arrows indicate the direction of the magnetic moments. Fig. 1.1(a) is adapted from ref. [25], Fig. 1.1(b) from ref. [26] and Fig. 1.1(c) from ref. [27].

A chiral magnetic skyrmion, as the Bloch skyrmion (see Box 2 for other types of skyrmions) displayed in Fig. 1.1(a), is a two-dimensional magnetic texture that is axi-symmetric, topologically protected and has particle like properties. Its dimensions are typically in the order of tens to hundreds of nanometers. Magnetic skyrmions can form two dimensional lattices like the hexagonal lattice[a] illustrated by Fig. 1.1(b). The modulation occurs in the plane perpendicular to the magnetic field. As shown in Fig. 1.1(c), these lattices extend to the third dimension, i.e. along the magnetic field, where 'tubes' of skyrmions are formed.

[a] Some authors refer to hexagonal skyrmion lattices as triangular skyrmion lattices.

skyrmions crystallize in a hexagonal lattice of which the modulation is perpendicular to the magnetic field. The observation of a skyrmion lattice in reciprocal space was rapidly followed by a real space observation by Yu et al. [28] in a thin film of semiconducting $Fe_{0.5}Co_{0.5}Si$ using Transmission Electron Microscopy (TEM). These discoveries were succeeded by the observation of skyrmion lattices in many other cubic helimagnets including FeGe [29], the Mott-insulator Cu_2OSeO_3 [30–32] and Co-Zn-Mn alloys [33–35]. Later, skyrmion lattices were detected beyond cubic helimagnets in (bulk) polar magnets [36–39] and in a tetragonal Heusler compound [40]. As a direct result of the different crystal structures, these materials do not host the Bloch skyrmions found in cubic helimagnets, but Néel and anti-skyrmions, respectively. The difference between the different types of experimentally observed skyrmions are further addressed in Box 2 and 3. In addition, individual skyrmions were for the first time detected, created and deleted with spin-

Box 2: Types of experimentally observed magnetic skyrmions

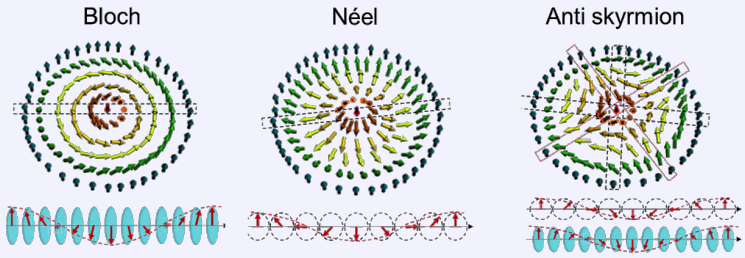

Figure 1.2: Different types of magnetic skyrmions that have been experimentally observed. The top row depicts the magnetic textures of three different types of skyrmions: the Bloch (left), Néel (middle) and Anti-skyrmion (right). The arrows point in the direction of the magnetic moments. The bottom row of figures show cross-sections of the magnetic textures of the top row along the radial direction, as indicated by the dashed and dotted rectangles. Image adapted with modifications from ref. [40].

Apart from the Bloch skyrmion discovered first in MnSi and later in other cubic chiral magnets with a $P2_13$ symmetry [24], other types of skyrmions have been observed experimentally. All these skyrmions have in common that the core has precisely the opposite magnetization from the outer boundary of the skyrmion. The crystal structure determines which type of skyrmion is observed in bulk magnetic materials.

In a Bloch skyrmion, a cross-section of the magnetic texture in the radial direction shows a transverse helix with an (anti-)clockwise orientation of the magnetic moments. In other words, the magnetic moments rotate in the tangential direction, i.e. perpendicular to the propagation direction of the helix. This is similar to a Bloch domain wall.

In a Néel skyrmion, as for example observed in polar magnets [36–39], a cross-sections of the magnetic texture shows an (anti-)clockwise rotating cyloid where the magnetic moments rotate in the radial direction, i.e. in a plane which contains the propagation direction of the cycloid. This is similar to a Néel domain wall.

In an anti-skyrmion, as first observed in the tetragonal Heusler compound $Mn_{1.4}Pt_{0.9}Pd_{0.1}Sn$ [40], the cross-section of the magnetic texture is spatially dependent. In the black dashed rectangles, the cross-section shows that the magnetic moments rotate like in a transverse helix, similar to a Bloch skyrmion. On the other hand, the cross-sections in the red dotted rectangles show that the magnetic moments rotate like in a cycloid, similar to a Néel skyrmion. Note that the different types of skyrmions can be defined by their topological charge and helicity, which is further explained in Box 3.

1

Box 3: Classification of skyrmions

In general, skyrmions can be uniquely classified by two numbers: the topological charge[a] or vorticity and the helicity. In order to understand these numbers, it is instructive to consider the mathematical description of a skyrmion, which is in spherical coordinates given by:

$$\hat{m}(\vec{r}) = (m_x, m_y, m_z) = (\cos[\Phi(\varphi)]\sin[\Theta(\vec{r})], \sin[\Phi(\varphi)]\cos[\Theta(\vec{r}), \cos[\Theta(\vec{r})]), \quad (1.1)$$

with $\hat{m}(\vec{r})$ the spatially dependent unit vector of the magnetization and $\vec{r}(x,y)$ the spatial coordinate expressed in polar coordinates as $\vec{r} = (\rho\cos[\varphi], \rho\sin[\varphi])$. Note that although the magnetization has three components, a skyrmion is a cylindrical object, implying that the magnetization does not have, in this coordinate frame, a z-dependence. Thus we can just consider the 2D case, where $\Theta(\vec{r})$ is the spatially dependent angle of $\hat{m}(\vec{r})$ with respect to the vertical (z) axis and Φ is defined as:

$$\Phi(\varphi) = n\varphi + \gamma, \quad (1.2)$$

where φ is defined as the angle with respect to the y-axis in the $x-y$ plane, n the vorticity and γ the helicity, which is effectively a phase difference. The coordinate frame is further illustrated by Fig. 1.3 for the cases of $n = 1$ and $\gamma = 0$ and $n = 1$ and $\gamma = \pi/2$.

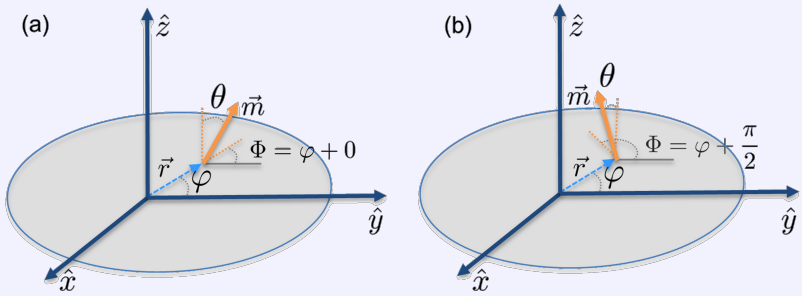

Figure 1.3: Illustration of the coordinate frame used to describe skyrmions for the case of (a) $n = 1$ and $\gamma = 0$ and (b) $n = 1$ and $\gamma = \pi/2$. The orange arrow indicates the unit vector of the magnetization $\vec{m}$, which is inclined with an angle Θ with the vertical (z) axis. The dotted gray arrow indicates the position vector $\vec{r}$ in the x-y plane, which length is given by ρ and which makes an angle φ with the y axis.

In fact, it turns out that the vorticity n of a skyrmion equals the topological charge of a skyrmion Q. The topological charge counts how often $\hat{m}$ wraps around the unit sphere and can be expressed as:

$$Q = \frac{1}{4\pi}\int\int\left[\hat{m}\cdot\left\{\frac{\partial\hat{m}}{\partial x}\times\frac{\partial\hat{m}}{\partial y}\right\}\right]d\vec{r}^2. \quad (1.3)$$

Substituting eq. 1.1 into eq. 1.3 leads to:

$$Q = \frac{1}{4\pi} 2\pi \left[\Phi(\varphi)\right]_{\varphi}^{\varphi=2\pi} = n, \tag{1.4}$$

provided that n can only be ± 1. This has an important implication: it establishes that a skyrmion is uniquely defined by its topological charge, which can only be ± 1, and its helicity. Figure 1.4 illustrates the magnetic textures of different types of skyrmions with varying Q and γ, including the Bloch skyrmion (Q = 1 and $\gamma = \pi/2$), Néel skyrmion (Q = 1 and γ = 0) and the anti-skyrmion (Q = -1 and γ = 0). Note that the fact that Q is always an integer provides topological protection and thus enhances the skyrmion's stability. In other words, there exists no continuous transformation which alters the magnetic configuration of a skyrmion leading to a configuration with a different topological charge, as for example a ferromagnetic, helimagnetic or paramagnetic state that all have a topological charge of 0.

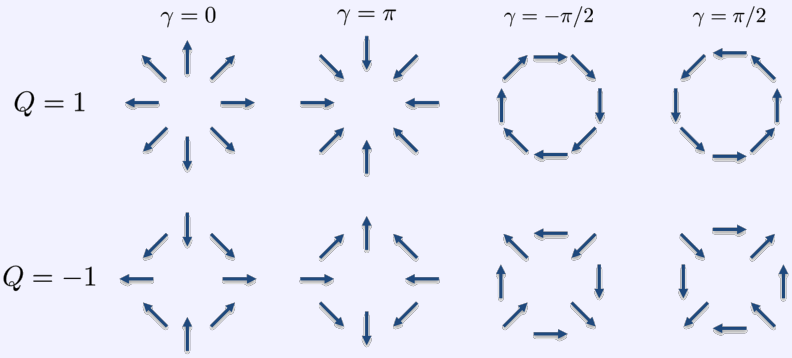

Figure 1.4: Schematic illustration of magnetic textures of different types of skyrmions with varying Q and γ, including the Bloch skyrmion (Q = 1 and $\gamma = \pi/2$), Néel skyrmion (Q = 1 and γ = 0) and the anti-skyrmion (Q = -1 and γ = 0). The arrows indicate the component of the magnetization $\vec{m}$ in the x-y plane of Fig. 1.3.

[a] Sometimes the word topological skyrmion number is used to refer to the concept of topological charge.

polarized scanning tunneling microscopy in PdFe bilayers on Ir(111) by Romming et al. (2013) [41].

The early studies of magnetic skyrmions triggered the emergence of a totally new field in magnetism: skyrmionics [42–46]. The activity in this field of research is driven both by the fundamental interest in new phenomena in condensed matter physics as well as by the potential perspectives of applying skyrmions in information storage devices. Indeed, it was soon recognized that the relatively small topologically protected skyrmions are exceptionally stable and can be manipulated with extremely small currents. Together with their relatively small size, these properties entail that magnetic skyr-

mions can potentially revolutionize data storage; skyrmions may conceivably increase the information density and may, at the same time, decrease the energy consumption of information storage devices. Moreover, skyrmions may play a pivotal role in green spintronics [41, 42, 46–54]. It is therefore no surprise that the current research in the field is centered around three main themes: (1) the discovery and synthesis of new skyrmion hosting materials, (2) the theoretical description and understanding of skyrmions and skyrmion hosting materials and (3) the fabrication of skyrmion utilizing devices.

The remainder of this thesis aims at increasing the understanding of skyrmions and their host materials, and in particular the understanding of cubic helimagnets. To this end, I first discuss the generic aspects of the phase diagrams of this most widely studied group of skyrmion hosting materials, followed by the particularities of selected individual compounds. Subsequently, these materials will be positioned within the entire family of skyrmion hosting materials.

1.1. SKYRMIONS AND HELIMAGNETISM IN CUBIC CHIRAL MAGNETS

Besides being the compounds where skyrmions were first observed in both bulk single crystals and thin films, cubic chiral magnets are probably the most widely studied skyrmion hosting materials. In fact, cubic chiral magnets and especially MnSi have already been extensively studied long before the observation of skyrmions in these systems, most notably in the 1970s and 1980s because of their weak itinerant ferromagnetic character and the long-period helimagnetic order induced by the Dzyaloshinsky-Moriya (DM) interaction [55–65].

1.1.1. GENERIC PHASE DIAGRAM AND MAGNETIC INTERACTION

The non-centrosymmetric crystal structure of cubic chiral magnets is at the heart of their magnetic properties. As illustrated in Fig. 1.5, the chiral crystallographic lattice has no inversion symmetry and can thus be distinguished from its center-inverted image. The absence of inversion symmetry implies that the DM interaction, which finds its origin in relativistic spin-orbit interactions interaction, is non-zero [55, 56].

In order to understand the magnetic properties of these systems, we consider a continuum model of the free energy f per unit cell. The use of such a continuum model is justifiable as the magnetic modulations in cubic helimagnets are typically long-ranged and comprise many unit cells. The model includes, besides the Zeeman interaction energy, three hierarchically ordered interactions with well-separated energy scales, being the strongest ferromagnetic interaction, the weaker DM interaction [55, 56], and the weakest anisotropy energy:

$$f = f_0(M) + \frac{-Ja^2}{2} \sum_{i=x,y,x} [\partial_i \hat{m} \cdot \partial_i \hat{m}] + aD\hat{m} \cdot \nabla \times \hat{m} - a^3 M \hat{m} \cdot \vec{B} + f_a, \tag{1.5}$$

with a the lattice constant, $\hat{m}$ the unit vector in the direction of the magnetization, and M the magnetization value and $f_0(M)$ the free energy density of a uniform state in zero

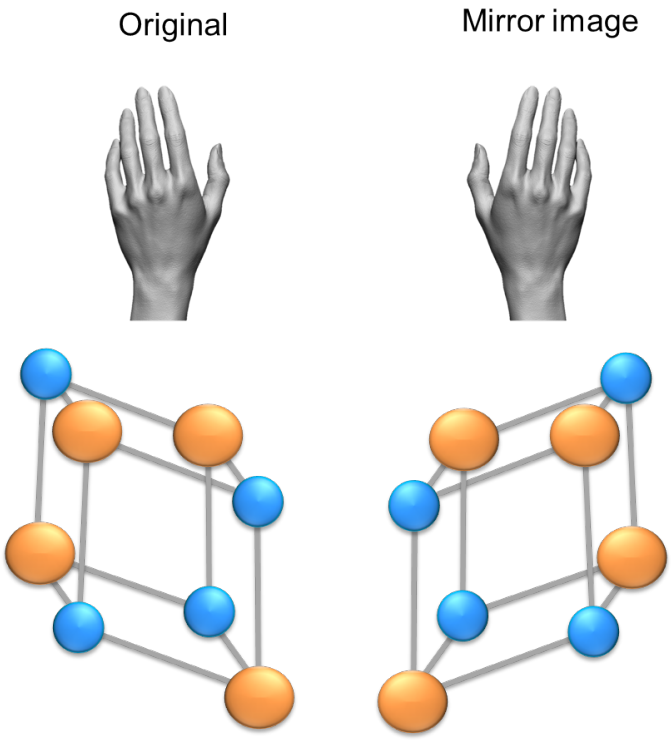

Figure 1.5: Illustration of two chiral objects: a hand and the crystal structure of a B20 compound as for example MnSi. Chiral objects are objects that can be distinguished from their mirror image. Top figure adapted with modifications from ref. [66].

magnetic field [43, 44, 57, 67]. The first term in eq. 1.5 is the ferromagnetic exchange interaction energy with strength J. In the case of $J > 0$, it favors a parallel arrangement of the magnetic moments. Differently, the second term in eq. 1.5, which is the DM interaction energy, is minimized if the magnetic moments are oriented perpendicular to each other [55, 56]. The third term represents the Zeeman or external field energy and is minimized when the magnetic field and the magnetic moments are oriented in the same direction. The last term in eq. 1.5 is the magnetic anisotropy energy f_a resulting from higher-order spin-orbit coupling.

HELICAL, CONICAL AND FIELD POLARIZED PHASE

The magnetic interactions considered in eq. 1.5 result in a phase diagram that is rather generic to cubic chiral magnets. This phase diagram, which reflects the hierarchy of the magnetic interactions, is depicted in Fig. 1.6. At zero magnetic field, a multi-domain helical phase is stabilized below the transition temperature T_C which is, as in a ferromagnet, proportional to J.[2] The periodicity of this helical phase, the helical pitch ℓ, is

[2] Small corrections to this proportionality have been proposed, see, e.g., ref. [23]

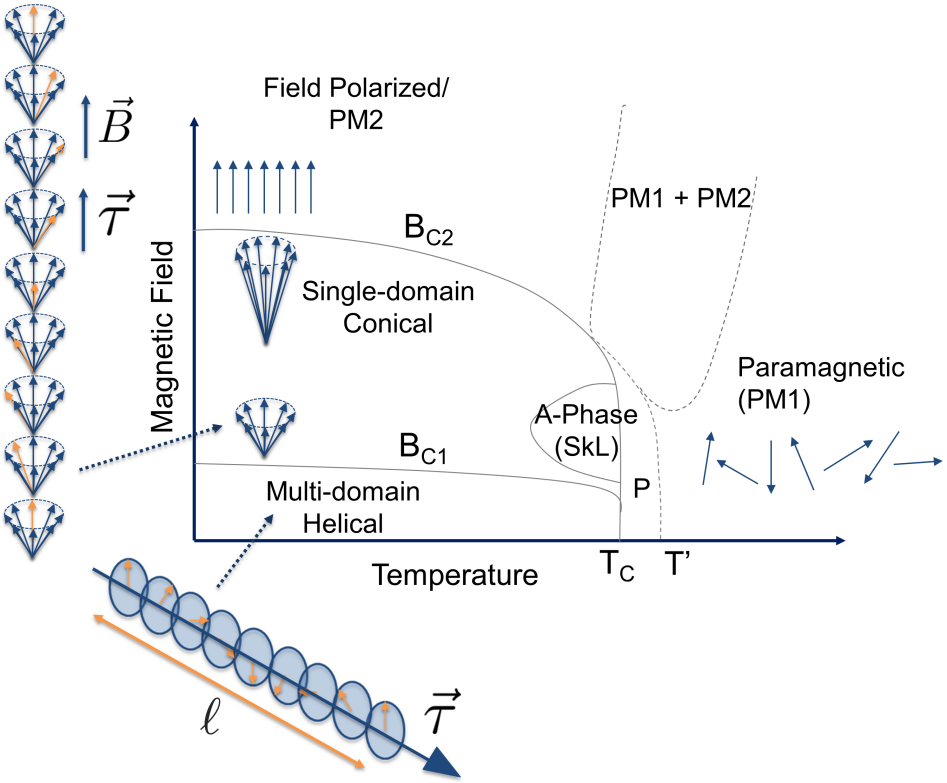

Figure 1.6: Schematic illustration of the generic magnetic phase diagram of a cubic helimagnet. In the multi-domain helical phase, the helices propagate along the crystallographic directions preferred by magnetic anisotropy, typically ⟨100⟩ or ⟨111⟩. The magnetic moments rotate at zero magnetic field in the plane perpendicular to the propagation vector $\vec{\tau}$ of the helix. For $B > B_{C1}$, the single-domain conical phase is stabilized, where the helices propagate along the direction of the magnetic field, i.e. $\vec{\tau} || \vec{B}$. In addition, the magnetic moments are no longer oriented perpendicular to $\vec{\tau}$ but incline towards the direction of the magnetic field. The cone closes at B_{C2}, and for $B > B_{C2}$ a field polarized state is stabilized, where the magnetic moments point along the magnetic field. The A-phase or Skyrmion Lattice (SkL) phase is schematically illustrated in Box 1. PM1 and PM2 denote the two paramagnetic phases which have different magnetizations and which coexist in a region of the magnetic phase diagram. P denotes the precursor phase, characterized by short-ranged, chiral and fluctuating helimagnetic correlations. T' marks the onset of the precursor phase. T_C denotes the transition temperature and ℓ is the pitch of the helix.

much longer than the lattice constant. As illustrated in Fig. 1.6, the magnetic moments in the helical phase are at zero magnetic field oriented perpendicular to the propagation vector of the helix $\vec{\tau}$, which is fixed by the magnetic anisotropy. The leading anisotropy term in the $P2_13$ space-group is the cubic anisotropy $f_{a1} = K(m_x^4 + m_y^4 + m_z^4)$, which aligns the helices either along the ⟨111⟩ crystallographic directions for $K < 0$ or along the ⟨100⟩ directions for $K > 0$ [57].

At a critical magnetic field of B_{C1}, the magnetic field reorients the helical spiral to-

wards its direction and thus overcomes the anisotropy, inducing a single-domain conical phase. In this conical phase the wavevector of the spiral is aligned along the magnetic field ($\vec{\tau}||\vec{B}$) and the magnetic moments progressively cant towards the direction of the magnetic field. With increasing magnetic field, this canting increases, i.e. the canting angle θ, being the angle between the helical propagation direction $\vec{\tau}$/magnetic field and the magnetic moments, decreases. This ultimately leads for $B > B_{C2}$ to an arrangement where all magnetic moments are parallel to the magnetic field. In other words, the field is for $B > B_{C2}$ strong enough to overcome the DM-interaction and induce a field polarized state.

The role magnetic interactions play in shaping the helimagnetic order and the magnetic phase diagram is illustrated by considering the conical spiral Ansatz:

$$\vec{m} = \cos\theta\hat{e_3} + \sin[\theta\cos(\vec{\tau}\cdot\vec{x})\hat{e_1} + \sin(\vec{\tau}\cdot\vec{x})\hat{e_2}], \tag{1.6}$$

with $(\hat{e_1}, \hat{e_2}, \hat{e_3})$ a set of orthogonal unit vectors. By substituting eq. 1.6 into eq. 1.5, one can derive that the pitch of the helical modulation is, in the absence of Zeeman and magnetic anisotropy energies, given by:

$$\ell = \frac{2\pi}{|\vec{\tau}|} = \frac{2\pi}{a}\frac{J}{D}, \tag{1.7}$$

as well as that the critical field B_{C2} at $T = 0$ K:

$$B_{C2}(T = 0\text{ K}) = \frac{D^2}{Ja^3M}. \tag{1.8}$$

In other words, both the helimagnetic pitch and the critical field B_{C2} depend on the relative strength of the interactions, while the transition temperature is (mainly) determined by the ferromagnetic exchange interaction. In fact, these relations are rather intuitive: if J is much larger than D, the DM-interaction can only accomplish a small twist of the magnetic moments relative to a parallel alignment, which leads to a very long helimagnetic pitch. At the same time, the gain in Zeeman energy of relatively small magnetic fields already outweighs the energetic gain of a helimagnetic modulation, effectuating that a field polarized state is induced.

A-PHASE AND SKYRMION LATTICES

The only ordered phase generic to cubic helimagnets left unaddressed is the A-phase. The A(nomalous)-phase, which occurs under moderate magnetic fields just below the transition temperature, was first mentioned as a distinct phase in 1982 by Kadowaki et al. [68] and has long been a mystery.[3] It has been, amongst others, suggested that the A-phase is a re-entrant paramagnetic state [68] or a modulated antiferromagnetic phase [63]. The identification of the A-phase as a skyrmion lattice phase was provided by the seminal publication of Mühlbauer et al. (2009) [24], who identified it as a skyrmion lattice phase on the basis of small angle neutron scattering measurements.

The stability of skyrmion lattices in this region of the phase diagram cannot be explained only on the basis of the continuum model of eq. 1.5. Indeed, additional ingredients are required to account for the thermodynamic stability of skyrmion lattices and

[3] Hints for the existence of the A-phase can also be seen in earlier work as for example ref. [61].

this has been attributed to additional terms including thermal fluctuations [24, 44, 69], spin exchange stiffness and/or uniaxial anisotropy [18, 20, 23, 70, 71]. On the other hand, it has been established that the crystallographic direction along which the magnetic field is applied has only a relatively small influence on the extent of the skyrmion lattice phase [72]. As further addressed in Section 1.1.2, Cu_2OSeO_3 [67, 73] forms an exception to this generic behavior.

In thermodynamic equilibrium, the skyrmion lattice phase is generally confined to a relatively small section of the phase diagram, of which the extent can be altered significantly by applying pressure [74–76] or electric fields [77–80]. In addition, *metastable* skyrmion lattices have been reported down to the lowest temperatures in most chiral magnets [81–85]. These low-temperature metastable or super-cooled skyrmions are typically induced by (fast) cooling through the A-phase. Both the cooling rates required to induce these low-temperature skyrmion lattices as well as the related lifetimes and stability are drastically different for the different compounds [81, 86]. In the formation and stability of these low-temperature skyrmion lattices anisotropies do play an important role, as also highlighted by the transition from a hexagonal to a square lattice arrangement that has been reported at low temperatures for β-Mn type $Co_8Zn_8Mn_4$ [82] and MnSi [84].

The skyrmions in the A-phase of cubic chiral magnets align in hexagonal lattices oriented perpendicular to the magnetic field. Considering this lattice as a rigid object leaves one degree of freedom for its orientation as it could, in the absence of anisotropy terms, freely rotate in the plane perpendicular to the magnetic field. As further addressed in Chapter 8 of this thesis, higher spin-orbit coupling terms, beyond fourth order [24, 87], align the skyrmion lattice along ⟨110⟩ for MnSi [24] or ⟨100⟩ for Cu_2OSeO_3 [31]. These anisotropic terms do not only lead to a specific orientation of the skyrmion lattice, but they also determine, in conjunction with the thermal and magnetic history [31, 88–90], the occurrence of single- or multi-domain skyrmion lattice phases [90].

PRECURSOR AND PARAMAGNETIC PHASES

The helimagnetic transition is in general of first order and is preceded by precursor phenomena that vary strongly in strength from one compound to another [91–97]. For instance, MnSi and $Mn_{1-x}Fe_xSi$ host intense chiral, isotropic, fluctuating helimagnetic correlations which occur in a temperature region of at least 1 K above T_C [91, 92, 94, 97, 98]. These short-ranged helimagnetic correlations are significantly weaker in $Fe_{1-x}Co_xSi$ [96] and (almost) absent in Cu_2OSeO_3. In addition, there is strong experimental and theoretical evidence that a phase separation occurs in the paramagnetic phase between two paramagnetic states, PM1 and PM2, characterized by different magnetizations. These two paramagnetic states could be seen as the magnetic analogue of a 'gas' and 'liquid' state, and coexist in a part of the magnetic phase diagram. Indications for this unusual behavior is provided by a strong imaginary component of the ac susceptibility (typically below 10 Hz, material dependent), as seen in the contour plots of Fig. 1.7, which likely arises from domain walls separating these two states [99].

Table 1.1: Overview of selected magnetic properties of commonly studied helimagnets. Other helimagnets that are not included in the table include $Mn_{1-x}Co_xSi$ [100–102], $Mn_{1-x}Al_xSi$ [103], $Mn_{1-x}Ga_xSi$ [103], $Mn_{1-x}Ir_xSi$ [104], $Mn_{1-x}Fe_xGe$ [105–107], $Mn_{1-x}Co_xGe$ [108], $Mn_{1-x}Rh_xGe$ [108], $Fe_{1-x}Co_xGe$ [109, 110], and Co-Zn-Mn alloys [33–35]. ℓ denotes the helimagnetic pitch, T_C the critical temperature and B_{C2} the magnetic field of the helical-to-conical transition at the lowest temperature. This value is only corrected for demagnetization effects for Cu_2OSeO_3. Note that the values for some quantities deviate between different studies. In these cases, our own data is listed and if this is absent, the tabulated values correspond to an average of the values reported in the literature.

Compound	T_C [K]	$\ell_{2.5K}$ [nm]	ℓ_{T_C} [nm]	B_{C2} [T]	Spontaneous Magnetization [μ_B/f.u.]	Propagation direction
MnSi	29	18	16	0.62	0.4	⟨111⟩
Cu_2OSeO_3	57			0.08	0.56	⟨100⟩
FeGe	278	67	70	0.27	0.9	⟨100⟩ / ⟨111⟩[4]
MnGe	170[5]	3.8	5.8	13	2	⟨100⟩
$Fe_{1-x}Co_xSi$						
0.1	10	45		0.05	0.08	
0.2	30	30		0.18	0.14	⟨100⟩
0.3	43	40		0.17	0.18	⟨100⟩
0.4	50	55		0.08	0.2	⟨100⟩
0.5	45	88		0.03	0.18	
0.6	24	175		0.01	0.13	
$Mn_{1-x}Fe_xSi$						
0.03	19	14	13	0.62	0.32	⟨111⟩
0.09	8	10	10	0.6	0.18	⟨110⟩
0.1	5	9	9	0.6	0.15	

1.1.2. PARTICULARITIES OF THE MAGNETIC PHASE DIAGRAMS OF CUBIC HELIMAGNETS

The focus in this section is on the specific magnetic phase diagrams of well-known cubic helimagnets including the stochiometric compounds MnSi, Cu_2OSeO_3, and FeGe as well as the doped materials $Mn_{1-x}Fe_xSi$ and $Fe_{1-x}Co_xSi$. Although the magnetic phase diagrams of cubic helimagnets are quite generic, interesting deviations and particularities of the different compounds do exist. Table 1.1 provides an overview of the relevant properties of these frequently studied cubic helimagnets. It shows that the transition temperature varies from a few Kelvin to room temperature and that the helimagnetic pitch ranges from about 4 nm for MnGe to over 170 nm for $Fe_{0.6}Co_{0.4}Si$. These properties and phase diagrams have mainly been determined by magnetization, susceptibility and SANS measurements (Box 4). In addition, Table 1.2 provides an overview of selected experimental studies on these materials.

[4] A transition of the propagation vector occurs in FeGe from ⟨111⟩ at low temperatures to ⟨100⟩ at high temperatures [111].

Table 1.2: Overview of selected experimental studies of commonly studied cubic helimagnets. Other helimagnets that are not included in the table include $Mn_{1-x}Co_xSi$ [100–102], $Mn_{1-x}Al_xSi$ [103], $Mn_{1-x}Ga_xSi$ [103], $Mn_{1-x}Ir_xSi$ [104], $Mn_{1-x}Fe_xGe$ [105–107], $Mn_{1-x}Co_xGe$ [108], $Mn_{1-x}Rh_xGe$ [108], $Fe_{1-x}Co_xGe$ [109, 110], $(Cu_{1-x}Ni_x)_2OSeO_3$ [112], $(Cu_{1-x}Zn_x)_2OSeO_3$ [113, 114], $Cu_2OSe_{1-x}Te_xO_3$ [115], and Co-Zn-Mn alloys [33–35].

Compound	Neutron Diffraction	Magnetization and Susceptibility	Specific Heat	(Topological) Hall effect	Other quantities (resistivity, ultrasound etc.)
MnSi	[24, 60, 63, 64, 84, 91, 92, 94, 97, 116–128]	[68, 72, 125, 129–131]	[132–134]	[81, 135, 136]	[59, 61, 62, 132, 133, 137–150]
Cu_2OSeO_3	[30–32, 67, 73, 76–80, 88–90, 151, 152]	[95, 153–158]	[159]		[160–179]
FeGe	[111, 180–182]	[93, 183–189]	[186, 190]		[184, 188, 191–195]
MnGe	[196–198]	[198, 199]	[199]	[200]	[198, 199, 201, 202]
$Fe_{1-x}Co_xSi$	[101, 203–207]	[101, 203, 208–212]	[212]		[101, 209, 211, 213]
0.1					
0.2	[87, 214]				[215]
0.3	[83, 96, 216]	[217, 218]			
0.4		[219]			
0.5					
0.6					
$Mn_{1-x}Fe_xSi$	[107, 220–222]	[102, 222–224]		[225–227]	[223, 228–232]
0.03					
0.09					
0.1	[233]	[234]			[234]

MnSi

MnSi is perhaps the most widely studied cubic chiral magnet and was, owing to its weakly itinerant character and helimagnetic properties, already the subject of numerous experimental and theoretical studies in the 1970s and 1980s [57, 57–65]. Below its transition

[5] Different values between 150 and 170 K have been reported, which is likely related to sample quality issues.

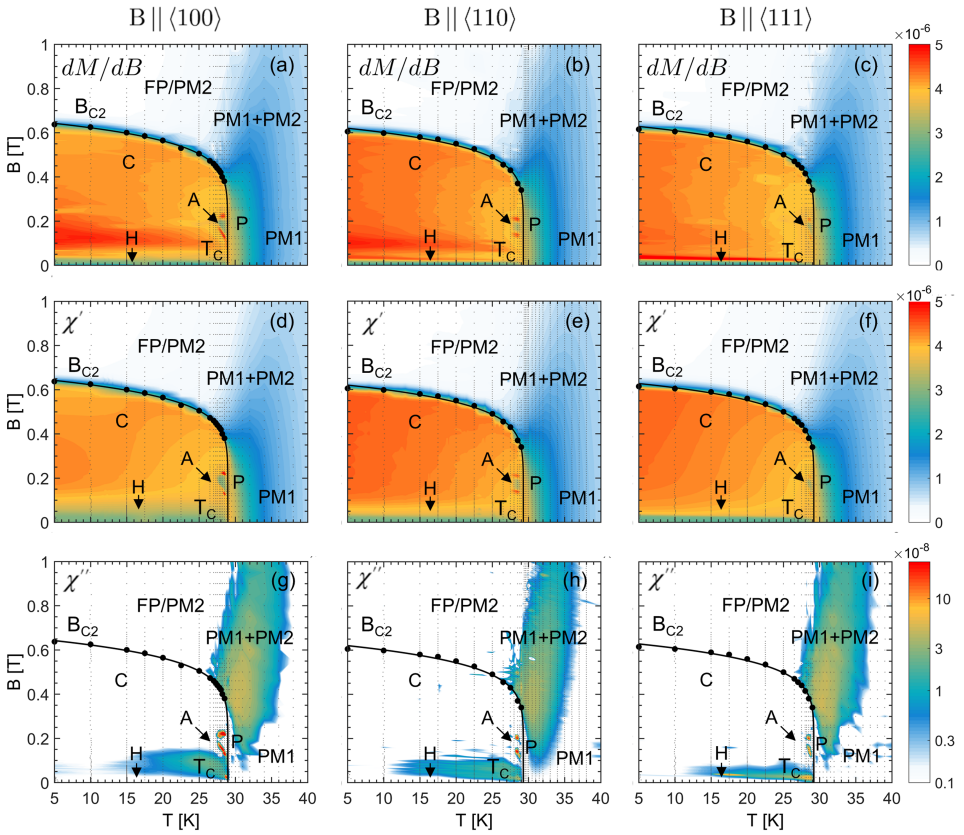

Figure 1.7: Contour plots showing (a) - (c) the derivative of the magnetization with respect to the magnetic field, dM/dB, the real (d) - (f) χ' and (g) - (i) imaginary χ'' component of the ac susceptibility at f = 5 Hz in units of m^3/mol of zero field cooled MnSi with the magnetic field applied along the (a),(d),(g) ⟨100⟩, (b),(e),(h) ⟨110⟩ and (c),(f),(i) ⟨111⟩ crystallographic direction. The magnetic field and susceptibility have not been corrected for demagnetization effects. The grey dots indicate the points at which the measurements were performed. B_{C2} marks the conical-to-field polarized transition and is defined by the inflection point of χ'. A indicates the A-phase, C the Conical phase, FP the Field Polarized phase, H the Helical phase, P the Precursor phase, PM1 and PM2 the Paramagnetic phases which coexist in a region under magnetic field and above the transition temperature. T_C is the critical temperature and is defined by the zero magnetic field maximum in χ'.

temperature of T_C = 29 K, helices propagate in the ⟨111⟩ crystallographic directions and have a pitch that varies between 16 nm at low temperatures and 18 nm at T_C.

Figure 1.7 presents phase diagrams of MnSi, obtained from contour plots of the real χ' and imaginary χ'' component of the ac susceptibility at a drive frequency of f = 5 Hz after zero field cooling (ZFC), and for magnetic fields applied along the three major crystallographic axes. For all the three crystallographic directions, the phases generic to cubic helimagnets, being the helical, conical, A-phase and field polarized state, are present. Differences between the three phase diagrams are seen in the extent of the A-phase pocket [72], which is about twice as large for $\vec{B}$ || ⟨100⟩ as for $\vec{B}$ || ⟨111⟩.

Box 4: Determining the magnetic phase diagram with SANS

Small Angle Neutron Scattering (SANS) has been an invaluable probe in determining the magnetic phase diagrams of cubic chiral magnets. In these experiments, SANS instruments are effectively used as single crystal diffractometers. The need for SANS is dictated by the relatively large magnetic structures, which lead, according to Bragg's law, to small scattering angles 2θ: $n\lambda = 2d\sin\theta$, where d is the periodicity (e.g. the pitch of the helix) and λ the wavelength of the neutron as given by the De Broglie relation. A typical (monochromatic) SANS instrument consists of a velocity selector, which selects one wavelength of neutrons coming from a neutron source (nuclear reactor or spallation source), a collimation area in which the neutron beam is collimated, a sample area where the sample and sample environment (e.g. a cryomagnet) are located, and a 2D detector located typically 2-20 m away from the sample.

Neutrons are only sensitive to the components of the magnetization perpendicular to the scattering vector $\vec{Q} = \vec{k}_f - \vec{k}_i$. This is reflected in the differential cross-section, which determines the amount of neutrons scattered into a solid angle $d\Omega$. Assuming that the scattering is elastic, the differential magnetic cross-section is given by:

$$\frac{d\sigma_{magnetic}}{d\Omega}(\vec{Q}) = \left\langle \vec{M}^*_\perp(\vec{Q}) \right\rangle \left\langle \vec{M}_\perp(\vec{Q}) \right\rangle + \vec{P}_i \vec{M}^*_\perp(\vec{Q}) \times \vec{M}_\perp(\vec{Q}), \tag{1.9}$$

where $\vec{M}_\perp(\vec{Q})$ is the Fourier transform of the magnetization component perpendicular to Q and $\vec{P}_i$ the polarization vector of the neutron beam. The last term in Eq. 1.9 is non-zero only in the presence of vector chirality and for a polarized neutron beam.

SANS probes (helical) modulations that propagate in the scattering plane, which is the same plane as the detector in Fig. 1.8. For this reason, in the case a magnetic field is applied, SANS experiments should be performed in at least two experimental configurations in order to get a complete overview of the helimagnetic correlations parallel and perpendicular to the applied magnetic field: Configuration 1, with the magnetic field parallel to the incoming neutron beam ($\vec{B} || \vec{k}_i$), is sensitive to modulations perpendicular to the magnetic field, as for example skyrmion lattices, and Configuration 2, with the magnetic field applied perpendicular to the incoming neutron beam ($\vec{B} \perp \vec{k}_i$), is sensitive to modulations along the magnetic field, as in the conical phase.

Typical scattering patterns of helimagnetic phases are given in Fig. 1.8 for the two experimental configurations. Often, one can determine the type of helimagnetic order from the topology of the scattering pattern that serve as a fingerprint of the helimagnetic phases. The position of the Bragg peaks or the maximum of the magnetic scattering is related to the pitch of the helix ℓ by $\ell = \frac{2\pi}{\tau}$, with τ the magnitude of the scattering vector.

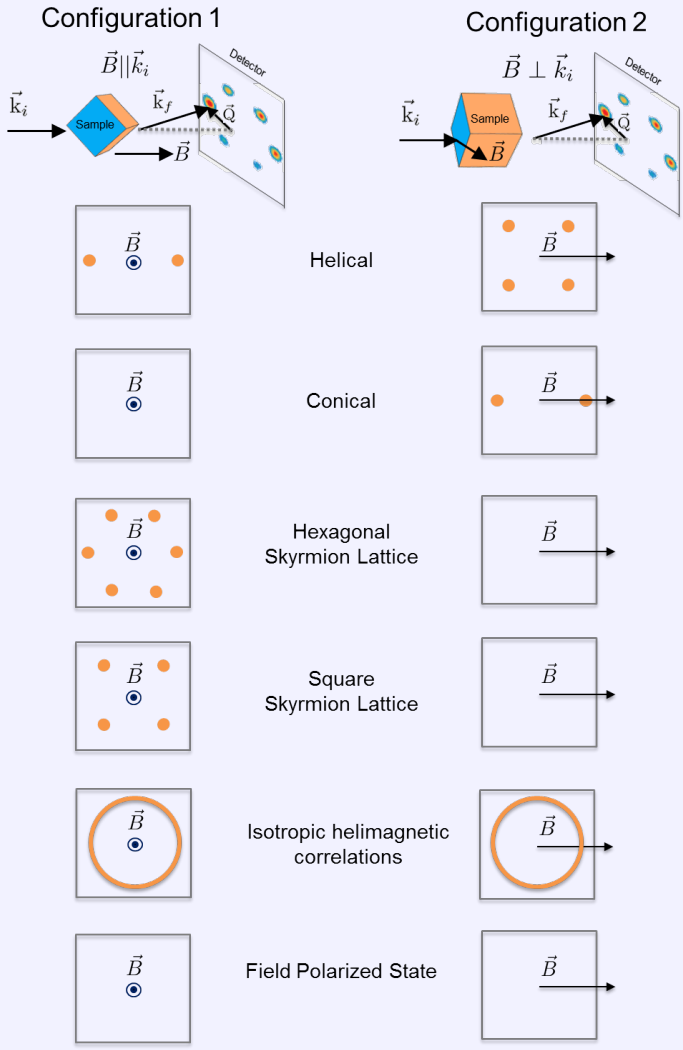

Figure 1.8: Schematic illustration of the two typical experimental set-ups of a SANS experiment to investigate helimagnetism in single crystals. In a SANS experiment, a neutron beam with an incoming wavevector $\vec{k}_i$ is scattered by a (single-crystal) sample (illustrated by the cube) under a small angle θ and is detected by a 2D detector. This scattering is due to momentum transfer: $\vec{Q} = \vec{k}_f - \vec{k}_i$, where $\vec{Q}$ is the scattering vector and $\vec{k}_f$ the final wavevector. In Configuration 1, the magnetic field is applied along the incoming neutron beam ($\vec{B}||\vec{k}_i$), whereas in Configuration 2 the magnetic field is applied perpendicular to the incoming neutron beam ($\vec{B} \perp \vec{k}_i$). The different helimagnetic phases lead to scattering patterns that are complementary for the two experimental configurations. The scattering patterns of the helical phase are provided for the case that the helices propagate along the ⟨100⟩ crystallographic directions and with the sample aligned such that the ⟨110⟩ direction is along the vertical axis, i.e. in the configuration most commonly used for these experiments.

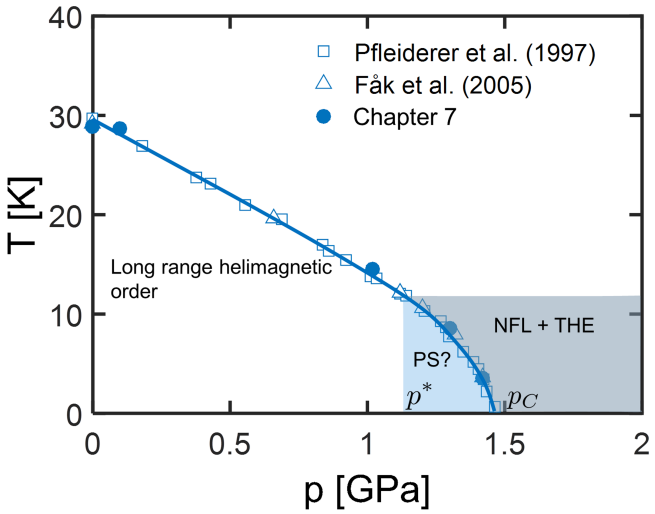

Figure 1.9: Zero magnetic field phase diagram of MnSi under hydrostatic pressure. The helimagnetic transition temperature is after refs. [236] and [237]. The non-Fermi liquid (NFL) and topological Hall effect (THE) behavior appears for pressures higher than p^* and p_C is the critical pressure, above which the helimagnetic order disappears. p^* also marks the onset of the alleged Phase Separated state (PS) where helimagnetic and paramagnetic volumes may coexist. Chapter 7 shows that skyrmion lattices and a conical phase are stabilized in parts of the region of the phase diagram governed by NFL and THE behavior.

In addition, the magnetic field direction has a pronounced influence on the helical-to-conical transition as well as on the extent of the helical phase [72, 125]. The helical-to-conical transition occurs for the easy axis of $\vec{B} \parallel \langle 111 \rangle$ at relatively low-magnetic fields and is sharp and of first order. It involves a sudden reorientation of the helices propagating along the three $\langle 111 \rangle$ directions that are not along the magnetic field to the fourth $\langle 111 \rangle$ direction oriented along the field. Differently, when the magnetic field is applied along the hard-axis, which is $\vec{B} \parallel \langle 100 \rangle$, the helical-to-conical transition is gradual and of second order, involving a smooth reorientation of the helices towards the direction of the magnetic field. Although the helices reorient continuously, the trajectory of the helices abruptly changes, and the helical-to-conical transition thus effectively involves two transitions for this particular direction of the field [125, 235].

A particularity of MnSi are the strong precursor phenomena above the transition temperature. In this region of the phase diagram, neutron scattering indicates isotropic, fluctuating and chiral helimagnetic correlations up to T_C+1 K [91, 92, 97, 120]. Magnetic fields suppress and partly align these isotropic helimagnetic correlations, and it has been suggested that they may drive the transition to first order [94] following a scenario originally developed by Brazovskii for liquid crystals [238]. However, the origin of the first order nature of the transition remains a topic of debate [147, 239].

Besides at ambient pressures, MnSi has also been studied extensively under hydrostatic pressure. As illustrated in Fig. 1.9, hydrostatic pressure reduces the transition temperature and even completely suppresses the long-range helimagnetic order at zero

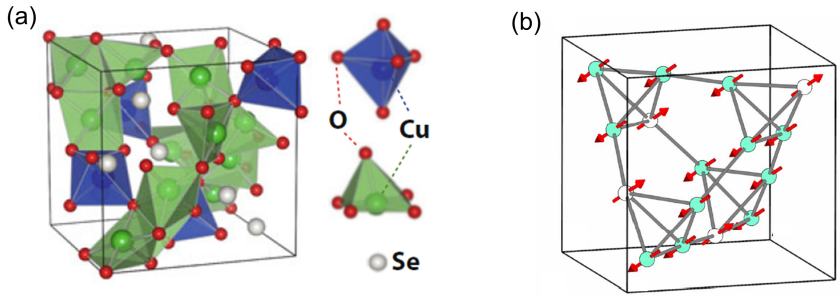

Figure 1.10: Crystallographic structure of Cu_2OSeO_3. (a) Position of the copper, oxygen and selenium atoms in the unit cell. (b) Position of the magnetic Cu^{2+} ions in the unit cell and the orientation of the spins. Panel (a) is adapted from ref. [43] and Panel (b) from ref. [160].

magnetic field above the critical pressure of $p_C \approx 1.4$ GPa. At intermediate pressures, qualitative differences occur at a characteristic pressure of $p^* \approx 1.2$ GPa. Indeed, non-Fermi liquid (NFL) and topological Hall effect (THE) behavior is found for $T > T_C$ [240–243], as well as that Chapter 7 reveals that conical spirals and skyrmion lattices are induced by the magnetic field above T_C. In addition, the propagation vector of the helices changes from $\langle 111 \rangle$ to $\langle 100 \rangle$, indicating a change in the sign of the cubic anisotropy. Furthermore, there is a controversy on whether the region of the phase diagram between p^* and p_C is characterized by phase separation between helimagnetic and paramagnetic volumes, [244, 245], or not [246].

Above p_C, it has been suggested that a partial magnetic order with slow dynamics persist that emerges without quantum criticality [240, 241, 245, 247, 248]. The phase diagram for $p > p_C$ is characterized by NFL and THE behavior, and the resistivity is thus characterized by a $T^{3/2}$ temperature dependence over an exceptionally large range of the phase diagram [240–243]. New results presented in Chapter 7 reveal that both skyrmion lattices and conical spirals are stabilized under magnetic field for $p > p_C$ in a small section of the phase diagram, even in the absence of helimagnetic correlations at zero magnetic field. These results elucidate earlier puzzling magnetization measurements [249]. However, no one-to-one relation is found between the appearance of skyrmion lattices and conical spirals on one side, and the NFL and THE behavior on the other side, as the latter extends over a much larger region of the phase diagram. A possible explanation for this paradox is that the phase, out of which a magnetic field induces long range order at low temperatures, is heterogeneous and consists of spirals, skyrmions and other topologically non-trivial magnetic textures.

Cu_2OSeO_3

The Mott-insulator Cu_2OSeO_3 was the first insulating compound where skyrmion lattices were detected [30, 31]. Although it has the same $P2_13$ space group with MnSi and other B20 compounds (See Fig. 1.5), its crystal structure, which is displayed in Fig. 1.10, is more complex. The Cu_2OSeO_3 unit cell contains 16 Cu^{2+} ions ($S = 1/2$) of two distinct types and with distinct interaction. This leads to the formation of four 'strong' tetrahe-

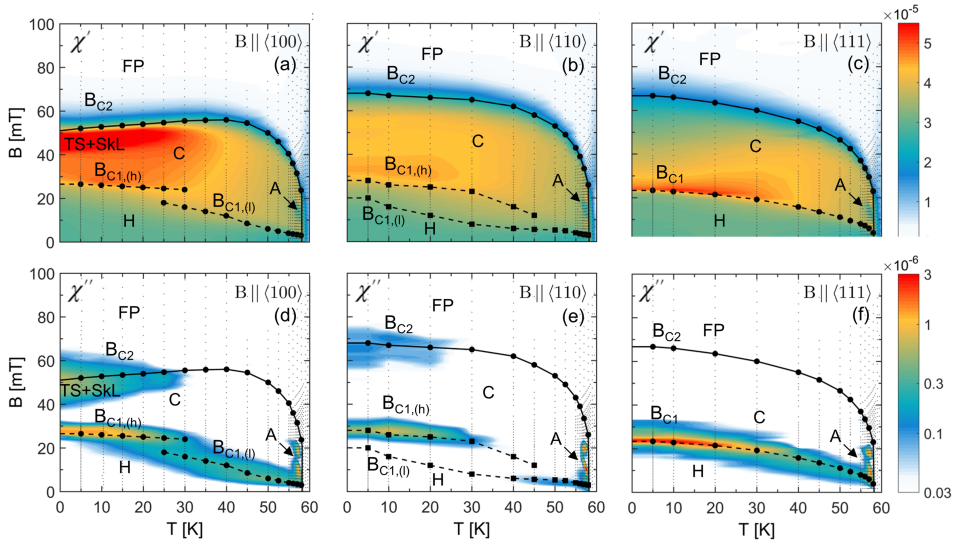

Figure 1.11: Contour plots showing ZFC (a) - (c) χ' and (d) - (f) χ'' at f = 10 Hz in units of $m^3/mol_{Cu^{2+}}$ of Cu_2OSeO_3 with the magnetic field applied along the (a),(d) ⟨100⟩, (b),(e) ⟨110⟩ and (c),(f) ⟨111⟩ crystallographic direction. The magnetic field values and susceptibility are corrected for demagnetization effects. The grey dots indicate the points at which the measurements were performed. B_{C1} marks the helical-to-conical transition and is for $\vec{B}$ || ⟨100⟩ and $\vec{B}$ || ⟨110⟩ split in a low ($B_{C1,(l)}$) and high magnetic field ($B_{C1,(h)}$) transition line. It is determined from the maximum (maxima) of χ'' for $\vec{B}$ || ⟨100⟩ and $\vec{B}$ || ⟨111⟩, and from the inflection point of χ' for $\vec{B}$ || ⟨110⟩. B_{C2} marks the conical-to-field polarized transition and is defined by the inflection point of χ'. A indicates the A-phase, C the Conical phase, FP the Field Polarized phase, H the Helical phase, TS the Tilted Spiral phase and SkL Skyrmion Lattice correlations. T_C is the critical temperature and is defined by the zero magnetic field maximum in χ'.

dra per unit cell. Within the strong tetrahedra, the spins align ferrimagnetically with a ratio of 3:1, leading to an effective spin of $S = 1$, thus a triplet state separated by a gap $\Delta \sim$ 275 K, i.e. $\sim 5T_C$, from the first excited state. These strong tetrahedra form well above T_C, effectively function as magnetic building blocks, and they are connected by 'weak' tetrahedra [160, 165]. The Mott-insulator Cu_2OSeO_3 was the first insulating compound where skyrmion lattices were detected [30, 31]. Although it has the same $P2_13$ space group with MnSi and other B20 compounds (See Fig. 1.5), its crystal structure, which is displayed in Fig. 1.10, is more complex. The Cu_2OSeO_3 unit cell contains 16 Cu^{2+} ions ($S = 1/2$) of two distinct types and with distinct interaction. This leads to the formation of four 'strong' tetrahedra per unit cell. Within the strong tetrahedra, the spins align ferrimagnetically with a ratio of 3:1, leading to an effective spin of $S = 1$, thus a triplet state separated by a gap $\Delta \sim$ 275 K, i.e. $\sim 5T_C$, from the first excited state. These strong tetrahedra form well above T_C, effectively function as magnetic building blocks, and they are connected by 'weak' tetrahedra [160, 165].

The composite nature of the strong tetrahedra spin together with the relatively weak value of Δ has an important effect on the spin-orbit coupling and the anisotropy terms [67]. The competition between the different anisotropy terms, most notably the cubic

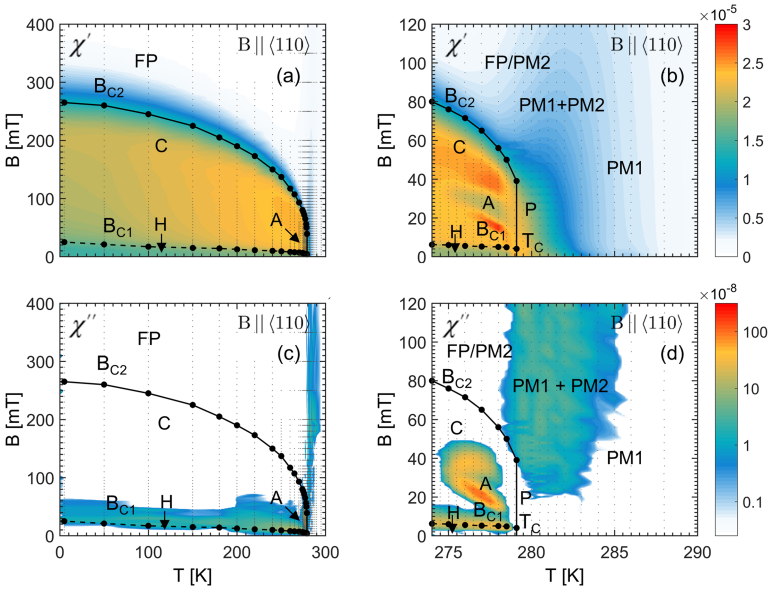

Figure 1.12: Contour plots showing ZFC (a) - (b) χ' and (c) - (d) χ'' at (a),(c) f = 5 Hz and (b),(d) f = 1 Hz in units of m^3/mol of FeGe with the magnetic field applied along the ⟨110⟩ crystallographic direction for (a),(c) the entire temperature region and (b),(d) in the region close to the transition temperature. The magnetic field values and susceptibility are uncorrected for demagnetization effects. The grey dots indicate the points at which the measurements were performed. B_{C1} marks the helical-to-conical transition and is determined from the inflection point of χ'. B_{C2} marks the conical-to-field polarized transition and is defined by the inflection point of χ'. A indicates the A-phase, C the Conical phase, FP the Field Polarized phase, H the Helical phase, P the Precursor phase, PM1 and PM2 the Paramagnetic phases which coexist in a region under magnetic field and above the transition temperature. T_C is the critical temperature and is defined by the maximum in χ'.

and exchange anisotropies, result in different phase diagrams for the magnetic field applied along the three crystallographic axes, as highlighted by the contour plots of χ' and χ'' in Fig. 1.11. These differences are much larger than for MnSi and are not confined to the extent of the helical phase and the nature of the helical-to-conical transition, but they also have a drastic effect on the conical-to-field polarized transition line. Moreover, a different helimagnetic phase, the tilted spiral phase, is found for $\vec{B}$ || ⟨100⟩ i.e. when the magnetic field is applied along the easy-axis, which is the propagation direction of the helices at zero magnetic field. In this phase, the propagation vector of the conical spiral tilts away from the direction of the magnetic field by up to 30° towards the ⟨111⟩ directions [67]. These tilted spirals coexist with a low-temperature skyrmion phase [73], which appears after zero field cooling only for $\vec{B}$ || ⟨100⟩.

As further shown in Chapter 9, fast field cooling with cooling rates in the order of 10 Ks^{-1} through the A-phase substantially enhances the intensity of low-temperature skyrmions. Furthermore, they induce metastable skyrmion lattices along the other two major crystallographic directions. These metastable skyrmion lattices are suppressed by high magnetic fields exceeding B_{C2}, but reappear when decreasing the magnetic field,

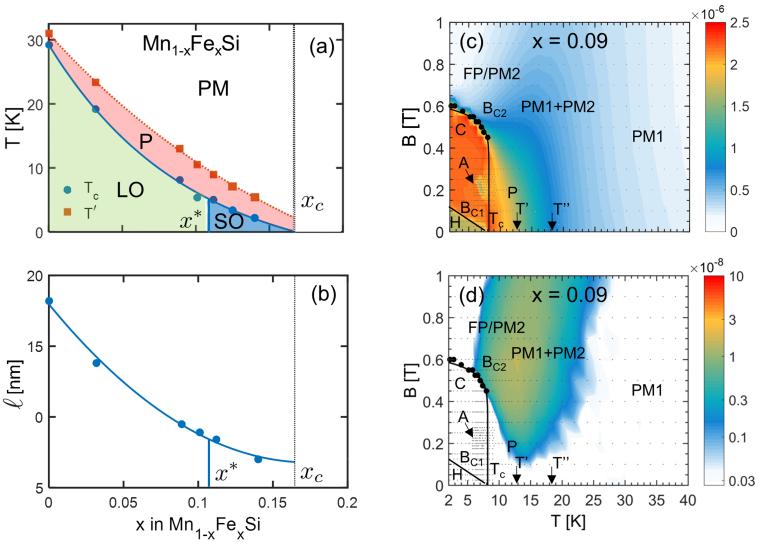

Figure 1.13: Magnetic phase diagrams of $Mn_{1-x}Fe_xSi$. (a) Fe concentration dependence of the critical temperature T_C and T'. The critical temperature T_C and T', which marks the onset of the (short-ranged) helimagnetic correlations in the precursor phase, are defined by the maximum and the high-temperature inflection point of the zero magnetic field temperature dependence of χ', respectively. (b) Fe concentration dependence of the pitch of the helix ℓ at zero magnetic field and $T = 2.5$ K. Contour plots showing ZFC (c) χ' and (d) χ'' at $f = 5$ Hz in units of m^3/mol of $Mn_{0.91}Fe_{0.09}Si$ with the magnetic field applied along the ⟨110⟩ crystallographic direction. The grey dots indicate the points at which the signal was recorded. B_{C1} marks the helical-to-conical transition and is determined from the inflection point of χ'. B_{C2} marks the conical-to-field polarized transition and is defined by the inflection point of χ'. A indicates the A-phase, C the Conical phase, FP the Field Polarized phase, H the Helical phase, P the Precursor phase, PM1 and PM2 the Paramagnetic phases which coexist in a region under magnetic field and above the transition temperature. SO marks the region of the phase diagram where isotropic helimagnetic correlations are found that appear elastic on the nanosecond time scale.

indicating a strong memory effect, possibly due to bobbers or torons that persist in the field polarized state [250].

As Cu_2OSeO_3 is a non-centrosymmetric insulator, it is also characterized by a strong magneto-electric coupling [77, 151, 156, 251, 252], which enables control of the skyrmionic order with electric fields, allowing one to extend or suppress the thermodynamically stable skyrmion phase [78–80]. Moreover, the sign and size of the electric field with respect to the magnetic field controls the specific orientation of the skyrmion lattice [77, 151].

FeGe

The cubic variant of FeGe, ϵ-FeGe has a relatively high T_C of 278 K and a long pitch of about 70 nm. At low temperatures, the helices propagate at zero magnetic field along ⟨111⟩. Around $T = 200$ K, the propagation direction crosses-over to ⟨100⟩ [111]. This crossover occurs over a wide temperature interval and involves a pronounced hysteresis and coexistence of the helices oriented along the two crystallographic directions.

It has been suggested that the magnetic phase diagram of FeGe is, in the proximity of the transition temperature considerably, more complicated than for other cubic helimagnets and involves strong precursor phenomena [93, 185]. In particular, several studies mainly focusing on the case of $\vec{B} \parallel \langle 100 \rangle$ provide indications that the A-phase in FeGe is segmented in different sub-phases [93, 181, 185]. On the other hand, the magnetic phase diagrams displayed in Fig. 1.12 for $\vec{B} \parallel \langle 110 \rangle$ and based on ac susceptibility measurements as well as ref. [44] do not provide such indications.

$Fe_{1-x}Co_xSi$

$Fe_{1-x}Co_xSi$ is helimagnetic over a wide composition range of $0.05 \lesssim x \lesssim 0.8$. A particular compound in this series, $Fe_{0.7}Co_{0.3}Si$, is the subject of Chapters 2-4. With cobalt doping, the strongly correlated (Kondo) insulator FeSi undergoes an insulator-to-metal transition at $x = 0.02$ [101, 253]. However, this system is commonly referred to as a semiconductor due to its relatively high resistivity at low temperatures [101, 213, 254].

The possibility to tune important physical properties by chemical substitution ensured that $Fe_{1-x}Co_xSi$ has been extensively studied. The transition temperature varies non-monotonically with Co doping and reaches its maximum of $T_C = 50$ K at $x = 0.4$, while the helimagnetic pitch increases with increasing Co substitution, reaching values of up to 180 nm for $x = 0.8$. Cobalt substitution also alters the magnetic chirality, which changes from left- to right-handed at $x = 0.65$ [206, 207]. Although the $\langle 100 \rangle$ crystallographic direction is the preferred propagation direction of the helices at zero magnetic field, the coupling of the helices to the crystallographic lattice is less strong than in stochiometric compounds such as MnSi and Cu_2OSeO_3 [83, 87, 205]. This coupling becomes weaker with increasing Co concentration [205], which is likely the result of chemical disorder. In addition, the helimagnetic transition in $Fe_{0.7}Co_{0.3}Si$ is much more gradual than in MnSi and involves the coexistence of weak short-ranged helimagnetic correlations and long-ranged ones over a relatively large temperature window of $\Delta T \approx 5$ K [96].

The magnetic phase diagrams of $Fe_{1-x}Co_xSi$ depend strongly on the magnetic history [83, 87, 212, 218]. Field cooling suppresses the helical phase, and significantly enlarges the skyrmion lattice phase, which extends down to the lowest temperatures if the sample is cooled through the A-phase [83, 87, 218].

$Mn_{1-x}Fe_xSi$

A main question adheres the stability condition of helimagnetism. A key to the answer is provided by studies of MnSi under hydrostatic pressure and by chemical doping, as in the case for $Mn_{1-x}Fe_xSi$. For this reason, $Mn_{1-x}Fe_xSi$ is another widely studied non-stochiometric cubic chiral magnet and the topic of Chapters 5 - 6.

Figure 1.13 depicts the dependence of the critical temperature and helimagnetic pitch on the Fe concentration, as well as the magnetic field-temperature phase diagram of $Mn_{0.91}Fe_{0.09}Si$ [255]. With increasing Fe substitution, both the transition temperature and the pitch decrease monotonically. In addition, the experimental results of Chapters 5 - 6 reveal at least two characteristic concentrations: $x^* \approx 0.11$ and $x_C \approx 0.17$. x^* corresponds to the concentration where the long-range helimagnetic periodicity disappears, whereas x_C is the concentration where the transition temperature vanishes. In addition,

at this concentration the sign of the average magnetic interactions changes from ferromagnetic for $x < x_C$, to anti-ferromagnetic for $x > x_C$.

The existence of these two characteristic concentrations implies that with doping at least three regions of the phase diagram can be identified: $x < x^*$, $x^* < x < x_C$ and $x > x_C$. For $x < x^*$, the magnetic phase diagram is qualitatively similar to the parent compound MnSi. However, for $x = 0.09$ the easy-axis is no longer $\langle 111 \rangle$ as in MnSi, but $\langle 110 \rangle$ [98]. For these compositions, the helimagnetic transition is, as for MnSi, sharp and of first order [256] and preceded by strong precursor phenomena that occur over a wider temperature range than for MnSi [98, 102, 220, 255, 256].

For $x^* < x < x_C$, the long-range helical periodicity breaks down, and helices with finite correlation lengths persist down to the lowest temperatures. These helimagnetic correlations are completely isotropic and appear similar to the ones in the precursor phase of MnSi, although they do not fluctuate on the nanosecond time-scale. Neutron Spin Echo (NSE) spectroscopy reveals that the helimagnetic correlations are elastic in the probed time scale. In addition, topological Hall resistivity measurements suggest that topologically non-trivial magnetic defects such as individual skyrmions, hedgehogs or torons may exist in this region of the phase diagram.

The magnetic compounds with $x > x_C$ show no signatures of a phase transition down to the lowest temperatures. However, pronounced deviations from paramagnetic behavior do occur at low temperatures [255]. Amongst others, this provides indications for a possible significant role of quantum fluctuations in these systems [102, 223, 224, 227, 231, 233], possibly characterizing x_C as a quantum critical point [102, 255]. Further studies of $Mn_{1-x}Fe_xSi$ are required to uncover the nature of the helimagnetic correlations in this part of the magnetic phase diagram and the role quantum fluctuations play therein.

1.2. SKYRMIONS IN OTHER SYSTEMS

Up to now, the focus was on chiral skyrmions in bulk cubic chiral magnets. In fact, as illustrated by Fig. 1.14, these materials are just a narrow selection of all materials that host topologically protected magnetic textures.

As already briefly touched upon in the beginning of this chapter, skyrmions have been observed in magnetic thin films, which was in fact already anticipated as early as 2001, e.g., long before the first experimental observation of skyrmions [21]. The first observation of skyrmions in thin films was in the B20 compound $Fe_{0.5}Co_{0.5}Si$ by Lorentz Transmission Electron Microscopy (TEM) [28]. Just like in other cubic helimagnets, skyrmions are found in thin films of this compound in a much larger fraction of the magnetic phase diagram than in their bulk equivalents [29, 257–261]. In fact, their stability region, both in terms of magnetic field and temperature range, strongly depends on the dimensions of the material and is found to increase with decreasing sample thickness [29]. This enhanced stability is attributed to surface effects [260, 262] and a pronounced role of (uniaxial) anisotropies [263]. Uniaxial anisotropy can also lead to elliptical distortions of both the skyrmion, helical and conical phases [264].

In addition, chiral skyrmions can also be stabilized at the interfaces of centrosymmetric materials [45, 46, 265–268]. In combination with strong spin-orbit coupling, as often found in heavy metals like platinum, iridium and palladium, the DMI interaction, resulting from the broken inversion symmetry at interfaces [269, 270], can stabilize these

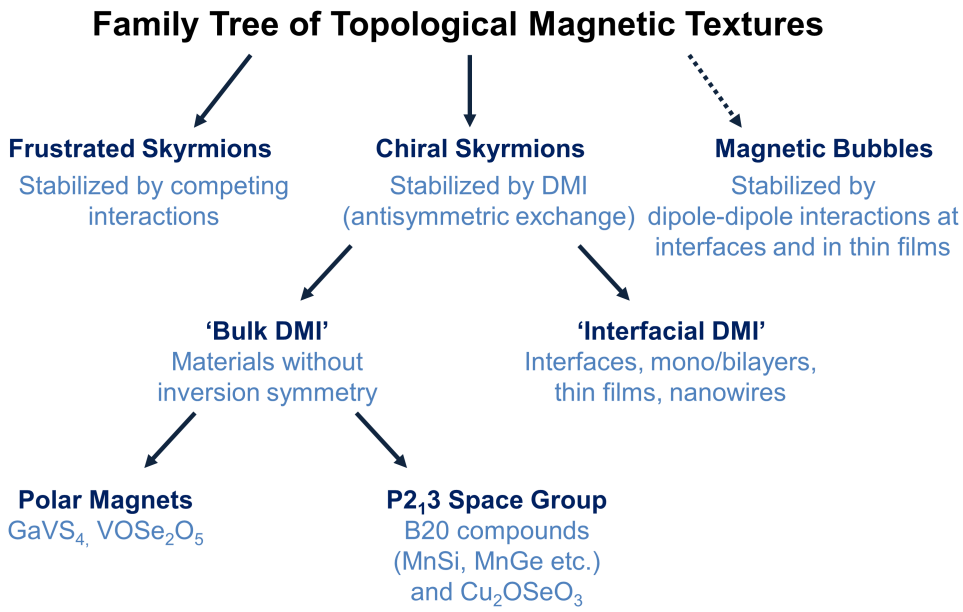

Figure 1.14: Family tree of topologically protected magnetic textures. The dashed arrow indicates that only some bubbles have non-trivial topology and can thus be qualified as topological magnetic textures.

skyrmions. One of the first experimental realizations of skyrmions stabilized by interfacial DM was in a Fe monolayer on a Ir(111) substrate by spin-polarized Scanning Tunneling Microscopy (sp-STM) [27, 41, 271]. These interfacial chiral skyrmions have already been observed at room temperature and without the application of external magnetic fields [272].

In fact, a non-zero DM interaction is not an essential prerequisite to stabilize skyrmions. It has been theoretically established that skyrmions can also be stabilized by competing magnetic interactions [273–276]. These so-called frustrated skyrmions may arise from e.g. next-neighbor ferromagnetic and longer-range anti-ferromagnetic interactions. Although comparable in size, which is in the order of a few nanometers and thus much smaller than their chiral counterparts, these frustrated skyrmions differ from spin vortices stabilized by competing interactions as in re-entrant spin glasses [277].

Another way to stabilize non-trivial magnetic textures is through dipole-dipole interactions. These magnetic textures, often named (chiral) bubbles, are typically much larger in size and are generally speaking not regarded as skyrmions. In general, these bobbers do not necessarily exhibit an integer topological charge,[6] which is a pivotal property of skyrmions [46].

[6] An exception are chiral bobbers.

1.3. OUTLOOK

The experimental discovery of skyrmions in 2009 emanated in an entire new field of research: skyrmionics. Since then, significant advances have been made. Skyrmions have been detected in many other materials, new types of skyrmions have been discovered experimentally, as well as that numerous studies have reinforced our general understanding of these quasi-particles and their host materials. In addition, enormous steps have been set in the creation, detection and control of the skyrmion's position and size, both at low and at room temperatures, which is vital for their future application in green spintronics and in information storage devices. At this moment, prototype devices as skyrmion racetrack memory [49, 278–285], skyrmion logic gates [286–289] and skyrmion radio frequency (rf) devices [290–293] have already been conceptualized and developed. However, the developed devices are still in their infancy and important steps as for example a more accurate control of the size of magnetic skyrmions have to be set prior to their successful application in commercially available products.

Besides the fact that skyrmions have already been observed in a dozen of (bulk) materials, the number of skyrmion host materials is still relatively small and (mainly) limited to ferromagnets. Pioneering efforts have already been made in the conceptualizations of anti-ferromagnetic skyrmions [294–297], but their experimental observation is awaiting. Another method to greatly expand the number of skyrmionic materials is by considering another stabilization mechanism than the DM interaction. As briefly touched upon before, skyrmions can be stabilized by means of competing magnetic interactions, which does not require a non-centrosymmetric crystal structure and can therefore significantly enlarge the scope of skyrmion hosting materials. In particular, these frustrated skyrmions are expected to be smaller than their chiral counter parts which makes them even more promising for applications in information storage. However, up to today these frustrated skyrmions have not been observed experimentally.

It is not only the number of skyrmion hosting materials that remains relatively limited, but also the number of different types of experimentally observed skyrmions. As shown in Box 3, other symmetries of skyrmions may exist that have not (yet) been observed experimentally. Moreover, the three dimensional generalization of the two dimensional magnetic skyrmion, named Hopfion, has been reported for liquid crystals [298], but not in magnetic systems so far, and therefore awaits further experimental and theoretical attention [299–306].

REFERENCES

[1] T. H. R. Skyrme, *A non-linear field theory,* Proceedings of the Royal Society Londen A **260**, 127 (1961).

[2] T. H. R. Skyrme, *Particle states of a quantized meson field,* Proceedings of the Royal Society Londen A **262**, 237 (1961).

[3] T. H. R. Skyrme, *A unified field theory of mesons and baryons,* Nuclear Physics **31**, 556 (1962).

[4] M. Rho and I. Zahed, *The Multifaceted Skyrmion*, 2nd ed. (World Scientific, Singapore, 2016).

[5] S. L. Sondhi, A. Karlhede, S. A. Kivelson, and E. H. Rezayi, *Skyrmions and the crossover from the integer to fractional quantum Hall effect at small Zeeman energies,* Physical Review B **47**, 16419 (1993).

[6] A. Schmeller, J. P. Eisenstein, L. N. Pfeiffer, and K. W. West, *Evidence for skyrmions and single spin flips in the integer quantized Hall effect,* Physical Review Letters **75**, 4290 (1995).

[7] H. A. Fertig, L. Brey, R. Côté, A. H. MacDonald, A. Karlhede, and S. L. Sondhi, *Hartree-Fock theory of Skyrmions in quantum Hall ferromagnets,* Physical Review B **55**, 10671 (1997).

[8] K. Yang, S. D. Sarma, and A. H. MacDonald, *Collective modes and skyrmion excitations in graphene SU(4) quantum Hall ferromagnets,* Physical Review B **74**, 075423 (2006).

[9] D. C. Wright and N. D. Mermin, *Crystalline liquids: the blue phases,* Reviews of Modern Physics **61**, 385 (1989).

[10] A. N. Bogdanov, U. K. Rößler, and A. A. Shestakov, *Skyrmions in nematic liquid crystals,* Physical Review E **67**, 016602 (2003).

[11] J.-i. Fukuda and S. Žumer, *Quasi-two-dimensional Skyrmion lattices in a chiral nematic liquid crystal,* Nature Communications **2**, 246 (2011).

[12] A. O. Leonov, I. E. Dragunov, U. K. Rößler, and A. N. Bogdanov, *Theory of skyrmion states in liquid crystals,* Physical Review E **90**, 042502 (2014).

[13] P. J. Ackerman, T. Boyle, and I. I. Smalyukh, *Squirming motion of baby skyrmions in nematic fluids,* Nature Communications **8**, 673 (2017).

[14] U. Al Khawaja and H. Stoof, *Skyrmions in a ferromagnetic Bose-Einstein condensate,* Nature **411**, 918 (2001).

[15] L. S. Leslie, A. Hansen, K. C. Wright, B. M. Deutsch, and N. P. Bigelow, *Creation and detection of skyrmions in a Bose-Einstein condensate,* Physical Review Letters **103**, 250401 (2009).

[16] T.-L. Ho, *Spinor Bose condensates in optical traps,* Physical Review Letters **81**, 742 (1998).

[17] S. Tsesses, E. Ostrovsky, K. Cohen, B. Gjonaj, N. Lindner, and G. Bartal, *Optical skyrmion lattice in evanescent electromagnetic fields,* Science **15**, eaau0227 (2018).

[18] A. N. Bogdanov and D. A. Yablonskii, *Thermodynamically stable 'vortices' in magnetically ordered crystals. the mixed state of magnets,* Zh. Eksp. Teor. Fiz **95**, 182 (1989).

[19] A. N. Bogdanov and D. A. Yablonskii, *Contribution to the theory of inhomogeneous states of magnets in the region of magnetic-field-induced phase transitions. Mixed state of antiferromagnets,* Journal of Experimental and Theoretical Physics **69**, 142 (1989).

[20] A. N. Bogdanov and A. Hubert, *Thermodynamically stable magnetic vortex states in magnetic crystals,* Journal of Magnetism and Magnetic Materials **138**, 255 (1994).

[21] A. N. Bogdanov and U. K. Rößler, *Chiral symmetry breaking in magnetic thin films and multilayers,* Physical Review Letters **87**, 037203 (2001).

[22] A. N. Bogdanov, U. K. Rößler, M. Wolf, and K.-H. Müller, *Magnetic structures and reorientation transitions in noncentrosymmetric uniaxial antiferromagnets,* Physical Review B **66**, 214410 (2002).

[23] U. K. Rößler, A. N. Bogdanov, and C. Pfleiderer, *Spontaneous skyrmion ground states in magnetic metals,* Nature **442**, 797 (2006).

[24] S. Mühlbauer, B. Binz, F. Jonietz, C. Pfleiderer, A. Rosch, A. Neubauer, R. Georgii, and P. Böni, *Skyrmion lattice in a chiral magnet,* Science **323**, 915 (2009).

[25] K. Everschor, *Current-induced dynamics of chiral magnetic structures: skyrmions, emergent electrodynamics and spin-transfer torques*, Ph.D. thesis, Universität zu Köln (2012).

[26] C. Schütte, *Skyrmions and Monopoles in Chiral Magnets & Correlated Heterostructures*, Ph.D. thesis, Universität zu Köln (2014).

[27] P. Milde, D. Köhler, J. Seidel, L. M. Eng, A. Bauer, A. Chacon, J. Kindervater, S. Mühlbauer, C. Pfleiderer, S. Buhrandt, *et al.*, *Unwinding of a skyrmion lattice by magnetic monopoles,* Science **340**, 1076 (2013).

[28] X. Z. Yu, Y. Onose, N. Kanazawa, J. H. Park, J. H. Han, Y. Matsui, N. Nagaosa, and Y. Tokura, *Real-space observation of a two-dimensional skyrmion crystal,* Nature **465**, 901 (2010).

[29] X. Z. Yu, N. Kanazawa, Y. Onose, K. Kimoto, W. Z. Zhang, S. Ishiwata, Y. Matsui, and Y. Tokura, *Near room-temperature formation of a skyrmion crystal in thin-films of the helimagnet FeGe,* Nature Materials **10**, 106 (2011).

[30] S. Seki, X. Z. Yu, S. Ishiwata, and Y. Tokura, *Observation of skyrmions in a multiferroic material,* Science **336**, 198 (2012).

[31] S. Seki, J.-H. Kim, D. S. Inosov, R. Georgii, B. Keimer, S. Ishiwata, and Y. Tokura, *Formation and rotation of skyrmion crystal in the chiral-lattice insulator Cu_2OSeO_3,* Physical Review B **85**, 220406 (2012).

[32] T. Adams, A. Chacon, M. Wagner, A. Bauer, G. Brandl, B. Pedersen, H. Berger, P. Lemmens, and C. Pfleiderer, *Long-wavelength helimagnetic order and skyrmion lattice phase in Cu_2OSeO_3,* Physical Review Letters **108**, 237204 (2012).

[33] Y. Tokunaga, X. Z. Yu, J. S. White, H. M. Rønnow, D. Morikawa, Y. Taguchi, and Y. Tokura, *A new class of chiral materials hosting magnetic skyrmions beyond room temperature,* Nature Communications **6**, 7638 (2015).

[34] K. Karube, J. S. White, D. Morikawa, M. Bartkowiak, A. Kikkawa, Y. Tokunaga, T. Arima, H. M. Rønnow, Y. Tokura, and Y. Taguchi, *Skyrmion formation in a bulk chiral magnet at zero magnetic field and above room temperature,* Physical Review Materials **1**, 074405 (2017).

[35] D. Morikawa, X. Yu, K. Karube, Y. Tokunaga, Y. Taguchi, T.-h. Arima, and Y. Tokura, *Deformation of Topologically-Protected Supercooled Skyrmions in a Thin Plate of Chiral Magnet $Co_8Zn_8Mn_4$,* Nano Letters **17**, 1637 (2017).

[36] I. Kézsmárki, S. Bordács, P. Milde, E. Neuber, L. M. Eng, J. S. White, H. M. Rønnow, C. D. Dewhurst, M. Mochizuki, K. Yanai, *et al.*, *Néel-type skyrmion lattice with confined orientation in the polar magnetic semiconductor GaV_4S_8,* Nature Materials **14**, 1116 (2015).

[37] S. Bordács, A. Butykai, B. Szigeti, J. S. White, R. Cubitt, A. O. Leonov, S. Widmann, D. Ehlers, H.-A. K. Nidda, V. Tsurkan, A. Loidl, and I. Kézsmárki, *Equilibrium Skyrmion Lattice Ground State in a Polar Easy-plane Magnet,* Scientific Reports **7**, 7584 (2017).

[38] S. Widmann, E. Ruff, A. Günther, H.-A. Krug von Nidda, P. Lunkenheimer, V. Tsurkan, S. Bordács, I. Kézsmárki, and A. Loidl, *On the multiferroic skyrmion-host GaV_4S_8,* Philosophical Magazine **97**, 3428 (2017).

[39] T. Kurumaji, T. Nakajima, V. Ukleev, A. Feoktystov, T.-h. Arima, K. Kakurai, and Y. Tokura, *Néel-Type Skyrmion Lattice in the Tetragonal Polar Magnet $VOSe_2O_5$,* Physical Review Letters **119**, 237201 (2017).

[40] A. K. Nayak, V. Kumar, T. Ma, P. Werner, E. Pippel, R. Sahoo, F. Damay, U. K. Rößler, C. Felser, and S. S. P. Parkin, *Magnetic Antiskyrmions Above Toom Temperature in Tetragonal Heusler Materials,* Nature **548**, 561 (2017).

[41] N. Romming, C. Hanneken, M. Menzel, J. E. Bickel, B. Wolter, K. von Bergmann, A. Kubetzka, and R. Wiesendanger, *Writing and deleting single magnetic skyrmions,* Science **341**, 636 (2013).

[42] N. Nagaosa and Y. Tokura, *Topological properties and dynamics of magnetic skyrmions,* Nature Nanotechnology **8**, 899 (2013).

[43] S. Seki and M. Mochizuki, *Skyrmions in Magnetic Materials* (Springer, 2015).

[44] A. Bauer and C. Pfleiderer, *Generic aspects of skyrmion lattices in chiral magnets,* in *Topological Structures in Ferroic Materials* (Springer, 2016) pp. 1–28.

[45] W. Jiang, G. Chen, K. Liu, J. Zang, S. G. E. te Velthuis, and A. Hoffmann, *Skyrmions in magnetic multilayers,* Physics Reports **704**, 1 (2017).

[46] A. Fert, N. Reyren, and V. Cros, *Magnetic skyrmions: Advances in Physics and Potential Applications,* Nature Materials **2**, 201731 (2017).

[47] N. S. Kiselev, A. N. Bogdanov, R. Schäfer, and U. Rößler, *Chiral skyrmions in thin magnetic films: new objects for magnetic storage technologies?* Journal of Physics D: Applied Physics **44**, 392001 (2011).

[48] X. Z. Yu, N. Kanazawa, W. Z. Zhang, T. Nagai, T. Hara, K. Kimoto, Y. Matsui, Y. Onose, and Y. Tokura, *Skyrmion flow near room temperature in an ultralow current density,* Nature Communications **3**, 988 (2012).

[49] A. Fert, V. Cros, and J. Sampaio, *Skyrmions on the track,* Nature Nanotechnology **8**, 152 (2013).

[50] J. Iwasaki, M. Mochizuki, and N. Nagaosa, *Current-induced skyrmion dynamics in constricted geometries,* Nature Nanotechnology **8**, 742 (2013).

[51] J. Hagemeister, N. Romming, K. von Bergmann, E. Y. Vedmedenko, and R. Wiesendanger, *Stability of single skyrmionic bits,* Nature Communications **6** (2015).

[52] R. Wiesendanger, *Nanoscale magnetic skyrmions in metallic films and multilayers: a new twist for spintronics,* Nature Reviews Materials **1**, 16044 (2016).

[53] A. O. Leonov, J. C. Loudon, and A. N. Bogdanov, *Spintronics via non-axisymmetric chiral skyrmions,* Applied Physics Letters **109**, 172404 (2016).

[54] F. Büttner, I. Lemesh, and G. S. D. Beach, *Theory of isolated magnetic skyrmions: From fundamentals to room temperature applications,* Scientific Reports **8**, 4464 (2018).

[55] I. E. Dzyaloshinskii, *A thermodynamic theory of "weak" ferromagnetism of antiferromagnetics,* Journal of Physics and Chemistry of Solids **4**, 241 (1958).

[56] T. Moriya, *Anisotropic Superexchange Interaction and Weak Ferromagnetism,* Physical Review **120**, 91 (1960).

[57] P. Bak and M. H. Jensen, *Theory of helical magnetic structures and phase transitions in MnSi and FeGe,* Journal of Physics C: Solid State Physics **13**, L881 (1980).

[58] K. Motoya, H. Yasuoka, Y. Nakamura, and J. H. Wernick, *Helical spin structure in MnSi-NMR studies,* Solid State Communications **19**, 529 (1976).

[59] S. Kusaka, K. Yamamoto, T. Komatsubara, and Y. Ishikawa, *Ultrasonic study of magnetic phase diagram of MnSi,* Solid State Communications **20**, 925 (1976).

[60] Y. Ishikawa, K. Tajima, D. Bloch, and M. Roth, *Helical spin structure in manganese silicide MnSi,* Solid State Communications **19**, 525 (1976).

[61] Y. Ishikawa, G. Shirane, J. A. Tarvin, and M. Kohgi, *Magnetic excitations in the weak itinerant ferromagnet MnSi,* Physical Review B **16**, 4956 (1977).

[62] Y. Ishikawa, T. Komatsubara, and D. Bloch, *Magnetic phase diagram of MnSi,* Physica B+C **86**, 401 (1977).

[63] B. Lebech, P. Harris, J. S. Pedersen, K. Mortensen, C. I. Gregory, N. R. Bernhoeft, M. Jermy, and S. A. Brown, *Magnetic phase diagram of MnSi,* Journal of Magnetism and Magnetic Materials **140**, 119 (1995).

[64] P. Harris, B. Lebech, H. S. Shim, K. Mortensen, and J. S. Pedersen, *Small-angle neutron-scattering studies of the magnetic phase diagram of MnSi,* Physica B: Condensed Matter **213**, 375 (1995).

[65] T. Moriya, *Spin fluctuations in itinerant electron magnetism*, Vol. 56 (Springer Science & Business Media, 2012).

[66] *3D Image of a hand,* http://www.3dscanstore.com/index.php?route=product/product&product_id=540 (2018), accessed: 2018-07-30.

[67] F. Qian, L. J. Bannenberg, H. Wilhelm, G. Chaboussant, L. M. DeBeer-Schmitt, M. P. Schmidt, A. Aqeel, T. T. M. Palstra, E. H. Brück, A. J. E. Lefering, C. Pappas, M. Mostovoy, and A. O. Leonov, *New magnetic phase of the chiral skyrmion material* Cu_2OSeO_3*,* Science Advances **4**, eaat7323 (2018).

[68] K. Kadowaki, K. Okuda, and M. Date, *Magnetization and magnetoresistance of MnSi. I,* Journal of the Physical Society of Japan **51**, 2433 (1982).

[69] S. Buhrandt and L. Fritz, *Skyrmion lattice phase in three-dimensional chiral magnets from Monte Carlo simulations,* Physical Review B **88**, 195137 (2013).

[70] A. B. Butenko, A. A. Leonov, U. K. Rößler, and A. N. Bogdanov, *Stabilization of skyrmion textures by uniaxial distortions in noncentrosymmetric cubic helimagnets,* Physical Review B **82**, 052403 (2010).

[71] U. K. Rößler, A. A. Leonov, and A. N. Bogdanov, *Chiral skyrmionic matter in noncentrosymmetric magnets,* in *Journal of Physics: Conference Series*, Vol. 303 (IOP Publishing, 2011) p. 012105.

[72] A. Bauer and C. Pfleiderer, *Magnetic phase diagram of MnSi inferred from magnetization and ac susceptibility,* Physical Review B **85**, 214418 (2012).

[73] A. Chacon, L. Heinen, M. Halder, A. Bauer, W. Simeth, S. Mühlbauer, H. Berger, M. Garst, A. Rosch, and C. Pfleiderer, *Observation of two independent skyrmion phases in a chiral magnetic material,* Nature Physics **14**, 936 (2018).

[74] A. Chacon, A. Bauer, T. Adams, F. Rucker, G. Brandl, R. Georgii, M. Garst, and C. Pfleiderer, *Uniaxial pressure dependence of magnetic order in MnSi,* Physical Review Letters **115**, 267202 (2015).

[75] Y. Nii, T. Nakajima, A. Kikkawa, Y. Yamasaki, K. Ohishi, J. Suzuki, Y. Taguchi, T. Arima, Y. Tokura, and Y. Iwasa, *Uniaxial stress control of skyrmion phase,* Nature Communications **6**, 8539 (2015).

[76] I. Levatić, P. Popčević, V. Šurija, A. Kruchkov, H. Berger, A. Magrez, J. S. White, H. M. Rønnow, and I. Živković, *Dramatic pressure-driven enhancement of bulk skyrmion stability,* Scientific Reports **6**, 21347 (2016).

[77] J. S. White, K. Prša, P. Huang, A. A. Omrani, I. Živković, M. Bartkowiak, H. Berger, A. Magrez, J. Gavilano, G. Nagy, *et al.*, *Electric-field-induced skyrmion distortion and giant lattice rotation in the magnetoelectric insulator Cu_2OSeO_3,* Physical Review Letters **113**, 107203 (2014).

[78] Y. Okamura, F. Kagawa, S. Seki, and Y. Tokura, *Transition to and from the skyrmion lattice phase by electric fields in a magnetoelectric compound,* Nature Communications **7**, 12669 (2016).

[79] A. J. Kruchkov, J. S. White, M. Bartkowiak, I. Živković, A. Magrez, and H. M. Rønnow, *Direct electric field control of the skyrmion phase in a magnetoelectric insulator,* Scientific Reports **8**, 10466 (2018).

[80] J. S. White, I. Živković, A. Kruchkov, M. Bartkowiak, A. Magrez, and H. M. Rønnow, *Electric-Field-Driven Topological Phase Switching and Skyrmion-Lattice Metastability in Magnetoelectric Cu_2OSeO_3,* Physical Review Applied **10**, 014021 (2018).

[81] H. Oike, A. Kikkawa, N. Kanazawa, Y. Taguchi, M. Kawasaki, Y. Tokura, and F. Kagawa, *Interplay between topological and thermodynamic stability in a metastable magnetic skyrmion lattice,* Nature Physics **12**, 62 (2016).

[82] K. Karube, J. S. White, N. Reynolds, J. L. Gavilano, H. Oike, A. Kikkawa, F. Kagawa, Y. Tokunaga, H. M. Rønnow, Y. Tokura, *et al.*, *Robust metastable skyrmions and their triangular-square lattice structural transition in a high-temperature chiral magnet,* Nature Materials **15**, 3752 (2016).

[83] L. J. Bannenberg, K. Kakurai, F. Qian, E. Lelièvre-Berna, C. D. Dewhurst, Y. Onose, Y. Endoh, Y. Tokura, and C. Pappas, *Extended skyrmion lattice scattering and long-time memory in the chiral magnet $Fe_{1-x}Co_xSi$,* Physical Review B **94**, 104406 (2016).

[84] T. Nakajima, H. Oike, A. Kikkawa, E. P. Gilbert, N. Booth, K. Kakurai, Y. Taguchi, Y. Tokura, F. Kagawa, and T. Arima, *Skyrmion Lattice Structural Transition in MnSi,* Science Advances **3**, e1602562 (2017).

[85] A. Bauer, A. Chacon, M. Halder, and C. Pfleiderer, *Skyrmion Lattices Far from Equilibrium,* in *Topology in Magnetism* (Springer, 2018) pp. 151–176.

[86] J. Wild, T. N. G. Meier, S. Pöllath, M. Kronseder, A. Bauer, A. Chacon, M. Halder, M. Schowalter, A. Rosenauer, J. Zweck, J. Müller, A. Rosch, C. Pfleiderer, and C. H. Back, *Entropy-limited topological protection of skyrmions,* Science Advances **3**, e1701704 (2017).

[87] W. Münzer, A. Neubauer, T. Adams, S. Mühlbauer, C. Franz, F. Jonietz, R. Georgii, P. Böni, B. Pedersen, M. Schmidt, *et al.*, *Skyrmion lattice in the doped semiconductor $Fe_{1-x}Co_xSi$,* Physical Review B **81**, 041203 (2010).

[88] K. Makino, J. D. Reim, D. Higashi, D. Okuyama, T. J. Sato, Y. Nambu, E. P. Gilbert, N. Booth, S. Seki, and Y. Tokura, *Thermal stability and irreversibility of skyrmion-lattice phases in Cu_2OSeO_3,* Physical Review B **95**, 134412 (2017).

[89] J. D. Reim, K. Makino, D. Higashi, Y. Nambu, D. Okuyama, T. J. Sato, E. P. Gilbert, N. Booth, and S. Seki, *Impact of minute-time-scale kinetics on the stabilization of the skyrmion-lattice in Cu_2OSeO_3,* in *Journal of Physics: Conference Series*, Vol. 828 (IOP Publishing, 2017) p. 012004.

[90] L. J. Bannenberg, F. Qian, R. M. Dalgliesh, N. Martin, G. Chaboussant, M. Schmidt, D. L. Schlagel, T. A. Lograsso, H. Wilhelm, and C. Pappas, *Reorientations, relaxations, metastabilities, and multidomains of skyrmion lattices,* Physical Review B **96**, 184416 (2017).

[91] S. V. Grigoriev, S. V. Maleyev, A. I. Okorokov, Y. O. Chetverikov, R. Georgii, P. Böni, D. Lamago, H. Eckerlebe, and K. Pranzas, *Critical fluctuations in MnSi near T_C: A polarized neutron scattering study,* Physical Review B **72**, 134420 (2005).

[92] C. Pappas, E. Lelievre-Berna, P. Falus, P. M. Bentley, E. Moskvin, S. Grigoriev, P. Fouquet, and B. Farago, *Chiral paramagnetic skyrmion-like phase in MnSi,* Physical Review Letters **102**, 197202 (2009).

[93] H. Wilhelm, M. Baenitz, M. Schmidt, U. K. Rößler, A. A. Leonov, and A. N. Bogdanov, *Precursor Phenomena at the Magnetic Ordering of the Cubic Helimagnet FeGe,* Physical Review Letters **107**, 127203 (2011).

[94] M. Janoschek, M. Garst, A. Bauer, P. Krautscheid, R. Georgii, P. Böni, and C. Pfleiderer, *Fluctuation-induced first-order phase transition in Dzyaloshinskii-Moriya helimagnets,* Physical Review B **87**, 134407 (2013).

[95] I. Živković, J. White, H. M. Rønnow, K. Prša, and H. Berger, *Critical scaling in the cubic helimagnet Cu_2OSeO_3,* Physical Review B **89**, 060401 (2014).

[96] L. J. Bannenberg, K. Kakurai, P. Falus, E. Lelièvre-Berna, R. M. Dalgliesh, C. D. Dewhurst, F. Qian, Y. Onose, Y. Endoh, Y. Tokura, and C. Pappas, *Universality of the helimagnetic transition in cubic chiral magnets: Small angle neutron scattering and neutron spin echo spectroscopy studies of FeCoSi,* Physical Review B **95**, 144433 (2017).

[97] C. Pappas, L. J. Bannenberg, E. Lelièvre-Berna, F. Qian, C. D. Dewhurst, R. M. Dalgliesh, D. L. Schlagel, T. A. Lograsso, and P. Falus, *Magnetic Fluctuations, Precursor Phenomena and Phase Transition in MnSi under Magnetic Field,* Physical Review Letters **119**, 047203 (2017).

[98] L. J. Bannenberg, R. M. Dalgliesh, T. Wolf, F. Weber, and C. Pappas, *Evolution of helimagnetic correlations in $Mn_{1-x}Fe_xSi$ with doping: A small-angle neutron scattering study,* Physical Review B **98**, 184431 (2018).

[99] *M. Mostovoy, Private Communication,* (2018).

[100] K. Motoya, H. Yasuoka, Y. Nakamura, and W. JH, *Magnetic Properties of MnSi–CoSi Solid Solution Alloys,* Journal Of The Physical Society Of Japan **44**, 1525 (1978).

[101] J. Beille, J. Voiron, and M. Roth, *Long period helimagnetism in the cubic B20 $Fe_xCo_{1-x}Si$ and $Co_xMn_{1-x}Si$ alloys,* Solid State Communications **47**, 399 (1983).

[102] A. Bauer, A. Neubauer, C. Franz, W. Münzer, M. Garst, and C. Pfleiderer, *Quantum phase transitions in single-crystal $Mn_{1-x}Fe_xSi$ and $Mn_{1-x}Co_xSi$: Crystal growth, magnetization, ac susceptibility, and specific heat,* Physical Review B **82**, 064404 (2010).

[103] C. Dhital, M. A. Khan, M. Saghayezhian, W. A. Phelan, D. P. Young, R. Y. Jin, and J. F. DiTusa, *Effect of negative chemical pressure on the prototypical itinerant magnet MnSi,* Physical Review B **95**, 024407 (2017).

[104] C. Dhital, L. DeBeer-Schmitt, Q. Zhang, W. Xie, D. P. Young, and J. F. DiTusa, *Exploring the origins of the Dzyaloshinskii-Moriya interaction in MnSi,* Physical Review B **96**, 214425 (2017).

[105] S. V. Grigoriev, N. M. Potapova, S.-A. Siegfried, V. A. Dyadkin, E. Moskvin, V. Dmitriev, D. Menzel, C. D. Dewhurst, D. Chernyshov, R. A. Sadykov, *et al.*, *Chiral Properties of Structure and Magnetism in $Mn_{1-x}Fe_xGe$ Compounds: When the Left and the Right are Fighting, Who Wins?* Physical Review Letters **110**, 207201 (2013).

[106] N. Kanazawa, K. Shibata, and Y. Tokura, *Variation of spin–orbit coupling and related properties in skyrmionic system $Mn_{1-x}Fe_xGe$,* New Journal of Physics **18**, 045006 (2016).

[107] S. V. Grigoriev, E. Altynbaev, S.-A. Siegfried, K. A. Pshenichnyi, D. Honnecker, A. Heinemann, and A. V. Tsvyashchenko, *Spin-wave dynamics in Mn-doped FeGe helimagnet: Small-angle neutron scattering study,* Journal of Magnetism and Magnetic Materials **459**, 159 (2018).

[108] N. Martin, M. Deutsch, G. Chaboussant, F. Damay, P. Bonville, L. N. Fomicheva, A. V. Tsvyashchenko, U. K. Rössler, and I. Mirebeau, *Long-period helical structures and twist-grain boundary phases induced by chemical substitution in the Mn_{1-x}(Co, Rh)$_x$Ge chiral magnet,* Physical Review B **96**, 020413 (2017).

[109] S. V. Grigoriev, S.-A. Siegfried, E. V. Altynbayev, N. M. Potapova, V. Dyadkin, E. V. Moskvin, D. Menzel, A. Heinemann, S. N. Axenov, L. N. Fomicheva, *et al.*, *Flip of spin helix chirality and ferromagnetic state in $Fe_{1-x}Co_xGe$ compounds,* Physical Review B **90**, 174414 (2014).

[110] M. J. Stolt, X. Sigelko, N. Mathur, and S. Jin, *Chemical Pressure Stabilization of the Cubic B20 Structure in Skyrmion Hosting $Fe_{1-x}Co_xGe$ Alloys,* Chemistry of Materials **30**, 1146 (2018).

[111] B. Lebech, J. Bernhard, and T. Freltoft, *Magnetic structures of cubic FeGe studied by small-angle neutron scattering,* Journal of Physics: Condensed Matter **1**, 6105 (1989).

[112] K. D. Chandrasekhar, H. C. Wu, C. L. Huang, and H. D. Yang, *Effects of Jahn–Teller distortion on the skyrmion stability of $(Cu_{1-x}Ni_x)_2OSeO_3$,* Journal of Materials Chemistry C **4**, 5270 (2016).

[113] H. C. Wu, T. Y. Wei, K. D. Chandrasekhar, T. Y. Chen, H. Berger, and H. D. Yang, *Unexpected observation of splitting of skyrmion phase in Zn doped Cu_2OSeO_3,* Scientific reports **5**, 13579 (2015).

[114] A. Štefančič, S. H. Moody, T. J. Hicken, M. T. Birch, G. Balakrishnan, S. A. Barnett, M. Crisanti, J. S. O. Evans, S. J. R. Holt, K. J. A. Franke, P. D. Hatton, B. M. Huddart, M. R. Lees, F. L. Pratt, C. C. Tang, M. N. Wilson, F. Xiao, and T. Lancaster, *Origin of skyrmion lattice phase splitting in Zn-substituted Cu_2OSeO_3,* Physical Review Materials **2**, 111402 (2018).

[115] H. C. Wu, K. D. Chandrasekhar, T. Y. Wei, K. J. Hsieh, T. Y. Chen, H. Berger, and H. D. Yang, *Physical pressure and chemical expansion effects on the skyrmion phase in Cu_2OSeO_3,* Journal of Physics D: Applied Physics **48**, 475001 (2015).

[116] S. Grigoriev, S. Maleyev, A. I. Okorokov, Y. O. Chetverikov, and H. Eckerlebe, *Field-induced reorientation of the spin helix in MnSi near T_C,* Physical Review B **73**, 224440 (2006).

[117] S. V. Grigoriev, S. V. Maleyev, A. I. Okorokov, Y. O. Chetverikov, P. Böni, R. Georgii, D. Lamago, H. Eckerlebe, and K. Pranzas, *Magnetic structure of MnSi under an applied field probed by polarized small-angle neutron scattering,* Physical Review B **74**, 214414 (2006).

[118] F. Jonietz, S. Mühlbauer, C. Pfleiderer, A. Neubauer, W. Münzer, A. Bauer, T. Adams, R. Georgii, P. Böni, R. A. Duine, *et al.*, *Spin transfer torques in MnSi at ultralow current densities,* Science **330**, 1648 (2010).

[119] T. Adams, S. Mühlbauer, C. Pfleiderer, F. Jonietz, A. Bauer, A. Neubauer, R. Georgii, P. Böni, U. Keiderling, K. Everschor, *et al.*, *Long-range crystalline nature of the skyrmion lattice in MnSi,* Physical Review Letters **107**, 217206 (2011).

[120] C. Pappas, E. Lelievre-Berna, P. Bentley, P. Falus, P. Fouquet, and B. Farago, *Magnetic fluctuations and correlations in MnSi: Evidence for a chiral skyrmion spin liquid phase,* Physical Review B **83**, 224405 (2011).

[121] S. V. Grigoriev, N. M. Potapova, E. V. Moskvin, V. A. Dyadkin, C. Dewhurst, and S. V. Maleyev, *Hexagonal spin structure of A-phase in MnSi: Densely packed skyrmion quasiparticles or two-dimensionally modulated spin superlattice?* JETP Letters **100**, 216 (2014).

[122] J. Kindervater, W. Häußler, M. Janoschek, C. Pfleiderer, P. Böni, and M. Garst, *Critical spin-flip scattering at the helimagnetic transition of MnSi,* Physical Review B **89**, 180408 (2014).

[123] S. V. Grigoriev, A. S. Sukhanov, E. V. Altynbaev, S.-A. Siegfried, A. Heinemann, P. Kizhe, and S. V. Maleyev, *Spin waves in full-polarized state of Dzyaloshinskii-Moriya helimagnets: Small-angle neutron scattering study,* Physical Review B **92**, 220415 (2015).

[124] S. Mühlbauer, J. Kindervater, T. Adams, A. Bauer, U. Keiderling, and C. Pfleiderer, *Kinetic small angle neutron scattering of the skyrmion lattice in MnSi,* New Journal of Physics **18**, 075017 (2016).

[125] A. Bauer, A. Chacon, M. Wagner, M. Halder, R. Georgii, A. Rosch, C. Pfleiderer, and M. Garst, *Symmetry breaking, slow relaxation dynamics, and topological defects at the field-induced helix reorientation in MnSi,* Physical Review B **95**, 024429 (2017).

[126] N. M. Chubova, E. V. Moskvin, V. Dyad'kin, C. Dewhurst, S. V. Maleev, and S. V. Grigor'ev, *Role of critical fluctuations in the formation of a skyrmion lattice in MnSi,* Journal of Experimental and Theoretical Physics **125**, 789 (2017).

[127] Y. Luo, S.-Z. Lin, D. M. Fobes, Z. Liu, E. D. Bauer, J. B. Betts, A. Migliori, J. D. Thompson, M. Janoschek, and B. Maiorov, *Anisotropic magnetocrystalline coupling of the skyrmion lattice in MnSi,* Physical Review B **97**, 104423 (2018).

[128] T. Reimann, A. Bauer, C. Pfleiderer, P. Böni, P. Trtik, A. Tremsin, M. Schulz, and S. Mühlbauer, *Neutron diffractive imaging of the skyrmion lattice nucleation in MnSi,* Physical Review B **97**, 020406 (2018).

[129] C. N. Guy, *Low field magnetic studies of a single crystal of MnSi,* Solid State Communications **25**, 169 (1978).

[130] M. L. Plumer, *Magnetic susceptibility and spin dynamics of MnSi,* Journal of Physics C: Solid State Physics **17**, 4663 (1984).

[131] L. Zhang, D. Menzel, C. Jin, H. Du, M. Ge, C. Zhang, L. Pi, M. Tian, and Y. Zhang, *Critical behavior of the single-crystal helimagnet MnSi,* Physical Review B **91**, 024403 (2015).

[132] S. M. Stishov, A. E. Petrova, S. Khasanov, G. K. Panova, A. A. Shikov, J. C. Lashley, D. Wu, and T. A. Lograsso, *Magnetic phase transition in the itinerant helimagnet MnSi: Thermodynamic and transport properties,* Physical Review B **76**, 052405 (2007).

[133] S. M. Stishov, A. E. Petrova, S. Khasanov, G. K. Panova, A. A. Shikov, J. C. Lashley, D. Wu, and T. A. Lograsso, *Heat capacity and thermal expansion of the itinerant helimagnet MnSi,* Journal of Physics: Condensed Matter **20**, 235222 (2008).

[134] A. Bauer, M. Garst, and C. Pfleiderer, *Specific heat of the skyrmion lattice phase and field-induced tricritical point in MnSi,* Physical Review Letters **110**, 177207 (2013).

[135] A. Neubauer, C. Pfleiderer, B. Binz, A. Rosch, R. Ritz, P. G. Niklowitz, and P. Böni, *Topological Hall effect in the A phase of MnSi,* Physical Review Letters **102**, 186602 (2009).

[136] V. V. Glushkov, I. I. Lobanova, V. Y. Ivanov, and S. V. Demishev, *Anomalous Hall effect in MnSi: Intrinsic to extrinsic crossover,* JETP Letters **101**, 459 (2015).

[137] M. L. Plumer and M. B. Walker, *Wavevector and spin reorientation in MnSi,* Journal of Physics C: Solid State Physics **14**, 4689 (1981).

[138] M. L. Plumer and M. B. Walker, *Magnetoelastic effects in the spin-density wave phase of MnSi,* Journal of Physics C: Solid State Physics **15**, 7181 (1982).

[139] G. Shirane, R. Cowley, C. Majkrzak, J. Sokoloff, B. Pagonis, C. H. Perry, and Y. Ishikawa, *Spiral magnetic correlation in cubic MnSi,* Physical Review B **28**, 6251 (1983).

[140] Y. Ishikawa, Y. Noda, Y. J. Uemura, C. F. Majkrzak, and G. Shirane, *Paramagnetic spin fluctuations in the weak itinerant-electron ferromagnet MnSi,* Physical Review B **31**, 5884 (1985).

[141] E. Franus-Muir, M. Plumer, and E. Fawcett, *Magnetostriction in the spin-density-wave phase of MnSi,* Journal of Physics C: Solid State Physics **17**, 1107 (1984).

[142] S. V. Grigoriev, S. V. Maleyev, E. V. Moskvin, V. A. Dyadkin, P. Fouquet, and H. Eckerlebe, *Crossover behavior of critical helix fluctuations in MnSi,* Physical Review B **81**, 144413 (2010).

[143] S. V. Demishev, A. V. Semeno, A. V. Bogach, V. V. Glushkov, N. E. Sluchanko, N. A. Samarin, and A. L. Chernobrovkin, *Is MnSi an itinerant-electron magnet? Results of ESR experiments,* JETP Letters **93**, 213 (2011).

[144] S. V. Demishev, V. V. Glushkov, I. I. Lobanova, M. A. Anisimov, V. Y. Ivanov, T. V. Ishchenko, M. S. Karasev, N. A. Samarin, N. E. Sluchanko, V. M. Zimin, *et al.*, *Magnetic phase diagram of MnSi in the high-field region,* Physical Review B **85**, 045131 (2012).

[145] A. E. Petrova and S. M. Stishov, *Field evolution of the magnetic phase transition in the helical magnet MnSi inferred from ultrasound studies,* Physical Review B **91**, 214402 (2015).

[146] M. Reiner, A. Bauer, M. Leitner, T. Gigl, W. Anwand, M. Butterling, A. Wagner, P. Kudejova, C. Pfleiderer, and C. Hugenschmidt, *Positron spectroscopy of point defects in the skyrmion-lattice compound MnSi,* Scientific Reports **6**, 29109 (2016).

[147] S. M. Stishov and A. E. Petrova, *Vollhardt invariant and phase transition in the helical itinerant magnet MnSi,* Physical Review B **94**, 140406 (2016).

[148] P. D. de Réotier, A. Maisuradze, A. Yaouanc, B. Roessli, A. Amato, D. Andreica, and G. Lapertot, *Unconventional magnetic order in the conical state of MnSi,* Physical Review B **95**, 180403 (2017).

[149] T. Weber, J. Waizner, G. S. Tucker, R. Georgii, M. Kugler, A. Bauer, C. Pfleiderer, M. Garst, and P. Böni, *Field dependence of nonreciprocal magnons in chiral MnSi,* Physical Review B **97**, 224403 (2018).

[150] K. Tsuruta, M. Mito, H. Deguchi, J. Kishine, Y. Kousaka, J. Akimitsu, and K. Inoue, *Nonlinear magnetic responses at the phase boundaries around helimagnetic and skyrmion lattice phases in MnSi: Evaluation of robustness of noncollinear spin texture,* Physical Review B **97**, 094411 (2018).

[151] J. S. White, I. Levatić, A. A. Omrani, N. Egetenmeyer, K. Prša, I. Živković, J. Gavilano, J. Kohlbrecher, M. Bartkowiak, H. Berger, *et al., Electric field control of the skyrmion lattice in Cu_2OSeO_3,* Journal of Physics: Condensed Matter **24**, 432201 (2012).

[152] V. Dyadkin, K. Prša, S. V. Grigoriev, J. S. White, P. Huang, H. M. Rønnow, A. Magrez, C. D. Dewhurst, and D. Chernyshov, *Chirality of structure and magnetism in the magnetoelectric compound Cu_2OSeO_3,* Physical Review B **89**, 140409 (2014).

[153] K. Kohn, *A new ferrimagnet Cu_2OSeO_3,* Journal of the Physical Society of Japan **42**, 2065 (1977).

[154] C. L. Huang, K. F. Tseng, C. C. Chou, S. Mukherjee, J. L. Her, Y. H. Matsuda, K. Kindo, H. Berger, and H. D. Yang, *Observation of a second metastable spin-ordered state in ferrimagnet Cu_2OSeO_3,* Physical Review B **83**, 052402 (2011).

[155] I. Živković, D. Pajić, T. Ivek, and H. Berger, *Two-step transition in a magnetoelectric ferrimagnet Cu_2OSeO_3,* Physical Review B **85**, 224402 (2012).

[156] A. A. Omrani, J. White, K. Prša, I. Živković, H. Berger, A. Magrez, Y.-H. Liu, J. H. Han, and H. M. Rønnow, *Exploration of the helimagnetic and skyrmion lattice phase diagram in Cu_2OSeO_3 using magnetoelectric susceptibility,* Physical Review B **89**, 064406 (2014).

[157] I. Levatić, V. Šurija, H. Berger, and I. Živković, *Dissipation processes in the insulating skyrmion compound Cu_2OSeO_3,* Physical Review B **90**, 224412 (2014).

[158] F. Qian, H. Wilhelm, A. Aqeel, T. T. M. Palstra, A. J. E. Lefering, E. H. Brück, and C. Pappas, *Phase diagram and magnetic relaxation phenomena in Cu_2OSeO_3,* Physical Review B **94**, 064418 (2016).

[159] V. A. Sidorov, A. E. Petrova, P. S. Berdonosov, V. A. Dolgikh, and S. M. Stishov, *Comparative study of helimagnets MnSi and Cu_2OSeO_3 at high pressures,* Physical Review B **89**, 100403 (2014).

[160] J.-W. G. Bos, C. V. Colin, and T. T. M. Palstra, *Magnetoelectric coupling in the cubic ferrimagnet Cu_2OSeO_3,* Physical Review B **78**, 094416 (2008).

[161] A. Maisuradze, Z. Guguchia, B. Graneli, H. M. Rønnow, H. Berger, and H. Keller, *μSR investigation of magnetism and magnetoelectric coupling in Cu_2OSeO_3,* Physical Review B **84**, 064433 (2011).

[162] Y. Onose, Y. Okamura, S. Seki, S. Ishiwata, and Y. Tokura, *Observation of magnetic excitations of skyrmion crystal in a helimagnetic insulator Cu_2OSeO_3,* Physical Review Letters **109**, 037603 (2012).

[163] S. Seki, S. Ishiwata, and Y. Tokura, *Magnetoelectric nature of skyrmions in a chiral magnetic insulator Cu_2OSeO_3*, Physical Review B **86**, 060403 (2012).

[164] A. Maisuradze, A. Shengelaya, H. Berger, D. M. Djokić, and H. Keller, *Magnetoelectric coupling in single crystal Cu_2OSeO_3 studied by a novel electron spin resonance technique,* Physical Review Letters **108**, 247211 (2012).

[165] O. Janson, I. Rousochatzakis, A. A. Tsirlin, M. Belesi, A. O. Leonov, U. K. Rößler, J. van den Brink, and H. Rosner, *The Quantum Nature of Skyrmions and Half-Skyrmions in Cu_2OSeO_3*, Nature Commununications **5** (2014).

[166] M. C. Langner, S. Roy, S. K. Mishra, J. C. T. Lee, X. W. Shi, M. Hossain, Y. D. Chuang, S. Seki, Y. Tokura, S. D. Kevan, *et al.*, *Coupled skyrmion sublattices in Cu_2OSeO_3*, Physical Review Letters **112**, 167202 (2014).

[167] T. Lancaster, R. C. Williams, I. O. Thomas, F. Xiao, F. L. Pratt, S. J. Blundell, J. C. Loudon, T. Hesjedal, S. J. Clark, P. D. Hatton, *et al.*, *Transverse field muon-spin rotation signature of the skyrmion-lattice phase in Cu_2OSeO_3*, Physical Review B **91**, 224408 (2015).

[168] Y. Okamura, F. Kagawa, S. Seki, M. Kubota, M. Kawasaki, and Y. Tokura, *Microwave magnetochiral dichroism in the chiral-lattice magnet Cu_2OSeO_3*, Physical Review Letters **114**, 197202 (2015).

[169] D. Hirobe, Y. Shiomi, Y. Shimada, J.-i. Ohe, and E. Saitoh, *Generation of spin currents in the skyrmion phase of a helimagnetic insulator Cu_2OSeO_3*, Journal of Applied Physics **117**, 053904 (2015).

[170] M. Mochizuki, *Microwave Magnetochiral Effect in Cu_2OSeO_3*, Physical Review Letters **114**, 197203 (2015).

[171] G. S. Tucker, J. White, J. Romhányi, D. Szaller, I. Kézsmárki, B. Roessli, U. Stuhr, A. Magrez, F. Groitl, P. Babkevich, *et al.*, *Spin excitations in the skyrmion host Cu_2OSeO_3*, Physical Review B **93**, 054401 (2016).

[172] A. Aqeel, N. Vlietstra, A. Roy, M. Mostovoy, B. J. van Wees, and T. T. M. Palstra, *Electrical detection of spiral spin structures in Pt | Cu_2OSeO_3 heterostructures,* Physical Review B **94**, 134418 (2016).

[173] S. L. Zhang, A. Bauer, D. M. Burn, P. Milde, E. Neuber, L. M. Eng, H. Berger, C. Pfleiderer, G. V. V. van der Laan, and T. Hesjedal, *Multidomain Skyrmion Lattice State in Cu_2OSeO_3*, Nano Letters **16**, 3285 (2016).

[174] S. L. Zhang, A. Bauer, H. Berger, C. Pfleiderer, G. V. Van Der Laan, and T. Hesjedal, *Resonant elastic x-ray scattering from the skyrmion lattice in Cu_2OSeO_3*, Physical Review B **93**, 214420 (2016).

[175] P. Y. Portnichenko, J. Romhányi, Y. A. Onykiienko, A. Henschel, M. Schmidt, A. S. Cameron, M. A. Surmach, J. A. Lim, J. T. Park, A. Schneidewind, *et al.*, *Magnon spectrum of the helimagnetic insulator Cu_2OSeO_3*, Nature Communications **7**, 10725 (2016).

[176] S. L. Zhang, G. Van Der Laan, and T. Hesjedal, *Direct experimental determination of the topological winding number of skyrmions in Cu_2OSeO_3*, Nature Communications **8**, 14619 (2017).

[177] D. M. Evans, J. A. Schiemer, M. Schmidt, H. Wilhelm, and M. A. Carpenter, *Defect dynamics and strain coupling to magnetization in the cubic helimagnet Cu_2OSeO_3*, Physical Review B **95**, 094426 (2017).

[178] N. J. Laurita, G. G. Marcus, B. A. Trump, J. Kindervater, M. B. Stone, T. M. McQueen, C. L. Broholm, and N. P. Armitage, *Low-energy magnon dynamics and magneto-optics of the skyrmionic Mott insulator Cu_2OSeO_3*, Physical Review B **95**, 235155 (2017).

[179] N. Prasai, B. A. Trump, G. G. Marcus, A. Akopyan, S. X. Huang, T. M. McQueen, and J. L. Cohn, *Ballistic magnon heat conduction and possible Poiseuille flow in the helimagnetic insulator Cu_2OSeO_3*, Physical Review B **95**, 224407 (2017).

[180] M. L. Plumer, *Wavevector and spin-flop transitions in cubic FeGe,* Journal of Physics: Condensed Matter **2**, 7503 (1990).

[181] E. Moskvin, S. V. Grigoriev, V. Dyadkin, H. Eckerlebe, M. Baenitz, M. Schmidt, and H. Wilhelm, *Complex chiral modulations in FeGe close to magnetic ordering,* Physical Review Letters **110**, 077207 (2013).

[182] S.-A. Siegfried, A. S. Sukhanov, E. V. Altynbaev, D. Honecker, A. Heinemann, A. V. Tsvyashchenko, and S. V. Grigoriev, *Spin-wave dynamics in the helimagnet FeGe studied by small-angle neutron scattering,* Physical Review B **95**, 134415 (2017).

[183] L. Lundgren, K. Blom, and O. Beckman, *Magnetic susceptibility measurements on cubic FeGe,* Physics Letters A **28**, 175 (1968).

[184] L. Lundgren, O. Beckman, V. Attia, S. P. Bhattacheriee, and M. Richardson, *Helical spin arrangement in cubic FeGe,* Physica Scripta **1**, 69 (1970).

[185] H. Wilhelm, M. Baenitz, M. Schmidt, C. Naylor, R. Lortz, U. K. Rößler, A. A. Leonov, and A. N. Bogdanov, *Confinement of chiral magnetic modulations in the precursor region of FeGe,* Journal of Physics: Condensed Matter **24**, 294204 (2012).

[186] L. Cevey, H. Wilhelm, M. Schmidt, and R. Lortz, *Thermodynamic investigations in the precursor region of FeGe,* Physica Status Solidi (b) **250**, 650 (2013).

[187] L. Zhang, H. Han, M. Ge, H. Du, C. Jin, W. Wei, J. Fan, C. Zhang, L. Pi, and Y. Zhang, *Critical phenomenon of the near room temperature skyrmion material FeGe,* Scientific Reports **6**, 22397 (2016).

[188] L. Xu, H. Han, J. Fan, D. Shi, D. Hu, H. Du, L. Zhang, Y. Zhang, and H. Yang, *Magnetic entropy change and accurate determination of curie temperature in single-crystalline helimagnet fege,* Europhysics Letters **117**, 47004 (2017).

[189] L. Xu, J. Fan, W. Sun, Y. Zhu, D. Hu, J. Liu, Y. Ji, D. Shi, and H. Yang, *Magnetic field-driven 3D-Heisenberg-like phase transition in single crystalline helimagnet FeGe,* Applied Physics Letters **111**, 052406 (2017).

[190] H. Wilhelm, A. O. Leonov, U. K. Rößler, P. Burger, F. Hardy, C. Meingast, M. E. Gruner, W. Schnelle, M. Schmidt, and M. Baenitz, *Scaling study and thermodynamic properties of the cubic helimagnet FeGe,* Physical Review B **94**, 144424 (2016).

[191] R. Wäppling and L. Häggström, *Mössbauer study of cubic FeGe,* Physics Letters A **28**, 173 (1968).

[192] R. Wäppling, L. Häggström, and E. Karlsson, *Magnetic Properties of FeGe Studied by Mössbauer Effect,* Physica Scripta **2**, 233 (1970).

[193] S. Haraldson and U. Smith, *The microwave resonance line shape in ferromagnetic cubic FeGe,* Journal of Physics and Chemistry of Solids **35**, 1237 (1974).

[194] S. Haraldson, L. Pettersson, and S. M. Bhagat, *Frequency and temperature dependence of spin resonances in cubic FeGe,* Journal of Magnetic Resonance (1969) **32**, 115 (1978).

[195] H. Yamada, K. Terao, H. Ohta, and E. Kulatov, *Electronic structure and magnetism of FeGe with B20-type structure,* Physica B: Condensed Matter **329**, 1131 (2003).

[196] O. L. Makarova, A. V. Tsvyashchenko, G. Andre, F. Porcher, L. N. Fomicheva, N. Rey, and I. Mirebeau, *Neutron diffraction study of the chiral magnet MnGe,* Physical Review B **85**, 205205 (2012).

[197] N. Kanazawa, J.-H. Kim, D. S. Inosov, J. S. White, N. Egetenmeyer, J. L. Gavilano, S. Ishiwata, Y. Onose, T. Arima, B. Keimer, *et al.*, *Possible skyrmion-lattice ground state in the B20 chiral-lattice magnet MnGe as seen via small-angle neutron scattering,* Physical Review B **86**, 134425 (2012).

[198] M. Deutsch, O. L. Makarova, T. C. Hansen, M. T. Fernandez-Diaz, V. A. Sidorov, A. V. Tsvyashchenko, N. Fomicheva, F. Porcher, S. Petit, K. Koepernik, *et al.*, *Two-step pressure-induced collapse of magnetic order in the MnGe chiral magnet,* Physical Review B **89**, 180407 (2014).

[199] J. F. DiTusa, S. B. Zhang, K. Yamaura, Y. Xiong, J. C. Prestigiacomo, B. W. Fulfer, P. W. Adams, M. I. Brickson, D. A. Browne, C. Capan, *et al.*, *Magnetic, thermodynamic, and electrical transport properties of the noncentrosymmetric B 20 germanides MnGe and CoGe,* Physical Review B **90**, 144404 (2014).

[200] N. Kanazawa, Y. Onose, T. Arima, D. Okuyama, K. Ohoyama, S. Wakimoto, K. Kakurai, S. Ishiwata, and Y. Tokura, *Large topological Hall effect in a short-period helimagnet MnGe,* Physical Review Letters **106**, 156603 (2011).

[201] N. Martin, M. Deutsch, F. Bert, D. Andreica, A. Amato, P. Bonfa, R. De Renzi, U. K. Rößler, P. Bonville, L. N. Fomicheva, *et al.*, *Magnetic ground state and spin fluctuations in MnGe chiral magnet as studied by muon spin rotation,* Physical Review B **93**, 174405 (2016).

[202] N. Martin, M. Deutsch, J.-P. Itie, J.-P. Rueff, U. Rössler, K. Koepernik, L. N. Fomicheva, A. V. Tsvyashchenko, and I. Mirebeau, *Magnetovolume effect, macroscopic hysteresis, and moment collapse in the paramagnetic state of cubic MnGe under pressure,* Physical Review B **93**, 214404 (2016).

[203] J. Beille, J. Voiron, F. Towfiq, M. Roth, and Z. Y. Zhang, *Helimagnetic structure of the $Fe_{1-x}Co_xSi$ alloys,* Journal of Physics F: Metal Physics **11**, 2153 (1981).

[204] K. Ishimoto, M. Ohashi, H. Yamauchi, and Y. Yamaguchi, *Itinerant Electron Ferromagnetism in $Fe_{1-x}Co_xSi$ Studied by Polarized Neutron Diffraction,* Journal of the Physical Society of Japan **61**, 2503 (1992).

[205] S. V. Grigoriev, V. A. Dyadkin, D. Menzel, J. Schoenes, Y. O. Chetverikov, A. I. Okorokov, H. Eckerlebe, and S. V. Maleyev, *Magnetic structure of $Fe_{1-x}Co_xSi$ in a magnetic field studied via small-angle polarized neutron diffraction,* Physical Review B **76**, 224424 (2007).

[206] S. V. Grigoriev, D. Chernyshov, V. A. Dyadkin, V. Dmitriev, S. V. Maleyev, E. V. Moskvin, D. Menzel, J. Schoenes, and H. Eckerlebe, *Crystal handedness and spin helix chirality in $Fe_{1-x}Co_xSi$,* Physical Review Letters **102**, 037204 (2009).

[207] S.-A. Siegfried, E. V. Altynbaev, N. M. Chubova, V. Dyadkin, D. Chernyshov, E. V. Moskvin, D. Menzel, A. Heinemann, A. Schreyer, and S. V. Grigoriev, *Controlling the Dzyaloshinskii-Moriya interaction to alter the chiral link between structure and magnetism for $Fe_{1-x}Co_xSi$,* Physical Review B **91**, 184406 (2015).

[208] M. Motokawa, S. Kawarazaki, H. Nojiri, and T. Inoue, *Magnetization measurements of $Fe_{1-x}Co_xSi$,* Journal of Magnetism and Magnetic Materials **70**, 245 (1987).

[209] H. Watanabe, i. Tazuke, and H. Nakajima, *Helical Spin Resonance and Magntization Measurement in Itinerant Helimagnet $Fe_{1-x}Co_xSi$ ($0.3 \leq x \leq 0.85$),* Journal of the Physical Society of Japan **54**, 3978 (1985).

[210] M. K. Chattopadhyay, S. B. Roy, and S. Chaudhary, *Magnetic properties of $Fe_{1-x}Co_xSi$ alloys,* Physical Review B **65**, 132409 (2002).

[211] M. K. Chattopadhyay, S. B. Roy, S. Chaudhary, K. J. Singh, and A. K. Nigam, *Magnetic response of $Fe_{1-x}Co_xSi$ alloys: A detailed study of magnetization and magnetoresistance,* Physical Review B **66**, 174421 (2002).

[212] A. Bauer, M. Garst, and C. Pfleiderer, *History dependence of the magnetic properties of single-crystal $Fe_{1-x}Co_xSi$,* Physical Review B **93**, 235144 (2016).

[213] Y. Onose, N. Takeshita, C. Terakura, H. Takagi, and Y. Tokura, *Doping dependence of transport properties in $Fe_{1-x}Co_xSi$,* Physical Review B **72**, 224431 (2005).

[214] K. Ishimoto, Y. Yamaguchi, J. Suzuki, M. Arai, M. Furusaka, and Y. Endoh, *Small-angle neutron diffraction from the helical magnet $Fe_{0.8}Co_{0.2}Si$,* Physica B: Condensed Matter **213**, 381 (1995).

[215] H. Watanabe, *Helical spin resonance in the cubic B-20 $Fe_{0.8}Co_{0.2}Si$ single crystal with a long-period helical spin structure,* Journal of the Physical Society of Japan **58**, 1035 (1989).

[216] M. Takeda, Y. Endoh, K. Kakurai, Y. Onose, J. Suzuki, and Y. Tokura, *Nematic-to-smectic transition of magnetic texture in conical state,* Journal of the Physical Society of Japan **78**, 093704 (2009).

[217] T. Y. Ou-Yang, G. J. Shu, C. D. Hu, and F. C. Chou, *Dynamic susceptibility study on the skyrmion phase stability of $Fe_{0.7}Co_{0.3}Si$,* Journal of Applied Physics **117**, 123903 (2015).

[218] L. J. Bannenberg, A. J. E. Lefering, K. Kakurai, Y. Onose, Y. Endoh, Y. Tokura, and C. Pappas, *Magnetic relaxation phenomena in the chiral magnet $Fe_{1-x}Co_xSi$: An ac susceptibility study,* Physical Review B **94**, 134433 (2016).

[219] S. S. Samatham and K. G. Suresh, *Critical exponents and universal magnetic behavior of noncentrosymmetric $Fe_{0.6}Co_{0.4}Si$,* Journal of Physics: Condensed Matter **30**, 215802 (2018).

[220] S. V. Grigoriev, V. A. Dyadkin, E. V. Moskvin, D. Lamago, T. Wolf, H. Eckerlebe, and S. V. Maleyev, *Helical spin structure of $Mn_{1-y}Fe_ySi$ under a magnetic field: Small angle neutron diffraction study,* Physical Review B **79**, 144417 (2009).

[221] S. V. Grigoriev, D. Chernyshov, V. A. Dyadkin, V. Dmitriev, E. V. Moskvin, D. Lamago, T. Wolf, D. Menzel, J. Schoenes, S. V. Maleyev, *et al.*, *Interplay between crystalline chirality and magnetic structure in $Mn_{1-x}Fe_xSi$,* Physical Review B **81**, 012408 (2010).

[222] S. V. Grigoriev, E. V. Moskvin, V. A. Dyadkin, D. Lamago, T. Wolf, H. Eckerlebe, and S. V. Maleyev, *Chiral criticality in the doped helimagnets $Mn_{1-y}Fe_ySi$,* Physical Review B **83**, 224411 (2011).

[223] S. V. Demishev, I. I. Lobanova, V. V. Glushkov, T. V. Ischenko, N. E. Sluchanko, V. A. Dyadkin, N. M. Potapova, and S. V. Grigoriev, *Quantum bicriticality in $Mn_{1-x}Fe_xSi$ solid solutions: Exchange and percolation effects,* JETP Letters **98**, 829 (2013).

[224] S. V. Demishev, A. N. Samarin, J. Huang, V. V. Glushkov, I. I. Lobanova, N. E. Sluchanko, N. M. Chubova, V. A. Dyadkin, S. V. Grigoriev, M. Y. Kagan, *et al.*, *Magnetization of $Mn_{1-x}Fe_xSi$ in high magnetic fields up to 50 T: Possible evidence of a field-induced Griffiths phase,* JETP letters **104**, 116 (2016).

[225] B. J. Chapman, M. G. Grossnickle, T. Wolf, and M. Lee, *Large enhancement of emergent magnetic fields in MnSi with impurities and pressure,* Physical Review B **88**, 214406 (2013).

[226] C. Franz, F. Freimuth, A. Bauer, R. Ritz, C. Schnarr, C. Duvinage, T. Adams, S. Blügel, A. Rosch, Y. Mokrousov, *et al.*, *Real-space and reciprocal-space Berry phases in the Hall effect of $Mn_{1-x}Fe_xSi$,* Physical Review Letters **112**, 186601 (2014).

[227] V. V. Glushkov, I. I. Lobanova, V. Y. Ivanov, V. V. Voronov, V. A. Dyadkin, N. M. Chubova, S. V. Grigoriev, and S. V. Demishev, *Scrutinizing Hall effect in $Mn_{1-x}Fe_xSi$: Fermi surface evolution and hidden quantum criticality,* Physical Review Letters **115**, 256601 (2015).

[228] S. Waki, Y. Nishihara, and S. Ogawa, *Spin fluctuation effects in $Mn_{1-x}Fe_xSi$,* Journal of Magnetism and Magnetic Materials **31**, 275 (1983).

[229] Y. Nishihara, S. Waki, and S. Ogawa, *Mössbauer study of $Mn_{1-x}Fe_xS$ in external magnetic fields,* Physical Review B **30**, 32 (1984).

[230] C. Meingast, Q. Zhang, T. Wolf, F. Hardy, K. Grube, W. Knafo, P. Adelmann, P. Schweiss, and H. v. Löhneysen, *Resistivity of $Mn_{1-x}Fe_xSi$ Single Crystals: Evidence for Quantum Critical Behavior,* Properties and Applications of Thermoelectric Materials , 261 (2009).

[231] S. V. Demishev, A. N. Samarin, V. V. Glushkov, M. I. Gilmanov, I. I. Lobanova, N. A. Samarin, A. V. Semeno, N. E. Sluchanko, N. M. Chubova, V. A. Dyadkin, and S. V. Grigoriev, *Anomalous spin relaxation and quantum criticality in $Mn_{1-x}Fe_xSi$ solid solutions,* JETP Letters **100**, 28 (2014).

[232] T. Goko, C. J. Arguello, A. Hamann, T. Wolf, M. Lee, D. Reznik, A. Maisuradze, R. Khasanov, E. Morenzoni, and Y. J. Uemura, *Restoration of quantum critical behavior by disorder in pressure-tuned (Mn, Fe) Si,* npj Quantum Materials **2**, 44 (2017).

[233] S. V. Demishev, I. I. Lobanova, A. V. Bogach, V. V. Glushkov, V. Y. Ivanov, T. Ischenko, N. Samarin, N. E. Sluchanko, S. Gabani, E. Čižmár, *et al.*, *Effect of a magnetic field on the intermediate phase in $Mn_{1-x}Fe_xSi$: Spin-liquid versus fluctuations scenario,* JETP letters **103**, 321 (2016).

[234] P. E. Siegfried, A. C. Bornstein, A. C. Treglia, T. Wolf, and M. Lee, *Multiple magnetic states within the A phase determined by field-orientation dependence of $Mn_{0.9}Fe_{0.1}Si$,* Physical Review B **96**, 220410 (2017).

[235] M. B. Walker, *Phason instabilities and successive wave-vector reorientation phase transitions in MnSi,* Physical Review B **40**, 9315 (1989).

[236] C. Pfleiderer, G. J. McMullan, S. R. Julian, and G. G. Lonzarich, *Magnetic quantum phase transition in MnSi under hydrostatic pressure,* Physical Review B **55**, 8330 (1997).

[237] B. Fåk, R. A. Sadykov, J. Flouquet, and G. Lapertot, *Pressure dependence of the magnetic structure of the itinerant electron magnet MnSi,* Journal of Physics: Condensed Matter **17**, 1635 (2005).

[238] S. A. Brazovskii, *Phase transition of an isotropic system to a nonuniform state,* Soviet Journal of Experimental and Theoretical Physics **41**, 85 (1975).

[239] A. M. Belemuk and S. M. Stishov, *Phase transitions in chiral magnets from Monte Carlo simulations,* Physical Review B **95**, 224433 (2017).

[240] C. Pfleiderer, S. Julian, and G. G. Lonzarich, *Non-fermi-liquid nature of the normal state of itinerant-electron ferromagnets,* Nature **414**, 427 (2001).

[241] N. Doiron-Leyraud, I. R. Walker, L. Taillefer, M. J. Steiner, S. R. Julian, and G. G. Lonzarich, *Fermi-liquid breakdown in the paramagnetic phase of a pure metal,* Nature **425**, 595 (2003).

[242] M. Lee, W. Kang, Y. Onose, Y. Tokura, and N. P. Ong, *Unusual Hall Effect Anomaly in MnSi under Pressure,* Phyisical Review Letters **102**, 1 (2009).

[243] R. Ritz, M. Halder, M. Wagner, C. Franz, A. Bauer, and C. Pfleiderer, *Formation of a topological non-Fermi liquid in MnSi,* Nature **497**, 231 (2013).

[244] W. Yu, F. Zamborszky, J. D. Thompson, J. L. Sarrao, M. E. Torelli, Z. Fisk, and S. E. Brown, *Phase inhomogeneity of the itinerant ferromagnet MnSi at high pressures,* Physical Review Letters **92**, 086403 (2004).

[245] Y. J. Uemura, T. Goko, I. M. Gat-Malureanu, J. P. Carlo, P. L. Russo, A. T. Savici, A. Aczel, G. J. MacDougall, J. A. Rodriguez, G. M. Luke, *et al.*, *Phase separation and suppression of critical dynamics at quantum phase transitions of MnSi and* $(Sr_{1-x}Ca_x)\,RuO_3$, Nature Physics **3**, 29 (2007).

[246] D. Andreica, P. D. de Réotier, A. Yaouanc, A. Amato, and G. Lapertot, *Absence of magnetic phase separation in MnSi under pressure,* Physical Review B **81**, 060412 (2010).

[247] C. Pfleiderer, D. Reznik, L. Pintschovius, H. v Lohneysen, *et al.*, *Partial order in the non-Fermi-liquid phase of MnSi,* Nature **427**, 227 (2004).

[248] C. Pfleiderer, P. Böni, T. Keller, U. K. Rößler, and A. Rosch, *Non-fermi liquid metal without quantum criticality,* Science **316**, 1871 (2007).

[249] C. Thessieu, C. Pfleiderer, A. N. Stepanov, and J. Flouquet, *Field dependence of the magnetic quantum phase transition in MnSi,* Journal of Physics: Condensed Matter **9**, 6677 (1997).

[250] A. O. Leonov and K. Inoue, *Homogeneous and heterogeneous nucleation of skyrmions in thin layers of cubic helimagnets,* arXiv preprint arXiv:1805.04990 (2018).

[251] E. Ruff, P. Lunkenheimer, A. Loidl, H. Berger, and S. Krohns, *Magnetoelectric effects in the skyrmion host material* Cu_2OSeO_3, Scientific Reports **5**, 15025 (2015).

[252] P. Milde, E. Neuber, A. Bauer, C. Pfleiderer, H. Berger, and L. M. Eng, *Heuristic description of magnetoelectricity of* Cu_2OSeO_3, Nano Letters **16**, 5612 (2016).

[253] M. A. Chernikov, L. Degiorgi, E. Felder, S. Paschen, A. D. Bianchi, H. R. Ott, J. L. Sarrao, Z. Fisk, and D. Mandrus, *Low-temperature transport, optical, magnetic and thermodynamic properties of $Fe_{1-x}Co_xSi$,* Physical Review B **56**, 1366 (1997).

[254] N. Manyala, Y. Sidis, J. F. DiTusa, G. Aeppli, D. P. Young, and Z. Fisk, *Large anomalous Hall effect in a silicon-based magnetic semiconductor,* Nature Materials **3**, 255 (2004).

[255] L. J. Bannenberg, F. Weber, A. J. E. Lefering, T. Wolf, and C. Pappas, *Magnetization and ac susceptibility study of the cubic chiral magnet $Mn_{1-x}Fe_xSi$,* Physical Review B **98**, 184430 (2018).

[256] L. J. Bannenberg, R. M. Dalglies, P. Fouquet, A. J. E. Lefering, T. Wolf, F. Weber, and C. Pappas, *Nuetron Spin Echo Spectroscopy study of $Mn_{1-x}Fe_xSi$,* In Preparation (2018).

[257] A. Tonomura, X. Yu, K. Yanagisawa, T. Matsuda, Y. Onose, N. Kanazawa, H. S. Park, and Y. Tokura, *Real-space observation of skyrmion lattice in helimagnet MnSi thin samples,* Nano Letters **12**, 1673 (2012).

[258] Y. Li, N. Kanazawa, X. Z. Yu, A. Tsukazaki, M. Kawasaki, M. Ichikawa, X. Jin, F. Kagawa, and Y. Tokura, *Robust formation of skyrmions and topological Hall effect anomaly in epitaxial thin films of MnSi,* Physical Review Letters **110**, 117202 (2013).

[259] S. A. Meynell, M. N. Wilson, J. C. Loudon, A. Spitzig, F. N. Rybakov, M. B. Johnson, and T. L. Monchesky, *Hall effect and transmission electron microscopy of epitaxial MnSi thin films,* Physical Review B **90**, 224419 (2014).

[260] A. O. Leonov, Y. Togawa, T. L. Monchesky, A. N. Bogdanov, J. Kishine, Y. Kousaka, M. Miyagawa, T. Koyama, J. Akimitsu, T. Koyama, *et al.*, *Chiral surface twists and skyrmion stability in nanolayers of cubic helimagnets,* Physical Review Letters **117**, 087202 (2016).

[261] Meynell, S A and Wilson, M N and Krycka, K L and Kirby, B J and Fritzsche, Helmut and Monchesky, T L, *Neutron study of in-plane skyrmions in MnSi thin films,* Physical Review B **96**, 054402 (2017).

[262] B. Dupé, M. Hoffmann, C. Paillard, and S. Heinze, *Tailoring magnetic skyrmions in ultra-thin transition metal films,* Nature Communications **5**, 4030 (2014).

[263] M. N. Wilson, A. B. Butenko, A. N. Bogdanov, and T. L. Monchesky, *Chiral skyrmions in cubic helimagnet films: The role of uniaxial anisotropy,* Physical Review B **89**, 094411 (2014).

[264] M. N. Wilson, E. A. Karhu, A. S. Quigley, U. K. Rößler, A. B. Butenko, A. N. Bogdanov, M. D. Robertson, and T. L. Monchesky, *Extended elliptic skyrmion gratings in epitaxial MnSi thin films,* Physical Review B **86**, 144420 (2012).

[265] B. Dupé, G. Bihlmayer, M. Böttcher, S. Blügel, and S. Heinze, *Engineering skyrmions in transition-metal multilayers for spintronics,* Nature Communications **7**, 11779 (2016).

[266] A. Soumyanarayanan, N. Reyren, A. Fert, and C. Panagopoulos, *Emergent phenomena induced by spin–orbit coupling at surfaces and interfaces,* Nature **539**, 509 (2016).

[267] A. Soumyanarayanan, M. Raju, A. G. Oyarce, A. K. C. Tan, M.-Y. Im, A. P. Petrović, P. Ho, K. H. Khoo, M. Tran, C. K. Gan, *et al.*, *Tunable room-temperature magnetic skyrmions in Ir/Fe/Co/Pt multilayers,* Nature Materials **16**, 898 (2017).

[268] M. Hoffmann, B. Zimmermann, G. P. Müller, D. Schürhoff, N. S. Kiselev, C. Melcher, and S. Blügel, *Antiskyrmions stabilized at interfaces by anisotropic Dzyaloshinskii-Moriya interactions,* Nature Communications **8**, 308 (2017).

[269] A. R. Fert, *Magnetic and transport properties of metallic multilayers,* in *Materials Science Forum*, Vol. 59 (Trans Tech Publ, 1990) pp. 439–480.

[270] M. Bode, M. Heide, K. Von Bergmann, P. Ferriani, S. Heinze, G. Bihlmayer, A. Kubetzka, O. Pietzsch, S. Blügel, and R. Wiesendanger, *Chiral magnetic order at surfaces driven by inversion asymmetry,* Nature **447**, 190 (2007).

[271] S. Heinze, K. Von Bergmann, M. Menzel, J. Brede, A. Kubetzka, R. Wiesendanger, G. Bihlmayer, and S. Blügel, *Spontaneous atomic-scale magnetic skyrmion lattice in two dimensions,* Nature Physics **7**, 713 (2011).

[272] O. Boulle, J. Vogel, H. Yang, S. Pizzini, D. de Souza Chaves, A. Locatelli, T. O. Menteş, A. Sala, L. D. Buda-Prejbeanu, O. Klein, *et al.*, *Room-temperature chiral magnetic skyrmions in ultrathin magnetic nanostructures,* Nature Nanotechnology **11**, 449 (2016).

[273] T. Okubo, S. Chung, and H. Kawamura, *Multiple-q states and the skyrmion lattice of the triangular-lattice Heisenberg antiferromagnet under magnetic fields,* Physical Review Letters **108**, 017206 (2012).

[274] A. O. Leonov and M. Mostovoy, *Multiply periodic states and isolated skyrmions in an anisotropic frustrated magnet,* Nature Communications **6**, 8275 (2015).

[275] S.-Z. Lin and S. Hayami, *Ginzburg-Landau theory for skyrmions in inversion-symmetric magnets with competing interactions,* Physical Review B **93**, 064430 (2016).

[276] A. O. Leonov and M. Mostovoy, *Edge states and skyrmion dynamics in nanostripes of frustrated magnets,* Nature Communications **8**, 14394 (2017).

[277] I. Mirebeau, N. Martin, M. Deutsch, L. J. Bannenberg, C. Pappas, G. Chaboussant, R. Cubitt, C. Decorse, and A. O. Leonov, *Spin textures induced by quenched disorder in a reentrant spin glass: Vortices versus "frustrated" skyrmions,* Physical Review B **98**, 014420 (2018).

[278] J. Sampaio, V. Cros, S. Rohart, A. Thiaville, and A. Fert, *Nucleation, stability and current-induced motion of isolated magnetic skyrmions in nanostructures,* Nature Nanotechnology **8**, 839 (2013).

[279] R. Tomasello, E. Martinez, R. Zivieri, L. Torres, M. Carpentieri, and G. Finocchio, *A strategy for the design of skyrmion racetrack memories,* Scientific Reports **4**, 6784 (2014).

[280] X. Zhang, Y. Zhou, M. Ezawa, G. Zhao, and W. Zhao, *Magnetic skyrmion transistor: skyrmion motion in a voltage-gated nanotrack,* Scientific Reports **5**, 11369 (2015).

[281] X. Zhang, G. P. Zhao, H. Fangohr, J. P. Liu, W. X. Xia, J. Xia, and F. J. Morvan, *Skyrmion-skyrmion and skyrmion-edge repulsions in skyrmion-based racetrack memory,* Scientific Reports **5**, 7643 (2015).

[282] W. Koshibae, Y. Kaneko, J. Iwasaki, M. Kawasaki, Y. Tokura, and N. Nagaosa, *Memory functions of magnetic skyrmions,* Japanese Journal of Applied Physics **54**, 053001 (2015).

[283] S. Woo, K. Litzius, B. Krüger, M.-Y. Im, L. Caretta, K. Richter, M. Mann, A. Krone, R. M. Reeve, M. Weigand, *et al., Observation of room-temperature magnetic skyrmions and their current-driven dynamics in ultrathin metallic ferromagnets,* Nature Materials **15**, 501 (2016).

[284] J. Müller, *Magnetic skyrmions on a two-lane racetrack,* New Journal of Physics **19**, 025002 (2017).

[285] P. F. Bessarab, G. P. Müller, I. S. Lobanov, F. N. Rybakov, N. S. Kiselev, H. Jónsson, V. M. Uzdin, S. Blügel, L. Bergqvist, and A. Delin, *Lifetime of racetrack skyrmions,* Scientific Reports **8**, 3433 (2018).

[286] Y. Zhou and M. Ezawa, *A reversible conversion between a skyrmion and a domain-wall pair in a junction geometry,* Nature Communications **5**, 4652 (2014).

[287] X. Zhang, M. Ezawa, and Y. Zhou, *Magnetic skyrmion logic gates: conversion, duplication and merging of skyrmions,* Scientific Reports **5**, 9400 (2015).

[288] X. Zhang, M. Ezawa, D. Xiao, G. P. Zhao, Y. Liu, and Y. Zhou, *All-magnetic control of skyrmions in nanowires by a spin wave,* Nanotechnology **26**, 225701 (2015).

[289] S. Luo, M. Song, X. Li, Y. Zhang, J. Hong, X. Yang, X. Zou, N. Xu, and L. You, *Reconfigurable Skyrmion Logic Gates,* Nano Letters **18**, 1180 (2018).

[290] J.-V. Kim, F. Garcia-Sanchez, J. Sampaio, C. Moreau-Luchaire, V. Cros, and A. Fert, *Breathing modes of confined skyrmions in ultrathin magnetic dots,* Physical Review B **90**, 064410 (2014).

[291] M. Carpentieri, R. Tomasello, R. Zivieri, and G. Finocchio, *Topological, non-topological and instanton droplets driven by spin-transfer torque in materials with perpendicular magnetic anisotropy and Dzyaloshinskii–Moriya Interaction,* Scientific Reports **5**, 16184 (2015).

[292] G. Finocchio, M. Ricci, R. Tomasello, A. Giordano, M. Lanuzza, V. Puliafito, P. Burrascano, B. Azzerboni, and M. Carpentieri, *Skyrmion based microwave detectors and harvesting,* Applied Physics Letters **107**, 262401 (2015).

[293] F. Garcia-Sanchez, J. Sampaio, N. Reyren, V. Cros, and J. V. Kim, *A skyrmion-based spin-torque nano-oscillator,* New Journal of Physics **18**, 075011 (2016).

[294] X. Zhang, Y. Zhou, and M. Ezawa, *Antiferromagnetic skyrmion: stability, creation and manipulation,* Scientific Reports **6**, 24795 (2016).

[295] C. Jin, C. Song, J. Wang, and Q. Liu, *Dynamics of antiferromagnetic skyrmion driven by the spin hall effect,* Applied Physics Letters **109**, 182404 (2016).

[296] R. Keesman, M. Raaijmakers, A. E. Baerends, G. T. Barkema, and R. A. Duine, *Skyrmions in square-lattice antiferromagnets,* Physical Review B **94**, 054402 (2016).

[297] J. Barker and O. A. Tretiakov, *Static and dynamical properties of antiferromagnetic skyrmions in the presence of applied current and temperature,* Physical Review Letters **116**, 147203 (2016).

[298] P. J. Ackerman, J. Van De Lagemaat, and I. I. Smalyukh, *Self-assembly and electrostriction of arrays and chains of hopfion particles in chiral liquid crystals,* Nature communications **6**, 6012 (2015).

[299] H. Hopf, *Über die Abbildungen der dreidimensionalen Sphäre auf die Kugelfläche,* Mathematische Annalen **104**, 637 (1931).

[300] N. R. Cooper, *Propagating magnetic vortex rings in ferromagnets,* Physical Review Letters **82**, 1554 (1999).

[301] A. B. Borisov and F. N. Rybakov, *Dynamical toroidal hopfions in a ferromagnet with easy-axis anisotropy,* JETP letters **90**, 544 (2009).

[302] A. B. Borisov and F. N. Rybakov, *Three-dimensional static vortex solitons in incommensurate magnetic crystals,* Low Temperature Physics **36**, 766 (2010).

[303] P. Sutcliffe, *Skyrmion knots in frustrated magnets,* Physical Review Letters **118**, 247203 (2017).

[304] J.-S. B. Tai and I. I. Smalyukh, *Static Hopf Solitons and Knotted Emergent Fields in Solid-State Noncentrosymmetric Magnetic Nanostructures,* Physical Review Letters **121**, 187201 (2018).

[305] P. Sutcliffe, *Hopfions in chiral magnets,* arXiv preprint arXiv:1806.06458 (2018).

[306] Y. Liu, R. Lake, and J. Zang, *Binding a hopfion in chiral magnet nanodisk,* Physical Review B **98**, 174437 (2018).

2

MAGNETIC RELAXATION PHENOMENA IN THE CHIRAL MAGNET $Fe_{1-x}Co_xSi$: AN AC SUSCEPTIBILITY STUDY

We present a systematic study of the ac susceptibility of the chiral magnet $Fe_{1-x}Co_xSi$ with $x = 0.30$ covering four orders of magnitude in frequencies from 0.1 Hz to 1 kHz, with particular emphasis to the pronounced history dependence. Characteristic relaxation times ranging from a few milliseconds to tens of seconds are observed around the skyrmion lattice A-phase, the helical-to-conical transition and in a region above T_C. The distribution of relaxation frequencies around the A-phase is broad, asymmetric and originates from multiple coexisting relaxation processes. The pronounced dependence of the magnetic phase diagram on the magnetic history and cooling rates as well as the asymmetric frequency dependence and slow dynamics suggest more complicated physical phenomena in $Fe_{0.7}Co_{0.3}Si$ than in other chiral magnets.

2.1. INTRODUCTION

The discovery of skyrmion lattices in cubic helimagnets such as MnSi [2], FeGe [3, 4], Cu_2OSeO_3 [5–7] and $Fe_{1-x}Co_xSi$ [8, 9] has increased the interest in non-centrosymmetric magnetic materials with Dzyaloshinsky-Moriya interactions [10, 11]. The skyrmion lattice phase is a periodic array of spin vortices observed in the A-phase, a region in the magnetic field (B) - temperature (T) phase diagram below the critical temperature T_C, and was first observed in reciprocal space in a single crystal of MnSi by neutron scattering [2] and subsequently in real space in a thin film of $Fe_{0.5}Co_{0.5}Si$ by Lorentz Transmission Microscopy [8].

This chapter has been published in Physical Review B **94**(13), 134433 (2016) [1].

The chiral skyrmions that form the skyrmion lattice are non-coplanar and topologically stable spin textures with dimensions significantly larger than the inter-atomic distances [12–15]. The potential application of skyrmions as low-current high-density information carriers and in other spintronic devices as well as the unexplored magnetic properties drive the scientific interest in this non-conventional magnetic ordering [15–18].

The helical order at zero field is stabilized in $Fe_{1-x}Co_xSi$ for a wide range of chemical substitution of $0.05 < x < 0.8$ [19–21]. As for other members of the B20 group such as MnSi and Cu_2OSeO_3, this helical order is a result of the balance between the strong ferromagnetic and the weaker Dzyaloshinsky-Moriya (DM) interactions that arises from the non-centrosymmetric crystal structure. The B - T phase diagrams of $Fe_{1-x}Co_xSi$ compounds are quantitatively similar to each other and to the other B20 group members. Below T_C, three ordered states dominate the phase diagram: a helical phase occurring at low fields $B < B_{C1}$, where the weak anisotropy fixes the orientation of the helices typically along the ⟨100⟩ or ⟨111⟩ crystallographic directions, a conical phase for intermediate fields $B_{C1} < B < B_{C2}$, where the magnetic field overcomes the anisotropy and orients the helices along the magnetic field, and the A-phase close to T_C, where the skyrmion lattice phase is stabilized. Magnetic fields exceeding B_{C2} overcome the DM interactions inducing a field-polarized state.

The ability to tune important physical properties by chemical substitution as well as the high degree of chemical disorder make $Fe_{1-x}Co_xSi$ of particular interest among the B20 compounds [22]. In particular, the amount of chemical substitution changes both the sign and the magnitude of the DM-interactions. It thus affects the T_C that ranges from a few Kelvin to 50 K and the magnetic chirality which changes from left handed to right-handed at $x = 0.65$ [23]. Additionally, it alters the pitch of the helical ordering from ~30 nm to ~200 nm as this pitch is proportional to the ratio of the ferromagnetic exchange to the DM interactions [20, 24].

Different from the archetype chiral system MnSi and other systems of the same family, $Fe_{1-x}Co_xSi$ appears to have a phase diagram depending on the magnetic history [9, 25, 26] and also on the applied cooling rates through T_C [26]. Additionally, neutron scattering shows that skyrmion lattice correlations may persist down to the lowest temperatures depending on the magnetic history of the sample [9, 26, 27]. Several dc magnetization [19, 21, 25, 28–30] and some ac susceptibility studies have been performed so far, but only with an ac drive frequency of 30 Hz [31] and 1000 Hz [22, 25]. Based on these studies, phase-diagrams have been deduced for a wide range of chemical substitution and field directions but no attention has been devoted to the frequency dependence [25, 31].

The ac susceptibility measurements presented here for $Fe_{0.7}Co_{0.3}Si$ complement previous neutron scattering as well as ac susceptibility studies as they span a broad frequency range of four orders in magnitude, from 0.1 Hz to 1000 Hz and have a particular emphasis on the influence of the magnetic hysteresis and the applied cooling rate. The results confirm the history dependence reported earlier and show a strong dependence of the imaginary component of the ac susceptibility on the ac drive frequency around the A-phase, helical-to-conical transition and in a region above T_C. Around the A-phase, the distribution of relaxation frequencies is found to be broad and asymmetric, indicating

the occurrence of multiple coexisting very slow relaxation processes.

The remainder of this paper is organized as follows. Section 2.2 discusses the experimental details, Section 2.3 the Zero Field Cooled (ZFC) ac susceptibility study at a frequency of 5 Hz and Section 2.4 the magnetic history and cooling rate dependence and the B - T phase diagrams for both ZFC and Field Cooling (FC) at a frequency of 5 Hz. Section 2.5 confers the frequency dependence, Section 2.6 shows B - T and phase diagrams for f = 0.1, 5 and 100 Hz after ZFC. Conclusions are given in Section 2.7.

2.2. EXPERIMENTAL DETAILS

The measurements were performed on a 20 mg single crystal of $Fe_{0.7}Co_{0.3}Si$ originating from the same batch as the crystal studied previously by neutron scattering [26, 32]. The crystal quality was tested with Laue X-ray diffraction and it was aligned with the [110] direction vertical within ± 10°. The sample has an irregular shape and its longest direction was roughly vertically oriented.

The real χ' and imaginary χ'' components of the ac susceptibility were measured with a MPMS-XL Quantum Design SQUID magnetometer using the extraction method. The dc field was applied along the vertical axis and the ac field of $0.1 \leq B_{AC} \leq 0.4$ mT was oriented parallel to the dc field. Several measurements in and around the A-phase at T = 41 K revealed that the susceptibility was independent of the ac field and subsequent measurements where performed with B_{ac} = 0.4 mT. Three specific protocols that are similar to those adopted for the previous neutron scattering experiment [26] have been used:

- ZFC temperature scans: the sample was cooled from 60 K to 6 K under zero field. Then a magnetic field was applied and the signal was recorded by stepwise increasing the temperature. The system was brought to thermal equilibrium before the measurement at each temperature commenced.
- FC temperature scans: the sample was brought to 60 K where a magnetic field was applied. The temperature was then decreased stepwise and the measurements commenced once the system reached the thermal equilibrium.
- Fast FC temperature scans: the sample was brought to 60 K where a magnetic field was applied. The temperature was then decreased with 10 $Kmin^{-1}$ to 30 K. Subsequently, the signal was recorded by decreasing the temperature stepwise and after waiting for the system to reach thermal equilibrium.

2.3. ZFC AC SUSCEPTIBILITY AT 5 HZ

Fig. 2.1(a) depicts the temperature dependence of χ' and χ'' at B = 0 mT and f = 5 Hz. A maximum in χ' at $T_C \approx 43.2$ K marks the transition to the helical order, which is characterized by a pitch of $\ell \sim 40$ nm [26, 32]. In the helical ordered phase, χ' drops by about 30% from its maximum value and remains almost constant for temperatures below 40 K, which is quantitatively similar to the behavior reported in the literature [22].

At higher temperatures, the susceptibility follows a Curie-Weiss behavior as can be inferred from the linear relation of the inverse susceptibility with temperature displayed

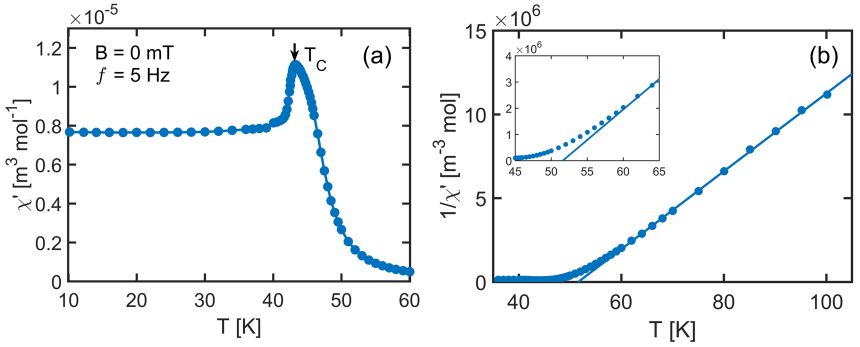

Figure 2.1: Zero field susceptibility for $Fe_{0.7}Co_{0.3}Si$ measured at $f = 5$ Hz. (a) Temperature dependence of χ'. (b) Inverse susceptibility that has been fitted to a Curie-Weiss law.

in Fig. 2.1(b). The corresponding fit with the Curie-Weiss law $\chi' = C/(T - T_{CW})$ reveals a Curie-Weiss temperature of $T_{CW} = 51.6 \pm 0.5$ K and a Curie constant of 4.3 ± 0.1 m^3 mol^{-1} $\times 10^{-5}$, which translates to 1.4 μ_B f.u.$^{-1}$ and is as such in good agreement with the literature [25]. Deviations from the Curie-Weiss law occur for temperatures below 62 K, i.e. approximately 1.4 T_C.

To evaluate the magnetic field dependence of the susceptibility, we display ZFC χ' in Figs. 2.2 (a)-(c) for various temperatures. For $T < 38$ K, Fig. 2.2 (a) shows that χ' increases with increasing magnetic field until the relatively low field of B_{C1} of the helical-to-conical transition. For 38 K $\leq T \leq$ 44 K, Fig. 2.2 (b) reveals a clear dip in χ' between ~20 - 45 mT which is maximal at 41 K. This dip marks the A-phase with its characteristic skyrmion lattice correlations. Fig. 2.2 (c) shows that above 44 K, χ' decreases monotonically with increasing magnetic field as well as with increasing temperature for a given magnetic field.

The corresponding evolution of χ'' is displayed in Figs. 2.2 (d)-(f) as a function of magnetic field. In these figures, two peaks around ~20 and ~45 mT are visible of which the latter one is slightly less intense. These peaks mark the boundary of the A-phase and appear for 34 K $\leq T \leq$ 43 K and thus over a much broader temperature range than the dip in χ', which is only seen between $T = 38$ K and $T = 42$ K. Similar peaks in χ'' have also been observed at the boundary of the A-phase for MnSi [33]and Cu_2OSeO_3 [34], but in a considerably less wide temperature range.

Another, although small, increase in χ'' is observed at high fields and is observed clearly in Fig. 2.2 (f). Additional measurements show that this feature does not disappear even at fields as high as 1 T. This non-zero χ'' persists above T_C up to 50 K and for fields exceeding 40 mT and has a broad maximum around 46 K. A similar effect has also been reported for Cu_2OSeO_3 [34] and a more elaborate discussion of this feature, including its frequency dependence, will be presented in Section 2.6.

An overview of the temperature and magnetic field dependence of χ' is given in Fig. 2.3. A well-defined maximum is visible at T_C at zero field. At 40 mT, the dip characteristic for the A-phase is visible slightly below T_C. At a field $B \sim 60$ mT, a kink appears at $T =$

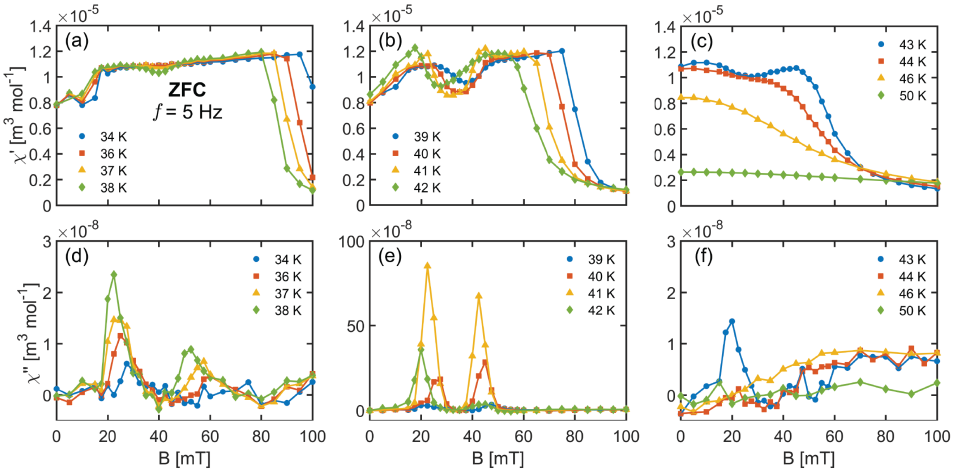

Figure 2.2: Magnetic field dependence of (a) - (c) χ' and (d) - (f) χ'' of $Fe_{0.7}Co_{0.3}Si$ at $f = 5$ Hz for the temperatures indicated. The field was applied after zero field cooling.

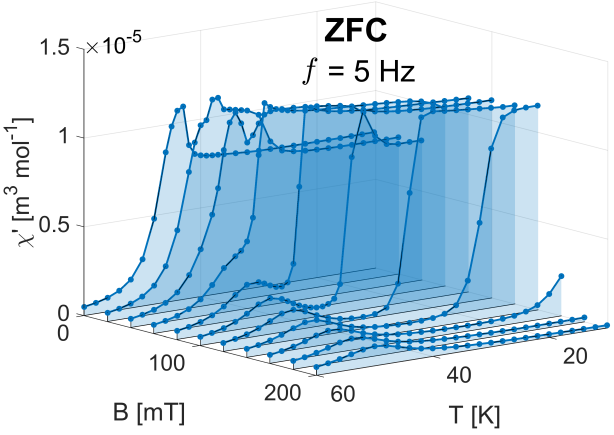

Figure 2.3: Temperature dependence of χ' of $Fe_{0.7}Co_{0.3}Si$ for several magnetic fields at $f = 5$ Hz. The field was applied after zero field cooling.

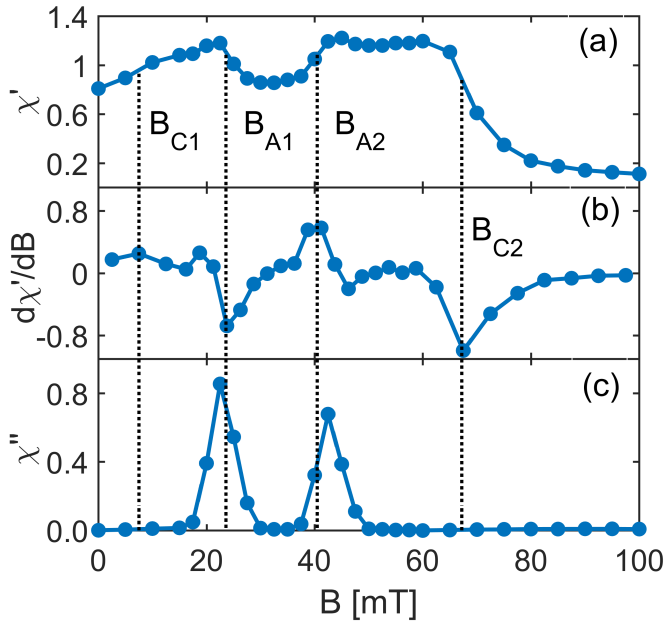

Figure 2.4: Magnetic field dependence at $T = 41$ K of (a) χ' in units of $m^3mol^{-1} \times 10^{-5}$, (b) $d\chi'/dB$ in units of $m^3mol^{-1}T^{-1} \times 10^{-3}$ and (c) χ'' in units of $m^3mol^{-1} \times 10^{-6}$. The field was applied after ZFC. The local maxima/minima of $d\chi'/dB$ define the lower critical field B_{C1}, the higher critical field B_{C2}, as well as the lower and upper boundaries of the A-phase B_{A1} and B_{A2}.

46 K, which marks the split of the single maximum for fields $B < 60$ mT into two separate maxima for $B > 60$ mT. The low temperature maximum is related to the DM interaction and shifts to lower temperatures for increasing magnetic fields and marks the B_{C2} transition from the conical to the field polarized state. The high temperature maximum reflects the ferromagnetic correlations and shifts to higher temperatures for increasing fields.

A similar behavior has been reported for other chiral magnets as MnSi [35], FeGe [36], and Cu_2OSeO_3 [37]. In these studies, the high temperature maximum has been interpreted as a smeared transition from the high-temperature paramagnetic to the low-temperature field polarized state [35, 36] and reflecting the classical ferromagnetic transition that would take place in the absence of DM interactions [37].

To actually extract a magnetic phase diagram from the previously presented susceptibility results requires stringent criteria for the determinations of the critical fields B_{C1} and B_{C2} and the boundaries of the A-phase B_{A1} and B_{A2}. Several criteria have been used in the literature, such as the maxima of χ'' and the inflection points of χ'. As it has been discussed previously for MnSi [33] and Cu_2OSeO_3 [34], different criteria lead to slightly different phase boundaries but not to significantly different physics.

Fig. 2.4 displays the magnetic field dependence after ZFC of χ', its derivative $d\chi'/dB$ and χ'' at $T = 41$ K, a temperature where all the phase boundaries are present. At the

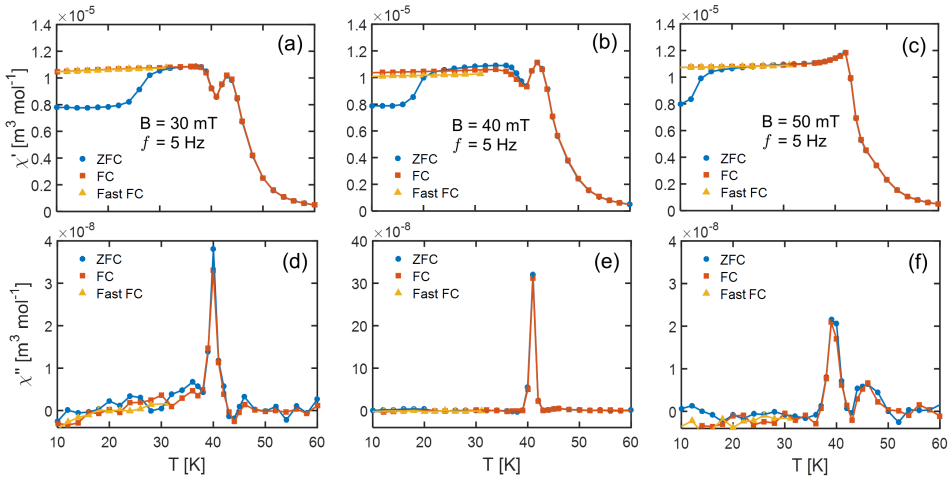

Figure 2.5: Temperature dependence of (a) - (c) χ' and (d) - (f) χ'' of $Fe_{0.7}Co_{0.3}Si$ at f = 5 Hz for the magnetic fields indicated. The magnetic field was applied after Zero Field Cooling (ZFC), Field Cooling (FC) and Fast Field Cooling (Fast FC).

borders of the A-phase, the extrema of $d\chi'/dB$ which correspond to the inflection points of χ', do not occur at exactly the same magnetic fields as the maxima of χ''. In fact, the maxima of χ'' lead to a slightly smaller value for B_{A1} and a slightly higher one for B_{A2} and thus to a larger pocket for the A-phase than the inflection points of χ'. A similar behavior has been found for both MnSi and Cu_2OSeO_3 [33, 34]. As χ'' is almost zero at both B_{C1} and B_{C2}, we choose the inflection points of χ' to determine all the phase boundaries.

2.4. HISTORY DEPENDENCE AT 5 HZ

The previous section only discussed the susceptibility after ZFC. However, it is known that there is a strong hysteretic behavior of $Fe_{1-x}Co_xSi$ [9, 25, 26] that also depends on the cooling rate [26]. For this reason, the ac susceptibility was also measured following the FC and Fast FC protocols described above. A selection of the results obtained with a frequency of 5 Hz is displayed in Figs. 2.5 (a)-(c) for χ' and in Figs. 2.5 (d)-(f) for χ' revealing a strong history dependence for χ' but not for χ''.

We start the discussion of the history dependence by comparing ZFC with FC. No differences exist above T_C. Below T_C, Figs. 2.5 (a) and (b) show a dip in χ' centered around 40 K, which is due to the A-phase. This dip does not appear in Fig. 5 (c), under a magnetic field of 50 mT, which exceeds B_{A2}.

At a lower temperature and for ZFC, χ' drops from $\sim 1.1 \times 10^{-5}$ $m^3mol^{-1}$to 0.8×10^{-5} m^3mol^{-1}. This reflects the conical-to-helical transition which occurs at lower temperatures for higher magnetic fields. No substantial decrease in χ' is observed for FC, implying that the conical phase extends to the lowest temperatures.

Another difference between ZFC and FC χ' is visible in Fig. 2.5 (b) at B = 40 mT in the conical phase between T = 20 K and 38 K. Here, χ' is slightly lower after FC than

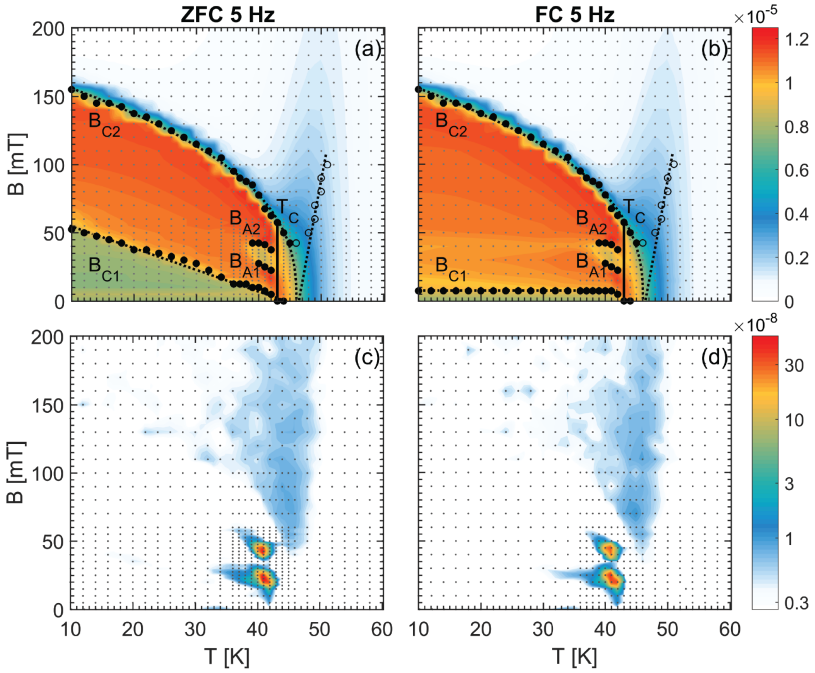

Figure 2.6: Contour plots showing (a) - (b) χ' and (c) - (d) χ'' in units of m^3mol^{-1} after ZFC and FC at $f = 5$ Hz as a function of temperature and magnetic field. B_{C1}, B_{A1}, B_{A2} and B_{C2} are defined by the inflection point of χ' and are indicated with black circles. The dashed line along B_{C2} indicate the fitted power law as described in the text. The grey dots indicate the points at which a signal has been recorded.

after ZFC. This effect is enhanced for Fast FC. These differences are consistent with the previously reported neutron scattering results where it was shown that skyrmion lattice correlations persist in FC mode outside the A-phase and increase in intensity for higher cooling rates [26]. Similarly to the A-phase, such skyrmion lattice correlations would lead to a reduction of χ', which is consistent with our observations.

The history, field and temperature dependence at 5 Hz of both χ' and χ'' are summarized in the contour plots depicted in Fig. 2.6. The helical phase shows up in the ZFC contour plot displayed in Fig. 2.6 (a) below B_{C1} and spans a wide section of the phase diagram. B_{C1} is temperature dependent, ranging from $B \sim 50$ mT at $T = 10$ K to $B \sim 10$ mT at $T = 40$ K.

This strong temperature dependence of B_{C1} is not visible in the contour map of χ' for FC as shown in Fig. 2.6(b). In the Field Cooled case, the helical phase covers a much smaller section of the phase diagram and is suppressed to fields $B_{C1} < 5$ mT in favor of the conical phase that covers a much larger part of the phase diagram. This suppression of the helical phase is consistent with previous neutron scattering experiments [26] and with (ac) susceptibility measurements of $Fe_{1-x}Co_xSi$ with different degrees of Co doping [25]. This strong temperature and history dependence of B_{C1} has not been

observed for MnSi and Cu_2OSeO_3, but is similar to the doped compounds $Mn_{1-x}Fe_xSi$ and $Mn_{1-x}Co_xSi$ [38], where the helical phase also covers a wide section of the magnetic phase diagram for ZFC.

In contrast to B_{C1}, the contour plots of χ' displayed in Figs. 2.6 (a) and (b) show no history dependence for the borders of the A-phase and the upper magnetic field boundary of the conical phase B_{C2}. The A-phase appears as a region with a locally lower χ' just below T_C in both Figs. 2.6 (a) and (b) and is bound by the previously defined B_{A1} and B_{A2}. Figs. 2.6(c) and (d) reveal two clear regions with a non-zero χ'' around B_{A1} and B_{A2}. However, neither the lower nor the higher temperature limits of the A-phase are delimited by χ'' implying that the temperature induced transitions to the A-phase are fundamentally different from the field induced ones. This is similar to MnSi [33] and Cu_2OSeO_3 [34].

The evolution of B_{C2} as a function of temperature can be described over the whole temperature range of the measurements by the power law $B_{C2} \propto (T_0 - T)^{0.39\pm0.04}$ where $T_0 = 46.1 \pm 0.4$ K, i.e. $\sim T_C + 3$ K and is indicated with a dotted line in Figs. 2.6 (a) and (b). This power law seems to mimic the temperature dependence of a Heisenberg model order parameter. A similar analysis has been performed for Cu_2OSeO_3 where an exponent of 0.25 was found [39], which thus suggest that B_{C2} varies much stronger with temperature for $Fe_{0.7}Co_{0.3}Si$ than for Cu_2OSeO_3.

Above T_C, the inflection point of χ' can be observed at $B \sim 45$ mT for $T = 46$ K. At higher temperatures, this inflection point occurs at magnetic fields that increase linearly with increasing temperature extrapolating at zero field to T_0. However, for $T > 48$ K, the minimum of $d\chi'/dT$ becomes very broad and the deduced inflection points are very inaccurate. For this reason they are not displayed in Fig. 2.6. The broad maxima in χ'' visible above T_C do not depend on history and will be discussed more extensively in a following section.

2.5. FREQUENCY DEPENDENCE

The results presented at the previous two sections were obtained with an ac drive frequency of 5 Hz only. Nevertheless, the existence of a non-zero χ'' implies a frequency dependence for both χ' and χ''. This is shown for ZFC in Fig. 2.7 which displays χ' and χ'' at $T = 41$ K as a function of magnetic field for several frequencies.

Figures 2.7 (a) and (b) show that this frequency dependence of χ' is concentrated at the boundary of the A-phase, and that the minimum in the center of the A-phase does not depend on the frequency. The two sharp maxima of χ' centered at $B = 22$ mT and $B = 42$ mT at the boundaries of the A-phase smoothen and soften with increasing frequency. We note that the baseline of χ' (and χ'') is slightly higher at 1 kHz by $\sim 10^{-7}$ m^3mol^{-1}, which is likely due to the onset of eddy currents.

The plots of χ'' visible in Figs. 2.7 (c) and (d) show two sharp maxima close to B_{A1} and B_{A2}. These two maxima exhibit a strong frequency dependence as their amplitude decreases significantly for frequencies exceeding 50 Hz resulting in a ~60% reduction at 1 kHz as compared with 50 Hz.

A more detailed picture of the effect of frequency on the ac susceptibility around the A-phase is given in Fig. 2.8, which displays χ' and χ'' after ZFC for $T = 41$ K as a function of frequency for several magnetic fields around B_{A1} and B_{A2}. Fig. 2.8(a) shows a rela-

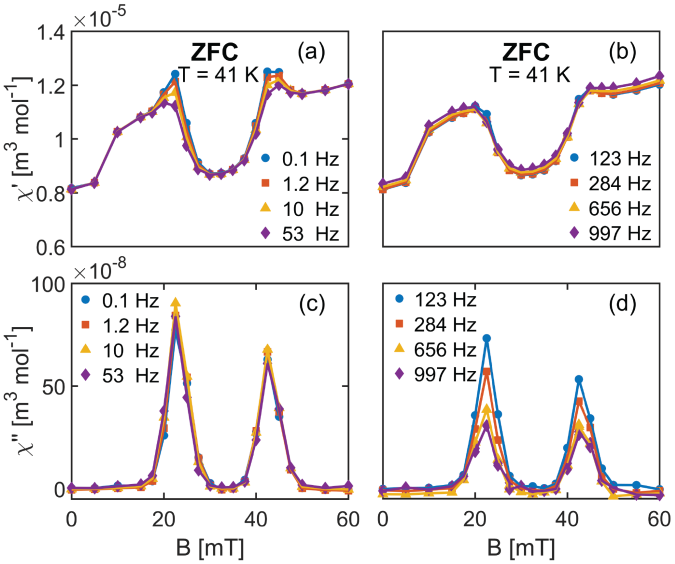

Figure 2.7: Magnetic field dependence of (a) - (b) χ' and (c) - (d) χ'' as a function of magnetic field for $T = 41$ K for the frequencies indicated.

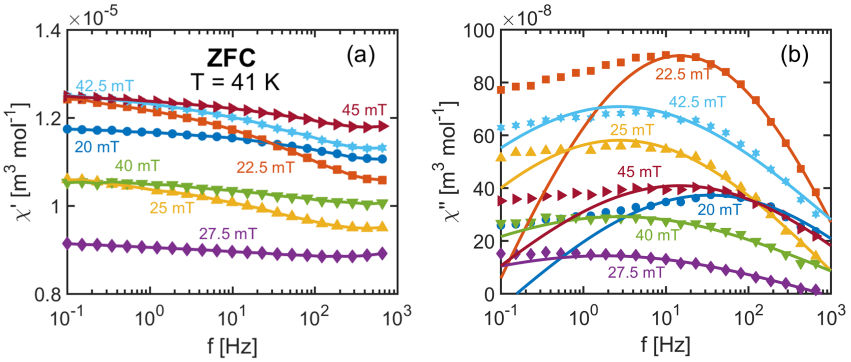

Figure 2.8: Frequency dependence of (a) χ' and (b) χ'' at various magnetic fields for $T = 41$ K. The solid lines in panel (b) indicate fits with the relation provided in eq. 2.3.

tively weak frequency dependence of χ' that decreases monotonically with increasing frequency for every magnetic field. In accordance with the behavior shown in Figs. 2.7 (a) and (b), this dependence is larger for the lower magnetic field limit of the A phase.

Figure 2.8 (b) reveals a very broad and asymmetric frequency dependence of χ''. The scans show that the frequencies at which the maxima of χ'' occur vary strongly with field. Around B_{A1}, the characteristic frequency varies from ~50 Hz at 20 mT to ~10 Hz at 22.5 mT, ~5 Hz at 25 mT, and is in the 0.1 Hz range at 27.5 mT. This indicates that the dynamics become significantly slower towards the center of the A-phase. A complementary behavior is found around B_{A2} where the characteristic frequencies increase substantially with increasing field. The corresponding macroscopic relaxation times indicate extremely slow dynamics in $Fe_{0.7}Co_{0.3}Si$ that possibly originate from rearrangements of large magnetic volumes.

Further insights in the relaxation processes behind the frequency dependence is provided by the Cole-Cole formalism that has been modified to include a distribution of relaxation times centered around a characteristic relaxation frequency f_0:

$$\chi(\omega) = \chi(\infty) + \frac{\chi(0) - \chi(\infty)}{1 + (i\omega\tau_0)^{1-\alpha}}, \tag{2.1}$$

where $\omega = 2\pi f$ denotes the angular frequency, $\chi(0)$ and $\chi(\infty)$ the isothermal and adiabatic susceptibility, respectively, $\tau_0 = 1/2\pi f_0$ the characteristic relaxation time and α a parameter that provides a measure of the width of the distribution of relaxation frequencies, being zero for a single relaxation process and one for an infinitely broad distribution. A non-zero value of α hence implies a stretched exponential relaxation possibly due to a distributions of energy barriers in a phase-space landscape [40]. Eq. 2.1 can be decomposed in the in- and out of phase components [41, 42]:

$$\chi(\omega)' = \chi(\infty) + \frac{(\chi(0) - \chi(\infty))[1 + (\omega\tau_0)^{1-\alpha}\sin(\pi\alpha/2)]}{1 + 2(\omega\tau_0)^{1-\alpha}\sin(\pi\alpha/2) + (\omega\tau_0)^{2(1-\alpha)}}, \tag{2.2}$$

$$\chi(\omega)'' = \frac{(\chi(0) - \chi(\infty))(\omega\tau_0)^{1-\alpha}\cos(\pi\alpha/2)}{1 + 2(\omega\tau_0)^{1-\alpha}\sin(\pi\alpha/2) + (\omega\tau_0)^{2(1-\alpha)}}. \tag{2.3}$$

The resulting fits for χ'' are displayed in Fig. 2.8 (b) and show clear discrepancies at low frequencies and hence fail to accurately describe the entire frequency dependence of the data. The single relaxation process Cole-Cole formalism, even with substantially non-zero values for α required for the fits, fails to describe the frequency dependence of χ' and χ''. The behavior observed indicates the existence of several co-existing relaxation processes which might originate from a coexistence of multiple phases as evidenced by neutron scattering [26]. These relaxation processes occur at low frequencies in $Fe_{0.7}Co_{0.3}Si$ and give rise to more complicated dynamics around the A-phase than in the non-doped compounds as for example Cu_2OSeO_3 [34] or MnSi.

2.6. PHASE DIAGRAM AND DISCUSSION

An overview of the effect of the frequency on the susceptibility over a wide magnetic field and temperature range is provided by Fig. 2.9 which displays contour plots of χ'

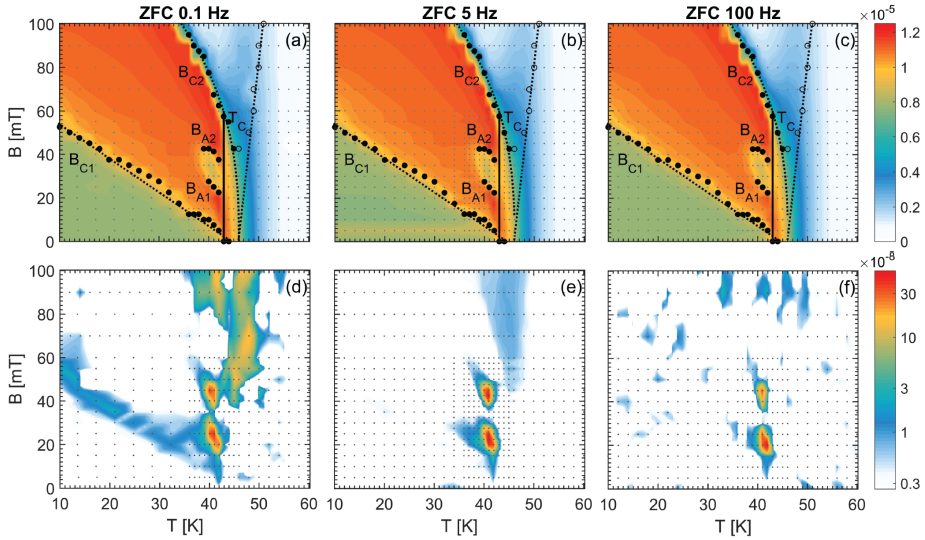

Figure 2.9: Contour plots showing (a) - (c) χ' and (d) - (f) χ'' in units of m^3mol^{-1} for ZFC at f = 0.1, 5 and 100 Hz as a function of temperature and magnetic field. B_{C1}, B_{A1}, B_{A2} and B_{C2} are defined by the inflection point of χ' and are indicated with black circles. The dashed line through the B_{C2} points indicate the fitted power law as described in the text in Section 2.4. The grey dots indicate the points at which a signal has been recorded.[42]

and χ'' at 0.1 Hz, 5 Hz and 100 Hz after ZFC. The helical-to-conical transition can be clearly identified by the increase in χ' visible at B_{C1} in Figs. 2.9 (a)-(c). On the other hand, Figs. 2.9(d)-(f) show that around B_{C1} χ'' is non-zero only at the lowest frequency of 0.1 Hz. This indicates that the helical-to-conical transition involves very slow dynamics and macroscopic relaxation times of the order of seconds. This is different from Cu_2OSeO_3 where the characteristic frequencies of the helical-to-conical transition are of the order of ~100 Hz [34], but could be more similar to MnSi where the characteristic frequency may be well below 10 Hz [33] or even below 0.1 Hz.

In addition, the contour maps of χ'' displayed in Figs. 2.9 (d)-(f) reveal a strong frequency dependence of the two regions with non-zero χ'' at the lower and higher magnetic field limit of the A-phase around B_{A1} and B_{A2}. Compared with 5 Hz, these regions span a smaller space in the B - T diagram at 100 Hz. This effect is enhanced for the 'pocket' of non-zero χ'' centered around 45 mT. At 0.1 Hz, the two pockets of non-zero χ'' seem to be larger than at 5 Hz.

Moreover, the contour maps of χ'' indicate that the non-zero values for χ'' visible at 5 Hz above T_C and B_{C2} and centered around T = 46 K are also visible at 0.1 Hz, where χ'' is about an order of magnitude larger but have disappeared at a frequency of 100 Hz. A frequency scan at T = 46 K and B = 60 mT reveals a monotonous decrease of χ'' with increasing frequency above 0.1 Hz, implying that the characteristic relaxation time associated with this feature exceeds ten seconds.[1] This region of non-zero χ'' above B_{C2} at

[1] At a frequency of 0.1 Hz, the SQUID has difficulties stabilizing the phase in a region from T = 42 to 50 K and

low frequencies has also been observed for Cu_2OSeO_3 (0.8 Hz) [34], MnSi (5 Hz) [43] and the soliton lattice system $Cr_{0.33}NbS_2$ [43] and might be a more generic feature of (cubic) helimagnets. As the origin of this signal remains unclear, we intend to further investigate this feature in the future.

The occurrence of metastable skyrmion lattice correlations at low temperatures under field cooling with cooling rates of ~0.1 $Kmin^{-1}$ for FC[2] and ~10 $Kmin^{-1}$ for Fast FC are exceptional and might also be related to the slow dynamics of the system probed by the frequency scans. The unwinding or decay of the skyrmion lattice correlations in $Fe_{0.7}Co_{0.3}Si$ is considerably slower than for MnSi, where much higher cooling rates of ~700 Ks^{-1} are required to freeze the skyrmion lattice correlations below the A-phase [18, 25–27]. In other words, the slow decay of skyrmion lattice correlations is likely related to the high degree of chemical disorder in the system and can be (partially) prevented with conventional cooling rates.

2.7. CONCLUSION

The systematic study of the ac susceptibility of $Fe_{0.7}Co_{0.3}Si$ presented above confirms the dependence of the magnetic phase diagram on the magnetic history and the applied cooling rates reported in previous studies. The transitions between the helical, conical and A-phase can be derived from χ' and show that for Zero Field Cooling the helical phase covers a wide section of the phase diagram with a critical field depending on temperature whereas no temperature dependence is found for Field Cooling.

The weak frequency dependence of χ' is in sharp contrast with the strong frequency dependence of χ''. Around the A-phase, this is an asymmetric and broad frequency dependence arising from several co-existing relaxation processes with characteristic relaxation times ranging from tens of milliseconds to several seconds. In addition, a χ'' signal is found at the helical-to-conical transition but only for the lowest frequency applied of 0.1 Hz. Moreover, a non-zero χ'' is observed above T_C at low frequencies and in a wide region of the phase diagram. Albeit the numerous similarities with other chiral systems, the pronounced history and cooling rate dependence of the magnetic phase diagram on the magnetic history as well as the asymmetric frequency dependence and slow dynamics are special to $Fe_{0.7}Co_{0.3}Si$ and suggest more complicated physical phenomena than in Cu_2OSeO_3 and MnSi.

REFERENCES

[1] L. J. Bannenberg, A. J. E. Lefering, K. Kakurai, Y. Onose, Y. Endoh, Y. Tokura, and C. Pappas, *Magnetic relaxation phenomena in the chiral magnet $Fe_{1-x}Co_xSi$: An ac susceptibility study,* Physical Review B **94**, 134433 (2016).

[2] S. Mühlbauer, B. Binz, F. Jonietz, C. Pfleiderer, A. Rosch, A. Neubauer, R. Georgii, and P. Böni, *Skyrmion lattice in a chiral magnet,* Science **323**, 915 (2009).

[3] X. Z. Yu, N. Kanazawa, Y. Onose, K. Kimoto, W. Z. Zhang, S. Ishiwata, Y. Matsui, and

fields below 50 mT, which is likely caused by the sample.

[2] The cooling rate reported here for FC refers to the average cooling rate between T = 40 K and 30 K.

Y. Tokura, *Near room-temperature formation of a skyrmion crystal in thin-films of the helimagnet FeGe,* Nature Materials **10**, 106 (2011).

[4] E. Moskvin, S. V. Grigoriev, V. Dyadkin, H. Eckerlebe, M. Baenitz, M. Schmidt, and H. Wilhelm, *Complex chiral modulations in FeGe close to magnetic ordering,* Physical Review Letters **110**, 077207 (2013).

[5] S. Seki, X. Z. Yu, S. Ishiwata, and Y. Tokura, *Observation of skyrmions in a multiferroic material,* Science **336**, 198 (2012).

[6] S. Seki, J.-H. Kim, D. S. Inosov, R. Georgii, B. Keimer, S. Ishiwata, and Y. Tokura, *Formation and rotation of skyrmion crystal in the chiral-lattice insulator Cu_2OSeO_3,* Physical Review B **85**, 220406 (2012).

[7] T. Adams, A. Chacon, M. Wagner, A. Bauer, G. Brandl, B. Pedersen, H. Berger, P. Lemmens, and C. Pfleiderer, *Long-wavelength helimagnetic order and skyrmion lattice phase in Cu_2OSeO_3,* Physical Review Letters **108**, 237204 (2012).

[8] X. Z. Yu, Y. Onose, N. Kanazawa, J. H. Park, J. H. Han, Y. Matsui, N. Nagaosa, and Y. Tokura, *Real-space observation of a two-dimensional skyrmion crystal,* Nature **465**, 901 (2010).

[9] W. Münzer, A. Neubauer, T. Adams, S. Mühlbauer, C. Franz, F. Jonietz, R. Georgii, P. Böni, B. Pedersen, M. Schmidt, *et al., Skyrmion lattice in the doped semiconductor $Fe_{1-x}Co_xSi$,* Physical Review B **81**, 041203 (2010).

[10] I. E. Dzyaloshinskii, *A thermodynamic theory of "weak" ferromagnetism of antiferromagnetics,* Journal of Physics and Chemistry of Solids **4**, 241 (1958).

[11] T. Moriya, *Anisotropic Superexchange Interaction and Weak Ferromagnetism,* Physical Review **120**, 91 (1960).

[12] A. N. Bogdanov and D. A. Yablonskii, *Thermodynamically stable 'vortices' in magnetically ordered crystals. the mixed state of magnets,* Zh. Eksp. Teor. Fiz **95**, 182 (1989).

[13] A. N. Bogdanov and A. Hubert, *Thermodynamically stable magnetic vortex states in magnetic crystals,* Journal of Magnetism and Magnetic Materials **138**, 255 (1994).

[14] U. K. Rößler, A. N. Bogdanov, and C. Pfleiderer, *Spontaneous skyrmion ground states in magnetic metals,* Nature **442**, 797 (2006).

[15] N. Nagaosa and Y. Tokura, *Topological properties and dynamics of magnetic skyrmions,* Nature Nanotechnology **8**, 899 (2013).

[16] A. Fert, V. Cros, and J. Sampaio, *Skyrmions on the track,* Nature Nanotechnology **8**, 152 (2013).

[17] N. Romming, C. Hanneken, M. Menzel, J. E. Bickel, B. Wolter, K. von Bergmann, A. Kubetzka, and R. Wiesendanger, *Writing and deleting single magnetic skyrmions,* Science **341**, 636 (2013).

[18] H. Oike, A. Kikkawa, N. Kanazawa, Y. Taguchi, M. Kawasaki, Y. Tokura, and F. Kagawa, *Interplay between topological and thermodynamic stability in a metastable magnetic skyrmion lattice,* Nature Physics **12**, 62 (2016).

[19] J. Beille, J. Voiron, F. Towfiq, M. Roth, and Z. Y. Zhang, *Helimagnetic structure of the $Fe_{1-x}Co_xSi$ alloys,* Journal of Physics F: Metal Physics **11**, 2153 (1981).

[20] J. Beille, J. Voiron, and M. Roth, *Long period helimagnetism in the cubic B20 $Fe_xCo_{1-x}Si$ and $Co_xMn_{1-x}Si$ alloys,* Solid State Communications **47**, 399 (1983).

[21] M. Motokawa, S. Kawarazaki, H. Nojiri, and T. Inoue, *Magnetization measurements of $Fe_{1-x}Co_xSi$,* Journal of Magnetism and Magnetic Materials **70**, 245 (1987).

[22] Y. Onose, N. Takeshita, C. Terakura, H. Takagi, and Y. Tokura, *Doping dependence of transport properties in $Fe_{1-x}Co_xSi$,* Physical Review B **72**, 224431 (2005).

[23] S.-A. Siegfried, E. V. Altynbaev, N. M. Chubova, V. Dyadkin, D. Chernyshov, E. V. Moskvin, D. Menzel, A. Heinemann, A. Schreyer, and S. V. Grigoriev, *Controlling the Dzyaloshinskii-Moriya interaction to alter the chiral link between structure and magnetism for $Fe_{1-x}Co_xSi$,* Physical Review B **91**, 184406 (2015).

[24] S. V. Grigoriev, D. Chernyshov, V. A. Dyadkin, V. Dmitriev, S. V. Maleyev, E. V. Moskvin, D. Menzel, J. Schoenes, and H. Eckerlebe, *Crystal handedness and spin helix chirality in $Fe_{1-x}Co_xSi$,* Physical Review Letters **102**, 037204 (2009).

[25] A. Bauer, M. Garst, and C. Pfleiderer, *History dependence of the magnetic properties of single-crystal $Fe_{1-x}Co_xSi$,* Physical Review B **93**, 235144 (2016).

[26] L. J. Bannenberg, K. Kakurai, F. Qian, E. Lelièvre-Berna, C. D. Dewhurst, Y. Onose, Y. Endoh, Y. Tokura, and C. Pappas, *Extended skyrmion lattice scattering and long-time memory in the chiral magnet $Fe_{1-x}Co_xSi$,* Physical Review B **94**, 104406 (2016).

[27] P. Milde, D. Köhler, J. Seidel, L. M. Eng, A. Bauer, A. Chacon, J. Kindervater, S. Mühlbauer, C. Pfleiderer, S. Buhrandt, *et al.*, *Unwinding of a skyrmion lattice by magnetic monopoles,* Science **340**, 1076 (2013).

[28] H. Watanabe, i. Tazuke, and H. Nakajima, *Helical Spin Resonance and Magntization Measurement in Itinerant Helimagnet $Fe_{1-x}Co_xSi$ ($0.3 \leq x \leq 0.85$),* Journal of the Physical Society of Japan **54**, 3978 (1985).

[29] M. K. Chattopadhyay, S. B. Roy, and S. Chaudhary, *Magnetic properties of $Fe_{1-x}Co_xSi$ alloys,* Physical Review B **65**, 132409 (2002).

[30] S. V. Grigoriev, V. A. Dyadkin, D. Menzel, J. Schoenes, Y. O. Chetverikov, A. I. Okorokov, H. Eckerlebe, and S. V. Maleyev, *Magnetic structure of $Fe_{1-x}Co_xSi$ in a magnetic field studied via small-angle polarized neutron diffraction,* Physical Review B **76**, 224424 (2007).

[31] T. Y. Ou-Yang, G. J. Shu, C. D. Hu, and F. C. Chou, *Dynamic susceptibility study on the skyrmion phase stability of $Fe_{0.7}Co_{0.3}Si$,* Journal of Applied Physics **117**, 123903 (2015).

[32] M. Takeda, Y. Endoh, K. Kakurai, Y. Onose, J. Suzuki, and Y. Tokura, *Nematic-to-smectic transition of magnetic texture in conical state,* Journal of the Physical Society of Japan **78**, 093704 (2009).

[33] A. Bauer and C. Pfleiderer, *Magnetic phase diagram of MnSi inferred from magnetization and ac susceptibility,* Physical Review B **85**, 214418 (2012).

[34] F. Qian, H. Wilhelm, A. Aqeel, T. T. M. Palstra, A. J. E. Lefering, E. H. Brück, and C. Pappas, *Phase diagram and magnetic relaxation phenomena in Cu_2OSeO_3,* Physical Review B **94**, 064418 (2016).

[35] C. Thessieu, C. Pfleiderer, A. N. Stepanov, and J. Flouquet, *Field dependence of the magnetic quantum phase transition in MnSi,* Journal of Physics: Condensed Matter **9**, 6677 (1997).

[36] H. Wilhelm, M. Baenitz, M. Schmidt, U. K. Rößler, A. A. Leonov, and A. N. Bogdanov, *Precursor Phenomena at the Magnetic Ordering of the Cubic Helimagnet FeGe,* Physical Review Letters **107**, 127203 (2011).

[37] I. Živković, J. White, H. M. Rønnow, K. Prša, and H. Berger, *Critical scaling in the cubic helimagnet Cu_2OSeO_3,* Physical Review B **89**, 060401 (2014).

[38] A. Bauer, A. Neubauer, C. Franz, W. Münzer, M. Garst, and C. Pfleiderer, *Quantum phase transitions in single-crystal $Mn_{1-x}Fe_xSi$ and $Mn_{1-x}Co_xSi$: Crystal growth, magnetization, ac susceptibility, and specific heat,* Physical Review B **82**, 064404 (2010).

[39] I. Levatić, P. Popčević, V. Šurija, A. Kruchkov, H. Berger, A. Magrez, J. S. White, H. M. Rønnow, and I. Živković, *Dramatic pressure-driven enhancement of bulk skyrmion stability,* Scientific Reports **6**, 21347 (2016).

[40] I. Campbell, *Ordering and relaxation in spin glasses,* Physical Review B **33**, 3587 (1986).

[41] D. Huser, A. J. Van Duyneveldt, G. J. Nieuwenhuys, and J. A. Mydosh, *Phenomenological model for the frequency dependence of the susceptibility of spin glasses and related compounds,* Journal of Physics C: Solid State Physics **19**, 3697 (1986).

[42] C. Dekker, A. F. M. Arts, H. W. de Wijn, A. J. Van Duyneveldt, and J. A. Mydosh, *Activated dynamics in a two-dimensional Ising spin glass: $Rb_2Cu_{1-x}Co_xF_4$,* Physical Review B **40**, 11243 (1989).

[43] K. Tsuruta, M. Mito, Y. Kousaka, J. Akimutsu, J. Kishine, and K. Inoue, Private Communication (2016).

3

EXTENDED SKYRMION LATTICE SCATTERING AND LONG-TIME MEMORY IN THE CHIRAL MAGNET $Fe_{1-x}Co_xSi$

Small angle neutron scattering measurements on a bulk single crystal of the doped chiral magnet $Fe_{1-x}Co_xSi$ with $x = 0.3$ reveal a pronounced effect of the magnetic history and cooling rates on the magnetic phase diagram. The extracted phase diagrams are qualitatively different for zero and field cooling and reveal a metastable skyrmion lattice phase outside the A-phase for the latter case. These thermodynamically metastable skyrmion lattice correlations coexist with the conical phase and can be enhanced by increasing the cooling rate. They appear in a wide region of the phase diagram at temperatures below the A-phase but also at fields considerably smaller or higher than the fields required to stabilize the A-phase.

3.1. INTRODUCTION

Spin chirality generated by Dzyaloshinsky-Moriya (DM) interactions [2, 3] is the focus of interest due to the emergence of chiral skyrmions [4–10], which are non-coplanar and topologically stable spin textures. These can form a unique type of long-range magnetic order, a skyrmion lattice (SkL), as observed in the isostructural B20 transition-metal silicides, TMSi (TM=Mn, Fe, Co), and germanides like FeGe by neutron scattering [7, 9, 11] and in real space by Lorentz transmission microscopy [8, 12]. In these bulk cubic helimagnets, the SkL correlations appear spontaneously in the so called A-Phase, a small pocket in the magnetic field (B), temperature (T) phase diagram slightly below the transition temperature T_C [7, 8]. In confined geometries such as thin films [12] or nanowires

This chapter has been published in Physical Review B **94**(10), 104406 (2016) [1].

[13], this narrow pocket expands and tends to cover a substantial part of the phase diagram below T_C up to the lowest temperature.

Recent findings show that it is also possible in bulk MnSi to quench the thermodynamically stable SkL into a metastable state by rapid cooling down to low temperatures [14]. Additionally, short range order that may be associated with isolated skyrmions has been found outside the A-Phase in MnSi [15]. Thus the experimentally observed stability limits of chiral skyrmions and SkL in the reference cubic helimagnets seem to be less well defined and established than assumed so far. On the other hand, it is theoretically established that metastable SkL and single skyrmions should exist over a broad range of the phase diagram [5, 16], as supported by recent findings on thin films [17] or on the bulk polar magnetic semiconductor GaV_4S_8 [18].

The small angle neutron scattering (SANS) results presented below go further in this direction and show strong memory effects and very weak patterns with the characteristic SkL sixfold symmetry that coexist with the conical phase, indicating the stabilization of SkL outside the usual thermodynamic equilibrium limits in the bulk cubic helimagnet $Fe_{1-x}Co_xSi$, $x = 0.3$. The sample belongs to the semi-conducting system $Fe_{1-x}Co_xSi$, which is characterized by very long helix periods from $\ell \sim 25$ nm to 300 nm [19, 20] and by a change of magnetic chirality from left to right handed as the amount of Co doping increases, triggered by the change of the chemical lattice chirality at $x = 0.2$ [21]. $Fe_{0.7}Co_{0.3}Si$ has a right handed, or clockwise, chirality and the helices propagate along the [100] crystallographic directions. Similar to chiral magnets of the same family, the ground state results from the competition between three terms in the Hamiltonian: a strong ferromagnetic exchange, a weaker DM interaction and a weakest anisotropy [22]. Below the transition temperature T_C a helical order sets in with ℓ proportional to the ratio of ferromagnetic exchange to DM interactions and with the helices fixed to the chemical lattice by anisotropy. This hierarchy is also found in the $B-T$ phase diagram, where a weak critical field B_{C1} is enough to overcome the anisotropy, unpin the helices from the chemical lattice and orient them along its direction leading to the conical phase. A higher magnetic field B_{C2} is subsequently required to overcome the DM interactions and ferromagnetically align the magnetic moments inducing the spin polarized phase. The A-phase occurs in a narrow region below T_C and for intermediate magnetic fields between B_{C1} and B_{C2} [9, 23–26].

A phase diagram depending on the magnetic history has already been reported in $Fe_{1-x}Co_xSi$ by neutron scattering [9] and specific heat or magnetic susceptibility measurements [27]. We chose to systematically investigate this effect and cooled the sample through T_C following three specific protocols: Zero Field Cooling (ZFC) and slow or fast Field Cooling (FC). Our results show a pronounced history effects and the existence of SkL correlations over a very extended region of the phase diagram when applying field cooling. These SkL correlation can be enhanced by increasing the cooling rate and do not only exist at temperatures below the A-phase.

3.2. EXPERIMENTAL DETAILS

The experiments were performed on the Small Angle Neutron Scattering (SANS) instrument D33 of the ILL using a monochromatic neutron beam with a wavelength λ=0.6 nm and $\Delta\lambda/\lambda = 10\%$ and on the same $Fe_{0.7}Co_{0.3}Si$ single crystal (~ 0.1 cm^3) used in a previ-

ous investigation[26]. The sample was oriented with the [$\bar{1}$10] axis vertical and the [001] axis parallel to $\vec{k}_i$, the incoming neutron beam wavevector. The data were normalized to standard monitor counts and a measurement at T=60 K was used for the background correction. The magnetic field $\vec{B}$ was applied parallel to $\vec{k}_i$ a configuration, where only helical modulations that propagate perpendicularly to $\vec{B}$ may fulfill the Bragg condition and give rise to scattering. The results are thus complementary to the previous investigation [26], where the magnetic field was applied *perpendicular* to the neutron beam and in the SANS detector plane. The magnetic field was applied following three specific protocols:

- ZFC temperature scans: the sample was cooled down to 2 K under zero magnetic field, then a magnetic field was applied and the patterns were recorded by increasing the temperature in steps of 2 K every 6 min.
- FC temperature scans: the magnetic field was applied at 60 K and the measurements were performed by decreasing the temperature in steps of 0.5 K every 10 min between 45 K and 42 K, in steps of 1 K every 5 min between 41 K and 30 K and between 30 K and 2 K in steps of 2 K every 5 min.
- Fast FC temperature scans: the magnetic fields of 43 mT or 54 mT were applied at 60 K and the sample was immediately brought to 30 K at a cooling rate of ~ 3 K/min. The measurements were subsequently performed by decreasing the temperature to 2 K in steps of 2 K every 5 min.

3.3. EXPERIMENTAL RESULTS

First, we present the ZFC results that are summarized in Fig. 3.1, which shows typical SANS patterns for (a) B = 43 mT and (b) 65 mT, azimuthally averaged intensity at B = 43 mT (c), the temperature and magnetic field dependence of ℓ (d) and finally a $B-T$ contour plot of the integrated SANS intensity illustrating the occurrence of the different phases (e). The patterns at low temperatures displayed in panels (a) and (b) show four broad peaks that are the fingerprint of the helical order along the ⟨100⟩ crystallographic directions. By increasing the temperature the intensity almost vanishes at 30 K. This is the signature of the conical phase, where helices are aligned by the magnetic field and they do not fulfill the Bragg condition in the configuration of this experiment ($\vec{B} \| \vec{k}_i$) and thus do not scatter neutrons. Additional information on this phase can be found in the previous work [26], where a complementary experimental set-up with $\vec{B} \perp \vec{k}_i$ was used.

By further increasing the temperature the scattered intensity increases for B = 43 mT and scattering patterns reappear for $T \geq 38$ K as shown in Fig. 3.1(a) for T = 40 K and 42 K. However, the observed pattern is not the six-fold SkL symmetry of MnSi [7] but a ring as illustrated by the azimuthally averaged intensities shown in panel (c). This behavior is similar to $Fe_{0.8}Co_{0.2}Si$ where such a ring-like pattern was found and was attributed to the combination of disorder, arising from the solution of Fe and Co in the chemical lattice, and magneto-crystalline anisotropy [9]. The azimuthal intensity plots also show that the four helical peaks visible at low temperatures do not have exactly the same intensity, reflecting a slight misalignment of the sample as pointed out in the previous investigation [26].

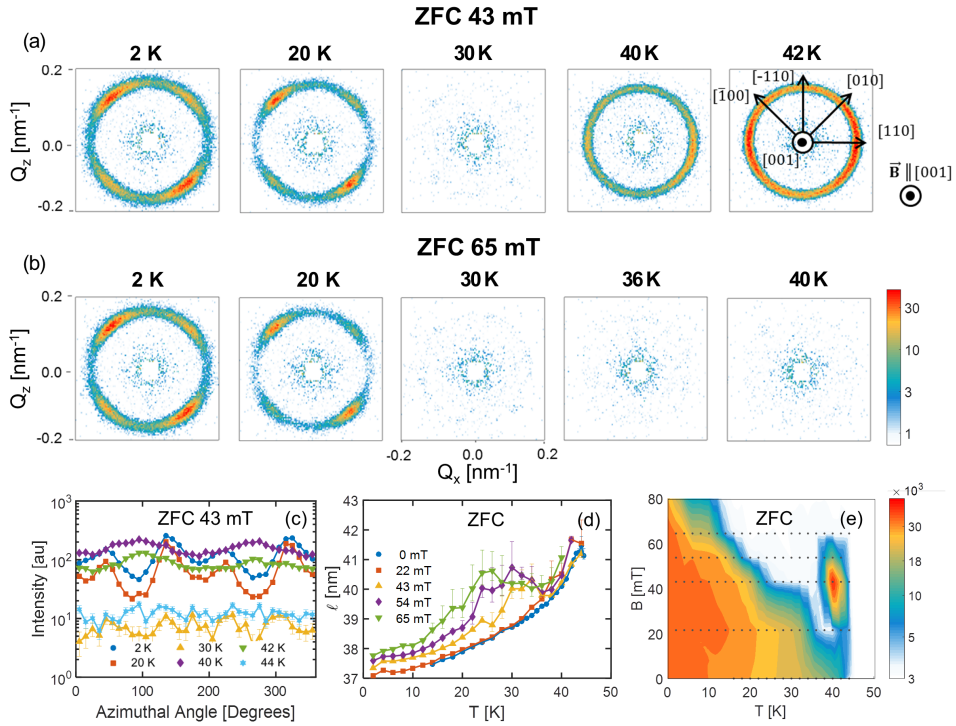

Figure 3.1: SANS results obtained in ZFC configuration. Characteristic patterns at 43 mT and 65 mT are shown in panels (a) and (b). The azimuthal average of the SANS intensity at 43 mT is given in (c) for selected temperatures. The temperature dependence of the helical modulation period ℓ is given in (d) for the magnetic fields indicated. The deduced magnetic field and temperature dependence of the total scattered intensity is given as a contour plot (e) and the dashed lines mark the magnetic fields corresponding to the patterns of (a) and (b).

Fig. 3.1(d) depicts the temperature dependence period of the helical modulations ℓ that has been derived from the momentum transfer Q where the scattered intensity is maximum: $\ell = 2\pi/Q$. As the temperature increases from 2 to 40 K, ℓ increases substantially by about 14 %, which suggests a weakening of the DM interaction with respect to the ferromagnetic exchange. In addition for $B > 22$ mT, a non-monotonic temperature dependence is found with ℓ going through a minimum at the A-Phase and then through a maximum at a lower temperature which depends on the magnetic field.

FC results are summarized in Fig. 3.2, which is complementary to Fig. 3.1: the patterns in panels (a) and (b) are given for the same magnetic fields as for ZFC and reveal substantial differences. In contrast to ZFC, the helical phase is confined to magnetic fields below 10 mT. In the A-phase at B = 43 mT a ring-shaped scattering is found for T = 40 K and 42 K, shown in Fig. 3.2(a), but in contrast to ZFC the six-fold symmetry characteristic of the SkL phase is visible in the FC patterns as well as in the corresponding azimuthal plots shown in panel (c). This six-fold symmetry pattern remains, although weak, clearly visible, even when the temperature is further decreased below 38 K, which suggests the coexistence of a weak SkL with the conical phase. SkL correlations therefore

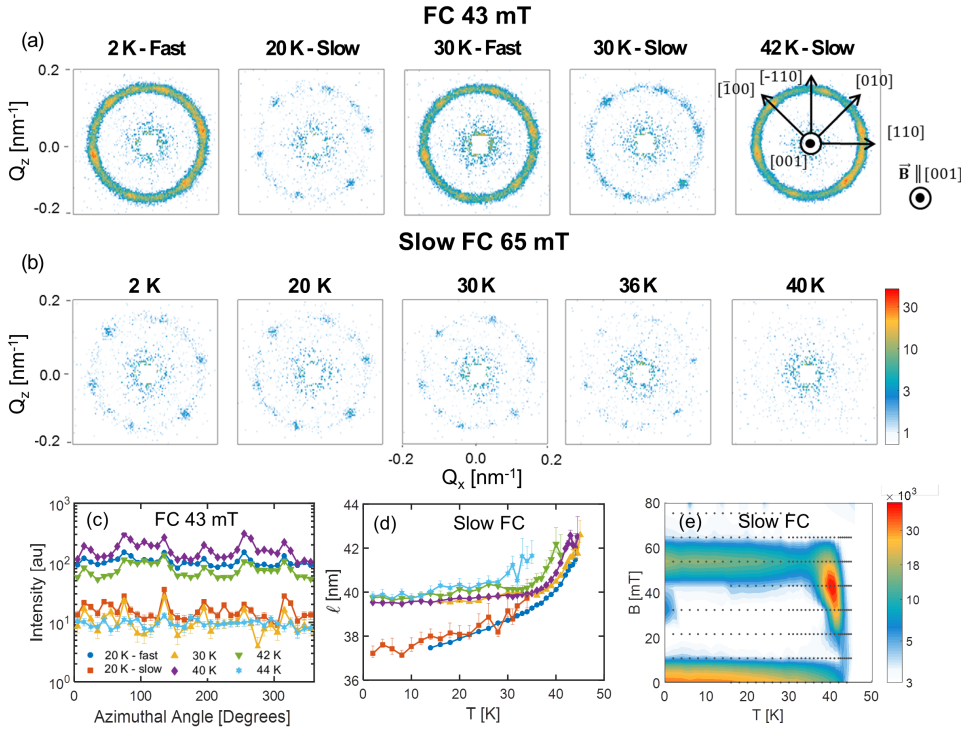

Figure 3.2: SANS results obtained in FC configuration. Characteristic patterns at 43 mT and 65 mT are shown in panels (a) and (b). As mentioned in the text we differentiate between fast and slow field cooling. The azimuthal average of the SANS intensity at 43 mT is given in (c) for selected temperatures. The temperature dependence of the helical modulation period ℓ is given in (d) for slow FC and the magnetic fields indicated. The deduced slow FC magnetic field and temperature dependence of the total scattered intensity is given as a contour plot (e) and the dashed lines mark the magnetic fields corresponding to the patterns of (a) and (b).

seem to freeze by cooling the sample in a magnetic field, and this effect depends on the cooling rate through the A-phase as shown by the different SANS patterns for slow and fast FC at 20 K and 30 K in Fig. 3.2(a). This freezing of the correlations is also seen in the evolution of ℓ in Fig. 3.2(d), which for B >22 mT locks-in to the value at ~38 K while cooling down, which is in sharp contrast with the ZFC behavior shown in Fig. 3.1(d).

For the slightly higher magnetic field of 55 mT the patterns of Fig. 3.3 show that the A-phase clearly extends down to 2 K. In this case, fast FC leads to higher scattered intensities than slow FC, although with the same symmetry and overall shape of the scattering patterns. The $B-T$ SANS intensity map in Fig. 3.2(e) illustrates the boundaries of the A-phase, which extend to the lowest temperatures between B = 45 and 65 mT. However, outside this A-phase region, weak six-fold symmetry patterns appear with an intensity about 100 times weaker than in the A-phase, similarly to what is shown in Fig. 3.2 (a) and (b). In addition, at intermediate magnetic fields (10 <B <35 mT) and for T <30 K, weak four-fold symmetry patterns are found, also with intensities about 100 times weaker than

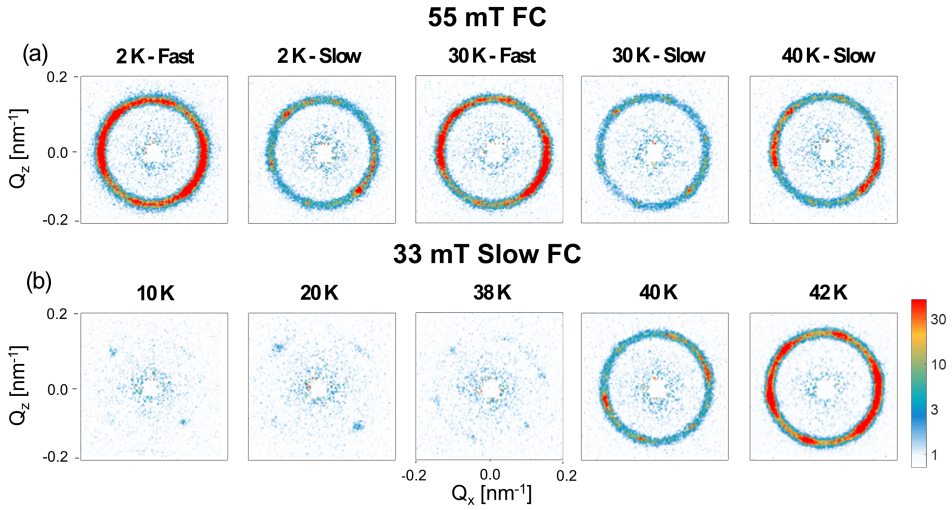

Figure 3.3: Characteristic SANS patterns at (a) 33 mT and (b) 55 mT recorded for fast and slow field cooling.

for the ZFC case. They become stronger as the temperature decreases, resulting in a small pocket of a relatively low intensity in the contour plot of the scattered intensity of Fig. 3.2(e).

3.4. DISCUSSION

The results presented above lead to the phase diagrams of Fig. 3.4, which highlight the differences between ZFC and slow FC. The ZFC phase diagram reveals that the conical phase extends, as in the doped compound $Mn_{1-x}Fe_xSi$ and $Mn_{1-x}Co_xSi$ [28] to much larger fields than in undoped compounds as MnSi and Cu_2OSeO_3 as well as that they reveal a temperature dependence of B_{C1} for ZFC. The conical phase is greatly suppressed for the FC case where there are regions where metastable SkL or helical correlations coexist with the conical phase under field cooling conditions.

These SkL correlations exist over a very extended region of the phase diagram until the lowest temperature and are not only found at temperatures below the thermodynamically stable A-phase. The very low intensity, almost two orders of magnitude lower than at the A-phase, could possibly indicate surface or edge pinning [29, 30] that may stabilize these chiral correlations in directions perpendicular to the applied magnetic field.

On the other hand, the existence of (isolated) biskyrmion and multiskyrmion states within the conical phase arising from an attractive interskyrmion potential has been established theoretically [31]. However, the results presented here rather support *lattices* of skyrmions rather than *isolated* skyrmions and are as such more in agreement with the theoretical computations of [16]. They predict the stabilization of metastable skyrmion *lattices* over a large fraction of the phase diagram below T_C. These metastable skyrmion lattice are formed by cooling through the precursor region above T_C where they are nu-

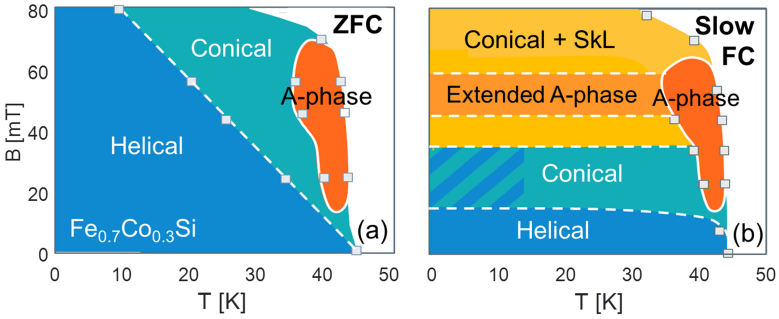

Figure 3.4: Proposed phase diagrams of $Fe_{0.7}Co_{0.3}Si$ deduced from the SANS patterns and intensities for (a) Zero Field Cooling (ZFC) and (b) Slow Field Cooling (Slow FC) showing the helical, conical and A-phases. The slow FC diagram of panel (b) also shows the extended A-phase as well as the $B-T$ areas where helical or skyrmion lattice correlations coexist with the conical phase.

cleated. A subsequent drop in temperature below T_C turns the skyrmion lattices in metastable states of which the stability increases with decreasing T [16].

These theoretical predictions are also inline with the differences observed between Fast and Field Cooling. During fast field cooling, the exposure of the skyrmion lattice to the region just below T_C where the energy barrier heights are relatively small, is limited as compared to slow field cooling. This results in a smaller deterioration of the SkL correlations for the fast FC case and a stronger intensity at lower temperatures.

A recent experimental study showed that metastable SkL correlations can also be quenched by applying extremely high cooling rates of ~700 Ks^{-1} in MnSi [14]. These high cooling rates are required to circumvent the unwinding of the SkL as observed in bulk $Fe_{0.5}Co_{0.5}Si$ by [32] with magnetic force microscopy. However, the cooling rates applied in this study are more than three orders of magnitude higher, suggesting that the unwinding of the Skl in $Fe_{0.7}Co_{0.3}Si$ occurs at a totally different timescale than in MnSi. The observation of these metastable skyrmion lattice phase over macroscopic time scales in $Fe_{0.7}Co_{0.3}Si$ may be attributed to the combination of quenched chemical disorder that is due to the solid solution of Fe and Co.

3.5. CONCLUSION

To conclude, we observe a pronounced history and cooling-rate dependence of the magnetic phase diagram below T_C in $Fe_{0.7}Co_{0.3}Si$. By cooling under field, metastable skyrmion lattice correlations are observed outside the thermodynamically stable A-phase until the lowest temperature. These thermodynamic metastable skyrmion lattice correlations coexist with the conical phase and do not only appear at temperatures below the A-phase but also at fields smaller or higher than the fields required to stabilize the A-phase. The intensity of these skyrmion lattice correlations can be enhanced by increasing the cooling rate as the increased cooling limit possibly reduces the unwinding of the SkL in a region just below T_C. The observation of these phenomena with the macroscopic cooling rates used in a neutron scattering experiment may be related to the quenched chemical disorder from the solid solution of Fe and Co.

REFERENCES

[1] L. J. Bannenberg, K. Kakurai, F. Qian, E. Lelièvre-Berna, C. D. Dewhurst, Y. Onose, Y. Endoh, Y. Tokura, and C. Pappas, *Extended skyrmion lattice scattering and long-time memory in the chiral magnet $Fe_{1-x}Co_xSi$,* Physical Review B **94**, 104406 (2016).

[2] I. E. Dzyaloshinskii, *A thermodynamic theory of "weak" ferromagnetism of antiferromagnetics,* Journal of Physics and Chemistry of Solids **4**, 241 (1958).

[3] T. Moriya, *Anisotropic Superexchange Interaction and Weak Ferromagnetism,* Physical Review **120**, 91 (1960).

[4] A. N. Bogdanov and D. A. Yablonskii, *Thermodynamically stable 'vortices' in magnetically ordered crystals. the mixed state of magnets,* Zh. Eksp. Teor. Fiz **95**, 182 (1989).

[5] A. N. Bogdanov and A. Hubert, *Thermodynamically stable magnetic vortex states in magnetic crystals,* Journal of Magnetism and Magnetic Materials **138**, 255 (1994).

[6] U. K. Rößler, A. N. Bogdanov, and C. Pfleiderer, *Spontaneous skyrmion ground states in magnetic metals,* Nature **442**, 797 (2006).

[7] S. Mühlbauer, B. Binz, F. Jonietz, C. Pfleiderer, A. Rosch, A. Neubauer, R. Georgii, and P. Böni, *Skyrmion lattice in a chiral magnet,* Science **323**, 915 (2009).

[8] X. Z. Yu, Y. Onose, N. Kanazawa, J. H. Park, J. H. Han, Y. Matsui, N. Nagaosa, and Y. Tokura, *Real-space observation of a two-dimensional skyrmion crystal,* Nature **465**, 901 (2010).

[9] W. Münzer, A. Neubauer, T. Adams, S. Mühlbauer, C. Franz, F. Jonietz, R. Georgii, P. Böni, B. Pedersen, M. Schmidt, *et al.*, *Skyrmion lattice in the doped semiconductor $Fe_{1-x}Co_xSi$,* Physical Review B **81**, 041203 (2010).

[10] N. Nagaosa and Y. Tokura, *Topological properties and dynamics of magnetic skyrmions,* Nature Nanotechnology **8**, 899 (2013).

[11] E. Moskvin, S. V. Grigoriev, V. Dyadkin, H. Eckerlebe, M. Baenitz, M. Schmidt, and H. Wilhelm, *Complex chiral modulations in FeGe close to magnetic ordering,* Physical Review Letters **110**, 077207 (2013).

[12] X. Z. Yu, N. Kanazawa, Y. Onose, K. Kimoto, W. Z. Zhang, S. Ishiwata, Y. Matsui, and Y. Tokura, *Near room-temperature formation of a skyrmion crystal in thin-films of the helimagnet FeGe,* Nature Materials **10**, 106 (2011).

[13] H. Du, J. P. DeGrave, F. Xue, D. Liang, W. Ning, J. Yang, M. Tian, Y. Zhang, and S. Jin, *Highly Stable Skyrmion State in Helimagnetic MnSi Nanowires,* Nano Letters **14**, 2026 (2014).

[14] H. Oike, A. Kikkawa, N. Kanazawa, Y. Taguchi, M. Kawasaki, Y. Tokura, and F. Kagawa, *Interplay between topological and thermodynamic stability in a metastable magnetic skyrmion lattice,* Nature Physics **12**, 62 (2016).

[15] S. V. Grigoriev, N. M. Potapova, E. V. Moskvin, V. A. Dyadkin, C. Dewhurst, and S. V. Maleyev, *Hexagonal spin structure of A-phase in MnSi: Densely packed skyrmion quasiparticles or two-dimensionally modulated spin superlattice?* JETP Letters **100**, 216 (2014).

[16] M. N. Wilson, A. B. Butenko, A. N. Bogdanov, and T. L. Monchesky, *Chiral skyrmions in cubic helimagnet films: The role of uniaxial anisotropy,* Physical Review B **89**, 094411 (2014).

[17] N. Romming, A. Kubetzka, C. Hanneken, K. von Bergmann, and R. Wiesendanger, *Field-dependent size and shape of single magnetic skyrmions,* Physical Review Letters **114**, 177203 (2015).

[18] I. Kézsmárki, S. Bordács, P. Milde, E. Neuber, L. M. Eng, J. S. White, H. M. Rønnow, C. D. Dewhurst, M. Mochizuki, K. Yanai, *et al.*, *Néel-type skyrmion lattice with confined orientation in the polar magnetic semiconductor GaV_4S_8,* Nature Materials **14**, 1116 (2015).

[19] J. Beille, J. Voiron, F. Towfiq, M. Roth, and Z. Y. Zhang, *Helimagnetic structure of the $Fe_{1-x}Co_xSi$ alloys,* Journal of Physics F: Metal Physics **11**, 2153 (1981).

[20] M. Ishida, Y. Endoh, S. Mitsuda, Y. Ishikawa, and M. Tanaka, *Crystal Chirality and Helicity of the Helical Spin Density Wave in MnSi. II. Polarized Neutron Diffraction,* Journal of the Physical Society of Japan **54**, 2975 (1985).

[21] S. V. Grigoriev, D. Chernyshov, V. A. Dyadkin, V. Dmitriev, S. V. Maleyev, E. V. Moskvin, D. Menzel, J. Schoenes, and H. Eckerlebe, *Crystal handedness and spin helix chirality in $Fe_{1-x}Co_xSi$,* Physical Review Letters **102**, 037204 (2009).

[22] P. Bak and M. H. Jensen, *Theory of helical magnetic structures and phase transitions in MnSi and FeGe,* Journal of Physics C: Solid State Physics **13**, L881 (1980).

[23] J. Beille, J. Voiron, and M. Roth, *Long period helimagnetism in the cubic B20 $Fe_xCo_{1-x}Si$ and $Co_xMn_{1-x}Si$ alloys,* Solid State Communications **47**, 399 (1983).

[24] K. Ishimoto, Y. Yamaguchi, J. Suzuki, M. Arai, M. Furusaka, and Y. Endoh, *Small-angle neutron diffraction from the helical magnet $Fe_{0.8}Co_{0.2}Si$,* Physica B: Condensed Matter **213**, 381 (1995).

[25] S. V. Grigoriev, V. A. Dyadkin, D. Menzel, J. Schoenes, Y. O. Chetverikov, A. I. Okorokov, H. Eckerlebe, and S. V. Maleyev, *Magnetic structure of $Fe_{1-x}Co_xSi$ in a magnetic field studied via small-angle polarized neutron diffraction,* Physical Review B **76**, 224424 (2007).

[26] M. Takeda, Y. Endoh, K. Kakurai, Y. Onose, J. Suzuki, and Y. Tokura, *Nematic-to-smectic transition of magnetic texture in conical state,* Journal of the Physical Society of Japan **78**, 093704 (2009).

[27] A. Bauer, M. Garst, and C. Pfleiderer, *History dependence of the magnetic properties of single-crystal $Fe_{1-x}Co_xSi$,* Physical Review B **93**, 235144 (2016).

[28] A. Bauer, A. Neubauer, C. Franz, W. Münzer, M. Garst, and C. Pfleiderer, *Quantum phase transitions in single-crystal $Mn_{1-x}Fe_xSi$ and $Mn_{1-x}Co_xSi$: Crystal growth, magnetization, ac susceptibility, and specific heat,* Physical Review B **82**, 064404 (2010).

[29] H. Du, R. Che, L. Kong, X. Zhao, C. Jin, C. Wang, J. Yang, W. Ning, R. Li, C. Jin, X. Chen, J. Zang, Y. Zhang, and M. Tian, *Edge-mediated skyrmion chain and its collective dynamics in a confined geometry,* Nature Communications **6**, 8504 (2015).

[30] F. N. Rybakov, A. B. Borisov, S. Blügel, and N. S. Kiselev, *New Type of Stable Particle-like States in Chiral Magnets,* Physical Review Letters **115**, 117201 (2015).

[31] A. O. Leonov, T. L. Monchesky, J. C. Loudon, and A. N. Bogdanov, *Three-dimensional chiral skyrmions with attractive interparticle interactions,* Journal of Physics: Condensed Matter **28**, 35LT01 (2016).

[32] P. Milde, D. Köhler, J. Seidel, L. M. Eng, A. Bauer, A. Chacon, J. Kindervater, S. Mühlbauer, C. Pfleiderer, S. Buhrandt, *et al.*, *Unwinding of a skyrmion lattice by magnetic monopoles,* Science **340**, 1076 (2013).

4

UNIVERSALITY OF THE HELIMAGNETIC TRANSITION IN CUBIC CHIRAL MAGNETS: SMALL ANGLE NEUTRON SCATTERING AND NEUTRON SPIN ECHO SPECTROSCOPY STUDIES OF $Fe_{1-x}Co_xSi$

We present a comprehensive Small Angle Neutron Scattering (SANS) and Neutron Spin Echo Spectroscopy (NSE) study of the structural and dynamical aspects of the helimagnetic transition in $Fe_{1-x}Co_xSi$ with $x = 0.30$. In contrast to the sharp transition observed in the archetype chiral magnet MnSi, the transition in $Fe_{1-x}Co_xSi$ is gradual and long-range helimagnetic ordering coexists with short-range correlations over a wide temperature range. The dynamics are more complex than in MnSi and involve long relaxation times with a stretched exponential relaxation which persists even under magnetic field. These results in conjunction with an analysis of the hierarchy of the relevant length scales show that the helimagnetic transition in $Fe_{1-x}Co_xSi$ differs substantially from the transition in MnSi and question the validity of a universal approach to the helimagnetic transition in chiral magnets.

This chapter has been published in Physical Review B **95**(14), 144433 (2017) [1].

4.1. INTRODUCTION

Cubic helimagnets such as MnSi, FeGe, Cu_2OSeO_3 and $Fe_{1-x}Co_xSi$ attract a great amount of attention due to the observation of chiral skyrmions and their lattices [2, 3, 3–6]. These chiral skyrmions have dimensions significantly larger than the lattice constant, are topologically protected and may have applications in spintronics and novel devices for information storage [7–9].

In these chiral magnets, a long-range helimagnetic order of the magnetic moments exists at zero field below the critical temperature T_C. The helimagnetic ordering is the result of the competition between three hierarchically-ordered interactions [10], of which the strongest is the ferromagnetic exchange interaction favoring parallel spin alignment. The twist of the spins is induced by the weaker Dzyaloshinsky-Moriya (DM) interaction that results from the absence of a center of symmetry of the crystallographic structure [11, 12]. The propagation vector of the resulting helical arrangement of the magnetic moments is fixed by anisotropy. If a magnetic field is applied that is sufficiently strong to overcome the anisotropy, it aligns the helices along its direction and induces the so called conical phase. Within this conical phase, skyrmion lattice correlations are stable in a small pocket just below T_C [2, 4–6], and metastable in a much larger region of the magnetic phase diagram [6, 13, 14].

In helimagnets, theory predicts at zero magnetic field a first order transition to the helimagnetic state [10]. In the archetype chiral magnet MnSi this is indeed confirmed by sharp anomalies of the thermal expansion [15, 16], heat capacity [16, 17], and ultrasound absorption [18, 19] at T_C. In this system, strong fluctuating correlations build up just above T_C and thus precede the first order phase transition. These correlations show up as a ring of intensive diffuse neutron scattering spreading over a surface with radius $\tau = 2\pi/\ell$ [20], where ℓ denotes the pitch of the helix. The origin of this precursor phase remains subject to debate. Based on the observations that these correlations are totally chiral up to $\sim T_C + 1$ K, it was suggested that this scattering might emanate from a chiral spin liquid phase which would be the magnetic equivalent of the blue phase observed in liquid crystals [21]. It has also been argued that the correlations drive the transition to first order as suggested by Brazovskii in a theory originally developed for liquid crystals [22, 23]. This approach provides a good description of the temperature dependence of the susceptibility and correlation length, but does not explain all intriguing features of the precursor phase and the transition in MnSi. [24, 25] Studies of the helimagnetic transition to other cubic chiral magnets are scarce. In fact only Cu_2OSeO_3 has been studied by a critical scaling analysis and in this case, the Brazovskii approach was found to be less conclusive than for MnSi [24, 26].

In this work, we address the open question of the helimagnetic transition in the semiconductor $Fe_{1-x}Co_xSi$ and at the same time of the theoretically expected universality of the helimagnetic transition in cubic chiral magnets [23]. $Fe_{1-x}Co_xSi$ is of particular interest as important physical properties can be altered by tuning the chemical substitution which changes both the sign and the magnitude of the DM-interaction. The helical order is stabilized over a wide range of concentrations of $0.05 < x < 0.8$ [27–29]. By changing the concentrations, T_C changes from a few Kelvin to 50 K and the pitch ℓ from ~30 nm to ~200 nm [28, 30]. Furthermore, the sign of the chirality alters from left to right-handed at $x = 0.65$ [31].

The specific composition of the sample used in this work, $Fe_{0.7}Co_{0.3}Si$, has a T_C of approximately 43 K and a pitch of ℓ ~40 nm. We present the results of Small Angle Neutron Scattering (SANS) measurements that provide structural information on the magnetic correlations as well as SANS in combination with polarization analysis to determine the degree of magnetic chirality. These measurements are complemented by the investigation of the associated dynamics by Neutron Spin Echo Spectroscopy (NSE). The combined experimental findings show that the helimagnetic transition in $Fe_{0.7}Co_{0.3}Si$ is gradual and involves slow and complicated dynamics and is as such quantitatively different from the transition in MnSi, which challenges the validity of an universal approach to the helimagnetic transition for chiral magnets.

4.2. EXPERIMENTAL DETAILS

The measurements were performed with the $Fe_{0.7}Co_{0.3}Si$ single crystal (~0.1 cm^3) that was used for previous neutron scattering studies[13, 32] and originates from the same batch as the sample for the ac susceptibility measurements.[33] The sample was oriented with the $[\bar{1}10]$ axis vertical for all experiments.

SANS measurements were performed on the instruments D33 at the Institute Laue Langevin and LARMOR at ISIS. At D33, the monochromatic neutron beam had an incident wavelength of λ = 0.6 nm with $\Delta\lambda/\lambda$ = 10% and the magnetic field $\vec{B}$ was applied along $\vec{k}_i$, the wavevector of the incoming neutron beam. Complementary measurements with $\vec{B} \perp \vec{k}_i$ were performed on the time-of-flight SANS instrument LARMOR at the ISIS neutron spallation source where neutrons with wavelengths of $0.8 \leq \lambda \leq 1.6$ nm where used. The SANS patterns were normalized to standard monitor counts and background corrected using a measurement at 60 K, a temperature which corresponds to ~1.5 T_C. Measurements with $\vec{B} \perp \vec{k}_i$ were performed after either Zero Field Cooling (ZFC) the sample or by Field Cooling (FC) through T_C. As the results did not depend on the specific magnetic history and the specific protocol, most measurements were recorded with a ZFC protocol.

Neutron Spin Echo, SANS with polarization analysis and spherical polarimetry were performed on the NSE spectrometer IN15 at the Institut Laue Langevin using a polarized neutron beam with a polarization of 95% and a monochromatization of $\Delta\lambda/\lambda$ = 15%. At zero field, both the paramagnetic NSE, SANS with polarization analysis and spherical polarimetry measurement were performed with λ = 0.8 nm. The measurements under magnetic field were performed with λ = 1.2 nm and in the ferromagnetic NSE configuration [34, 35]. For these measurements the magnetic field was applied perpendicular to the incident neutron beam ($\vec{B} \perp \vec{k}_i$), a configuration where the chiral scattering of the sample does not depolarize the scattered neutron beam [36]. All NSE spectra were averaged over the entire detector and a background correction was performed when required using a high temperature measurement at 60 K.

4.3. EXPERIMENTAL RESULTS

4.3.1. SANS

We commence the presentation of the experimental results with the SANS patterns displayed in Fig. 4.1 for the configuration where the magnetic field was parallel to the in-

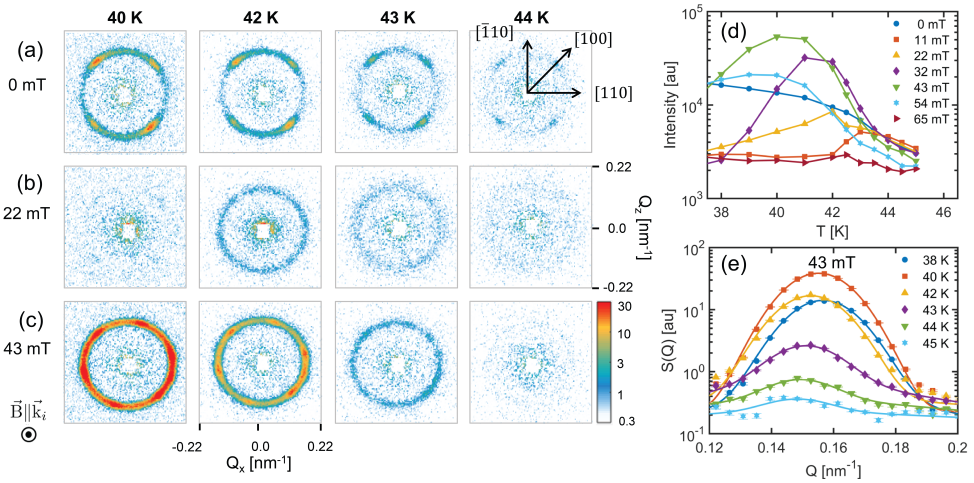

Figure 4.1: SANS results obtained at D33 by applying the magnetic field along the incident neutron beam ($\vec{B} \parallel \vec{k}_i$). Characteristic patterns are shown for B = 0 mT, 22 mT and 43 mT in panels (a) - (c). Panel (d) displays the temperature dependence of the total scattered intensity for selected magnetic fields. Panel (e) shows $S(Q)$ in arbitrary units, deduced by radially averaging the scattered intensity at a magnetic field of 43 mT, for the temperatures indicated. The solid lines indicate the best fits of eq. 4.1 to the data.

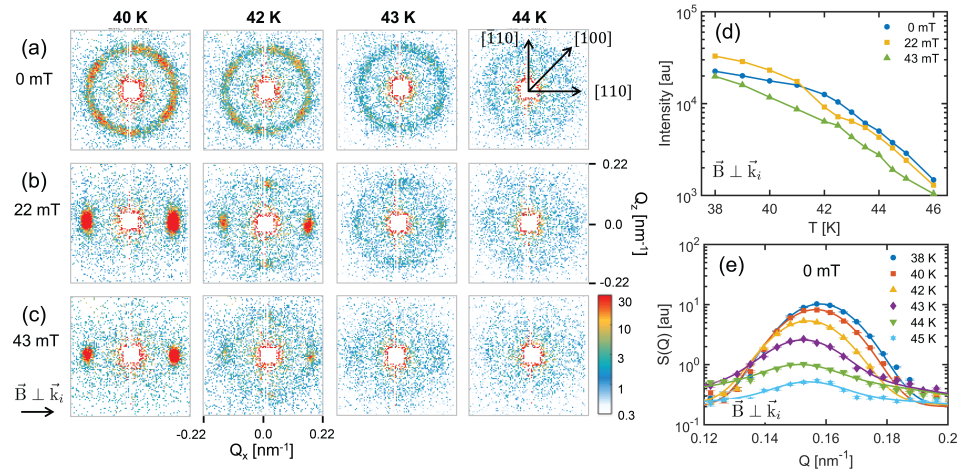

Figure 4.2: SANS results obtained at LARMOR by applying the magnetic field perpendicular to the incident neutron beam ($\vec{B} \perp \vec{k}_i$). Characteristic patterns are shown for B = 0 mT, 22 mT and 43 mT in panels (a) - (c). Panel (d) displays the temperature dependence of the total scattered intensity for selected magnetic fields. Panel (e) shows $S(Q)$ in arbitrary units, deduced by radially averaging the scattered intensity at a magnetic field of 0 mT, for the temperatures indicated. The solid lines indicate the best fits of eq. 4.1 to the data.

coming neutron beam ($\vec{B} \,||\, \vec{k}_i$), and in Fig. 4.2 for the complementary set-up where the magnetic field was applied perpendicular to it ($\vec{B} \perp \vec{k}_i$). These results bear the signatures of the different phases present below T_C.

At $T = 40$ K four peaks show up at zero field, which are smeared over a ring with radius $\tau = 2\pi/\ell$ and do not have exactly the same intensities due to a slight misalignment of the crystal [13, 32]. These peaks are the signature of the helical phase, where helices are aligned along the ⟨100⟩ crystallographic directions. By increasing the magnetic field the scattering patterns change and at $B = 22$ mT there is no scattered intensity for $\vec{B} \parallel \vec{k}_i$, as shown in Fig. 4.1(b). On the other hand, only two peaks along the magnetic field direction are found for $\vec{B} \perp \vec{k}_i$ (Fig. 4.2(b)). These patterns are characteristic of the conical phase, where all helices are oriented along the magnetic field and Bragg peaks are thus only visible along the field direction in the configuration where $\vec{B} \perp \vec{k}_i$.

By further increasing the magnetic field a ring of intensity with radius τ appears. As illustrated by the patterns at $B = 43$ mT, this ring is only visible for $\vec{B} \parallel \vec{k}_i$ and as such indicates the onset of the A-phase and skyrmion lattice correlations. These, however, do not lead to the characteristic six-fold pattern found in MnSi due to a combination of magneto-crystalline anisotropy and chemical disorder that is specific to $Fe_{1-x}Co_xSi$ [6, 13]. We note that the skyrmion lattice correlations coexist with the conical phase as the scattering patterns of $\vec{B} \perp \vec{k}_i$ reveal two peaks along the magnetic field direction originating from the conical correlations at the same fields and temperatures for which the skyrmion lattice is stabilized.

By increasing the temperature to $T = 42$ and 43 K, thus approaching $T_C \approx 43$ K, the behavior remains roughly the same. However some differences show up as for example the A-phase ring of scattering appears also at $B = 22$ mT in Fig. 4.1(b). Furthermore, a broad ring of diffuse scattering is seen at $T = 43$ K, which resembles the ring of diffuse scattering visible above T_C in MnSi. The patterns in Fig. 4.2 indicate that the ring is very weak and coexists with the Bragg peaks of the conical phase and the spots of the A-phase. Above $T = 44$ K, the intensity of the helical Bragg peaks decreases significantly and are superimposed to a weak ring of diffuse scattering that persists under magnetic field for both configurations.

The temperature dependence of the total scattered intensity, obtained by integrating the SANS patterns, is given for selected magnetic fields in Fig. 4.1(d) and Fig. 4.2(d) for $\vec{B} \,||\, \vec{k}_i$ and $\vec{B} \perp \vec{k}_i$ respectively. At zero magnetic field the intensity increases gradually with decreasing temperature with no particular change at T_C. For $T \gtrsim T_C$ a magnetic field suppresses part of the scattered intensity in both configurations.

Below T_C, the temperature dependence is similar for all magnetic fields in the configuration $\vec{B} \perp \vec{k}_i$. On the contrary, for $\vec{B} \,||\, \vec{k}_i$ a magnetic field has dramatic effects with non-monotonic temperature and magnetic field dependencies. Indeed, even a field of $B = 11$ mT is large enough to suppress most of the magnetic scattering below T_C. Just below T_C, diffuse scattering starts to build up at this field, leading to a kink at a temperature that provides the best estimation of T_C from the SANS data. At higher magnetic fields the marked maxima are due to the onset of the A-phase, which appears as additional intensity and is stabilized for $22 \leq B \leq 54$ mT. At even higher magnetic fields, as for example for $B = 66$ mT, the scattered intensity in this configuration is negligible at all temperatures.

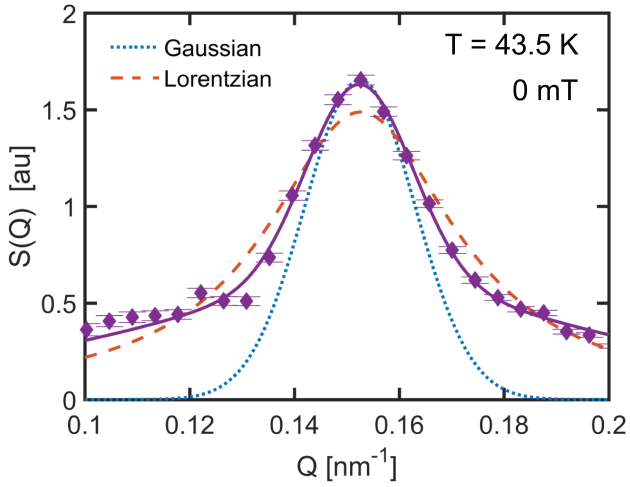

Figure 4.3: Comparison of a Gaussian, Lorentzian and a weighted superposition of a Gaussian and a Lorentzian (solid purple line) to fit $S(Q)$ at $B = 0$ mT and $T = 43.5$ K.

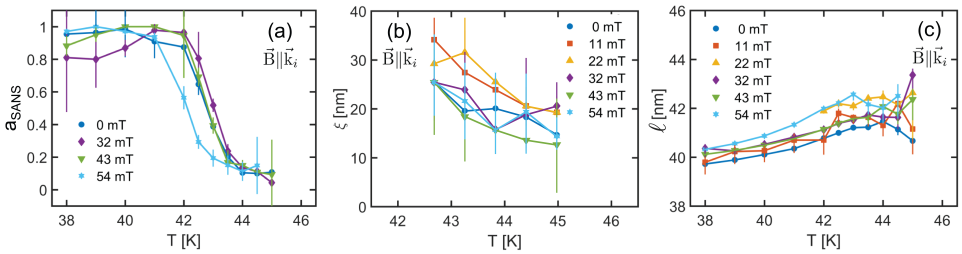

Figure 4.4: The elastic fraction a_{SANS}, the correlation length ξ and the pitch of the helical modulation ℓ as a function of temperature for the magnetic fields indicated as derived from the measurements on D33 where the field was applied parallel to the neutron beam ($\vec{B} \parallel \vec{k}_i$).

A further step in the quantitative analysis of the SANS data is the analysis of the momentum transfer, Q, dependence of the scattered intensity $S(Q)$. $S(Q)$ is obtained in arbitrary units by radial averaging the scattered intensity and is shown in Fig. 4.1(e) for 43 mT and Fig. 4.2(e) for 0 mT. Both plots show well defined maxima centered at $\tau = 2\pi/\ell$ and with line-shapes that vary with temperature. In such a plot, Bragg peaks have a Gaussian shape since they are expected to be resolution limited. This contrasts the broad Q-dependence expected for diffuse scattering. In the case of fluctuating correlations with a characteristic correlation length ξ the Ornstein-Zernike formalism predicts the Lorentz function:

$$S(Q) = \frac{C}{(Q - 2\pi/\ell)^2 + 1/\xi^2}, \tag{4.1}$$

with C the Curie constant. Another similar but more complex function has been suggested for chiral magnets,[20] but our experimental results lack the accuracy required to confirm deviations from eq. 4.1. For this reason the data have been analyzed using the simpler Ornstein-Zernike form, convoluted with the corresponding instrumental Gaussian shaped resolution functions.

At temperatures close to T_C, neither a Gaussian nor a Lorentzian function provides a satisfactory description of $S(Q)$ as illustrated in Fig. 4.3 for T = 43.5 K. The line shape is satisfactorily reproduced by a weighted superposition of the two functions where the relative weight of the Gaussian function provides an estimate for the elastic fraction a_{SANS}. All $S(Q)$ data have been fitted in this way leading to the values for a_{SANS}, the correlation length ξ and the pitch ℓ displayed in Fig. 4.4.

The elastic fraction, displayed in Fig. 4.4(a), is 100% well below T_C, but decreases with increasing temperature above $T \approx 41$ K and becomes zero within a temperature range of ~ 3 K at $T \approx 44$ K. The deduced values for the correlation length ξ are displayed in Fig. 4.4(b) and show within the experimental accuracy a similar trend for all magnetic fields. At T = 42.5 K, $\xi \sim 30$ nm, or $\xi \sim 0.75 \cdot \ell$ and decreases with increasing temperature to $\xi \sim 0.35 \cdot \ell$ at 45 K.

The pitch of the helix ℓ shown in Fig. 4.4(c) only depends weakly on the magnetic field. The temperature dependence of ℓ is consistent with earlier measurements [13] as ℓ increases by ~4% between T = 38 and 44 K. As the pitch of the helix is proportional to the ratio of the ferromagnetic exchange and the DM interaction, this temperature dependence suggests a slight change in the balance between the two interactions in favor of the ferromagnetic exchange.

4.3.2. NSE

The relaxation of the magnetic correlations above T_C has been investigated by NSE at B = 0 and 50 mT. The corresponding intermediate scattering functions $I(Q,t)$ are displayed as a function of the Fourier time t in Fig. 4.5(a) and (b), respectively. Above T_C, at 46 K for B = 0 mT and 42.5 K for B = 50 mT, the relaxation is exponential and $I(Q,t)$ decays from 1 to 0 when t increases by less than two orders of magnitude. However, when the temperature decreases and approaches T_C, the relaxation stretches and covers a much larger time domain. In addition, $I(Q,t)$ at zero field levels off at the longest Fourier times to an elastic component, a_{NSE}, that increases with decreasing temperature. The time de-

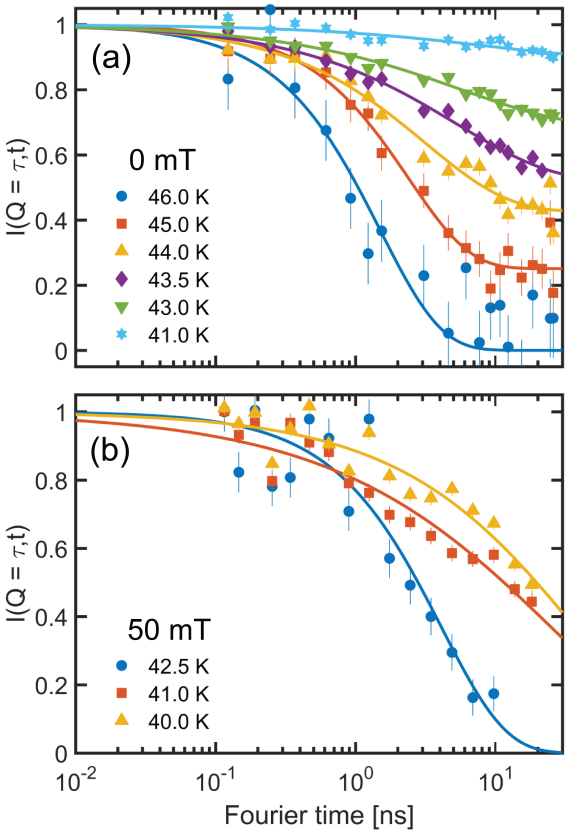

Figure 4.5: Neutron Spin Echo spectroscopy results. Panels (a) and (b) show the intermediate scattering function $I(Q,t)$ measured at (a) 0 mT and (b) 50 mT. The solid lines indicate the fits with the relation provided in eq. 4.2.

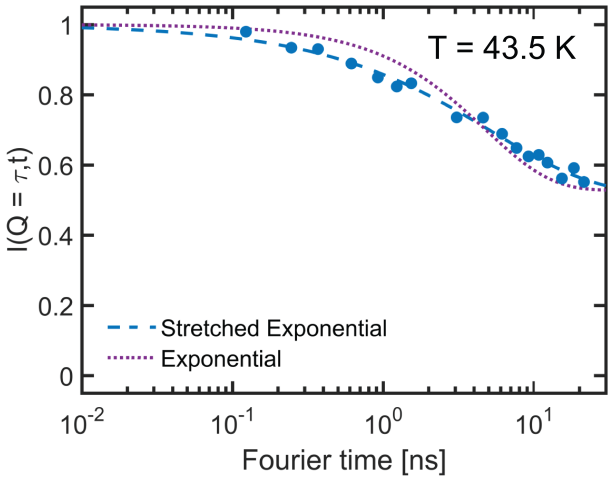

Figure 4.6: Comparison of a fit of the intermediate scattering function $I(Q,t)$ to eq. 4.2 exponential ($\beta = 1$) and a stretched exponential fit ($0 \leq \beta \leq 1$) for $B = 0$ mT and $T = 43.5$ K.

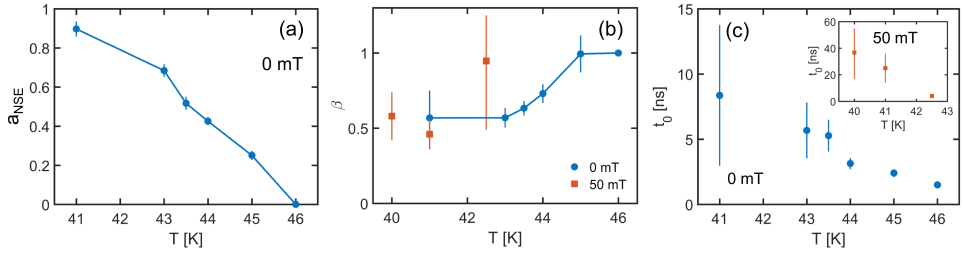

Figure 4.7: Obtained parameters from fitting the intermediate scattering function $I(Q,t)$ with the relation provided in eq. 4.2. Panel (a) shows the elastic fraction a_{NSE}, panel (b) the relaxation time t_0 and panel (c) the stretching exponent β as a function of temperature at $B = 0$ mT and $B = 50$ mT.

cay of $I(Q,t)$ has therefore been fitted by a superposition of the elastic component and a stretched exponential relaxation:

$$I(Q,t) = (1 - a_{NSE}) \exp\left[-(t/t_0)^{\beta}\right] + a_{NSE} \tag{4.2}$$

with t_0 the characteristic relaxation time and β the stretching exponent. The necessity to include the stretching exponent β is illustrated in Fig. 4.6, which displays the time decay of $I(Q,t)$ at T = 43.5 K and shows that the fit with a simple exponential (β = 1) is poor. The decay is more stretched than an exponential and leads in this case to $\beta \sim 0.6$.

The temperature dependence of the parameters deduced from the fit of the NSE spectra at zero field is given in Fig. 4.7. At T = 46 K, $a_{NSE} \sim 0$, but the elastic fraction increases roughly linearly with decreasing temperature reaching ~ 90% at T = 41 K, which is in qualitative agreement with the values obtained from the SANS measurements a_{SANS} displayed in Fig. 4.4(a). The stretching exponent β depicted in Fig. 4.7 (b) is equal to one well above 45 K but decreases with decreasing temperature and reaches $\beta \sim 0.57$ at 41 K. The characteristic relaxation times t_0, displayed in Fig. 4.7(c), increase gradually with decreasing temperature from t_0 = 1.7 ns at 46 K to t_0 = 8 ns at T = 41 K, indicating a slowing down of the relaxation with decreasing temperature approaching T_C.

The data at B = 50 mT are less precise than at zero field, as they have been collected in the ferromagnetic NSE configuration that is sensitive to background corrections. The spectra do not allow a reliable determination of a_{NSE} and for this reason no data are given in Fig. 4.7 (a). On the other hand, the stretching exponent β shows a similar behavior as at zero field. In contrast to β, the characteristic relaxation times are almost doubled as compared with zero field and reach t_0 ~40 ns at T = 40 K. As such, these longer relaxation times indicate a considerable slowing down of the dynamics under field.

4.4. DISCUSSION

In the following we will discuss our experimental findings in the context of the literature, and in particular in comparison with the archetype chiral magnet MnSi. As a first step, we determine the characteristic length scales relevant to the transition, discuss their hierarchy and the applicability of the Brazovskii approach suggested for MnSi [23]. Subsequently, we directly compare the helimagnetic transitions in $Fe_{0.7}Co_{0.3}Si$ and MnSi and highlight the particularities of $Fe_{0.7}Co_{0.3}Si$.

4.4.1. CHARACTERISTIC LENGTHS AND THE BRAZOVSKII APPROACH

It has been suggested that the helimagnetic transition is governed by a hierarchy of characteristic lengths reflecting the relative strength of the interactions [10, 23]: the Ginzburg length ξ_G, the Dzyaloshinsky-Moriya (DM) length ξ_{DM}, and ξ_{cub}, the length associated with the cubic anisotropy. The Ginzburg length quantifies the strength of the interactions between the magnetic fluctuations, which are strong in the limit of $\xi_G > \xi(T)$, whereas they can be considered as a perturbation in the other limit $\xi(T) < \xi_G$. The Dzyaloshinsky-Moriya (DM) length is related to the pitch of the helix ℓ by $\xi_{DM} = \ell/2\pi$ and the cubic anisotropy length reflects the influence of the cubic anisotropy.

If the Ginzburg length is much larger than the length scale associated with the DM interaction, i.e. $\xi_G >> \xi_{DM}$, the interactions between the fluctuations should govern

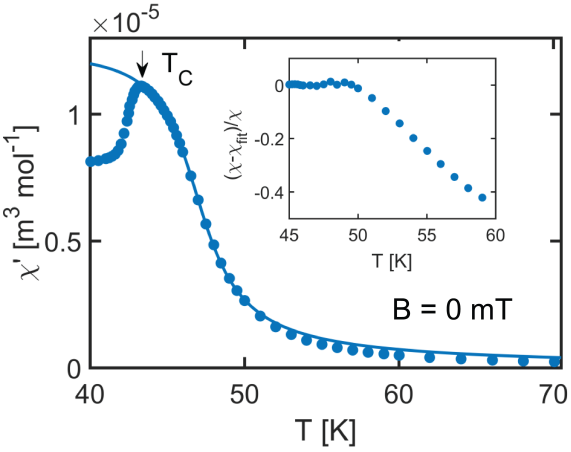

Figure 4.8: Zero field ac susceptibility as a function of temperature measured at $f = 5$ Hz and reproduced from ref. [33]. The solid line indicates the fit to the relation of eq. 4.3. The inset shows the relative difference of the measured data to the fit with eq. 4.3.

the behavior close to the transition, driving it to first order as suggested by Brazovskii [22, 23]. Also for $\xi_G < \xi_{DM}$ the transition is driven by fluctuations and expected to be of first order following the Bak and Jensen (1980) approach in this so called Wilson-Fisher renormalization group limit. So far, the helimagnetic transition and the role of the characteristic lengths remain largely unexplored and have only been discussed for the case of MnSi[23] and Cu_2OSeO_3 [26].

Whereas the DM length can be obtained directly from the pitch of the helix, the cubic anisotropy length can only be derived from the temperature dependence of the correlation length. On the other hand, the Ginzburg length can be obtained both from the correlation length and the macroscopic susceptibility. As the accuracy of the experimentally determined correlation length is limited, we are unable to determine the cubic anisotropy length and we derive the Ginzburg length from the susceptibility data of ref. [33] reproduced in Fig. 4.8. For this purpose, we fit the real component of the ac susceptibility χ' with [22, 23]:

$$\chi' = \frac{\chi'_0}{1+\sigma^2 Z^2(T)}, \tag{4.3}$$

where χ_0 is a constant, σ equals the ratio of the DM and Ginzburg length ($\sigma = \xi_{DM}/\xi_G$) and $Z(T)$ is given by:

$$Z(T) = \frac{\sqrt[3]{2}\epsilon + (1+\sqrt{1-2\epsilon^3})^{2/3}}{\sqrt[3]{2}(1+\sqrt{1-2\epsilon^3})^{1/3}}, \tag{4.4}$$

where $\epsilon = (T - T_{MF})/T_0$ is a relative measure of the distance to the mean field temperature T_{MF}.

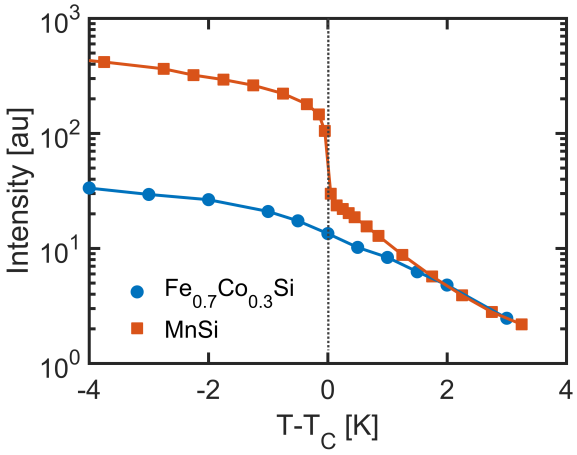

Figure 4.9: Total background corrected scattered intensity obtained by summing the entire detector as a function of temperature at $B = 0$ mT for $Fe_{0.7}Co_{0.3}Si$ and MnSi as measured on LARMOR. MnSi data adapted from [37] and scaled at the highest temperature indicated.

Equation 4.3 provides a good description of the temperature dependence of χ' up to $T \approx 50$ K as shown in Fig. 4.8, leading to estimates of $\chi_0 = 1.27 \pm 0.03\ 10^{-5}$ m^3 mol^{-1}, $T_{MF} = 48.3 \pm 0.2$ K, $T_0 = 3.2 \pm 0.2$ K and $\sigma = 1.39 \pm 0.08$. As illustrated by the inset of Fig. 4.8, substantial and systematic deviations occur above 50 K. The value of $\xi_{DM} \approx 6.3$ nm derived from the neutron data (Fig. 4.4(c)) translates σ to $\xi_G \sim 4.5$ nm. Both lengths are thus much shorter than the correlation lengths, which exceed 10 nm in the probed temperature range below 45 K (see Fig. 4.4(b)).

As $\sigma > 1$, and therefore $\xi_G < \xi_{DM}$, the applicability of the Brazovskii approach for $Fe_{0.7}Co_{0.3}Si$ is questionable. The obtained value for σ of 1.39 is much larger than the value found for MnSi [23] ($\sigma \approx 0.50$) but is in fact reasonably similar to the value of $\sigma = 1.18(1)$ found for Cu_2OSeO_3 [26]. The comparison of the characteristic lengths therefore indicates that the helimagnetic transition in $Fe_{0.7}Co_{0.3}Si$ should be different from that in MnSi.

4.4.2. COMPARISON WITH MNSI AND OTHER CUBIC HELIMAGNETS

The difference between $Fe_{0.7}Co_{0.3}Si$ and MnSi is highlighted by comparing the total scattered intensity at zero field as displayed in Fig. 4.9. The total intensity is obtained by summing the intensity over the entire detector and thus also outside the Bragg peak positions. At high temperatures a similar temperature dependence is found for both chiral magnets. Differences in intensity start to develop at $T_C + 2$ K although the chiral behavior is similar in this region. In MnSi, an increase of intensity indicates the onset of the precursor phase and strong buildup of chiral correlations, which ultimately results in a jump of scattered intensity by more than an order of magnitude within a narrow region of 0.2 K around T_C. This jump is as such a signature of the first-order nature of the transition. In contrast to MnSi, in $Fe_{0.7}Co_{0.3}Si$ the increase of scattered intensity with

decreasing temperature is gradual and without strong indication for a precursor phase and a jump in intensity at T_C.

The onset of the helimagnetic order is thus very different for the two chiral magnets. This is in agreement with specific heat measurements as the sharp peak visible at T_C for MnSi [17] or Cu_2OSeO_3 [38] has not been seen for $Fe_{0.7}Co_{0.3}Si$ [39]. The gradual transition manifests itself also by the coexistence of long-range helimagnetic order and short-range chiral correlations. This coexistence occurs in $Fe_{0.7}Co_{0.3}Si$ over a wide temperature range of ~5 K, whereas in MnSi this region does not exceed ~0.4 K [21, 36].

In addition, Fig. 4.9 shows that the build-up of correlations above T_C in the precursor region is not as strong as for MnSi. In the later, intensive correlations start to build up in this region of the phase diagram. This is also the case for $Fe_{0.7}Co_{0.3}Si$ but the probed correlations are much weaker, possibly because the precursor phenomena are partially suppressed by substitutional disorder. The precursor phase and the associated precursor phenomena in cubic chiral magnets have been subject to intensive theoretical and experimental studies [4, 40–42]. It has been suggested that a softening of the magnetization plays an important role in the formation of isolated skyrmions and other localized magnetic states in this region of the phase diagram [4, 40–43].

The dynamics of the helimagnetic transition as probed by NSE also reveal major differences between the two chiral magnets. Whereas the dynamics of MnSi can be described by a simple exponential, the dynamics of $Fe_{0.7}Co_{0.3}Si$ around T_C can only be accounted for by a stretched exponential relaxation [21, 37]. This implies that the relaxation stretches over several orders of magnitude in time and involves a broad distribution of relaxation times. The corresponding stretching exponents are close to the values found in disordered systems such as glass forming systems [44, 45]. In addition, the associated characteristic relaxation times at zero field for $Fe_{0.7}Co_{0.3}Si$ can be as long as 10 ns, and are therefore much longer than for MnSi where they do not exceed 1 ns [21, 37]. These long relaxation times combined with the stretched exponential relaxation suggest the relaxation of large magnetic volumes, which are likely inhomogeneous in size and structure. Similar conclusions have also been drawn from ac susceptibility measurements below T_C, which however probe much longer, macroscopic, relaxation times [33].

The SANS and NSE results show that the helical transition in $Fe_{0.7}Co_{0.3}Si$ is gradual and involves more complicated and slower dynamics, than in MnSi. The hierarchy of the characteristic length scales puts $Fe_{0.7}Co_{0.3}Si$ closer to Cu_2OSeO_3 than to MnSi, but this hierarchy in itself does not explain the particularities of the helimagnetic transition in $Fe_{0.7}Co_{0.3}Si$. Moreover, neither the Brazovskii nor the Wilson Fisher approach can describe the transition in $Fe_{1-x}Co_xSi$ as both approaches predict a sharp first order helimagnetic transition that is in both cases driven by fluctuations [10, 22, 23].

One important factor that could possibly explain the different transition in $Fe_{1-x}Co_xSi$ is the chemical disorder that arises from the solid solution of Fe and Co in $Fe_{0.7}Co_{0.3}Si$. In conjunction with the effect of the cobalt concentration on the sign of the DM-interaction, the chemical disorder might be an additional source of frustration. This chemical disorder could effectively 'smear' the phase transition and make it appear more continuous. This would explain the broad distribution of relaxation times and the stretched exponential relaxation probed by NSE. However, we note that the stretched exponen-

tial relaxation does not reflect the inhomogeneous relaxation of regions with different chiralities as the magnetic chirality is 100% close to T_C.

4.4.3. TRANSITION UNDER MAGNETIC FIELD

The SANS results show that the transition under field remains similar to the one at zero field up to 40 mT. For these relatively low magnetic fields, the scattered intensity above T_C is similar to the intensity at zero field. Furthermore both the correlation lengths and the elastic fractions remain almost unchanged. For fields exceeding 40 mT, the scattered intensity decreases until it is almost completely suppressed for fields above 60 mT. This is highly similar to the behavior of the transition in MnSi, where the scattered intensity is also suppressed by large enough magnetic fields [37].

In addition, the dynamics of the transition to the conical phase, probed by NSE, slows down considerably under magnetic field. Compared to zero field, the relaxation times under field almost quadruple and can be as long as 40 ns at B = 50 mT. Although the magnetic field induces much sharper peaks in the conical phase than at zero field (Fig. 4.2, the relaxation remains strongly non-exponential. Therefore, the broad distribution of relaxation times is not affected by the magnetic field.

4.5. SUMMARY AND CONCLUSION

In conclusion, SANS and NSE reveal a very gradual and smeared transition around T_C that differs substantially from the sharp first order phase transition in MnSi. Magnetic correlations that are partially chiral but much weaker than in MnSi coexist in a wide temperature range with the long-range helimagnetic order. The relaxation around T_C is broad, non-exponential, even under magnetic field, and is much slower and more complex than in MnSi. The hierarchy of interactions and of the deduced length scales places $Fe_{0.7}Co_{0.3}Si$ closer to Cu_2OSeO_3 than to MnSi, but cannot explain all the particularities of the helimagnetic transition. The large differences between the transition in $Fe_{1-x}Co_xSi$ and other systems of the same family challenges the validity of an universal approach to the helimagnetic transition in chiral magnets.

REFERENCES

[1] L. J. Bannenberg, K. Kakurai, P. Falus, E. Lelièvre-Berna, R. M. Dalgliesh, C. D. Dewhurst, F. Qian, Y. Onose, Y. Endoh, Y. Tokura, and C. Pappas, *Universality of the helimagnetic transition in cubic chiral magnets: Small angle neutron scattering and neutron spin echo spectroscopy studies of FeCoSi,* Physical Review B **95**, 144433 (2017).

[2] S. Mühlbauer, B. Binz, F. Jonietz, C. Pfleiderer, A. Rosch, A. Neubauer, R. Georgii, and P. Böni, *Skyrmion lattice in a chiral magnet,* Science **323**, 915 (2009).

[3] X. Z. Yu, Y. Onose, N. Kanazawa, J. H. Park, J. H. Han, Y. Matsui, N. Nagaosa, and Y. Tokura, *Real-space observation of a two-dimensional skyrmion crystal,* Nature **465**, 901 (2010).

[4] H. Wilhelm, M. Baenitz, M. Schmidt, U. K. Rößler, A. A. Leonov, and A. N. Bogdanov,

Precursor Phenomena at the Magnetic Ordering of the Cubic Helimagnet FeGe, Physical Review Letters **107**, 127203 (2011).

[5] S. Seki, X. Yu, S. Ishiwata, and Y. Tokura, *Observation of skyrmions in a multiferroic material,* Science **336**, 198 (2012).

[6] W. Münzer, A. Neubauer, T. Adams, S. Mühlbauer, C. Franz, F. Jonietz, R. Georgii, P. Böni, B. Pedersen, M. Schmidt, *et al., Skyrmion lattice in the doped semiconductor $Fe_{1-x}Co_xSi$,* Physical Review B **81**, 041203 (2010).

[7] N. Nagaosa and Y. Tokura, *Topological properties and dynamics of magnetic skyrmions,* Nature Nanotechnology **8**, 899 (2013).

[8] A. Fert, V. Cros, and J. Sampaio, *Skyrmions on the track,* Nature Nanotechnology **8**, 152 (2013).

[9] N. Romming, C. Hanneken, M. Menzel, J. E. Bickel, B. Wolter, K. von Bergmann, A. Kubetzka, and R. Wiesendanger, *Writing and deleting single magnetic skyrmions,* Science **341**, 636 (2013).

[10] P. Bak and M. H. Jensen, *Theory of helical magnetic structures and phase transitions in MnSi and FeGe,* Journal of Physics C: Solid State Physics **13**, L881 (1980).

[11] I. E. Dzyaloshinskii, *A thermodynamic theory of "weak" ferromagnetism of antiferromagnetics,* Journal of Physics and Chemistry of Solids **4**, 241 (1958).

[12] T. Moriya, *Anisotropic Superexchange Interaction and Weak Ferromagnetism,* Physical Review **120**, 91 (1960).

[13] L. J. Bannenberg, K. Kakurai, F. Qian, E. Lelièvre-Berna, C. D. Dewhurst, Y. Onose, Y. Endoh, Y. Tokura, and C. Pappas, *Extended skyrmion lattice scattering and long-time memory in the chiral magnet $Fe_{1-x}Co_xSi$,* Physical Review B **94**, 104406 (2016).

[14] H. Oike, A. Kikkawa, N. Kanazawa, Y. Taguchi, M. Kawasaki, Y. Tokura, and F. Kagawa, *Interplay between topological and thermodynamic stability in a metastable magnetic skyrmion lattice,* Nature Physics **12**, 62 (2016).

[15] M. Matsunaga, Y. Ishikawa, and T. Nakajima, *Magneto-volume effect in the weak itinerant ferromagnet MnSi,* Journal of the Physical Society of Japan **51**, 1153 (1982).

[16] S. M. Stishov, A. E. Petrova, S. Khasanov, G. K. Panova, A. A. Shikov, J. C. Lashley, D. Wu, and T. A. Lograsso, *Magnetic phase transition in the itinerant helimagnet MnSi: Thermodynamic and transport properties,* Physical Review B **76**, 052405 (2007).

[17] A. Bauer, M. Garst, and C. Pfleiderer, *Specific heat of the skyrmion lattice phase and field-induced tricritical point in MnSi,* Physical Review Letters **110**, 177207 (2013).

[18] S. Kusaka, K. Yamamoto, T. Komatsubara, and Y. Ishikawa, *Ultrasonic study of magnetic phase diagram of MnSi,* Solid State Communications **20**, 925 (1976).

[19] A. E. Petrova and S. M. Stishov, *Ultrasonic studies of the magnetic phase transition in MnSi,* Journal of Physics: Condensed Matter **21**, 196001 (2009).

[20] S. V. Grigoriev, S. V. Maleyev, A. I. Okorokov, Y. O. Chetverikov, R. Georgii, P. Böni, D. Lamago, H. Eckerlebe, and K. Pranzas, *Critical fluctuations in MnSi near T_C: A polarized neutron scattering study,* Physical Review B **72**, 134420 (2005).

[21] C. Pappas, E. Lelievre-Berna, P. Falus, P. M. Bentley, E. Moskvin, S. Grigoriev, P. Fouquet, and B. Farago, *Chiral paramagnetic skyrmion-like phase in MnSi,* Physical Review Letters **102**, 197202 (2009).

[22] S. A. Brazovskii, *Phase transition of an isotropic system to a nonuniform state,* Soviet Journal of Experimental and Theoretical Physics **41**, 85 (1975).

[23] M. Janoschek, M. Garst, A. Bauer, P. Krautscheid, R. Georgii, P. Böni, and C. Pfleiderer, *Fluctuation-induced first-order phase transition in Dzyaloshinskii-Moriya helimagnets,* Physical Review B **87**, 134407 (2013).

[24] V. A. Sidorov, A. E. Petrova, P. S. Berdonosov, V. A. Dolgikh, and S. M. Stishov, *Comparative study of helimagnets MnSi and Cu_2OSeO_3 at high pressures,* Physical Review B **89**, 100403 (2014).

[25] S. M. Stishov and A. E. Petrova, *Vollhardt invariant and phase transition in the helical itinerant magnet MnSi,* Physical Review B **94**, 140406 (2016).

[26] I. Živković, J. White, H. M. Rønnow, K. Prša, and H. Berger, *Critical scaling in the cubic helimagnet Cu_2OSeO_3*, Physical Review B **89**, 060401 (2014).

[27] J. Beille, J. Voiron, F. Towfiq, M. Roth, and Z. Y. Zhang, *Helimagnetic structure of the $Fe_{1-x}Co_xSi$ alloys,* Journal of Physics F: Metal Physics **11**, 2153 (1981).

[28] J. Beille, J. Voiron, and M. Roth, *Long period helimagnetism in the cubic B20 $Fe_xCo_{1-x}Si$ and $Co_xMn_{1-x}Si$ alloys,* Solid State Communications **47**, 399 (1983).

[29] M. Motokawa, S. Kawarazaki, H. Nojiri, and T. Inoue, *Magnetization measurements of $Fe_{1-x}Co_xSi$,* Journal of Magnetism and Magnetic Materials **70**, 245 (1987).

[30] S. V. Grigoriev, D. Chernyshov, V. A. Dyadkin, V. Dmitriev, S. V. Maleyev, E. V. Moskvin, D. Menzel, J. Schoenes, and H. Eckerlebe, *Crystal handedness and spin helix chirality in $Fe_{1-x}Co_xSi$,* Physical Review Letters **102**, 037204 (2009).

[31] S.-A. Siegfried, E. V. Altynbaev, N. M. Chubova, V. Dyadkin, D. Chernyshov, E. V. Moskvin, D. Menzel, A. Heinemann, A. Schreyer, and S. V. Grigoriev, *Controlling the Dzyaloshinskii-Moriya interaction to alter the chiral link between structure and magnetism for $Fe_{1-x}Co_xSi$,* Physical Review B **91**, 184406 (2015).

[32] M. Takeda, Y. Endoh, K. Kakurai, Y. Onose, J. Suzuki, and Y. Tokura, *Nematic-to-smectic transition of magnetic texture in conical state,* Journal of the Physical Society of Japan **78**, 093704 (2009).

[33] L. J. Bannenberg, A. J. E. Lefering, K. Kakurai, Y. Onose, Y. Endoh, Y. Tokura, and C. Pappas, *Magnetic relaxation phenomena in the chiral magnet $Fe_{1-x}Co_xSi$: An ac susceptibility study,* Physical Review B **94**, 134433 (2016).

[34] B. Farago and F. Mezei, *Study of magnon dynamics in Fe near T_C by modified neutron spin echo techniques,* Physica B+C **136**, 100 (1986).

[35] C. Pappas, E. Lelièvre-Berna, P. Bentley, E. Bourgeat-Lami, E. Moskvin, M. Thomas, S. V. Grigoriev, and V. Dyadkin, *Polarimetric neutron spin echo: Feasibility and first results,* Nuclear Instruments and Methods in Physics Research Section A **592**, 420 (2008).

[36] C. Pappas, E. Lelievre-Berna, P. Bentley, P. Falus, P. Fouquet, and B. Farago, *Magnetic fluctuations and correlations in MnSi: Evidence for a chiral skyrmion spin liquid phase,* Physical Review B **83**, 224405 (2011).

[37] C. Pappas, L. J. Bannenberg, E. Lelièvre-Berna, F. Qian, C. D. Dewhurst, R. M. Dalgliesh, D. L. Schlagel, T. A. Lograsso, and P. Falus, *Magnetic Fluctuations, Precursor Phenomena and Phase Transition in MnSi under Magnetic Field,* Physical Review Letters **119**, 047203 (2017).

[38] T. Adams, A. Chacon, M. Wagner, A. Bauer, G. Brandl, B. Pedersen, H. Berger, P. Lemmens, and C. Pfleiderer, *Long-wavelength helimagnetic order and skyrmion lattice phase in Cu_2OSeO_3,* Physical Review Letters **108**, 237204 (2012).

[39] A. Bauer, M. Garst, and C. Pfleiderer, *History dependence of the magnetic properties of single-crystal $Fe_{1-x}Co_xSi$,* Physical Review B **93**, 235144 (2016).

[40] U. K. Rößler, A. N. Bogdanov, and C. Pfleiderer, *Spontaneous skyrmion ground states in magnetic metals,* Nature **442**, 797 (2006).

[41] H. Wilhelm, M. Baenitz, M. Schmidt, C. Naylor, R. Lortz, U. K. Rößler, A. A. Leonov, and A. N. Bogdanov, *Confinement of chiral magnetic modulations in the precursor region of FeGe,* Journal of Physics: Condensed Matter **24**, 294204 (2012).

[42] E. Moskvin, S. V. Grigoriev, V. Dyadkin, H. Eckerlebe, M. Baenitz, M. Schmidt, and H. Wilhelm, *Complex chiral modulations in FeGe close to magnetic ordering,* Physical Review Letters **110**, 077207 (2013).

[43] S. V. Grigoriev, N. M. Potapova, E. V. Moskvin, V. A. Dyadkin, C. Dewhurst, and S. V. Maleyev, *Hexagonal spin structure of A-phase in MnSi: Densely packed skyrmion quasiparticles or two-dimensionally modulated spin superlattice?* JETP Letters **100**, 216 (2014).

[44] F. Mezei, W. Knaak, and B. Farago, *Neutron spin echo study of dynamic correlations near the liquid-glass transition,* Physical Review Letters **58**, 571 (1987).

[45] J. Colmenero, A. Arbe, D. Richter, B. Farago, and M. Monkenbusch, *Dynamics of Glass Forming Polymers by Neutron Spin Echo,* Neutron Spin Echo Spectroscopy , 268 (2003).

5

MAGNETIZATION AND AC SUSCEPTIBILITY STUDY OF THE CUBIC CHIRAL MAGNET $Mn_{1-x}Fe_xSi$

We present a comprehensive and systematic magnetization and ac susceptibility study of $Mn_{1-x}Fe_xSi$ over an extensive range of ten Fe concentrations between x = 0 - 0.32. With increasing Fe substitution, the critical temperature decreases but the magnetic phase diagrams remain qualitatively unaltered for $x \leq x^* \approx 0.11$ with clear boundaries between the helical, conical, and skyrmion lattice phase as well as an enhanced precursor phase. A notably different behavior sets in for x = 0.11, 0.13 and 0.14, where certain characteristics of helimagnetic correlations persist, but without clear phase boundaries. Although a qualitative change already sets in at x^*, the transition temperature and spontaneous magnetization vanish only at x_C = 0.17 where also the average magnetic interactions change sign. Although the Curie-Weiss temperature reaches -12 K for x = 0.32, no signature of long-range magnetic order is found down to the lowest temperature, indicating a possible significant role for quantum fluctuations in these systems.

5.1. INTRODUCTION

In cubic chiral magnets, the Dzyaloshinskii-Moriya interaction that arises from the noncentrosymmetric crystallographic lattice of these compounds plays a crucial role in stabilizing the helimagnetic order [2, 3]. In the archetype chiral magnet MnSi, the competition of the Dzyaloshinskii-Moriya with the ferromagnetic exchange leads to a helimagnetic order with a pitch of approximately 18 nm. At zero field and below the critical temperature of $T_C \approx 29$ K, a weaker anisotropy term fixes the propagation direction of the

This chapter has been published in Physical Review B **98**(18), 184430 (2018) [1].

resulting spiral to the ⟨111⟩ crystallographic direction, resulting in a multi-domain helimagnetic phase [4, 5]. Relatively weak magnetic fields orient the helices towards their direction, stabilizing a single-domain conical phase, whereas larger magnetic fields destroy the helimagnetic correlations and induce a field-polarized phase. Specific interest in these materials is devoted to the skyrmion lattice phase that is stabilized under magnetic fields and in the vicinity of T_C [6–8].

The interest in helimagnetic and skyrmionic order resulted in the study of several cubic chiral magnets other than MnSi. Of special interest is $Mn_{1-x}Fe_xSi$ where the magnetic interactions can be tuned by chemical substitution and where quantum criticality might play a role. In this system, Fe substitution results in a continuous suppression of T_C to lower temperatures and the existence of at least two quantum critical points (QCPs) have been reported [9–13]. The first alleged QCP at $x^* \approx 0.11$ is possibly associated with the suppression of the long-range helimagnetic order and might be partly hidden by short-range magnetic correlations. For $x > x^*$, it has been suggested that short range order persists in a phase that bears characteristics of a Griffiths phase [9], and where an anomalous Hall effect has been attributed to topological contributions [11, 14]. The second QCP, suggested to appear at $x^{**} \approx 0.24$, should be related to the suppression of short-range order [9–13]. Furthermore, susceptibility and magnetization measurements at high magnetic fields bear signatures of an underlying putative ferromagnetic quantum critical point at $x_C \approx 0.19$ [15]. However, in this study only $Mn_{1-x}Fe_xSi$ compounds up to $x = 0.19$ are considered and no indications are reported for a change of behavior around $x^* \approx 0.11$.

To elucidate the nature of the magnetic order in $Mn_{1-x}Fe_xSi$ and especially the above mentioned specific points, we present a comprehensive study of the magnetic phase diagram as a function of both temperature and magnetic field for $Mn_{1-x}Fe_xSi$. This study is the first that systematically considers an extremely broad range of Fe substitution from $x = 0$ to $x = 0.32$. The results show that with Fe dilution, the long-range helimagnetic order is suppressed in $Mn_{1-x}Fe_xSi$ and that the critical temperature slides to lower temperatures. The boundaries between the helical, conical and skyrmion lattice phase remain clearly visible for $x \leq 0.11$, while at the same time the precursor phenomena that occur in MnSi [16–19] span a wider section of the magnetic field B - temperature T phase diagram. A qualitative change sets in for $x \geq 0.11$ where the helimagnetic transition becomes gradual and for which it is no longer possible to distinguish between the helical, conical and skyrmion lattice phase. This change of behavior indeed identifies $x^* = 0.11$ as a special point of the phase diagram. Moreover, we identify $x_C = 0.17$ as the composition where both the transition temperature and the spontaneous magnetization vanish. x_C is also the concentration where the sign of the Curie-Weiss temperature changes. Although the Curie-Weiss temperature reaches -12 K for $x = 0.32$, and the effective magnetic moment remains non-zero, no signature of long-range magnetic order is observed down to the lowest temperature, hinting that quantum fluctuations may play an important role.

5.2. EXPERIMENTAL DETAILS

Single crystals of $Mn_{1-x}Fe_xSi$ with nominal Fe concentration x = 0.03, 0.09, 0.10, 0.11, 0.13, 0.14, 0.19, 0.25 and 0.32 were grown using the Bridgeman method. The samples used for this series of measurements were cut from larger single crystals and have an irregular shape and a mass that varies between 20 and 150 mg. The measurements on the reference sample MnSi were performed on a small 7.5 mg cubic crystal cut from the large single crystal that was used in previous experiments [19, 20].

Several measurements have been performed to assure high-quality samples. First of all, the composition of the samples was checked with a PANalytical Axios X-ray Fluorescence spectrometer (XRF), revealing slightly different Fe concentrations of x = 0.032, 0.089, 0.101, 0.112, 0.125, 0.140, 0.185, 0.251 and 0.318, respectively. Second, the quality of the samples was assessed by neutron and x-ray Laue diffraction and Scanning Electron Microscopy (SEM). Third, zero-field susceptibility measurements were performed on several small pieces cut out of the large crystals. These measurements revealed no significant differences between the different pieces, indicating negligible composition variations within the samples.

The magnetization M and the real χ' and imaginary components χ'' of the ac susceptibility were measured with a MPMS-XL Quantum Design superconducting quantum interference device (SQUID) magnetometer using the extraction method. All samples were aligned with the $[\bar{1}10]$ crystallographic direction vertical, along which both the dc field and an ac drive field of $0.01 \leq B_{ac} \leq 0.4$ mT were applied.

After checking that the susceptibility was independent of the ac drive field, subsequent measurements were performed with B_{ac} = 0.4 mT. The measurements as a function of temperature were performed by first zero cooling the sample from 40 K for x = 0, 0.03 and 0.09 and 30 K for $x \geq 0.10$ to 1.8 K. Subsequently, the desired magnetic field was applied and the signal was recorded by stepwise increasing the temperature. The system was brought to thermal equilibrium at each temperature before the measurement commenced. The measurements as a function of field were performed by first zero field cooling the sample from 40 K for x = 0, 0.03 and 0.09 and 30 K for $x \geq 0.10$ to the temperature of interest. Subsequently, the measurements were performed by stepwise increasing the magnetic field.

Table 5.1: Overview of the $Mn_{1-x}Fe_xSi$ compositions studied. Their composition was verified with X-ray Fluorescence Spectroscopy (XRF). The critical temperature T_C is defined by the maximum in χ' (if any). T' marks the onset of the (short-ranged) helimagnetic correlations and is defined as the high-temperature inflection point of χ' (if any). T'' is the highest temperature where the fitted Curie-Weiss law deviates by more than 5% from the experimental data. The Curie-Weiss temperature T_{CW} and constant C are obtained from the best fit of the zero field susceptibility to the Curie Weiss law $\chi' = C/(T - T_{CW})$. The fits to the data are displayed in Fig. 5.2. μ_{eff} is the effective magnetic moment and obtained from the Curie-Weiss constant. The spontaneous magnetization at $T = 2.5$ K, $m_{0\text{T},2.5\text{K}}$ is obtained by extrapolating the magnetization from the high-magnetic field field-polarized regime to zero field as illustrated by the inset of Fig. 5.6.

x_{nom}	x_{XRF}	T_C [K]	T' [K]	T_C-T' [K]	T'' [K]	T_{CW} [K]	C [10^{-6} m^3 mol^{-1}]	μ_{eff} [μ_B f.u.$^{-1}$]	μ_{eff} [μ_B Mn^{-1}]	$m_{0\text{T},2.5\text{K}}$ [μ_B f.u.$^{-1}$]
0	0	29.2	31.0	1.8	31.5(2)	28.1(4)	8.7(1)	2.2	2.2	0.393
0.03	0.032	19.2	23.4	4.2	26.3(3)	21.0(6)	8.1(1)	2.1	2.1	0.32
0.09	0.089	8.1	13.0	4.9	18.2(4)	11.8(4)	4.9(2)	1.7	1.9	0.183
0.10	0.101	5.4	10.5	5.1	13.9(5)	8.6(3)	4.7(3)	1.6	1.8	0.15
0.11	0.112	5.0	9.0	4.0	9.5(5)	6.0(6)	4.1(4)	1.5	1.7	0.122
0.13	0.125	3.4	7.1	3.7	8.2(5)	5.1(6)	3.7(4)	1.5	1.7	0.09
0.14	0.14	2.4	5.4	3	5.7(4)	2.2(5)	2.8(4)	1.3	1.5	0.052
0.19	0.185	-	-	-	11(2)	-3(1)	2.6(4)	1.3	1.6	-
0.25	0.252	-	-	-	10(1)	-8(2)	2.9(3)	1.3	1.7	-
0.32	0.318	-	-	-	6(1)	-12(2)	1.8(3)	1	1.4	-

5.3. SUSCEPTIBILITY AT ZERO MAGNETIC FIELD

Figure 5.1(a) depicts the temperature dependence of χ' measured for the different compositions of $Mn_{1-x}Fe_xSi$ at zero field and at a frequency of $f = 5$ Hz. For the reference undoped system MnSi, a sharp maximum occurs at $T_C = 29.2$ K, characteristic of the first order transition to the helimagnetic state. This sharp maximum is followed by an almost temperature independent χ' at lower temperatures. A similar behavior is also found for $Mn_{1-x}Fe_xSi$ with $x < 0.11$ but with a T_C that shifts to lower temperatures with increasing Fe concentration as tabulated in Table 5.1.

The zero field temperature dependence of χ' for $x \geq 0.11$ is qualitatively different from the one for $x \leq 0.10$. For $x = 0.11$, 0.13 and 0.14 the sharp maximum of χ' at T_C is replaced by a broad one, on the basis of which a transition temperature can still be determined. Furthermore, Fig. 5.1(b) shows that the temperature dependence of χ'' also reveals a different behavior for $x = 0.11$, 0.13 and 0.14 than for $x \leq 0.11$. Whereas for $x \leq 0.11$ χ'' is zero at all temperatures studied, a finite χ'' signal is found for $T < T_C$. Hence, on the basis of these results we identify $x^* \approx 0.11$ as a characteristic Fe concentration where the helimagnetic ground state changes.

Although a broad maximum in the temperature evolution of χ' is still visible for $x = 0.11$, 0.13 and 0.14, no maximum is found for $x = 0.19$, 0.25 and 0.32. For these concentrations, χ' increases with decreasing temperature down to the lowest temperature studied, and no transition temperature can be extracted from the data. In addition, χ'' is always zero in the studied temperature range for these compositions. As we will further discuss below, based on the evolution of T_C with Fe doping we determine a critical concentration $x_C \approx 0.17$ where $T_C \to 0$.

The next step in the analysis of the zero field susceptibility is to fit the high temperature data to the Curie-Weiss law $\chi' = C/(T - T_{CW})$, which allows one to extract two important quantities: the Curie-Weiss constant C and the Curie Weiss temperature T_{CW}. The corresponding fits to the data are shown in Fig. 5.2, which also displays the inverse of χ' versus temperature. At sufficiently high temperatures, i.e. well above T_C, the Curie-Weiss law provides a satisfactory description of the temperature dependence of χ'. The parameters obtained from the fit are tabulated in Table 5.1 and are in good agreement with published values for $x = 0.0$ [15] and 0.11 [13]. The Curie-Weiss constant of 8.7 10^{-6} m^3 mol^{-1} for MnSi translates to an effective magnetic moment of $\mu_{\text{eff}} = 2.2$ μ_B f.u.$^{-1}$. The effective magnetic moment first decreases monotonically with increasing Fe concentration and amounts to ~ 1.7 μ_B per Mn ion for $x = 0.11$. For higher Fe concentrations, μ_{eff} levels off at about 1.0-1.3 μ_B f.u.$^{-1}$.

The most important result of the Curie-Weiss analysis is the Curie-Weiss temperature that becomes negative for $x > x_C$. This is illustrated by Fig. 5.3, which displays the evolution of T_{CW} with Fe substitution: T_{CW} decreases monotonically with increasing Fe substitution and becomes negative for $x \gtrsim 0.16$-0.17. This indicates that the average magnetic interactions, which are ferromagnetic for $x < x_C$, become effectively antiferromagnetic for $x > x_C$.

Deviations from Curie-Weiss behavior appear when the temperature decreases and comes to the vicinity of T_C. These deviations reflect magnetic correlations that build up just above T_C in a region that in MnSi has been identified as a precursor region [15, 17–19, 21]. We identify the high temperature border of the precursor phase by introducing two

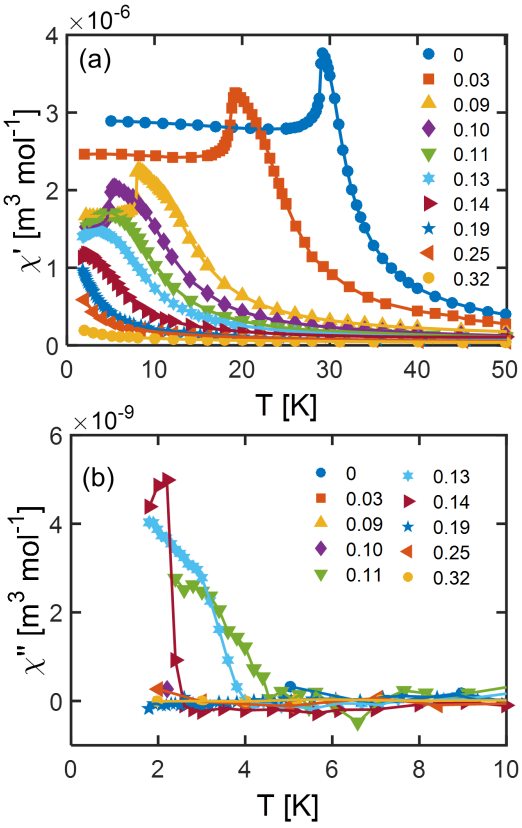

Figure 5.1: Temperature dependence of the (a) real component χ' and (b) imaginary component χ'' of the ac susceptibility of $Mn_{1-x}Fe_xSi$ for the compositions indicated in the legend. The data were measured at zero magnetic field and at a frequency of $f = 5$ Hz.

characteristic temperatures: T', defined as the high-temperature inflection point of χ', and T'', the highest temperature where the fitted Curie-Weiss law deviates by more than 5% from the experimental data. These characteristic temperatures are listed in Table 5.1 for all studied compositions. No inflection point is found for $x = 0.19$, 0.25 and 0.32 within the investigated temperature window and thus T' cannot be determined for these compositions.

The effect of Fe substitution on T_C and the extent of the precursor region are further illustrated by Fig. 5.4, where both T_C and T' are plotted versus x. Both characteristic temperatures decrease with increasing Fe concentration and this decay is best accounted for by an exponential function [1]. An extrapolation of the Fe concentration dependence of T_C leads to $T_C \to 0$ at $x_C \approx 0.17$, which is in excellent agreement with the

[1] It has been suggested in ref. [15] that T_C follows a square-root dependence. However, our data is better described by an exponential function than by a square root dependence.

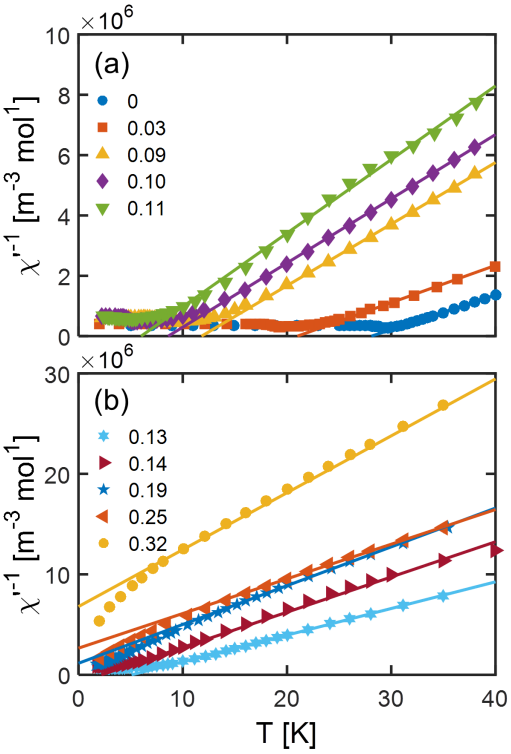

Figure 5.2: Inverse magnetic susceptibility as a function of temperature for $Mn_{1-x}Fe_xSi$ with (a) $x = 0.0$, 0.03, 0.09, 0.10, 0.11 and (b) $x = 0.13$, 0.14, 0.19, 0.25 and 0.32. The solid lines indicate the best fits of the Curie-Weiss law, i.e. $\chi' = C/(T - T_{CW})$, to the experimental data. The fitted parameters are displayed in Table 5.1.

concentration where the Curie-Weiss temperature changes sign. The difference between T_C and T', i.e. the temperature width of the precursor phase, varies non-monotonically with increasing x. It amounts to 1.8 K for MnSi and increases up to 5.1 K for $x = 0.10$. This increase indicates a widening of the precursor region with increasing doping for $x \leq 0.10$ as also reported elsewhere [15, 22]. On the contrary, for $x > x^*$, the difference between T_C and T' decreases considerably indicating a shrinking of the precursor region for these higher doped samples.

The zero field susceptibility results indicate that the magnetic behavior for $x \leq x^* \approx 0.11$ is distinctively different from the one for $x > x^*$. Moreover, one can make a clear distinction between $x = 0.11$, 0.13 and 0.14, i.e. $x^* < x < x_C$ and $x = 0.19$, 0.25 and 0.32, i.e. $x > x_C$. These conclusions are substantiated by the data we obtained under magnetic field and which will be discussed in the following sections.

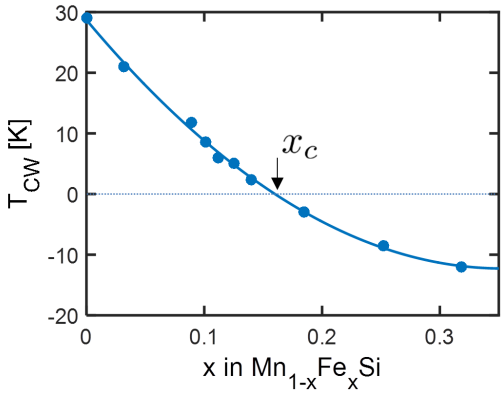

Figure 5.3: Concentration dependence of the Curie Weiss temperature T_{CW} in $Mn_{1-x}Fe_xSi$, as obtained from the best fit of the zero field susceptibility to the Curie Weiss law, i.e. $\chi' = C/(T - T_{CW})$. The corresponding fits to the data are displayed in Fig. 5.2. The continuous line indicates a fit of the data to $T_{CW} = ax^2 + bx + c$ with a = 3.2(0.5) 10^2, b = -2.3(0.2) 10^2 and c = 29(1). x_C is the critical Fe concentration at which the (extrapolated) value of the critical temperature becomes zero.

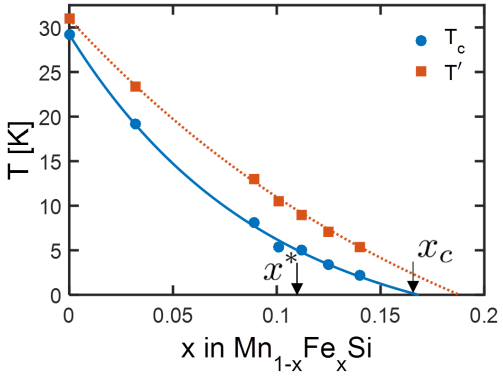

Figure 5.4: The critical temperature T_C, defined by the maximum in χ' (see Fig. 5.1) and T' as a function of x in $Mn_{1-x}Fe_xSi$. T' marks the onset of the (short-ranged) helimagnetic correlations and is defined as the high-temperature inflection point of χ'. The continuous line indicates a fit of the data to $T_C = a\exp[-bx] + c$ with a = 35(7), b = 11(4) and c = -6(2). The dotted line indicates a fit of the data to $T' = a\exp[-bx] + c$ with a = 51(9), b = 5(2) and c = -20(9). x_C is the critical Fe concentration at which the (extrapolated) value of the critical temperature becomes zero.

5.4. MAGNETIC FIELD

5.4.1. MAGNETIZATION CURVES

Fig 5.5(a) presents the magnetization as a function of magnetic field for different compositions of $Mn_{1-x}Fe_xSi$ at T = 2.5 K for $x \leq 0.11$ and at T = 1.8 K for $x \geq 0.14$. The measurements for MnSi are characteristic for a cubic helimagnet below its transition

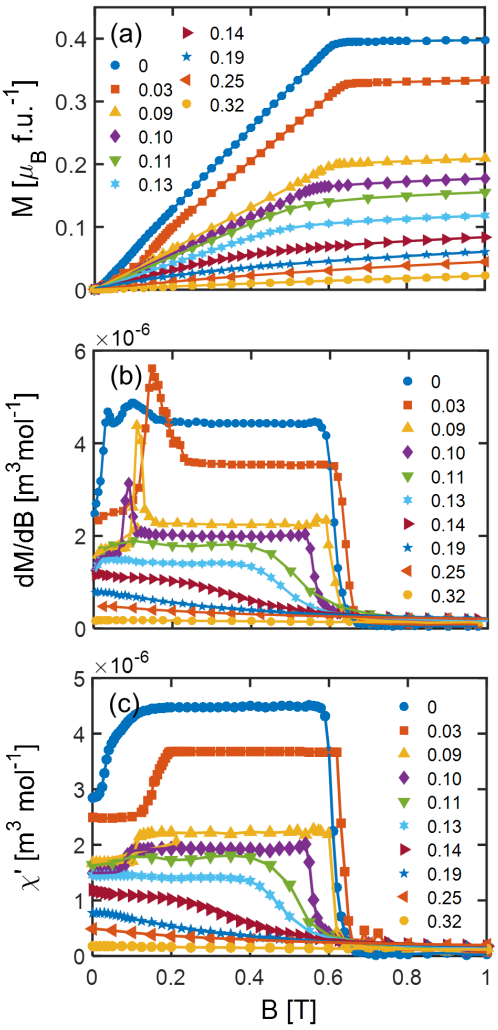

Figure 5.5: Magnetic field dependence of the (a) magnetization M, (b) its derivative with respect to the magnetic field, dM/dB, and (c) the real component of the susceptibility χ' measured at $f = 5$ Hz. The composition of the $Mn_{1-x}Fe_xSi$ samples are provided in the legend. The measurements were performed at $T = 2.5$ K for $x \leq 0.13$ and at $T = 1.8$ K for $x \geq 0.14$. The magnetic field was applied along the ⟨110⟩ crystallographic direction.

temperature: M increases almost linearly with field in the helical and conical phase and levels of abruptly when reaching the field polarized state at B_{C2}. By extrapolating the magnetization from the high-magnetic field field-polarized state to zero field, one obtains the spontaneous magnetization. The derived spontaneous magnetization at T = 2.5 K, $m_{0T,2.5K}$, is shown in Fig. 5.6 and amounts to $m_{0T,2.5K} = 0.40\ \mu_B$ f.u.$^{-1}$, which is in good agreement with the literature [15]. The spontaneous magnetization of the Fe

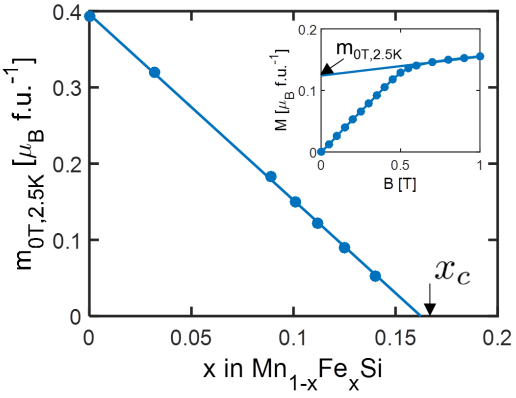

Figure 5.6: Concentration dependence of the spontaneous magnetization at T = 2.5 K, $m_{2.5K,0\,T}$ of $Mn_{1-x}Fe_xSi$ as a function of x. $m_{0T,2.5K}$ is obtained by extrapolating the magnetization from the high-magnetic field field-polarized regime to zero field as illustrated by the inset. The continuous line indicates a fit of $m_{0T,2.5K} = ax + b$ with a = 2.5(1) and b = 0.40(1) to the data. This fit extrapolates to $m_{0T,2.5K}$ = 0 at $x \approx$ 0.17, i.e. at $\approx x_C$, the Fe concentration at which also $T_C \to 0$.

5

doped samples decreases linearly with increasing Fe doping and extrapolates to zero at $x \approx 0.17$. It thus appears that both T_C and the spontaneous magnetization vanish at x_C $\approx$ 0.17.

More information is derived from the derivative of the magnetization with respect to the magnetic field, dM/dB, and from χ'. The data, presented in Fig. 5.5(b) and (c), show for MnSi two clear anomalies. At high magnetic fields, a sharp drop of dM/dB is seen at B_{C2}, which we define by the inflection point of dM/dB versus magnetic field. B_{C2} marks the disappearance of the conical modulations and the onset of the field polarized state. At a lower magnetic field a relatively broad anomaly indicates the helical-to-conical transition at $B_{C1} \sim 0.10$ T. At this transition, the helices reorient from the ⟨111⟩ crystallographic directions at zero magnetic field towards the magnetic field that was applied along the ⟨110⟩ crystallographic direction. The pronounced difference between dM/dB in Fig. 5.5(b) and χ' in Fig. 5.5(c) indicates that this reorientation occurs over macroscopic times [23], as also reported for other cubic helimagnets [24, 25].

Fe doping results in a pronounced decrease of the magnetization, but for $x \leq 0.10$ the shape of the magnetization curve, its derivative dM/dB and χ' remain the same. Furthermore, the two anomalies seen for MnSi at B_{C1} and B_{C2} are clearly present. The situation is different for $x \geq 0.11$, i.e. $x \geq x^*$, where no anomaly at B_{C1} can be detected. This implies that one can no longer distinguish between a helical and a conical phase. The high-magnetic field anomaly at B_{C2} persists for x = 0.11, 0.13 and 0.14 but becomes distinctively different than for $x < x^*$: instead of a steep drop of dM/dB and χ' within $\sim$ 0.03 T at B_{C2}, the decrease is much more gradual and covers a wide magnetic field range of up to 0.3 T for x = 0.14. The data thus indicate a much more gradual transition to the high-magnetic field field-polarized state for $x^* < x < x_C$ than for $x < x^*$.

For $x > x_C$, the magnetization curves, the derivative dM/dB and χ' are markedly dif-

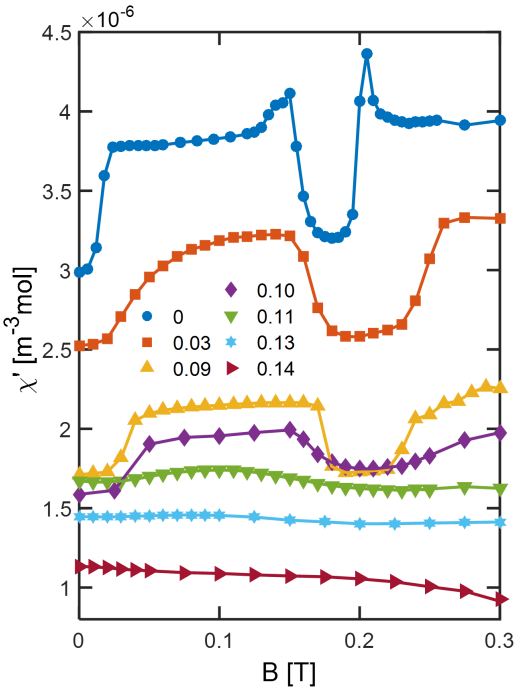

Figure 5.7: Magnetic field dependence of χ' at f = 5 Hz for $Mn_{1-x}Fe_xSi$ and for the compositions indicated in the legend. The temperatures are chosen to correspond to the respective center of the A-phase and are T = 28.5 K for x = 0.0, T = 17.4 K for x = 0.03, T = 7.0 K for x = 0.09, T = 4.2 K for x = 0.10, T = 4.0 K for x = 0.11, T = 2.5 K for x = 0.13 and T = 1.8 K for x = 0.14. The magnetic field was applied along the ⟨110⟩ crystallographic direction.

ferent from the curves for $x < x_C$. For x = 0.19, 0.25 and 0.32, dM/dB and χ' decrease monotonically with increasing field and there are no anomalies or inflection points up to B = 5 T, i.e. the largest field measured. In addition, dM/dB and χ' coincide with each other which indicates the absence of any magnetic relaxation phenomena at macroscopic time scales.

The magnetization data presented above confirm the conclusions derived from the the zero field susceptibility that with increasing Fe doping, two characteristic concentrations can be indentified: x^* and x_C. For $x < x^*$ the response of the magnetization to a magnetic field closely resembles that of MnSi with clear anomalies of its field derivative at B_{C1} and B_{C2}. For $x^* < x < x_C$ a finite spontaneous magnetization persists as well as a (smeared) anomaly at high magnetic fields, but the anomaly at B_{C1} disappeared. Finally for $x > x_C$ there are no indications for a phase transition, no spontaneous magnetization can be determined and no anomalies as a function of magnetic field can be detected.

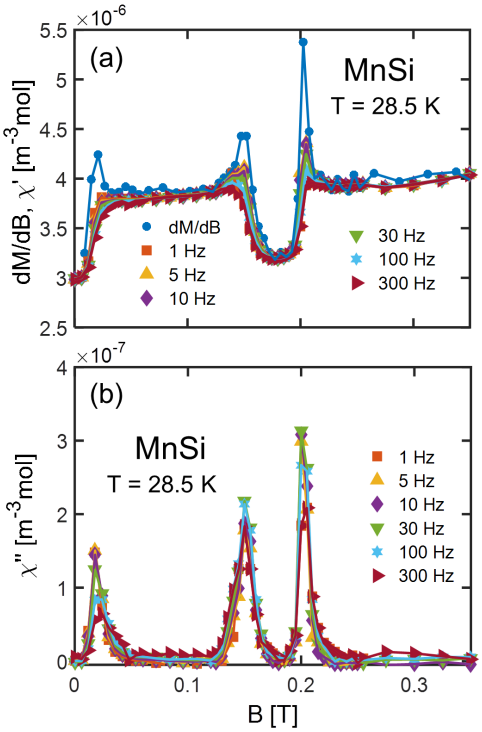

Figure 5.8: Magnetic field dependence of (a) dM/dB and χ' and (b) χ'' of MnSi for the frequencies indicated. The data have been collected at $T = 28.5$ K which corresponds to the center of the A-phase. The magnetic field was applied along the ⟨110⟩ crystallographic direction.

5.4.2. SKYRMION LATTICE PHASE

The experimental results also provide new insights on the effect of Fe doping on the stability and extent of the skyrmion lattice pocket. For this reason we have plotted in Fig. 5.7 for several $Mn_{1-x}Fe_xSi$ compositions χ' versus magnetic field for temperatures that correspond to the center of the A-phase. In the reference system MnSi, the increase of χ' at low magnetic fields marks the transition from the helical to the conical phase. At higher fields, a clear dip of χ', occurs which is characteristic of the skyrmion lattice phase [26]. This dip is surrounded by two sharp maxima in χ' that mark the borders of the skyrmion lattice phase.

With increasing Fe concentration, the dip that marks the A-phase widens and its center shifts to higher magnetic fields. It thus appears that the field region where skyrmion lattice correlations are stabilized is enhanced by Fe doping. This confirms similar conclusions drawn from Hall effect measurements [14]. For $x = 0.10$ and 0.11 the dip becomes shallow and its boundaries are smeared. Finally, the dip completely disappears for $x = 0.13$ and 0.14. These results indicate that the skyrmion lattice correlations are gradually suppressed for $x > 0.09$.

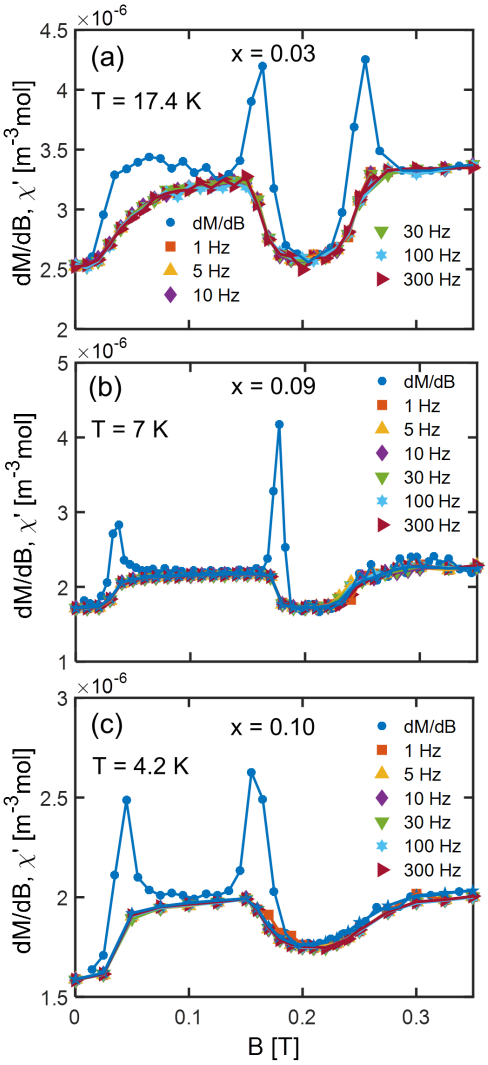

Figure 5.9: Magnetic field dependence of dM/dB and χ' of $Mn_{1-x}Fe_xSi$ measured at the indicated frequencies. The measurements have been performed at (a) $T = 17.4$ K for $x = 0.03$, (b) $T = 7.0$ K at $x = 0.09$ and (c) $T = 4.2$ K for $x = 0.10$. These temperatures correspond to the respective centers of the A-phase. The magnetic field was applied along the ⟨110⟩ crystallographic direction.

The frequency dependence of χ' as well as a comparison with dM/dB is provided in Fig. 5.8(a) for MnSi. With increasing magnetic field, dM/dB shows three clear peaks marking the helical-to-conical transition and the lower- and higher field limits of the A-phase, respectively. Around these phase boundaries χ' is significantly smaller than dM/dB at all frequencies measured, including those as low as 1 Hz. This implies that

these phase transitions involve macroscopic relaxation times. This is confirmed by the corresponding χ'' curves displayed in Fig. 5.8(b). They reveal two clear peaks at the lower- and higher field boundaries of the A-phase. An analysis of χ'' as a function of frequency at a constant field indicates that the characteristic frequencies are in the order of tens of Hertz. In addition, it shows that the frequency dependence cannot be described by a simple single exponential relaxation, but is much broader, as for $Fe_{1-x}Co_xSi$ [27].

The frequency dependence of χ' around the A-phase changes substantially with Fe doping. This is illustrated by Figure 5.9, which provides the magnetic field dependence of dM/dB and χ' for several drive frequencies at temperatures that correspond to the center of the A-phase for x = 0.03, 0.09 and 0.10. The results reveal that the peak in dM/dB seen for MnSi at the low magnetic field limit of the A-phase persists up to x = 0.10, while the one at the high magnetic field limit is absent at x = 0.09 and 0.10. In addition, Figure 5.9 shows no substantial differences between χ' measured at different frequencies and no χ'' signal is detected down to the lowest frequency of 1 Hz. However, a considerable difference exists between dM/dB and χ'. This result implies that the characteristic frequencies of the magnetic response at the border of the A-phase shift with increasing Fe doping to lower values, outside of our experimental frequency window.

5

5.4.3. OVERVIEW OF THE EFFECT OF DOPING

An overview of the effect of Fe doping on the magnetic properties of $Mn_{1-x}Fe_xSi$ under magnetic field is provided by the waterfall plots in Fig. 5.10. They depict the temperature dependence of χ' measured at f = 5 Hz for various magnetic fields and for all the compositions investigated. For MnSi [Fig. 5.10(a)] the maximum of χ' persists up to a magnetic field of $B \gtrsim 0.35$ T. At this magnetic field, the maximum evolves into a kink and a new maximum appears at a higher temperature. Thus, the single maximum for fields $B \lesssim 0.35$ T splits into two well-separated features for $B \gtrsim 0.35$ T. This is a generic feature of cubic chiral magnets, and has been, besides in MnSi [28], observed in Cu_2OSeO_3 [25, 29], FeGe [30] and $Fe_{1-x}Co_xSi$ [27, 31]. The low-temperature kink reflects the DM interaction and marks the onset of the conical phase along the B_{C2} line. With increasing field the kink becomes more gradual, shifts to lower temperatures and finally disappears for $B \gtrsim 0.65$ T. The high-temperature maximum reflects the ferromagnetic interaction and broadens, decreases in amplitude and shifts to higher temperatures with increasing magnetic field.

The occurrence of a single maximum at low magnetic fields and the subsequent split in two features at higher magnetic fields persists up to $x \approx x_C$. On the other hand, the behavior below T_C changes dramatically already at x^*. Whereas for $x < x^*$ the features marking the borders between the helical, conical and skyrmion lattice phases are clearly present, they are absent for $x^* < x < x_C$ substantiating our earlier conclusion based on the magnetization data. The differences in the magnetic behavior for $x < x^*$ and $x^* < x < x_C$ will be further addressed in Section V.

For $x > x_C$, χ' increases monotonically with decreasing temperature and there are no anomalies that may indicate a phase transition. However, the magnetic behavior is not purely paramagnetic. Deviations from Curie-Weiss and paramagnetic behavior are observed below T'', i.e. the highest temperature where the fitted Curie-Weiss law deviates by 5% from the experimental data. These deviations are most pronounced for

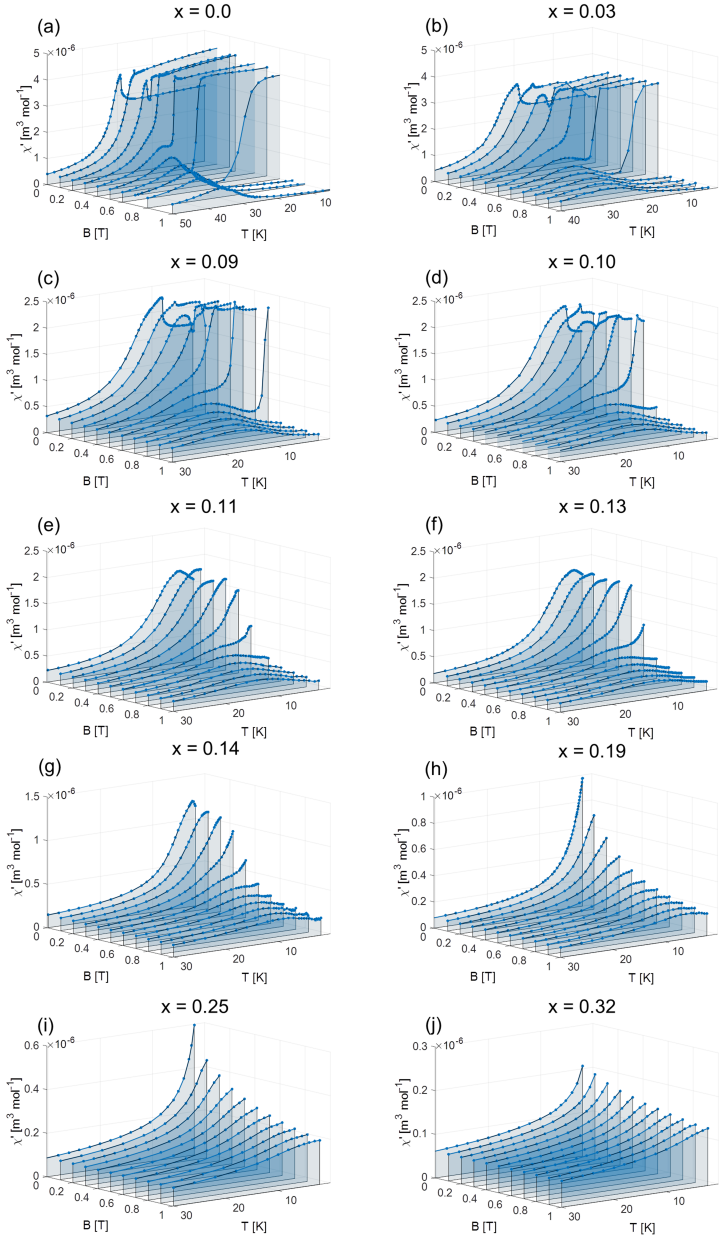

Figure 5.10: Waterfall plot of the temperature dependence of χ' for several magnetic fields at f = 5 Hz of $Mn_{1-x}Fe_xSi$ with (a) x = 0.0, (b) x = 0.03, (c) x = 0.09, (d) x = 0.10, (e) x = 0.11, (f) x = 0.13, (g) x = 0.14, (h) x = 0.19, (i) x = 0.25 and (j) x = 0.32. The magnetic field was applied along the ⟨110⟩ crystallographic direction.

x = 0.19, and somewhat smaller for x = 0.25 and 0.32. They occur for x = 0.19, 0.25 and 0.32 at T'' = 11 K, 10 K and 6 K, respectively, and become more evident with decreasing temperature.

5.5. PHASE DIAGRAMS AND DISCUSSION

A comprehensive overview of the effect of Fe doping on the magnetic properties and the magnetic phase diagram of $Mn_{1-x}Fe_xSi$ is provided by the contour plots of Figs. 5.11 and 5.12. They show χ' and χ'' over a wide magnetic field and temperature range and substantiate our earlier conclusion that the studied $Mn_{1-x}Fe_xSi$ compositions can be categorized in three different groups: $x < x^*$, $x^* < x < x_C$ and $x > x_C$. For this reason, we discuss the phase diagrams separately for these three groups.

For $x < x^* \approx 0.11$ [Figs. 5.11(a)-(c)], the contour plots show the same generic behavior as for MnSi and other B20 compounds. However, some subtle differences occur with respect to MnSi. First, the helical-to-conical transition line (B_{C1}) is virtually temperature independent for MnSi but has a a negative slope for the doped samples. Such a temperature dependent transition line has also been observed in $Fe_{1-x}Co_xSi$ [24, 27, 31, 32] and as in $Fe_{1-x}Co_xSi$ it disappears when cooling the sample under magnetic field [15]. On the other hand, the conical-to-field polarized transition line (B_{C2}) has a similar temperature dependence as for MnSi. The black continuous lines in Fig. 5.11(a)-(c) show that the B_{C2} transition line can be well accounted for by a power law $B_{C2} \propto (T - T_C)^n$, with n = 0.14(2), 0.15(2), 0.09(3), 0.10(4) for x = 0.0, 0.03, 0.09 and 0.10, respectively. The fitted values of n are much lower than for Cu_2OSeO_3 (n = 0.25) [29] and $Fe_{1-x}Co_xSi$ (n = 0.40) [29], and show that the temperature dependence of B_{C2} in $Mn_{1-x}Fe_xSi$ is relatively weak at low temperatures.

A second difference between the contour plots of MnSi and the Fe doped samples is the disappearance of the χ'' signal at f = 5 Hz around B_{C1} and the phase boundaries of the A-phase. For the reference system MnSi, a strong χ'' signal occurs at the helical-to-conical transition (B_{C1}), and the lower- and higher field boundaries of the A-phase. These signals disappear for $x > 0.03$, as they shift outside the frequency window as addressed in the previous section. On the other hand, a prominent feature is the region of χ'' above T_C and under magnetic field that persists up to x = 0.13. This prominent feature is generic to cubic chiral magnets [25, 27, 33] and will be addressed in more detail in another manuscript.

The magnetic phase diagrams for $x^* < x < x_C$ [Fig. 5.11(d)-(f) and Fig. 5.12(d)-(f)] bear certain similarities with the ones for $x < x^*$ but also some remarkable differences. As for $x < x^*$, one can still distinguish (i) a clear region of the phase diagram with an increased but relatively constant χ' at low temperatures, i.e. for $T < T_C$, (ii) a field induced transition to a field polarized state and (iii) a clear (ferromagnetic) maximum as a function of temperature above the transition temperature. These similarities indicate that helimagnetic correlations are still stabilized at low temperatures.

The differences between the magnetic phase diagrams for $x < x^*$ and $x^* < x < x_C$ are more remarkable than the similarities. The first main difference is the absence of boundaries between the different magnetic phases below T_C, implying that one can no longer distinguish between the helical, conical and skyrmion lattice phase for $x > x^*$. Another main difference is in the nature of the transition between the precursor phase

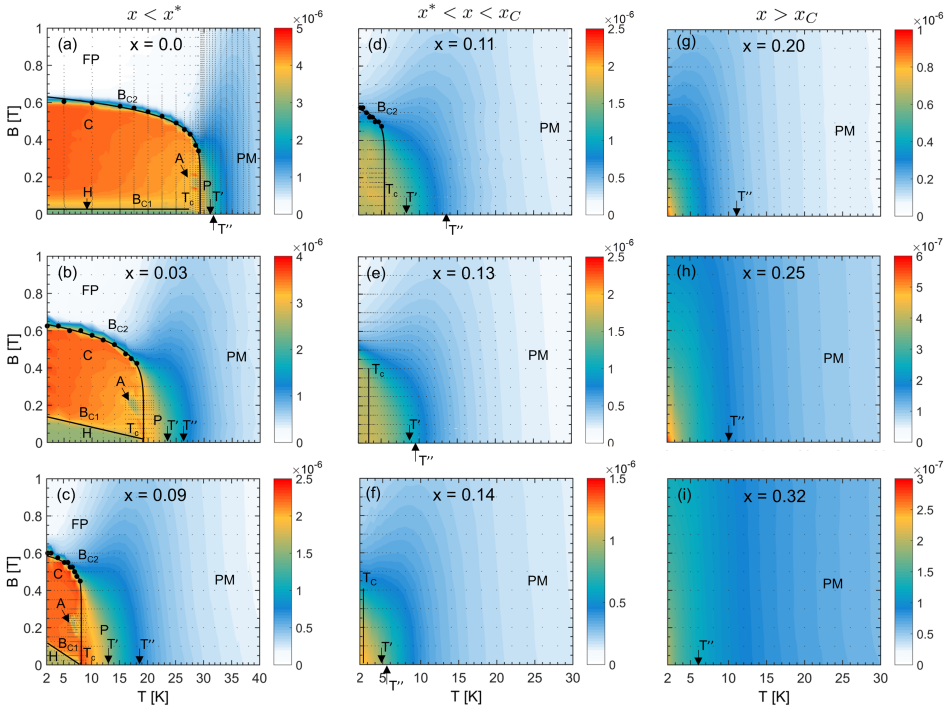

Figure 5.11: Contour plots showing ZFC χ' at f = 5 Hz in units of m^3mol^{-1} of $Mn_{1-x}Fe_xSi$ with (a) x = 0.0, (b) x = 0.03, (c) x = 0.09, (d) x = 0.11, (e) x = 0.13, (f) x = 0.14, (g) x = 0.19, (h) x = 0.25 and (i) x = 0.32. The measurements were performed as a function of field for x = 0.0 and as a function of temperature for $x \geq 0.03$. The grey dots indicate the points at which the signal was recorded. The B_{C1} line marks the helical-to-conical transition line and is indicated with a black continuous line. B_{C2} is defined by the inflection point of χ' and is indicated with black circles The black continuous line is a fit of the B_{C2} points to $B_{C2} = a(T_C - T)^n$. A indicates the A-phase, C the Conical phase, FP the Field Polarized phase, H the Helical phase, P the Precursor region and PM the Paramagnetic phase. T_C is the critical temperature and is defined by the maximum in χ' (if any). T' marks the onset of the (short-ranged) helimagnetic correlations and is defined as the high-temperature inflection point of χ' (if any) T'' is the highest temperature where the fitted Curie-Weiss law deviates by more than 5% from the experimental data. The magnetic field was applied along the ⟨110⟩ crystallographic direction.

just above T_C and the helimagnetic phase below T_C. This transition is much more gradual for $x^* < x < x_C$ than for $x < x^*$ as seen from the shape of the zero field susceptibility at T_C [Fig. 5.1]. A striking difference with MnSi, $x < x^*$, but also with the disordered helimagnet $Fe_{0.7}Co_{0.3}Si$, is the finite χ'' signal that appears at zero field [Fig. 5.1(b)] for $T < T_C$ and $x^* < x < x_C$. This indicates that not only the helimagnetic transition changes at x^*, but also the ground state. It might indicate a glassy behavior, as a non-zero χ'' is also observed in spin-glass systems. The helimagnetic ground state for $x^* < x < x_C$ is thus not only substantially different from that of MnSi, but also of the disordered helimagnet $Fe_{0.7}Co_{0.3}Si$. For the latter, the magnetic phase diagram and zero field susceptibility bears close similarities to those of $Mn_{1-x}Fe_xSi$ with $x < x^*$, although the helimagnetic transition is remarkably different [34]. These observations substantiate the conclusion

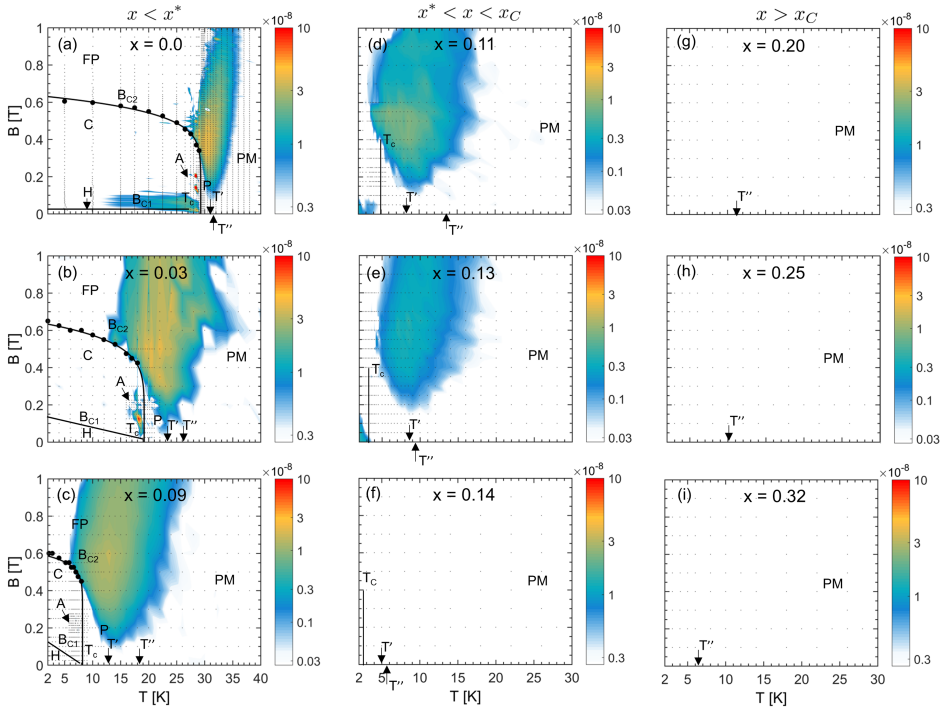

Figure 5.12: Contour plots showing ZFC χ'' at f = 5 Hz in units of m^3mol^{-1} of $Mn_{1-x}Fe_xSi$ with (a) x = 0.0, (b) x = 0.03, (c) x = 0.09, (d) x = 0.11, (e) x = 0.13, (f) x = 0.14, (g) x = 0.19, (h) x = 0.25 and (i) x = 0.32. The measurements were performed as a function of field for x = 0.0 and as a function of temperature for $x \geq 0.03$. The grey dots indicate the points at which the signal was recorded. The B_{C1} line marks the helical-to-conical transition line and is indicated with a black continuous line. B_{C2} is defined by the inflection point of χ' and is indicated with black circles The black continuous line is a fit of the B_{C2} points to $B_{C2} = a(T_C - T)^n$. A indicates the A-phase, C the Conical phase, FP the Field Polarized phase, H the Helical phase, P the Precursor region and PM the Paramagnetic phase. The magnetic field was applied along the ⟨110⟩ crystallographic direction.

that x^* is a characteristic point of the phase diagram.

The magnetic phase diagrams for $x > x_C$ [Fig. 5.11(g)-(j)] hardly bear similarities with the ones for $x < x_C$. Rather, the contour plots show for all magnetic fields a monotonically increasing χ' with decreasing temperature, and for every temperature a monotonically decreasing χ' with increasing field, and no measurable χ'' signal. Although this is also expected for a paramagnetic state, clear deviations from paramagnetic behavior are observed below T'' where short-range correlations set in.

The systematic study on the effect of disorder on the (heli)magnetic correlations in $Mn_{1-x}Fe_xSi$ reveals the existence of two characteristic concentrations, x^* and x_C. The importance of x^* was unnoticed in a previous magnetization, susceptibility and specific heat study [15]. On the other hand, resistivity [9] and Electron Spin Resonance (ESR) measurements [10] provide indications for the existence of x^*. On the basis of these results, it has been suggested that x^* is a quantum critical point. The results presented

in this paper do not provide direct support for this hypothesis. They rather indicate that the increased disorder renders the long-range helimagnetic order unstable. However, this is not a gradual evolution with increasing dilution, but rather an abrupt change at x^*.

The other characteristic concentration, x_C, corresponds to the point where T_C is suppressed to zero temperature although the effective magnetic moment (Table 5.1) is not reduced dramatically. Therefore, this point is a candidate for a quantum critical point. It is also the point at which the Curie-Weiss temperature changes sign, indicating a qualitative change of behavior.

Although the average interactions become anti-ferromagnetic for $x > x_C$, with T_{CW} = -12 K for $x = 0.32$, no long-range magnetic order is observed down to the lowest temperature. The failure of the system to order can be attributed to quantum fluctuations as also suggested in earlier work [9–11, 13, 15], and possibly to a (quantum) spin liquid behavior [13]. However, additional measurements focusing on the structure and dynamics of the magnetic correlations are required to elucidate the nature of the magnetic correlations in this section of the x-T phase diagram.

5.6. CONCLUSION

In summary, the systematic study of the magnetic susceptibility and magnetization of $Mn_{1-x}Fe_xSi$ with x = 0 - 0.32 presented above unambiguously identifies two characteristic Fe concentrations: $x^* \approx 0.11$, where a cross-over occurs from a sharp to a gradual helimagnetic transition, and $x_C \approx 0.17$ where the critical temperature and spontaneous magnetization vanish and the Curie-Weiss temperature changes sign. The identification of these two characteristic points implies that the studied compounds can be categorized in three groups: $x < x^*$, $x^* < x < x_C$ and $x > x_C$. The magnetic phase diagrams for $x < x^*$ bear close similarities with the one for MnSi and other cubic helimagnets. On the other hand, they are substantially different for $x^* < x < x_C$ for which a clear transition temperature can be determined. However, this transition is gradual and it is no longer possible to identify clear boundaries between the helical, conical and skyrmion lattice phases. Together with the appearance of a non-zero χ'' for $T < T_C$, it suggests that the helimagnetic ground state is significantly different from that for $x < x^*$. For $x > x_C$ the average interactions become anti-ferromagnetic and albeit deviations from paramagnetic behavior are seen when approaching zero temperature, no indication of long range magnetic order is found. The nature of the ground state for both $x^* < x < x_C$ and $x > x_C$ is an open question that deserves future experimental and theoretical attention.

REFERENCES

[1] L. J. Bannenberg, F. Weber, A. J. E. Lefering, T. Wolf, and C. Pappas, *Magnetization and ac susceptibility study of the cubic chiral magnet $Mn_{1-x}Fe_xSi$,* Physical Review B **98**, 184430 (2018).

[2] I. E. Dzyaloshinskii, *A thermodynamic theory of "weak" ferromagnetism of antiferromagnetics,* Journal of Physics and Chemistry of Solids **4**, 241 (1958).

[3] T. Moriya, *Anisotropic Superexchange Interaction and Weak Ferromagnetism,* Physical Review **120**, 91 (1960).

[4] Y. Ishikawa, K. Tajima, D. Bloch, and M. Roth, *Helical spin structure in manganese silicide MnSi,* Solid State Communications **19**, 525 (1976).

[5] P. Bak and M. H. Jensen, *Theory of helical magnetic structures and phase transitions in MnSi and FeGe,* Journal of Physics C: Solid State Physics **13**, L881 (1980).

[6] S. Mühlbauer, B. Binz, F. Jonietz, C. Pfleiderer, A. Rosch, A. Neubauer, R. Georgii, and P. Böni, *Skyrmion lattice in a chiral magnet,* Science **323**, 915 (2009).

[7] S. Seki and M. Mochizuki, *Skyrmions in Magnetic Materials* (Springer, 2015).

[8] A. Bauer and C. Pfleiderer, *Generic aspects of skyrmion lattices in chiral magnets,* in *Topological Structures in Ferroic Materials* (Springer, 2016) pp. 1–28.

[9] S. V. Demishev, I. I. Lobanova, V. V. Glushkov, T. V. Ischenko, N. E. Sluchanko, V. A. Dyadkin, N. M. Potapova, and S. V. Grigoriev, *Quantum bicriticality in $Mn_{1-x}Fe_xSi$ solid solutions: Exchange and percolation effects,* JETP Letters **98**, 829 (2013).

[10] S. V. Demishev, A. N. Samarin, V. V. Glushkov, M. I. Gilmanov, I. I. Lobanova, N. A. Samarin, A. V. Semeno, N. E. Sluchanko, N. M. Chubova, V. A. Dyadkin, and S. V. Grigoriev, *Anomalous spin relaxation and quantum criticality in $Mn_{1-x}Fe_xSi$ solid solutions,* JETP Letters **100**, 28 (2014).

[11] V. V. Glushkov, I. I. Lobanova, V. Y. Ivanov, V. V. Voronov, V. A. Dyadkin, N. M. Chubova, S. V. Grigoriev, and S. V. Demishev, *Scrutinizing Hall effect in $Mn_{1-x}Fe_xSi$: Fermi surface evolution and hidden quantum criticality,* Physical Review Letters **115**, 256601 (2015).

[12] S. V. Demishev, A. N. Samarin, J. Huang, V. V. Glushkov, I. I. Lobanova, N. E. Sluchanko, N. M. Chubova, V. A. Dyadkin, S. V. Grigoriev, M. Y. Kagan, *et al.*, *Magnetization of $Mn_{1-x}Fe_xSi$ in high magnetic fields up to 50 T: Possible evidence of a field-induced Griffiths phase,* JETP letters **104**, 116 (2016).

[13] S. V. Demishev, I. I. Lobanova, A. V. Bogach, V. V. Glushkov, V. Y. Ivanov, T. Ischenko, N. Samarin, N. E. Sluchanko, S. Gabani, E. Čižmár, *et al.*, *Effect of a magnetic field on the intermediate phase in $Mn_{1-x}Fe_xSi$: Spin-liquid versus fluctuations scenario,* JETP letters **103**, 321 (2016).

[14] C. Franz, F. Freimuth, A. Bauer, R. Ritz, C. Schnarr, C. Duvinage, T. Adams, S. Blügel, A. Rosch, Y. Mokrousov, *et al.*, *Real-space and reciprocal-space Berry phases in the Hall effect of $Mn_{1-x}Fe_xSi$,* Physical Review Letters **112**, 186601 (2014).

[15] A. Bauer, A. Neubauer, C. Franz, W. Münzer, M. Garst, and C. Pfleiderer, *Quantum phase transitions in single-crystal $Mn_{1-x}Fe_xSi$ and $Mn_{1-x}Co_xSi$: Crystal growth, magnetization, ac susceptibility, and specific heat,* Physical Review B **82**, 064404 (2010).

[16] S. V. Grigoriev, S. V. Maleyev, A. I. Okorokov, Y. O. Chetverikov, R. Georgii, P. Böni, D. Lamago, H. Eckerlebe, and K. Pranzas, *Critical fluctuations in MnSi near T_C: A polarized neutron scattering study,* Physical Review B **72**, 134420 (2005).

[17] C. Pappas, E. Lelievre-Berna, P. Falus, P. M. Bentley, E. Moskvin, S. Grigoriev, P. Fouquet, and B. Farago, *Chiral paramagnetic skyrmion-like phase in MnSi,* Physical Review Letters **102**, 197202 (2009).

[18] M. Janoschek, M. Garst, A. Bauer, P. Krautscheid, R. Georgii, P. Böni, and C. Pfleiderer, *Fluctuation-induced first-order phase transition in Dzyaloshinskii-Moriya helimagnets,* Physical Review B **87**, 134407 (2013).

[19] C. Pappas, L. J. Bannenberg, E. Lelièvre-Berna, F. Qian, C. D. Dewhurst, R. M. Dalgliesh, D. L. Schlagel, T. A. Lograsso, and P. Falus, *Magnetic Fluctuations, Precursor Phenomena and Phase Transition in MnSi under Magnetic Field,* Physical Review Letters **119**, 047203 (2017).

[20] L. J. Bannenberg, F. Qian, R. M. Dalgliesh, N. Martin, G. Chaboussant, M. Schmidt, D. L. Schlagel, T. A. Lograsso, H. Wilhelm, and C. Pappas, *Reorientations, relaxations, metastabilities, and multidomains of skyrmion lattices,* Physical Review B **96**, 184416 (2017).

[21] S. Grigoriev, S. Maleyev, A. I. Okorokov, Y. O. Chetverikov, and H. Eckerlebe, *Field-induced reorientation of the spin helix in MnSi near T_C,* Physical Review B **73**, 224440 (2006).

[22] S. V. Grigoriev, V. A. Dyadkin, E. V. Moskvin, D. Lamago, T. Wolf, H. Eckerlebe, and S. V. Maleyev, *Helical spin structure of $Mn_{1-y}Fe_ySi$ under a magnetic field: Small angle neutron diffraction study,* Physical Review B **79**, 144417 (2009).

[23] A. Bauer, A. Chacon, M. Wagner, M. Halder, R. Georgii, A. Rosch, C. Pfleiderer, and M. Garst, *Symmetry breaking, slow relaxation dynamics, and topological defects at the field-induced helix reorientation in MnSi,* Physical Review B **95**, 024429 (2017).

[24] L. J. Bannenberg, K. Kakurai, F. Qian, E. Lelièvre-Berna, C. D. Dewhurst, Y. Onose, Y. Endoh, Y. Tokura, and C. Pappas, *Extended skyrmion lattice scattering and long-time memory in the chiral magnet $Fe_{1-x}Co_xSi$,* Physical Review B **94**, 104406 (2016).

[25] F. Qian, H. Wilhelm, A. Aqeel, T. T. M. Palstra, A. J. E. Lefering, E. H. Brück, and C. Pappas, *Phase diagram and magnetic relaxation phenomena in Cu_2OSeO_3,* Physical Review B **94**, 064418 (2016).

[26] A. Bauer and C. Pfleiderer, *Magnetic phase diagram of MnSi inferred from magnetization and ac susceptibility,* Physical Review B **85**, 214418 (2012).

[27] L. J. Bannenberg, A. J. E. Lefering, K. Kakurai, Y. Onose, Y. Endoh, Y. Tokura, and C. Pappas, *Magnetic relaxation phenomena in the chiral magnet $Fe_{1-x}Co_xSi$: An ac susceptibility study,* Physical Review B **94**, 134433 (2016).

[28] C. Thessieu, C. Pfleiderer, A. N. Stepanov, and J. Flouquet, *Field dependence of the magnetic quantum phase transition in MnSi,* Journal of Physics: Condensed Matter **9**, 6677 (1997).

[29] I. Živković, J. White, H. M. Rønnow, K. Prša, and H. Berger, *Critical scaling in the cubic helimagnet Cu_2OSeO_3*, Physical Review B **89**, 060401 (2014).

[30] H. Wilhelm, M. Baenitz, M. Schmidt, U. K. Rößler, A. A. Leonov, and A. N. Bogdanov, *Precursor Phenomena at the Magnetic Ordering of the Cubic Helimagnet FeGe,* Physical Review Letters **107**, 127203 (2011).

[31] A. Bauer, M. Garst, and C. Pfleiderer, *History dependence of the magnetic properties of single-crystal $Fe_{1-x}Co_xSi$,* Physical Review B **93**, 235144 (2016).

[32] S. V. Grigoriev, V. A. Dyadkin, D. Menzel, J. Schoenes, Y. O. Chetverikov, A. I. Okorokov, H. Eckerlebe, and S. V. Maleyev, *Magnetic structure of $Fe_{1-x}Co_xSi$ in a magnetic field studied via small-angle polarized neutron diffraction,* Physical Review B **76**, 224424 (2007).

[33] K. Tsuruta, M. Mito, H. Deguchi, J. Kishine, Y. Kousaka, J. Akimitsu, and K. Inoue, *Nonlinear magnetic responses at the phase boundaries around helimagnetic and skyrmion lattice phases in MnSi: Evaluation of robustness of noncollinear spin texture,* Physical Review B **97**, 094411 (2018).

[34] L. J. Bannenberg, K. Kakurai, P. Falus, E. Lelièvre-Berna, R. M. Dalgliesh, C. D. Dewhurst, F. Qian, Y. Onose, Y. Endoh, Y. Tokura, and C. Pappas, *Universality of the helimagnetic transition in cubic chiral magnets: Small angle neutron scattering and neutron spin echo spectroscopy studies of FeCoSi,* Physical Review B **95**, 144433 (2017).

6

EVOLUTION OF HELIMAGNETIC CORRELATIONS IN $Mn_{1-x}Fe_xSi$ WITH DOPING: A SANS STUDY

We present a comprehensive small angle neutron scattering study of the doping dependence of the helimagnetic correlations in $Mn_{1-x}Fe_xSi$. The long-range helimagnetic order in $Mn_{1-x}Fe_xSi$ is suppressed with increasing Fe content and disappears for $x > x^* \approx 0.11$, i.e. well before $x_C \approx 0.17$ where the transition temperature vanishes. For $x > x^*$, only finite isotropic helimagnetic correlations persist which bear similarities with the magnetic correlations found in the precursor phase of MnSi. Magnetic fields gradually suppress and partly align these short-ranged helimagnetic correlations along their direction through a complex magnetization process.

6.1. INTRODUCTION

Tuning the interactions in magnetic materials by pressure or chemical substitution is a well-visited route to discover new and exotic phases of condensed matter. In chiral magnetism, the most notable example is the effect of hydrostatic pressure on the properties of the archetype chiral magnet MnSi. In this system, the helimagnetic order at ambient pressure results from the competition between the ferromagnetic exchange and the Dzyaloshinsky-Moriya (DM) [2, 3] interaction that arises from the non-centrosymmetric crystal structure of this B20 compound [4]. The helical order, of which the propagation vector is fixed to the ⟨111⟩ crystallographic directions by magnetic anisotropy, is suppressed under pressure at $p_C \approx 1.4$ GPa. Above p_C, partial magnetic order with slow dynamics persists in a Non-Fermi Liquid phase that emerges without quantum criticality [5–7]. Additionally, topological contributions to the Hall effect hint that magnetic correlations with non-trivial topology similar to the skyrmion lattice phase at ambient pressure [8, 9] are stabilized in this region of the phase diagram [10].

This chapter has been published in Physical Review B **98**(18), 184431 (2018) [1].

Another way of tuning the chiral magnetic order is by chemically substituting MnSi with iron. In $Mn_{1-x}Fe_xSi$, the helimagnetic order is suppressed with increasing Fe concentration, with the spontaneous magnetization [11, 12], Curie-Weiss [12] and transition temperature T_C [11, 12] extrapolating to 0 at $x_C \approx 0.17$. Remarkably, a change of magnetic behavior is already observed at $x^* \approx 0.11$ by magnetization [12], magnetic susceptibility [12], resistivity [13] and Electron Spin Resonance (ESR) measurements [14]. Based on these results, it has been suggested that x^* is a candidate for a quantum critical point (QCP), possibly associated with the suppression of the long-range helimagnetic order [13, 15–17]. However, despite all these studies, the nature of x^* and the magnetic correlations for $x^* < x < x_C$ remain unclear.

In the following we address these points and discuss the helimagnetic order in non-stochiometric $Mn_{1-x}Fe_xSi$ around the first characteristic concentration x^*. With small angle neutron scattering (SANS), we systematically study the evolution of the (heli) magnetic correlations as a function of both temperature and magnetic field. In particular, we investigate the effect of dilution on the helimagnetic correlations and compare the topology of the magnetic correlations for $x = 0, 0.03, 0.09, 0.10$, i.e. $x < x^*$ with that of $x = 0.11, 0.14$, i.e. $x > x^*$. All measurements were performed by systematically applying the magnetic field both perpendicular and parallel to the incoming neutron beam. In this way, we present an overview of the topology of all helimagnetic correlations both perpendicular and parallel to the magnetic field in a way that is not provided by previous studies.

The results show that with increasing Fe concentration, the helices at zero magnetic field first reorient from ⟨111⟩ to the ⟨110⟩ crystallographic directions and that the long-range helimagnetic order in $Mn_{1-x}Fe_xSi$ disappears at x^*. For $x > x^*$ finite isotropic helimagnetic correlations set-in and which bear similarities to those seen in the precursor phase in MnSi [18–21]. Magnetic fields gradually suppress and only partly align the helices along their direction through a complex magnetization process.

6.2. EXPERIMENTAL

Single crystals of $Mn_{1-x}Fe_xSi$ with nominal Fe concentration $x = 0.03, 0.09, 0.10, 0.11$ and 0.14 were grown using the Bridgeman method and are listed in Table 6.1. The composition of the single crystals was checked with a PANalytical Axios x-ray Fluorescence Spectrometer and revealed Fe concentrations of 0.032, 0.089, 0.101, 0.112, 0.140 respectively. The samples originate from exactly the same batches as the samples of our previous magnetization and susceptibility study [12]. They have an irregular shape and their dimensions vary from $\sim 5\times5\times5$ mm^3 to $\sim 10\times10\times15$ mm^3. The measurements on MnSi were performed on the same cubic single crystal with dimensions $\sim 5\times5\times5$ mm^3 used in previous experiments [21–23]. The structure of all single crystals was checked with an x-ray Laue camera and the $x = 0, 0.03, 0.10, 0.11$ and 0.14 samples were aligned with the $[\bar{1}10]$ crystallographic direction vertical. The $x = 0.09$ sample was aligned with the [001] direction vertical.

The SANS measurements were performed on the time-of-flight instrument Larmor of the ISIS neutron spallation source using neutrons with wavelengths of $0.09 \leq \lambda \leq 1.25$ nm. The samples were placed at a distance of 4.4 m from the detector that consists of 80 ^{3}He tubes, each 8 mm wide. The SANS patterns were normalized to standard

Table 6.1: Overview of the $Mn_{1-x}Fe_xSi$ compositions studied. Their composition was verified with X-ray Fluorescence Spectroscopy (XRF). The critical temperature has been determined from magnetic susceptibility [12] and for $x \leq x^*$ from the inflection point of the temperature dependence of the total scattered intensity at zero magnetic field. The pitch of the helical modulation ℓ is tabulated for T = 2.5 K and $T = T_C$.

x_{nom}	x_{XRF}	T_C [K] (SQUID)	T_C [K] (SANS)	$\ell_{2.5K}$ [nm]	ℓ_{T_C} [nm]
0	0	29.2	28.8	18.2	16.0
0.03	0.032	19.2	19.2	13.8	13.2
0.09	0.089	8.1	7.8	9.5	9.7
0.10	0.101	5.4	5.5	8.9	9.0
0.11	0.112	5.0	-	8.4	8.5
0.14	0.140	2.4	-	7.0	7.0

monitor counts and background corrected using a high temperature measurement. The magnetic field was applied using a 3D vector cryomagnet either parallel ($\vec{B}||\vec{k}_i$) or perpendicular ($\vec{B} \perp \vec{k}_i$) to the incoming neutron beam designated by its wavevector $\vec{k}_i$. All measurements were performed by first zero field cooling the sample to the lowest temperature of interest. Then a magnetic field was applied and the signal was recorded by stepwise increasing the temperature. The system was brought to thermal equilibrium before the measurement at each temperature commenced.

6.3. ZERO MAGNETIC FIELD

Figure 6.1 depicts typical SANS patterns recorded at zero magnetic field and for different temperatures and compositions. The results for MnSi are displayed in Fig. 6.1(a) and are in good agreement with the literature [18, 20, 21, 24]: above T_C, a diffuse isotropic ring of scattering appears with radius $\tau = 2\pi/\ell$, where ℓ is the pitch of the helical modulation. This ring, which originates from isotropic, chiral and fluctuating helimagnetic correlations, intensifies and narrows when approaching $T_C \sim$ 28.7 K. Below T_C, the ring disappears and two Bragg peaks mark the onset of the helical order oriented along the ⟨111⟩ directions. The patterns displayed in Fig. 6.1(b) for x = 0.03 show a qualitatively similar behavior, but with a lower transition temperature of $T_C \sim$ 19.2 K.

By further increasing the Fe concentration, the propagation direction of the helix below T_C changes from ⟨111⟩ to ⟨110⟩, as can be inferred from the alignment of the Bragg peaks along the ⟨110⟩ directions for x = 0.09 [Fig. 6.1 (c)]. This change of propagation direction is accompanied with a broadening of the Bragg peaks, which are no longer well-defined spots as for x = 0 and 0.03 [Fig. 6.1(a),(b)], but smeared on a ring with radius $\tau = 2\pi/\ell$ [1]. A slight increase of the Fe concentration to x = 0.10 considerably enhances the broadening, indicating an ill-defined orientation of the helix and a weakening of the magnetic anisotropy, which is possibly due to the increased chemical disorder [25].

The long-range helimagnetic order with a well-defined propagation direction disap-

[1] The rocking scans reveal a considerable broadening of the helical Bragg peaks on the surface of a sphere with radius $\tau = 2\pi/\ell$

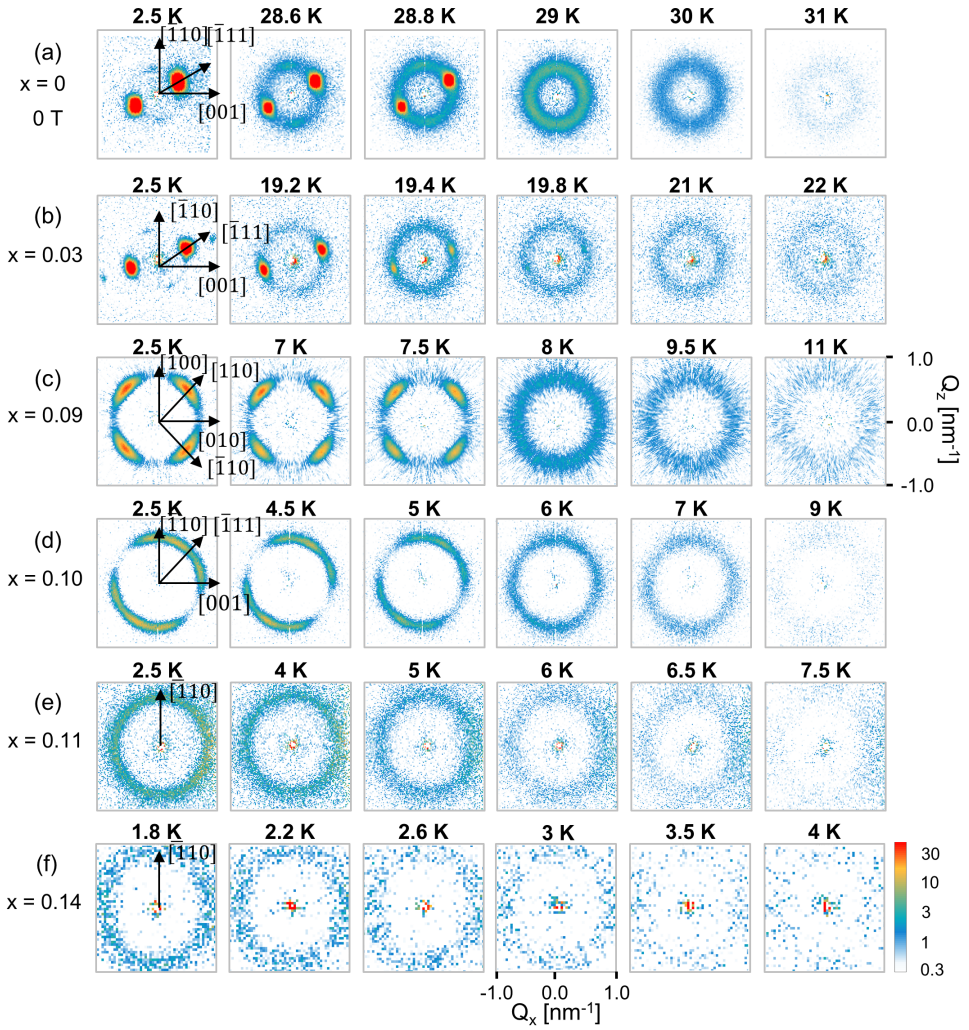

Figure 6.1: SANS patterns recorded at zero magnetic field and different temperatures for $Mn_{1-x}Fe_xSi$ with (a) $x = 0$, (b) $x = 0.03$, (c) $x = 0.09$, (d) $x = 0.10$, (e) $x = 0.11$ and (f) $x = 0.14$.

pears for $x > x^*$. For $x = 0.11$ and 0.14, broad isotropic rings of scattering instead of Bragg peaks are observed down to the lowest temperature measured, which are well below the respective transition temperatures inferred from susceptibility measurements [Table 6.1]. These rings of scattering intensify but remain broad with decreasing temperature and indicate finite helimagnetic correlations.

The effect of dilution on the zero-field helimagnetic order is further illustrated by Figure 6.2(a), which displays the normalized scattering function $S(Q)$ at $B = 0$ T and below the transition temperature for several compositions. $S(Q)$ is obtained by radial averag-

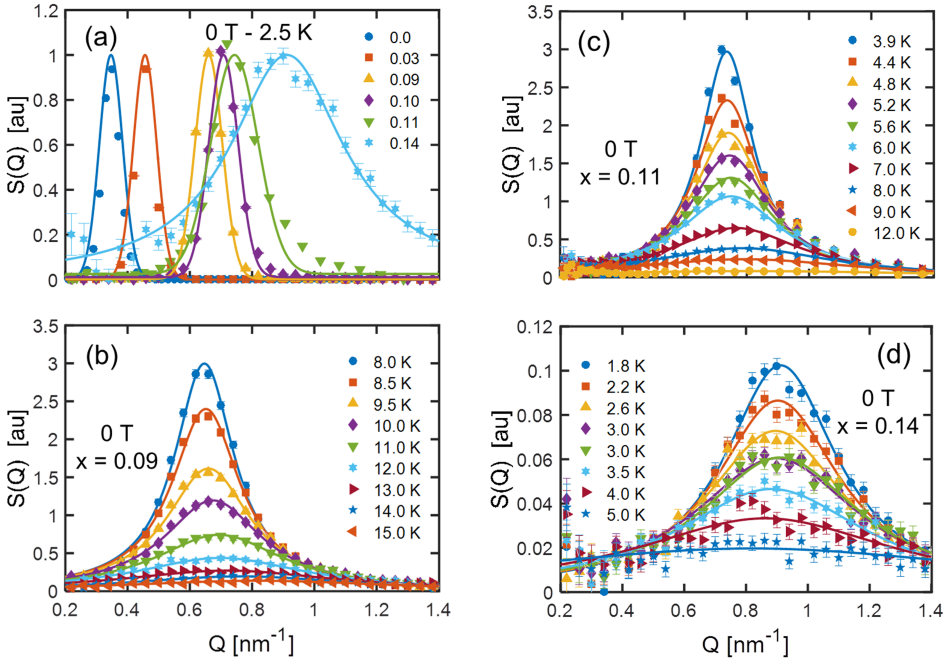

Figure 6.2: The scattering function $S(Q)$, deduced by radially averaging the scattered intensity and at zero field for $Mn_{1-x}Fe_xSi$. In Panel (a) S(Q) is determined for $T < T_C$ and the Fe concentrations indicated in the legend. $S(Q)$ was measured at $T = 2.5$ K for $x \leq 0.11$ and $T = 2.0$ K for $x = 0.14$ and is normalized to its maximum value. Panels (b) - (d) show $S(Q)$ at the indicated temperatures for (b) $x = 0.09$, (c) $x = 0.11$ and (d) $x = 0.14$. In Panel (a) the solid lines indicate the best fits of the data to a Gaussian for $x < 0.11$ where the width of the Gaussian is fixed by the instrumental resolution. For $x \geq 0.11$ and in Panels (b)-(d) the solid lines represent the best fits of eq. 6.1 (convoluted with the instrumental resolution) to the data.

ing the SANS patterns of Fig. 6.1 and is thus a one dimensional representation of the two dimensional scattering patterns. The line shape of $S(Q)$ is dramatically different for $x > x^*$ than for $x < x^*$. Indeed, for $x \leq 0.10$, $S(Q)$ has a Gaussian lineshape with a constant FWHM of $\Delta Q/Q \approx 0.16$ that roughly corresponds to the resolution of the instrument. On the other hand, for $x = 0.11$ and especially for $x = 0.14$, $S(Q)$ is no longer resolution limited but broad, as indicated by the respective FWHM of $\Delta Q/Q \approx 0.23$ for $x = 0.11$ and $\Delta Q/Q \approx 0.65$ for $x = 0.14$. As further illustrated by Figs. 6.2(b)-(d), which display $S(Q)$ at different temperatures for $x = 0.09$, 0.11 and 0.14, $S(Q)$ remains for $x > x^*$ broad down to the lowest temperature measured (1.8 K) indicating that helimagnetic correlations with finite correlation lengths persist to the lowest temperatures.

The extent of the helimagnetic correlations can be quantified by the correlation lengths ξ derived using the Ornstein-Zernike relation:

$$S(Q) = C/\left((Q - 2\pi/\ell)^2 + \xi^{-2}\right), \tag{6.1}$$

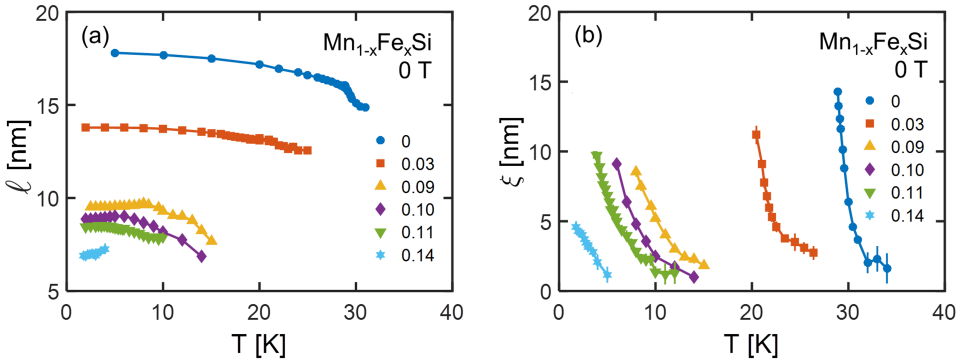

Figure 6.3: Temperature dependence of (a) the magnetic correlation length ξ and (b) the pitch of the helical modulation ℓ at zero magnetic field and for the $Mn_{1-x}Fe_xSi$ compositions indicated in the legend. The values of ξ are obtained by fitting $S(Q)$ to equation 6.1. For $x \leq 0.10$ and $T < T_C$, ℓ was obtained from fitting $S(Q)$ to a Gaussian centered at $\tau = 2\pi/\ell$. For $T < T_C$ and $x \leq 0.10$, the linewidth of $S(Q)$ is limited by the experimental resolution and ξ cannot be determined.

6

with C the Curie constant and ℓ the pitch of the helix. The temperature dependence of both ℓ and ξ are displayed in Fig. 6.3. For the sake of clarity, the values of ℓ at $T = 2.5$ K and at T_C are also provided in Table 6.1. The results show a qualitatively similar behavior for all compositions with $x < x^*$: the correlation length increases monotonically with decreasing temperature and reaches approximately the pitch of the helix at T_C. Differently, for $x > x^*$, ξ increases monotonically down to the lowest temperature, reaching for $x = 0.14$ a value of 5 nm $\sim 2/3\ell$ at 1.8 K.

Furthermore, Fig. 6.3(b) shows that ℓ decreases monotonically with increasing Fe concentration: at $T = 2.5$ K, it decreases from 18.2 nm for $x = 0$ to 6.2 nm for $x = 0.14$. As further addressed in the discussion, this indicates a strengthening of the DM interaction with respect to the ferromagnetic exchange interaction.

6.4. MAGNETIC FIELD

6.4.1. MEASUREMENTS AT $T = 2$ K

Figure 6.4 displays SANS patterns recorded as a function of magnetic field for $Mn_{1-x}Fe_xSi$ with (a),(b) $x = 0.09$, (c),(d) $x = 0.11$ at $T = 2.5$ K and (e),(f) $x = 0.14$ at $T = 2$ K, i.e. for $T < T_C$. These SANS patterns have been collected in two complementary experimental configurations: one with the magnetic field parallel to the incoming neutron beam ($\vec{B}||\vec{k}_i$) and one in which the field is perpendicular to the incoming neutron beam ($\vec{B} \perp \vec{k}_i$).

Fig. 6.4(a) shows SANS patterns for $x = 0.09$ with $\vec{B}||\vec{k}_i$ i.e. the configuration that is sensitive to helical modulations perpendicular to the magnetic field. At zero magnetic field, the pattern displays four smeared Bragg peaks oriented along the ⟨110⟩ crystallographic directions that originate from the helical phase. For $B = 0.1$ T two of these peaks disappear completely, while the other two considerable weaken in intensity. For magnetic fields exceeding 0.1 T, the scattered intensity is negligible, as expected for the

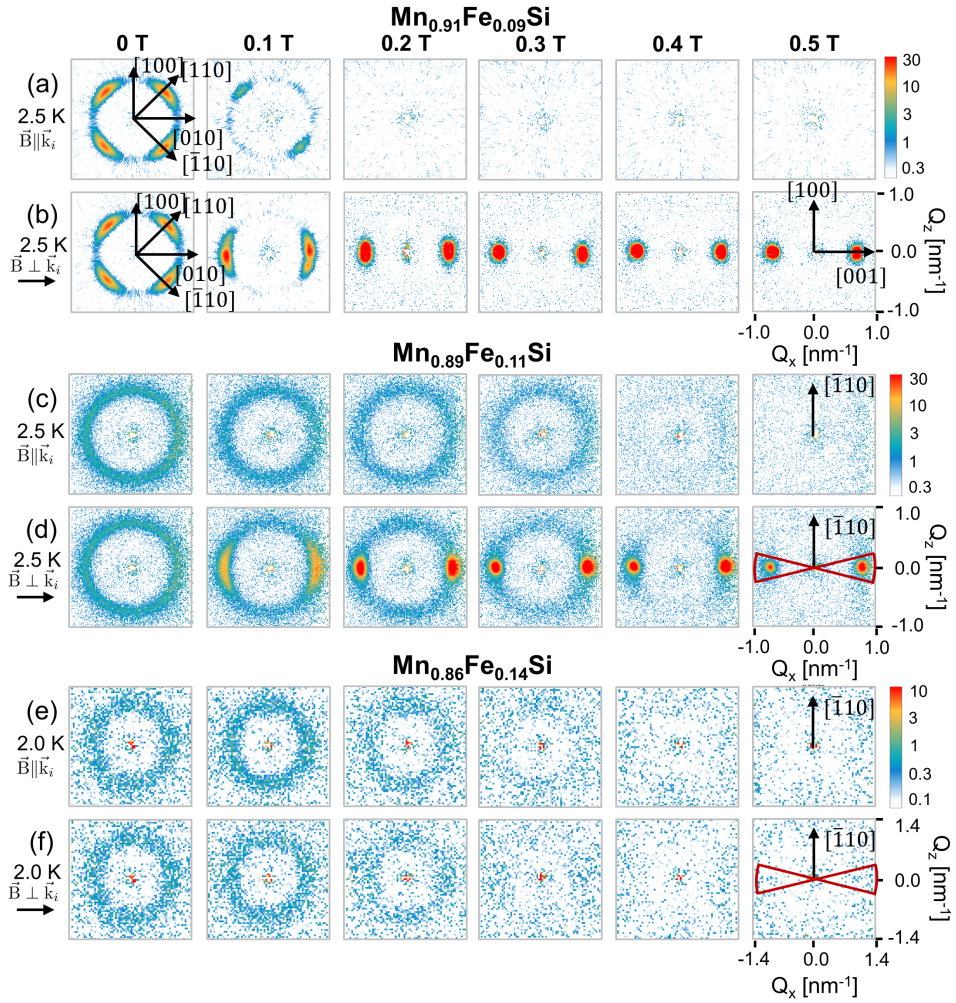

Figure 6.4: SANS patterns measured at $T < T_C$ as a function of the magnetic field for $Mn_{1-x}Fe_xSi$ with (a),(b) $x = 0.09$ at $T = 2.5$ K, (c),(d) $x = 0.11$ at $T = 2.5$ K and (e),(f) $x = 0.14$ at $T = 2.0$ K. The magnetic field was applied (a),(c),(f) parallel to the incoming neutron beam ($\vec{B}||\vec{k}_i$) and (b),(d),(e) perpendicular to it ($\vec{B} \perp \vec{k}_i$). The two 30° red wedges in Panels (d) and (f) indicate the section of the detector over which the radial integration was performed to obtain $S(Q)$ for $\vec{B} \perp \vec{k}_i$.

conical phase where all helices are oriented along the magnetic field.

A complementary picture is provided by the SANS patterns of Fig. 6.4(b) measured with $\vec{B} \perp \vec{k}_i$ and which probes helical modulations oriented along the magnetic field. In this configuration, spots of scattered intensity are found along the horizontal field direction for $B \gtrsim 0.05$ T. Together with the disappearance of the Bragg peaks for $\vec{B}||\vec{k}_i$, this behavior marks the conical phase in which the propagation direction of the helices changes from along the ⟨110⟩ crystallographic direction to the direction of the magnetic

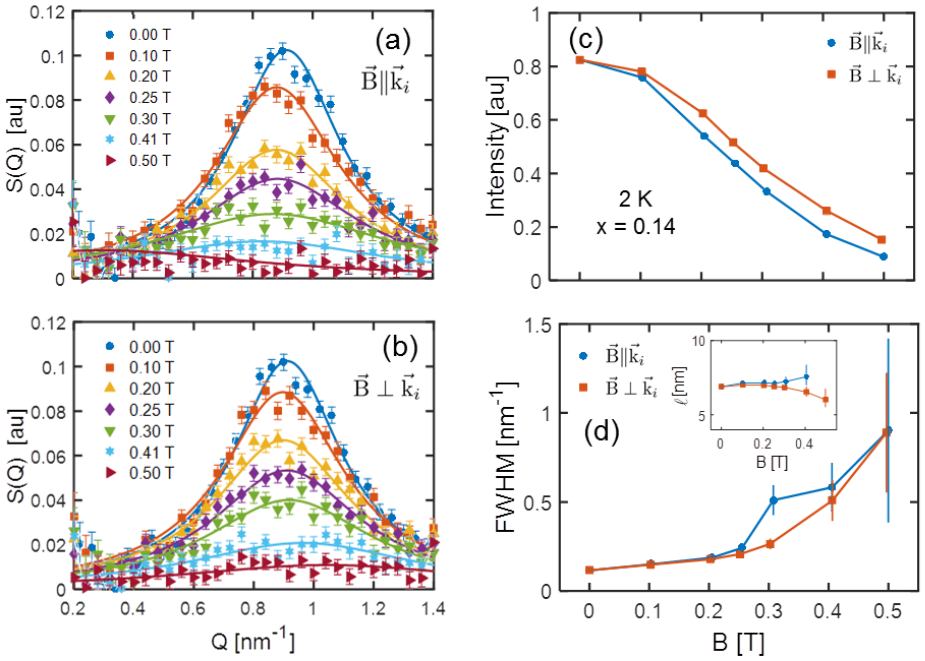

Figure 6.5: SANS results under magnetic field for $Mn_{0.89}Fe_{0.14}Si$ at $T = 2.0$ K. Panel (a) shows the scattering function $S(Q)$ in arbitrary units obtained by radial averaging the scattered intensity over the entire detector with the magnetic field applied parallel to the incoming neutron beam ($\vec{B}||\vec{k}_i$). Panel (b) shows $S(Q)$ in arbitrary units with the magnetic field applied perpendicular to the incoming neutron beam ($\vec{B} \perp \vec{k}_i$). In the latter case, $S(Q)$ is deduced from radial averaging the scattered intensity over the two 30° wedges along the magnetic field direction indicated in Fig. 6.4(f). Panel (c) shows the magnetic field dependence of the total scattered intensity obtained by summing the intensity over the entire detector for $\vec{B}||\vec{k}_i$ and over the two 30° wedges along the magnetic field for $\vec{B} \perp \vec{k}_i$. Panel (d) shows the magnetic field dependence of the Full-Width-Half-Maximum of $S(Q)$ and the inset shows the field dependence of the pitch of the helix ℓ as obtained from fitting the data of (a),(b) to eq. 6.1. These fits are indicated by the solid lines in Panels (a) and (b).

field. These Bragg peaks disappear for $B \gtrsim 0.6$ T, marking the onset of the field polarized state (not shown).

The patterns for $x = 0.11$ that are displayed in Fig. 6.4(c),(d) are qualitatively different from the ones for $x \leq x^*$. They show at zero field the isotropic ring of scattering discussed in the previous section. This isotropic scattering gradually disappears under magnetic field when the magnetic field is applied along $\vec{k}_i$ [Fig. 6.4(c)]. This is consistent with the patterns for $\vec{B} \perp \vec{k}_i$ [Fig. 6.4(d)], which show that the scattering concentrates along the field direction, ultimately leading to intense spots at high magnetic fields. However, the alignment of the helices along the magnetic field is very gradual and the intense Bragg-like spots coexist with a weaker ring of scattering up to $B = 0.5$ T. For $B \gtrsim 0.6$ T, the scattered intensity vanishes (not shown), indicating the onset of the field polarized state.

The alignment of the helimagnetic correlations by the magnetic field for $x = 0.14$ is considerably weaker than for $x = 0.11$. Although a slightly larger fraction of the helimag-

netic correlations is still oriented along the magnetic field for $B \geq 0.20$ T, this effect is much smaller than for $x = 0.11$. The effect of the magnetic field is also seen on the scattering function $S(Q)$ displayed in Figure 6.5(a) and (b) for $T = 2.0$ K. $S(Q)$ is obtained by radial averaging over the entire detector for $\vec{B}||\vec{k}_i$ [Fig. 6.5(a)], and over the two wedges of $\pm 15°$ around the magnetic field direction, indicated in Fig. 6.4(d), for $\vec{B} \perp \vec{k}_i$ [Fig. 6.5(b)]. The results show that for both experimental configurations, $S(Q)$ broadens considerably with increasing magnetic fields and decreases in intensity.

The decrease of the scattered intensity of $S(Q)$ is also seen in the magnetic field dependence of the total scattered intensity of Fig. 6.5(c) and is more pronounced for $\vec{B}||\vec{k}_i$ than for $\vec{B} \perp \vec{k}_i$. The decrease in intensity can be the result of either the suppression of the helimagnetic correlations as a whole, or the orientation of individual magnetic moments towards the magnetic field as for example the case in the conical phase for $x < x^*$. In addition, $S(Q)$ broadens for $x = 0.14$ considerably with increasing magnetic field, as highlighted by the magnetic field dependence of the Full Width Half Maximum (FWHM) of $S(Q)$ displayed in Fig. 6.5(d). This behavior is very different from the behavior found for smaller Fe dopings and indicates that the characteristic correlation length decreases substantially with increasing magnetic field: from ~ 5 nm at $B = 0$ T to $\xi \sim 2$ nm or approximately $1/4\ \ell$ at $B = 0.5$ T. This indicates a complex magnetization process in which the magnetic field first breaks the longer helical correlations, which are possibly those that encompass the lowest degree of disorder. In contrast, the shorter helices appear to be more robust, as is is also the case for vortices in re-entrant spin glasses [26].

6.4.2. SKYRMION LATTICE PHASE

The impact of Fe substitution on the skyrmion lattice correlations in $Mn_{1-x}Fe_xSi$ is illustrated by Fig. 6.6 which displays the total scattered intensity for four different Fe concentrations as a function of temperature at $B = 0.20$ T, i.e. in the heart of the skyrmion lattice phase. The magnetic field was applied both parallel ($\vec{B}||\vec{k}_i$) and perpendicular ($\vec{B} \perp \vec{k}_i$) to the incoming neutron beam.

For all compositions, the intensity above T_C is (almost) the same for both experimental configurations, as expected for isotropic correlations. In contrast, at low temperatures the intensity for $\vec{B} \perp \vec{k}_i$ is significantly higher than the one for $\vec{B}||\vec{k}_i$, as expected for the conical phase. In the intermediate temperature region, the onset of skyrmion lattice correlations leads to a different and non-monotonic evolution of the scattered intensity with temperature.

MnSi and $x = 0.09$ show basically the same behavior with a sharp maximum in intensity for $\vec{B}||\vec{k}_i$ occurring in a temperature region of about ± 1 K below T_C. Together with the characteristic six-fold symmetric scattering pattern displayed in the inset of Fig. 6.6(a),(b), this maximum marks the skyrmion lattice phase [8, 27, 28]. We note that skyrmion lattice correlations coexist with conical correlations, as seen from the finite amount of scattering in the configuration where $\vec{B} \perp \vec{k}_i$.

With dilution, the skyrmion lattice scattering weakens considerably. In addition, for $x = 0.10$ an isotropic ring of scattering instead of a clear six-fold symmetric pattern is found. This is similar to $Fe_{1-x}Co_xSi$ [29, 30], and the absence of the six-fold symmetric pattern is likely related to a weakening of the 4th and 6th order cubic anisotropy terms responsible for the alignment of the skyrmion lattice with respect to the crystallographic

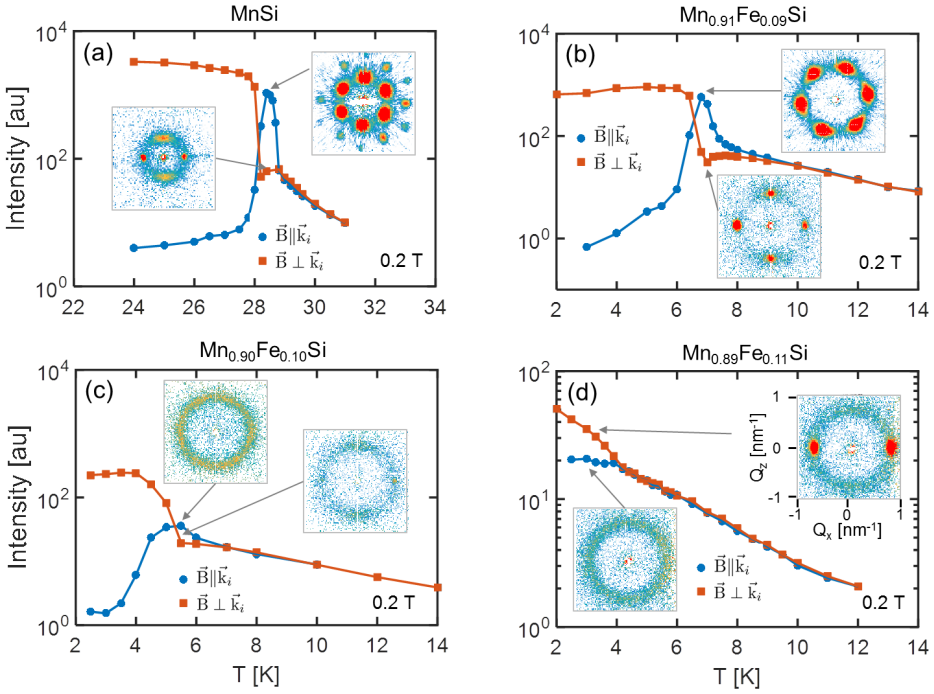

Figure 6.6: Temperature dependence of the total scattered intensity at $B = 0.20$ T for $Mn_{1-x}Fe_xSi$ with (a) $x = 0$, (b) $x = 0.09$, (c) $x = 0.10$, and (d) $x = 0.11$. The field was applied both parallel ($\vec{B}||\vec{k}_i$) and perpendicular ($\vec{B} \perp \vec{k}_i$) to the incoming neutron beam. The insets show characteristics SANS patterns at the indicated temperatures for both field configurations.

one [8, 22, 29]. The disappearance of Bragg peaks at low magnetic fields is also consistent with the broadening of the helical Bragg peaks that also indicates a weakening of the anisotropy with increasing Fe substitution.

A substantially different behavior unfolds for $x = 0.11$, where there are no clear indication for skyrmion lattice correlations [Fig. 6.6(d)]. These results are consistent with conclusions derived from magnetic susceptibility measurements [12]. On the other hand, the sizable topological Hall effect reported for this composition [31] possibly indicates the existence of individual or disorganized clusters of skyrmions in this region of the magnetic phase diagram.

6.4.3. PHASE DIAGRAMS

An overview of the effect of the Fe concentration on the magnetic field - temperature phase diagram of several $Mn_{1-x}Fe_xSi$ compositions is provided by Figures 6.7 and 6.8 which display contour plots of the scattered intensity as a function of temperature and magnetic field for both $\vec{B}||\vec{k}_i$ and $\vec{B} \perp \vec{k}_i$. The contour plots are in excellent agreement with the phase diagrams published in ref. [12] that are derived from magnetic susceptibility measurements.

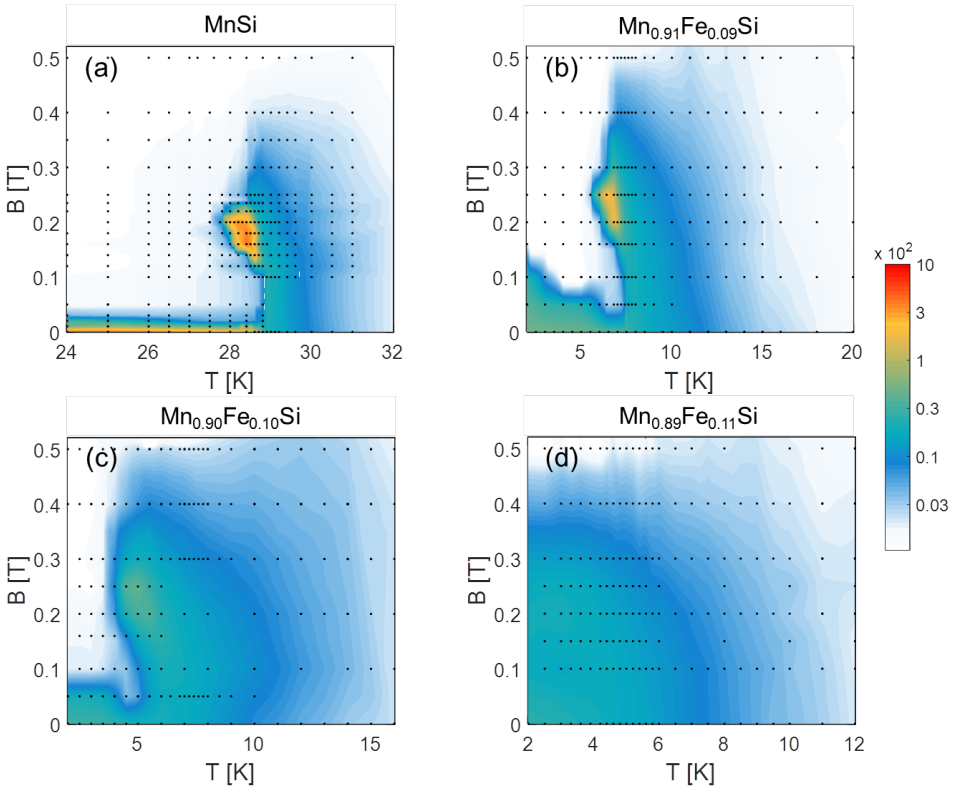

Figure 6.7: Contour plots showing the total scattered SANS intensity in arbitrary units in the configuration where the magnetic field was applied parallel to the incoming neutron beam ($\vec{B}||\vec{k}_i$) for $Mn_{1-x}Fe_xSi$ with (a) $x = 0$, (b) $x = 0.09$, (c) $x = 0.10$, and (d) $x = 0.11$. The black dots indicate the points at which the SANS measurements were performed.

Fig. 6.7(a) shows the contour plot of the scattered intensity of MnSi with $\vec{B}||\vec{k}_i$. At low magnetic fields and below $T_C \sim 28.7$ K, the high intensity originates from the helical phase. Magnetic fields beyond 0.05 T align the helices towards their direction, leading to almost zero scattered intensity in this configuration. On the other hand, the onset of the conical phase is accompanied by a strong increase in intensity in the complementary experimental configuration with $\vec{B} \perp \vec{k}_i$ [Fig. 6.8(a)]. In this configuration, the scattered intensity of the conical phase is suppressed for $B \gtrsim 0.5$ T, i.e. in the field polarized state in which the magnetic field aligns the individual magnetic moments along its direction.

Just below T_C and in a magnetic field range of 0.14 - 0.22 T, a pocket of increased intensity shows up in the contour plot for $\vec{B}||\vec{k}_i$. As discussed in the previous section, the increased intensity in this pocket, also known as the A-phase, originates from skyrmion lattice correlations that orient perpendicular to the applied magnetic field. In the complementary configuration of Fig. 6.8(a), a clear decrease in intensity is seen in this region of the phase diagram, indicating a partial suppression of the conical correlations.

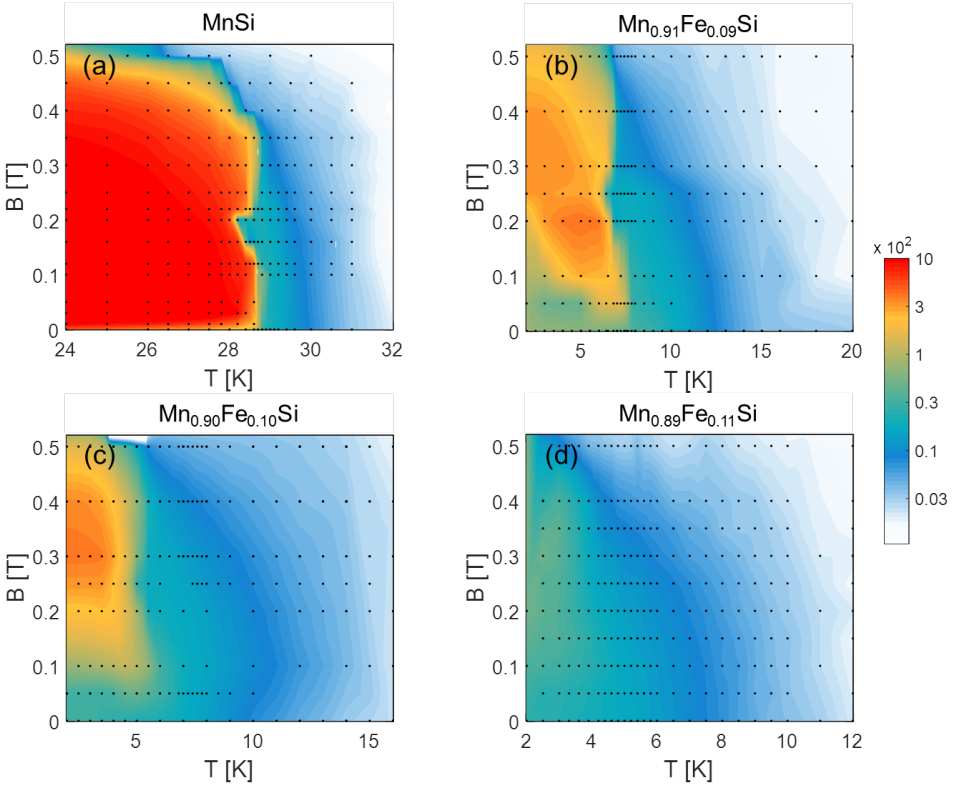

Figure 6.8: Contour plots showing the total scattered SANS intensity in arbitrary units in the configuration where the magnetic field was applied perpendicular to the incoming neutron beam ($\vec{B} \perp \vec{k}_i$) for $Mn_{1-x}Fe_xSi$ with (a) $x = 0$, (b) $x = 0.09$, (c) $x = 0.10$, and (d) $x = 0.11$. The black dots indicate the points at which the SANS measurements were performed.

The magnetic field - temperature contour plots of the scattered intensity for $x = 0.09$ and $x = 0.10$ look qualitatively similar to each other and to the ones for MnSi. However, some subtle differences are visible. Similar to $Fe_{1-x}Co_xSi$ [29, 30, 32, 33], and consistent with susceptibility measurements [11, 12], the transition line from the helical to the conical phase is no longer horizontal, but shifts to higher magnetic fields with decreasing temperature. Furthermore, the increase of the scattered intensity for $\vec{B}||\vec{k}_i$ in the A-phase is less pronounced, representing a weakening of the skyrmion lattice correlations. This weakening is accompanied by a relative increase of the intensity originating from conical correlations that coexist with the skyrmion lattice correlations.

The contour plots for $x = 0.11$ bear some similarities to the ones for $x \leq x^*$ but also reveal substantial differences. In contrast to the contour plots for $x \leq x^*$, the scattered intensity for $\vec{B}||\vec{k}_i$ [Fig. 6.7(d)] persists until the lowest temperature measured and for magnetic fields up to 0.45 T. In the complementary configuration of Fig. 6.8(d) with $\vec{B} \perp \vec{k}_i$, the intensity is enhanced by the magnetic field for temperatures lower than $T_C \lesssim 5$ K.

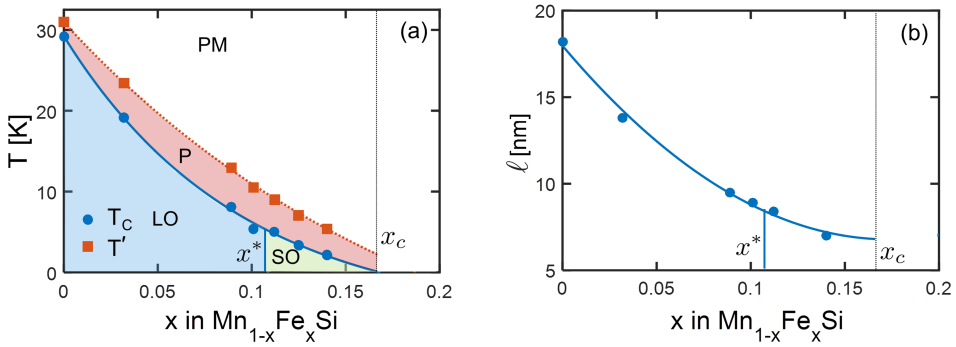

Figure 6.9: Fe concentration dependence of (a) the critical temperature T_C and T' and (b) the pitch of the helix ℓ. The critical temperature T_C and T', which marks the onset of the (short-ranged) helimagnetic correlations in the precursor phase are adapted from ref. [12]. The continuous blue and dotted red lines in Panel (a) indicate best fits of the data and correspond to $T_C = a\exp[-bx] + c$ with a = 35(7), b = 11(4) and c = -6(2) and to $T' = a\exp[-bx]+c$ with a = 51(9), b = 5(2) and c = -20(9), respectively. The blue continuous line in Panel (b) indicates the fit of $\ell = ax^2 + bx + c$ to the data, yielding a = 3(1) 10^2, b = 1.3(3) 10^2 and c = 18.0(9). LO indicates long-range helimagnetic order, SO short-range helimagnetic order, P the precursor phase and PM the paramagnetic phase.

These results indicate that the helimagnetic correlations are only partly oriented by the magnetic field, even at relatively large fields. In addition, the contour plots provide no indication of a skyrmion lattice phase.

Above T_C, all contour plots show a similar gradual decrease of the scattered intensity with increasing temperature and for all magnetic fields up to $B \sim 0.3$ T. For higher fields, this intensity decreases gradually in the configuration with $\vec{B}||\vec{k}_i$, whereas it persists for the complementary one. This is not surprising, as sufficiently large magnetic fields suppress or align the helimagnetic correlations along their direction [21]. The intensive scattering above T_C defines the precursor region, which occurs over a temperature range that increases substantially with increasing Fe doping for $x < x^*$ [11, 12, 25, 34].

6.5. DISCUSSION

The experimental results are summarized in the concentration dependence of the transition temperature, derived from previous susceptibility measurements [12], and the pitch of the helix ℓ depicted in Fig. 6.9. These plots show that the transition temperature vanishes at $x_C \approx 0.17$ and that Fe substitution leads to a significant reduction of the helimagnetic pitch ℓ. In addition, a transition from long-ranged helimagnetic correlations to a state with short-range helimagnetic correlations occurs already at $x^* \approx 0.11$.

In order to understand the evolution of the helimagnetic order with x, we consider the free energy per unit cell of a cubic chiral magnet such as $Mn_{1-x}Fe_xSi$. This free energy is the sum of the ferromagnetic energy, DM energy, Zeeman energy and magnetic anisotropy energy f_a, and is given by:

$$f = \frac{Ja^2}{2} \sum_{i=x,y,x} [\partial_i \hat{m} \cdot \partial_i \hat{m}] + aD\hat{m} \cdot \nabla \times \hat{m} - a^3 M \hat{m} \cdot \vec{B} + f_a, \tag{6.2}$$

with a the lattice constant, $\hat{m}$ the unit vector in the direction of the magnetization, M the magnetization value, and J and D the strength of the ferromagnetic exchange and DM interaction, respectively [27, 28, 35]. By substituting the conical spiral Ansatz, i.e. $\hat{m} = \cos\theta \hat{e_3} + \sin[\theta \cos(\vec{\tau} \cdot \vec{x})\hat{e_1} + \sin(\vec{\tau} \cdot \vec{x})\hat{e_2}]$, with θ the cone angle, $\vec{\tau}$ the helical propagation vector and $(\hat{e_1}, \hat{e_2}, \hat{e_3})$ a set of orthogonal unit vectors, one can derive that the pitch of the helical modulation is in the absence of Zeeman and magnetic anisotropy energies given by: $\ell = \frac{2\pi}{a}\frac{J}{D}$ and the field at which the conical-to-field polarized transition occurs at $T = 0$ K by $B_{C2}(0\text{K}) = \frac{D^2}{Ja^3M}$ [35]. In addition, the transition temperature T_C is proportional to J.

By comparing these expressions with the experimental results, we obtain that $J \to 0$ for $x \to x_c$. On the other hand, ℓ is reduced from $\sim$ 18 nm for $x = 0.0$ to $\sim$ 6 nm at $x = 0.14$, i.e. by a factor of ≈ 3, implying that D/J and thus the relative strength of the DM interaction increases with dilution. The DM interaction itself originates from the anisotropic exchange between the spins of the magnetic atoms and is thus a first-order correction to the Heisenberg exchange in spin-orbit coupling λ: $D \propto J\frac{\lambda}{\Delta}$, with Δ the typical electron excitation energy on the site of the magnetic atom [3, 35]. Thus, $D/J \propto \frac{\lambda}{\Delta} \propto \ell$, and although J vanishes at x_C, the ratio of D/J should remain finite, which is in good agreement with the experimental findings. Similar considerations explain why $\mu_0 H_{C2}(0\text{K})$ does not increase substantially as $x \to x_C$.

The helimagnetic order is already affected at dopings well below x_c. The helimagnetic spiral reorients at $x = 0.09$ from the $\langle 111 \rangle$ to the $\langle 110 \rangle$ crystallographic directions. Such a reorientation cannot be explained from the anisotropy term responsible for $\vec{\tau} \parallel \langle 111 \rangle$ at $x = 0$, $f_{a1} = K(m_x^4 + m_y^4 + m_z^4)$, as this term only has minima for $\vec{\tau} \parallel \langle 111 \rangle$ for $K < 0$ and $\vec{\tau} \parallel \langle 100 \rangle$ for $K > 0$ [4]. It therefore implies that other anisotropic terms become relevant. In fact, such a deviation from $\vec{\tau} \parallel \langle 100 \rangle$ or $\langle 111 \rangle$ is not unique to $Mn_{1-x}Fe_xSi$ but has been reported for the partially ordered state in MnSi under hydrostatic pressure [5, 36].

As the helices do not align along a specific crystallographic lattice direction for $x > x^*$, we deduce that either the magnetic anisotropy is very weak or that disorder smears the effect of anisotropy. However, solely the differences in the anisotropy cannot explain the quantitatively different behavior for $x > x^*$. Indeed, the correlation length remains finite for these dopings down to the lowest temperature and magnetic fields do not raise the directional degeneracy as they do not align all helices along their direction. Differences between the magnetic behavior have also been reported based on measurements of bulk quantities [12–14] and it has been suggested that the crossover at x^* is due to quantum fluctuations that destabilize the long-range helimagnetic order [13, 15–17]. In this approach, x^* would be a quantum critical point. We conjecture that this is not necessarily the case as the disappearance of long-range helimagnetic correlations might be due to chemical disorder. This hypothesis is supported by the data obtained under magnetic field [Fig. 6.5] that show a complex magnetization process. In this process, the

magnetic field first breaks the longer helices, possibly those that encompass the lowest degree of disorder, whereas the shorter helices are more robust.

The isotropic zero magnetic field SANS patterns in combination with the finite helical correlations for $x > x^* \approx 0.11$ indicate that x^* is associated with the disappearance of long-range periodic helimagnetic order and that the short-ranged helimagnetic correlations for $x > x^*$ are completely degenerate in space. However, from these results it is not clear whether this helimagnetic state fluctuates, as in the precursor phase in MnSi above T_C [19, 21], or not. The final answer can be given by additional inelastic neutron scattering or muon spin spectroscopy experiments.

6.6. CONCLUSION

In conclusion, the results show that the helimagnetic order in $Mn_{1-x}Fe_xSi$ is suppressed with increasing Fe content. The long-range helimagnetic correlations, which reorient at zero magnetic from ⟨111⟩ at low Fe concentrations towards ⟨110⟩ at $x = 0.09$, disappear completely for $x > x^*$. The helices have for $x > x^*$ finite lengths, are completely degenerate in space, and bear similarities to those found in the precursor phase of MnSi. Magnetic fields gradually suppress and partly align these helices along their direction trough a complex magnetization process.

REFERENCES

[1] L. J. Bannenberg, R. M. Dalgliesh, T. Wolf, F. Weber, and C. Pappas, *Evolution of helimagnetic correlations in $Mn_{1-x}Fe_xSi$ with doping: A small-angle neutron scattering study,* Physical Review B **98**, 184431 (2018).

[2] I. E. Dzyaloshinskii, *A thermodynamic theory of "weak" ferromagnetism of antiferromagnetics,* Journal of Physics and Chemistry of Solids **4**, 241 (1958).

[3] T. Moriya, *Anisotropic Superexchange Interaction and Weak Ferromagnetism,* Physical Review **120**, 91 (1960).

[4] P. Bak and M. H. Jensen, *Theory of helical magnetic structures and phase transitions in MnSi and FeGe,* Journal of Physics C: Solid State Physics **13**, L881 (1980).

[5] C. Pfleiderer, D. Reznik, L. Pintschovius, H. v Lohneysen, *et al.*, *Partial order in the non-Fermi-liquid phase of MnSi,* Nature **427**, 227 (2004).

[6] C. Pfleiderer, P. Böni, T. Keller, U. K. Rößler, and A. Rosch, *Non-fermi liquid metal without quantum criticality,* Science **316**, 1871 (2007).

[7] Y. J. Uemura, T. Goko, I. M. Gat-Malureanu, J. P. Carlo, P. L. Russo, A. T. Savici, A. Aczel, G. J. MacDougall, J. A. Rodriguez, G. M. Luke, *et al.*, *Phase separation and suppression of critical dynamics at quantum phase transitions of MnSi and $(Sr_{1-x}Ca_x)$ RuO_3,* Nature Physics **3**, 29 (2007).

[8] S. Mühlbauer, B. Binz, F. Jonietz, C. Pfleiderer, A. Rosch, A. Neubauer, R. Georgii, and P. Böni, *Skyrmion lattice in a chiral magnet,* Science **323**, 915 (2009).

[9] A. Neubauer, C. Pfleiderer, B. Binz, A. Rosch, R. Ritz, P. G. Niklowitz, and P. Böni, *Topological Hall effect in the A phase of MnSi,* Physical Review Letters **102**, 186602 (2009).

[10] R. Ritz, M. Halder, M. Wagner, C. Franz, A. Bauer, and C. Pfleiderer, *Formation of a topological non-fermi liquid in mnsi,* Nature **497**, 231 (2013).

[11] A. Bauer, A. Neubauer, C. Franz, W. Münzer, M. Garst, and C. Pfleiderer, *Quantum phase transitions in single-crystal $Mn_{1-x}Fe_xSi$ and $Mn_{1-x}Co_xSi$: Crystal growth, magnetization, ac susceptibility, and specific heat,* Physical Review B **82**, 064404 (2010).

[12] L. J. Bannenberg, F. Weber, A. J. E. Lefering, T. Wolf, and C. Pappas, *Magnetization and ac susceptibility study of the cubic chiral magnet $Mn_{1-x}Fe_xSi$,* Physical Review B **98**, 184430 (2018).

[13] S. V. Demishev, I. I. Lobanova, V. V. Glushkov, T. V. Ischenko, N. E. Sluchanko, V. A. Dyadkin, N. M. Potapova, and S. V. Grigoriev, *Quantum bicriticality in $Mn_{1-x}Fe_xSi$ solid solutions: Exchange and percolation effects,* JETP Letters **98**, 829 (2013).

[14] S. V. Demishev, A. N. Samarin, V. V. Glushkov, M. I. Gilmanov, I. I. Lobanova, N. A. Samarin, A. V. Semeno, N. E. Sluchanko, N. M. Chubova, V. A. Dyadkin, and S. V. Grigoriev, *Anomalous spin relaxation and quantum criticality in $Mn_{1-x}Fe_xSi$ solid solutions,* JETP Letters **100**, 28 (2014).

[15] V. V. Glushkov, I. I. Lobanova, V. Y. Ivanov, V. V. Voronov, V. A. Dyadkin, N. M. Chubova, S. V. Grigoriev, and S. V. Demishev, *Scrutinizing Hall effect in $Mn_{1-x}Fe_xSi$: Fermi surface evolution and hidden quantum criticality,* Physical Review Letters **115**, 256601 (2015).

[16] S. V. Demishev, A. N. Samarin, J. Huang, V. V. Glushkov, I. I. Lobanova, N. E. Sluchanko, N. M. Chubova, V. A. Dyadkin, S. V. Grigoriev, M. Y. Kagan, *et al.*, *Magnetization of $Mn_{1-x}Fe_xSi$ in high magnetic fields up to 50 T: Possible evidence of a field-induced Griffiths phase,* JETP letters **104**, 116 (2016).

[17] S. V. Demishev, I. I. Lobanova, A. V. Bogach, V. V. Glushkov, V. Y. Ivanov, T. Ischenko, N. Samarin, N. E. Sluchanko, S. Gabani, E. Čižmár, *et al.*, *Effect of a magnetic field on the intermediate phase in $Mn_{1-x}Fe_xSi$: Spin-liquid versus fluctuations scenario,* JETP letters **103**, 321 (2016).

[18] S. V. Grigoriev, S. V. Maleyev, A. I. Okorokov, Y. O. Chetverikov, R. Georgii, P. Böni, D. Lamago, H. Eckerlebe, and K. Pranzas, *Critical fluctuations in MnSi near T_C: A polarized neutron scattering study,* Physical Review B **72**, 134420 (2005).

[19] C. Pappas, E. Lelievre-Berna, P. Falus, P. M. Bentley, E. Moskvin, S. Grigoriev, P. Fouquet, and B. Farago, *Chiral paramagnetic skyrmion-like phase in MnSi,* Physical Review Letters **102**, 197202 (2009).

[20] M. Janoschek, M. Garst, A. Bauer, P. Krautscheid, R. Georgii, P. Böni, and C. Pfleiderer, *Fluctuation-induced first-order phase transition in Dzyaloshinskii-Moriya helimagnets,* Physical Review B **87**, 134407 (2013).

[21] C. Pappas, L. J. Bannenberg, E. Lelièvre-Berna, F. Qian, C. D. Dewhurst, R. M. Dalgliesh, D. L. Schlagel, T. A. Lograsso, and P. Falus, *Magnetic Fluctuations, Precursor Phenomena and Phase Transition in MnSi under Magnetic Field,* Physical Review Letters **119**, 047203 (2017).

[22] L. J. Bannenberg, F. Qian, R. M. Dalgliesh, N. Martin, G. Chaboussant, M. Schmidt, D. L. Schlagel, T. A. Lograsso, H. Wilhelm, and C. Pappas, *Reorientations, relaxations, metastabilities, and multidomains of skyrmion lattices,* Physical Review B **96**, 184416 (2017).

[23] R. Sadykov, C. Pappas, L. J. Bannenberg, R. M. Dalgliesh, P. Falus, C. Goodway, and E. Lelievre-Berna, *1.5 GPa compact double-wall clamp cell for SANS and NSE studies at low temperatures and high magnetic fields,* Journal of Neutron Research **20**, 25 (2018).

[24] S. V. Grigoriev, V. A. Dyadkin, D. Menzel, J. Schoenes, Y. O. Chetverikov, A. I. Okorokov, H. Eckerlebe, and S. V. Maleyev, *Magnetic structure of $Fe_{1-x}Co_xSi$ in a magnetic field studied via small-angle polarized neutron diffraction,* Physical Review B **76**, 224424 (2007).

[25] S. V. Grigoriev, V. A. Dyadkin, E. V. Moskvin, D. Lamago, T. Wolf, H. Eckerlebe, and S. V. Maleyev, *Helical spin structure of $Mn_{1-y}Fe_ySi$ under a magnetic field: Small angle neutron diffraction study,* Physical Review B **79**, 144417 (2009).

[26] I. Mirebeau, N. Martin, M. Deutsch, L. J. Bannenberg, C. Pappas, G. Chaboussant, R. Cubitt, C. Decorse, and A. O. Leonov, *Spin textures induced by quenched disorder in a reentrant spin glass: Vortices versus "frustrated" skyrmions,* Physical Review B **98**, 014420 (2018).

[27] S. Seki and M. Mochizuki, *Skyrmions in Magnetic Materials* (Springer, 2015).

[28] A. Bauer and C. Pfleiderer, *Generic aspects of skyrmion lattices in chiral magnets,* in *Topological Structures in Ferroic Materials* (Springer, 2016) pp. 1–28.

[29] W. Münzer, A. Neubauer, T. Adams, S. Mühlbauer, C. Franz, F. Jonietz, R. Georgii, P. Böni, B. Pedersen, M. Schmidt, *et al.*, *Skyrmion lattice in the doped semiconductor $Fe_{1-x}Co_xSi$,* Physical Review B **81**, 041203 (2010).

[30] L. J. Bannenberg, K. Kakurai, F. Qian, E. Lelièvre-Berna, C. D. Dewhurst, Y. Onose, Y. Endoh, Y. Tokura, and C. Pappas, *Extended skyrmion lattice scattering and long-time memory in the chiral magnet $Fe_{1-x}Co_xSi$,* Physical Review B **94**, 104406 (2016).

[31] C. Franz, F. Freimuth, A. Bauer, R. Ritz, C. Schnarr, C. Duvinage, T. Adams, S. Blügel, A. Rosch, Y. Mokrousov, *et al.*, *Real-space and reciprocal-space Berry phases in the Hall effect of $Mn_{1-x}Fe_xSi$,* Physical Review Letters **112**, 186601 (2014).

[32] A. Bauer, M. Garst, and C. Pfleiderer, *History dependence of the magnetic properties of single-crystal $Fe_{1-x}Co_xSi$,* Physical Review B **93**, 235144 (2016).

[33] L. J. Bannenberg, A. J. E. Lefering, K. Kakurai, Y. Onose, Y. Endoh, Y. Tokura, and C. Pappas, *Magnetic relaxation phenomena in the chiral magnet $Fe_{1-x}Co_xSi$: An ac susceptibility study,* Physical Review B **94**, 134433 (2016).

[34] S. V. Grigoriev, E. V. Moskvin, V. A. Dyadkin, D. Lamago, T. Wolf, H. Eckerlebe, and S. V. Maleyev, *Chiral criticality in the doped helimagnets $Mn_{1-y}Fe_ySi$,* Physical Review B **83**, 224411 (2011).

[35] F. Qian, L. J. Bannenberg, H. Wilhelm, G. Chaboussant, L. M. DeBeer-Schmitt, M. P. Schmidt, A. Aqeel, T. T. M. Palstra, E. H. Brück, A. J. E. Lefering, C. Pappas, M. Mostovoy, and A. O. Leonov, *New magnetic phase of the chiral skyrmion material cu_2oseo_3,* Science Advances **4**, eaat7323 (2018).

[36] F. Krüger, U. Karahasanovic, and A. G. Green, *Quantum order-by-disorder near criticality and the secret of partial order in MnSi,* Physical Review Letters **108**, 067003 (2012).

7

SKYRMIONS AND SPIRALS IN MnSi UNDER HYDROSTATIC PRESSURE

The archetype cubic chiral magnet MnSi is home to some of the most fascinating states in condensed matter such as skyrmions or the occurrence of non-Fermi liquid behavior in conjunction with a topological Hall effect under hydrostatic pressure. Using small angle neutron scattering, we study the evolution of the helimagnetic correlations with increasing hydrostatic pressure and show that the helical propagation vector smoothly reorients from ⟨111⟩ *to* ⟨100⟩ *at intermediate pressures. At higher pressures, the helimagnetic order persists at zero magnetic field up to the critical pressure. Nevertheless, under magnetic field skyrmion lattices and conical spirals appear at low temperatures, even in the absence of any helimagnetic correlations at zero field. However, we find no one-to-one relation between the appearance of conical spirals and skyrmion lattices on one side, and the non-Fermi liquid and topological Hall effect behavior on the other side, as the latter extends over a much larger region of the phase diagram. A possible explanation for this paradox is that the phase, out of which a magnetic field induces long range order at low temperatures, is heterogeneous and consists of spirals, skyrmions and other topologically non-trivial magnetic defects.*

7.1. INTRODUCTION

A well-visited route to discover new and exotic states of matter is by tweaking the magnetic interactions through chemical substitution or hydrostatic pressure. The archetype chiral cubic magnet MnSi hosts some of the most peculiar states reported in condensed matter physics, such as skyrmion lattices [1, 2] and under hydrostatic pressure a non-Fermi liquid (NFL) phase [3, 4]. The NFL phase is characterized by a $T^{3/2}$ temperature dependence of the resistivity and emerges for $p > p_C \approx 1.4$ GPa without quantum criticality [5]. This phase is home to a sizable topological Hall effect (THE) [6–8], a key characteristic of topological non-trivial magnetic order. For $p > p_C$ the long range helimagnetic order at zero field is suppressed and a partial helimagnetic order has been reported

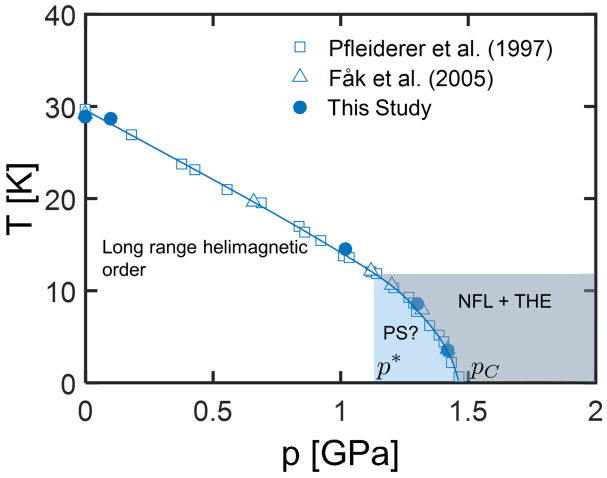

Figure 7.1: Zero magnetic field phase diagram of MnSi under hydrostatic pressure. The helimagnetic transition temperature is after refs. [11] and [12]. The non-Fermi liquid (NFL) and topological Hall effect (THE) behavior appears for pressures higher than p^* and p_C is the critical pressure, above which the helimagnetic order disappears. p^* also marks the onset of the alleged Phase Separated state (PS) where helimagnetic and paramagnetic volumes may coexist.

[9, 10], the nature of which and its relation to the NFL and THE signals remains an open question.

Substantial qualitative changes to the ground state of MnSi already occur at pressures lower than p_C. The NFL and THE behavior for $T > T_C$ has been reported for $p > p^* \approx 1.2$ GPa, as illustrated by Fig. 7.1. Furthermore, there is a controversy on whether the region of the phase diagram between p^* and p_C is characterized by phase separation between helimagnetic and paramagnetic volumes, [13, 14], or not [15].

In this work, we revisit the magnetic phase diagram of MnSi under hydrostatic pressure and elucidate the evolution of the helimagnetic correlations around p^* and p_C. For this reason, we performed small angle neutron scattering (SANS) experiments as a function of pressure and systematically applied the magnetic field both parallel and perpendicular to the incoming neutron beam, designated by its wavevector $\vec{k}_i$. In this way, we obtain a complete overview of both the helimagnetic and skyrmionic correlations that has not been provided by previous studies.

We find that at zero magnetic field the helical propagation vector $\vec{\tau}$ reorients around p^* from $\langle 111 \rangle$ at low pressures to $\langle 100 \rangle$ at high pressures. Surprisingly, for $p > p^*$, magnetic fields induce both conical spirals and skyrmion lattices above T_C. This occurs in the region of the phase diagram governed by NFL and THE behavior. Unexpectedly, this behavior extends also above p_C, where we do not find any indication of helimagnetic correlations at zero magnetic field, including partial helimagnetic order. Although these field-induced conical spirals and skyrmion lattices may explain the NFL and THE behavior, it is remarkable that the latter extends over a much larger region of the phase diagram. A possible explanation for this paradox is that the phase, out of which a mag-

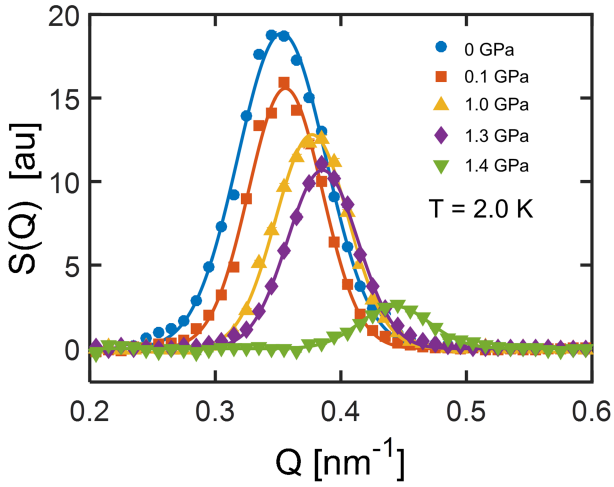

Figure 7.2: Scattering function $S(Q)$ at zero magnetic field, $T = 2$ K, and for the pressures indicated. $S(Q)$ was obtained by radially averaging the scattered intensity of the 2D SANS patterns. The continuous lines represent fits of Eq. 7.1 to the experimental data.

netic field induces long range order at low temperatures, is heterogeneous consisting of spirals, skyrmions and other topologically non-trivial magnetic defects.

7.2. EXPERIMENTAL DETAILS

The measurements were performed on a 110 mg single crystal of MnSi of approximately $2\times2\times3$ mm^3 in size which originates from the same batch as the samples used in [16–19]. It was aligned with the $[1\bar{1}0]$ crystallographic direction vertical and placed in a cylindrical teflon tube. High pressures were generated using a CuBe/TiZr double-wall clamp cell with a 50 - 50% mixture of FC770 and FC75 as pressure transmitter. Details of the pressure cell and the modus operandi can be found in ref. [20]. The SANS measurements were performed at the time-of-flight instrument LARMOR of the ISIS neutron source using neutrons with wavelengths $0.09 \leq \lambda \leq 1.25$ nm. The sample was located 4.4 m from the detector that consists of 80 ^{3}He tubes, each 8 mm wide. The magnetic field was applied with a 2T 3D vector field cryomagnet both parallel and perpendicular to the incoming neutron beam. We carefully eliminated the residual magnetic fields by warming up the entire cryomagnet prior to the measurements. All SANS patterns are normalized to standard monitor counts and background corrected using a high temperature measurement.

The scattering function $S(Q)$ is a one dimensional representation of the 2D SANS patterns and obtained from radially averaging the SANS patterns of e.g. Fig. 7.4. Fig. 7.2 shows example data at zero magnetic field and at $T = 2$ K for different pressures. The data were fitted to a Gaussian:

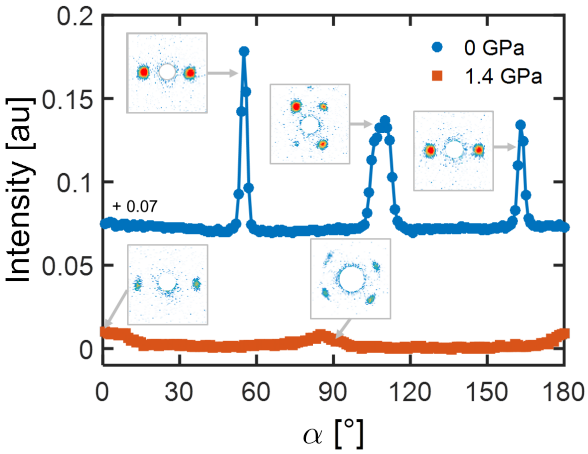

Figure 7.3: Rocking scan around the vertical $[1\bar{1}0]$ crystallographic direction at $p = 0$ and 1.4 GPa. α indicates the angle between the [001] crystallographic direction and the SANS detector plane. The data at $p = 0.0$ GPa are shifted by the value indicated in the plot.

$$S(Q) \propto \exp\left(-4\ln(2)\left[(Q - \frac{2\pi}{\ell})/\Delta\right]^2\right), \tag{7.1}$$

with ℓ the pitch of the helix and Δ the FWHM. The resulting values of ℓ at zero magnetic field are provided in Fig. 7.4(d). The integrated intensity is computed by summing all scattered intensity with a momentum transfer of $0.2 < Q < 1.2$ nm^{-1}.

7.3. RESULTS AND DISCUSSION

7.3.1. ZERO FIELD

Figure 7.4(a)-(c) displays characteristic SANS patterns collected at zero magnetic field and for different temperatures and pressures. The patterns for $p = 1.0$ GPa are very similar to the ones seen at zero pressure: below $T_C \approx 14$ K long range helical order sets-in with $\vec{\tau} \parallel \langle 111 \rangle$. However, above T_C, we do not observe the intense ring of scattering seen at ambient pressures, and which is characteristic of the precursor phase [16, 21–24]. In addition, the temperature evolution of the total scattered intensity shown in Fig. 7.4(d), obtained by summing the intensity over the entire SANS pattern, is different from that at lower pressures. For $p = 0$ and 0.1 GPa there is a clear kink at T_C, which is completely absent for higher pressures. We conclude that this diffuse scattering weakens considerably with increasing pressure, and at high pressures it does not exceed the background of the pressure cell.

When the pressure reaches 1.3 GPa, the helical Bragg peaks broaden substantially [Fig. 7.4(b)]. Thus the direction of $\vec{\tau}$ is relatively ill-defined. Surprisingly, if the pressure is further increased to 1.4 GPa, the peaks become again as sharp as for lower pressures. However, the helices are no longer aligned along $\langle 111 \rangle$ but along $\langle 100 \rangle$ (see Fig. 7.4(c)

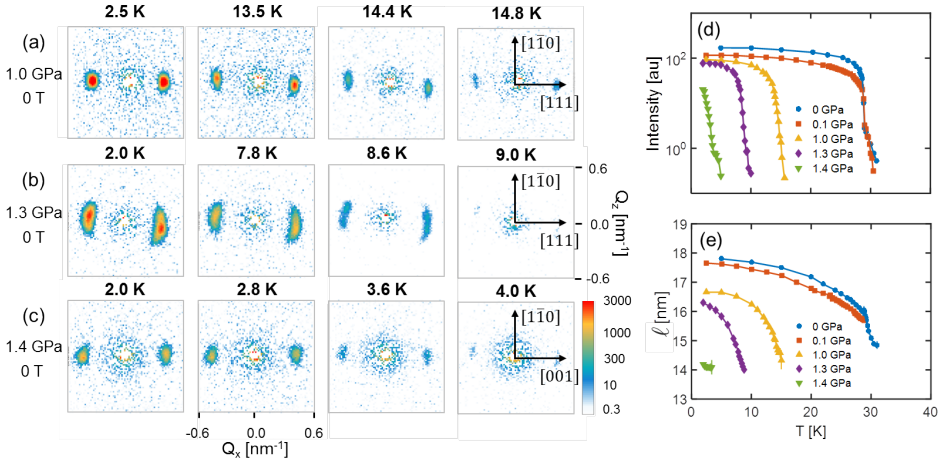

Figure 7.4: SANS results at zero magnetic field. Panels (a) - (c) display characteristic SANS patterns obtained at a pressure of (a) p = 1.0 GPa, (b) 1.3 GPa and (c) 1.4 GPa and for the temperatures indicated. Panel (d) displays the total scattered intensity as a function of temperature for the pressures indicated in the figure legend. The total scattered intensity is obtained by summing all the intensity of the SANS patterns. Panel (e) shows the temperature dependence of the pitch of the helix ℓ for the pressures indicated in the figure legend. ℓ is obtained from the maximum of a fit of a Gaussian to the radial averaged SANS patterns.

and the rocking scans of Fig. 7.3). This unexpected and novel result reveals that the direction of $\vec{\tau}$ crosses over around p^*. This effect can be accounted for by the cubic anisotropy, $f_{a1} = K(m_x^4 + m_y^4 + m_z^4)$, which has only minima at $\vec{\tau} \parallel \langle 111 \rangle$ for $K < 0$ and $\vec{\tau} \parallel \langle 100 \rangle$ for $K > 0$ [25]. Our results thus reveal that K changes sign around p^*, the region of the phase diagram where Larmor diffraction indicates an abrupt change of the spontaneous magnetostriction [5]. The change of the sign of K is accompanied by a relative weakening of the ferromagnetic exchange with respect to the Dzyaloshinsky-Moriya interaction. This is revealed by the decrease of the pitch of the helix $\ell \propto J/D$, shown in Fig. 7.4(e), which is consistent with earlier measurements [12]. Finally we note that the total scattered intensity at low temperatures does not reduce dramatically with increasing pressure, not even for $p > p^*$ [Fig. 7.4(d)]. Therefore, the magnetic moment does not vanish, in agreement with previous studies [11, 26–28].

7.3.2. MAGNETIC FIELD

The results under magnetic field are summarized by Fig. 7.5, which displays SANS patterns and contour plots of the total scattered intensity as a function of temperature and magnetic field at different pressures and for both experimental configurations: $\vec{B} || \vec{k}_i$ and $\vec{B} \perp \vec{k}_i$. These results clearly show three distinct regimes: $p < p^*$, $p^* < p < p_C$ and $p > p_C$.

For $p < p^*$, the magnetic field-temperature phase diagrams remain qualitatively the same as at zero pressure. This is illustrated by the contour plot of Fig. 7.5(a), which displays the total scattered intensity for p = 1.0 GPa and for $\vec{B} || \vec{k}_i$, the configuration sensitive

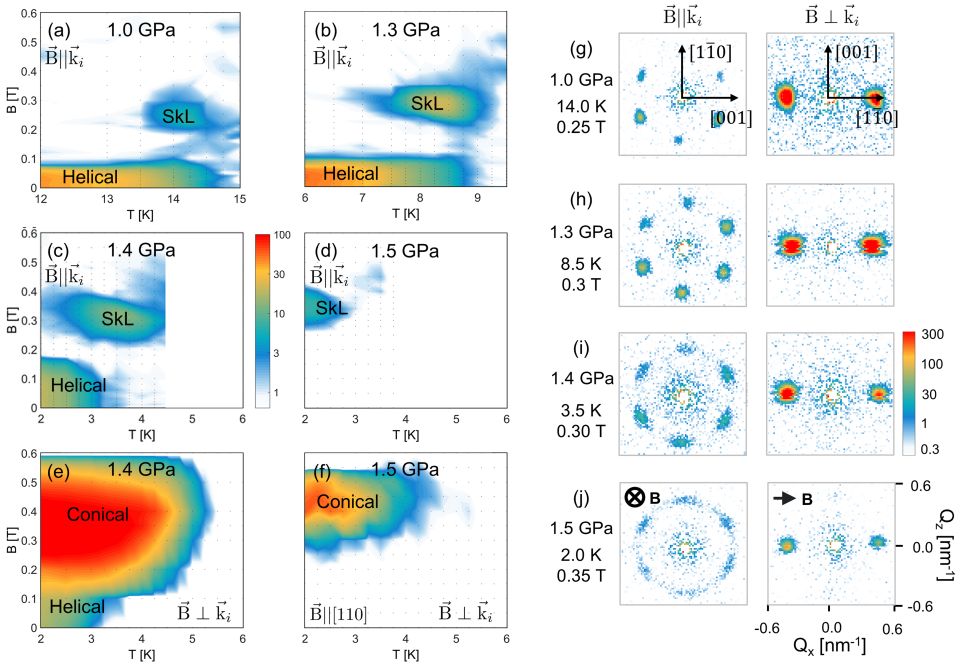

Figure 7.5: SANS results under magnetic field. Panels (a) - (f) display contour plots of the total scattered SANS intensity, as obtained from summing the intensity of the SANS patterns outside the direct beam, as a function of temperature and magnetic field and for the different pressures indicated. The magnetic field was in Panels (a) - (d) applied parallel to the incoming neutron beam designated by $\vec{k}_i$ ($\vec{B}||\vec{k}_i$) and in Panels (e) and (f) perpendicular to it ($\vec{B} \perp \vec{k}_i$). The grey dots indicate the points at which a measurement was performed. Panels (g) - (j) display characteristic SANS patterns for the indicated pressures, temperatures and magnetic fields and for the two experimental configurations.

to helical modulations perpendicular to the magnetic field. This plot shows two regions with intensity: at low magnetic fields and below T_C owing to the helical phase, and at intermediate magnetic fields, in the A-phase region, due to the six-fold symmetric SANS patterns [Fig. 7.5(g)] characteristic of the skyrmion lattice phase [1]. In the complementary configuration with $\vec{B} \perp \vec{k}_i$, which is sensitive to helimagnetic correlations parallel to the magnetic field, the SANS patterns show two peaks along the field [Fig. 7.5(g)], characteristic of the conical phase, which coexists with the skyrmion lattice in the A-phase.

The behavior changes considerably above p^*. For $p^* < p < p_C$ the skyrmion lattice appears at temperatures significantly higher than T_C [Fig. 7.5(b),(c)]. At $p = 1.3$ GPa $> p^*$, the skyrmion lattice phase persists up to $T = 9.4$ K, i.e. $T_C + 0.4$ K. At a slightly larger pressure of 1.4 GPa, the skyrmion lattice extends up to $T = 4.5$, i.e. $T_C + 1.5$ K, which is a most remarkable result. A similar but even more pronounced effect is seen for the conical phase, which, as shown by the contour plot of the total scattered intensity for $\vec{B} \perp \vec{k}_i$ [Fig. 7.5(e)], persists up to $T \approx 5.5$ K, i.e. up to $\approx 2T_C$.

Above p_C, the skyrmion lattice and conical spiral scattering appears under magnetic fields despite the absence of any scattering at zero field. This is illustrated by the pat-

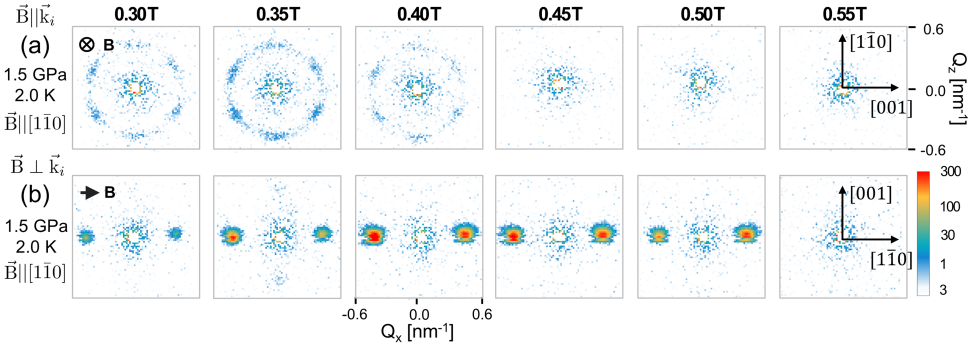

Figure 7.6: Characteristic SANS patterns at $p = 1.5$ GPa, $T = 2$ K, and for the magnetic fields indicated. The magnetic field was applied along the [1$\bar{1}$0] crystallographic direction and both parallel ($\vec{B}||\vec{k}_i$) and perpendicular ($\vec{B} \perp \vec{k}_i$) to the incoming neutron beam.

terns of Fig. 7.6 and the contour plots of Fig. 7.5(d),(f) for $p = 1.5$ GPa, which show that the skyrmion lattice scattering appears up to $T = 3$ K [Fig. 7.5(d)], whereas the conical scattering persists up to temperatures as high as $T = 4.5$ K [Fig. 7.5(f)]. The characteristic skyrmion lattice pattern of six peaks is seen for $\vec{B} \parallel \vec{k}_i$ [Fig. 7.5(j)], superimposed on a weak ring of scattering. These six maxima are noticeably broader along the ring than at lower pressures [Fig. 7.5(g)], suggesting that the sixth-order anisotropy, which couples the skyrmion to the crystallographic lattice [1, 17], becomes considerably weaker at these high pressures. On the other hand, the width of both the peaks and the ring is limited by the experimental resolution. Among the six skyrmion lattice maxima, two are oriented along the ⟨110⟩-crystallographic directions and their combination with the ring of scattering thus closely resembles the scattering that was previously attributed to a partial helimagnetic order [9, 10].

The intensity and extent of both the skyrmion lattice and conical scattering strongly depend on the magnetic history. As shown in Fig. 7.7, when the field is increased, skyrmion scattering appears between 0.22 and 0.43 T whereas it does not reappear when the magnetic field is decreased from 0.8 T, i.e. from the field-polarized state. On the other hand, with increasing field, the conical scattering appears at the same magnetic field as the skyrmion lattice phase, increases rapidly at ~0.4 T before vanishing at the field-polarized state. However, when the magnetic field is decreased from 0.8 T to zero, the conical scattering reappears and becomes even more intense, in particular below ~0.4 T. Furthermore, it extends down to very low fields.

The stabilization under magnetic field of skyrmion lattices and conical spirals at $T > T_C$ for $p^* < p < p_C$ and at $T > 0$ for $p > p_C$ is a remarkable observation, which sheds light on earlier puzzling magnetization results [26]. In the absence of well defined helimagnetic correlations at zero field, an important question is that of the ground state out of which a magnetic field can stabilize skyrmion lattices and conical spirals. If this state would consist of a partial helimagnetic order, as previously suggested [9, 10], one would expect a considerable amount of scattering to persist down to zero magnetic field.

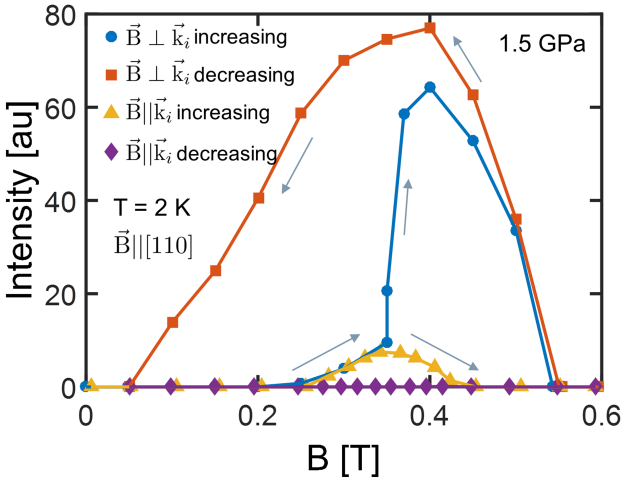

Figure 7.7: Magnetic field dependence of the total scattered intensity, as obtained from summing the intensity of the SANS patterns outside the direct beam, at T = 2 K and p = 1.5 GPa. The magnetic field was applied along the [1$\bar{1}$0] crystallographic direction and both parallel ($\vec{B}||\vec{k}_i$) and perpendicular ($\vec{B} \perp \vec{k}_i$) to the incoming neutron beam. The measurements were performed after zero field cooling the sample and as a function of both increasing and decreasing magnetic field.

However, this is not what we observe. One may argue that we are hindered by the background of the pressure cell that would mask the scattering of the partial helical order. On the other hand, as seen in Fig. 7.4(d), the background of the cell is small enough to let us observe the diffuse scattering of the precursor phase at low pressures, which is more than two orders of magnitude weaker than the maximum of the conical scattering at 1.5 GPa (Fig. 7.7). Therefore, we should have been able to observe the partial helical order if it would exist. As this is not the case, we conclude that for $p > p_C$ the magnetic correlations at zero field are not dominantly helimagnetic and for this reason they cannot be probed by a SANS experiment.

The conical spirals and skyrmion lattices appear for $p > p_C$ and for $p^* < p < p_C$ only in a small fraction of the magnetic phase diagram region where a sizable THE [6–8] and NFL [3, 4, 9, 10] behavior has been reported (Fig. 7.1). Thus, our results do not explain the THE and the NFL behavior. Nevertheless, they hint that it may be due to a heterogeneous phase consisting of conical spirals, individual skyrmions, or other topologically non-trivial defects, such as hedgehogs, torons [29–32], or other textures that cannot not be probed by our SANS experiment. Magnetic fields then induce the long ranged correlations probed by SANS only at the low temperature limit of this phase.

7.4. CONCLUSION

In conclusion, our SANS results shed light on the puzzling behavior of MnSi under pressure. With increasing pressure, first the helical propagation vector smoothly reorients from ⟨111⟩ to ⟨100⟩ around p^*. At higher pressures, helimagnetic order persists at zero

magnetic field up to p_C. Nevertheless, magnetic fields stabilize conical spirals and skyrmion lattices even in the absence of helimagnetic correlations at zero field, thus even above p_C. Furthermore, we find no one-to-one relation between the appearance of conical spirals and skyrmion lattices on one side, and the NFL and THE behavior on the other side, as the latter extends over a much larger region of the phase diagram. A possible explanation for this paradox is that the NFL and THE behavior occurs in a phase where spirals coexist with skyrmions and other topologically non-trivial magnetic defects. It is out of this heterogeneous phase that a magnetic field can induce long ranged correlations at low temperatures.

REFERENCES

[1] S. Mühlbauer, B. Binz, F. Jonietz, C. Pfleiderer, A. Rosch, A. Neubauer, R. Georgii, and P. Böni, *Skyrmion lattice in a chiral magnet,* Science **323**, 915 (2009).

[2] A. Neubauer, C. Pfleiderer, B. Binz, A. Rosch, R. Ritz, P. G. Niklowitz, and P. Böni, *Topological Hall effect in the A phase of MnSi,* Physical Review Letters **102**, 186602 (2009).

[3] C. Pfleiderer, S. Julian, and G. G. Lonzarich, *Non-fermi-liquid nature of the normal state of itinerant-electron ferromagnets,* Nature **414**, 427 (2001).

[4] N. Doiron-Leyraud, I. R. Walker, L. Taillefer, M. J. Steiner, S. R. Julian, and G. G. Lonzarich, *Fermi-liquid breakdown in the paramagnetic phase of a pure metal,* Nature **425**, 595 (2003).

[5] C. Pfleiderer, P. Böni, T. Keller, U. K. Rößler, and A. Rosch, *Non-fermi liquid metal without quantum criticality,* Science **316**, 1871 (2007).

[6] M. Lee, W. Kang, Y. Onose, Y. Tokura, and N. P. Ong, *Unusual Hall Effect Anomaly in MnSi under Pressure,* Phyisical Review Letters **102**, 1 (2009).

[7] R. Ritz, M. Halder, M. Wagner, C. Franz, A. Bauer, and C. Pfleiderer, *Formation of a topological non-Fermi liquid in MnSi,* Nature **497**, 231 (2013).

[8] R. Ritz, M. Halder, C. Franz, A. Bauer, M. Wagner, R. Bamler, A. Rosch, and C. Pfleiderer, *Giant generic topological Hall resistivity of MnSi under pressure,* Physical Review B **87**, 134424 (2013).

[9] C. Pfleiderer, D. Reznik, L. Pintschovius, H. v Lohneysen, *et al., Partial order in the non-Fermi-liquid phase of MnSi,* Nature **427**, 227 (2004).

[10] L. Pintschovius, D. Reznik, C. Pfleiderer, and H. von Löhneysen, *Partial magnetic order in the itinerant-electron magnet MnSi,* Pramana **63**, 117 (2004).

[11] C. Pfleiderer, G. J. McMullan, S. R. Julian, and G. G. Lonzarich, *Magnetic quantum phase transition in MnSi under hydrostatic pressure,* Physical Review B **55**, 8330 (1997).

[12] B. Fåk, R. A. Sadykov, J. Flouquet, and G. Lapertot, *Pressure dependence of the magnetic structure of the itinerant electron magnet MnSi,* Journal of Physics: Condensed Matter **17**, 1635 (2005).

[13] W. Yu, F. Zamborszky, J. D. Thompson, J. L. Sarrao, M. E. Torelli, Z. Fisk, and S. E. Brown, *Phase inhomogeneity of the itinerant ferromagnet MnSi at high pressures,* Physical Review Letters **92**, 086403 (2004).

[14] Y. J. Uemura, T. Goko, I. M. Gat-Malureanu, J. P. Carlo, P. L. Russo, A. T. Savici, A. Aczel, G. J. MacDougall, J. A. Rodriguez, G. M. Luke, *et al.*, *Phase separation and suppression of critical dynamics at quantum phase transitions of MnSi and* $(Sr_{1-x}Ca_x)\,RuO_3$, Nature Physics **3**, 29 (2007).

[15] D. Andreica, P. D. de Réotier, A. Yaouanc, A. Amato, and G. Lapertot, *Absence of magnetic phase separation in MnSi under pressure,* Physical Review B **81**, 060412 (2010).

[16] C. Pappas, L. J. Bannenberg, E. Lelièvre-Berna, F. Qian, C. D. Dewhurst, R. M. Dalgliesh, D. L. Schlagel, T. A. Lograsso, and P. Falus, *Magnetic Fluctuations, Precursor Phenomena and Phase Transition in MnSi under Magnetic Field,* Physical Review Letters **119**, 047203 (2017).

[17] L. J. Bannenberg, F. Qian, R. M. Dalgliesh, N. Martin, G. Chaboussant, M. Schmidt, D. L. Schlagel, T. A. Lograsso, H. Wilhelm, and C. Pappas, *Reorientations, relaxations, metastabilities, and multidomains of skyrmion lattices,* Physical Review B **96**, 184416 (2017).

[18] L. J. Bannenberg, F. Weber, A. J. E. Lefering, T. Wolf, and C. Pappas, *Magnetization and ac susceptibility study of the cubic chiral magnet* $Mn_{1-x}Fe_xSi$, Physical Review B **98**, 184430 (2018).

[19] L. J. Bannenberg, R. M. Dalgliesh, T. Wolf, F. Weber, and C. Pappas, *Evolution of helimagnetic correlations in* $Mn_{1-x}Fe_xSi$ *with doping: A small-angle neutron scattering study,* Physical Review B **98**, 184431 (2018).

[20] R. Sadykov, C. Pappas, L. J. Bannenberg, R. M. Dalgliesh, P. Falus, C. Goodway, and E. Lelievre-Berna, *1.5 GPa compact double-wall clamp cell for SANS and NSE studies at low temperatures and high magnetic fields,* Journal of Neutron Research **20**, 25 (2018).

[21] S. V. Grigoriev, S. V. Maleyev, A. I. Okorokov, Y. O. Chetverikov, R. Georgii, P. Böni, D. Lamago, H. Eckerlebe, and K. Pranzas, *Critical fluctuations in MnSi near* T_C*: A polarized neutron scattering study,* Physical Review B **72**, 134420 (2005).

[22] C. Pappas, E. Lelievre-Berna, P. Falus, P. M. Bentley, E. Moskvin, S. Grigoriev, P. Fouquet, and B. Farago, *Chiral paramagnetic skyrmion-like phase in MnSi,* Physical Review Letters **102**, 197202 (2009).

[23] M. Janoschek, M. Garst, A. Bauer, P. Krautscheid, R. Georgii, P. Böni, and C. Pfleiderer, *Fluctuation-induced first-order phase transition in Dzyaloshinskii-Moriya helimagnets,* Physical Review B **87**, 134407 (2013).

[24] L. J. Bannenberg, K. Kakurai, P. Falus, E. Lelièvre-Berna, R. M. Dalgliesh, C. D. Dewhurst, F. Qian, Y. Onose, Y. Endoh, Y. Tokura, and C. Pappas, *Universality of the helimagnetic transition in cubic chiral magnets: Small angle neutron scattering and neutron spin echo spectroscopy studies of FeCoSi,* Physical Review B **95**, 144433 (2017).

[25] P. Bak and M. H. Jensen, *Theory of helical magnetic structures and phase transitions in MnSi and FeGe,* Journal of Physics C: Solid State Physics **13**, L881 (1980).

[26] C. Thessieu, C. Pfleiderer, A. N. Stepanov, and J. Flouquet, *Field dependence of the magnetic quantum phase transition in MnSi,* Journal of Physics: Condensed Matter **9**, 6677 (1997).

[27] A. E. Petrova, V. Krasnorussky, J. Sarrao, and S. M. Stishov, *Tricritical behavior in MnSi at nearly hydrostatic pressure,* Physical Review B **73**, 052409 (2006).

[28] M. Otero-Leal, F. Rivadulla, S. S. Saxena, K. Ahilan, and J. Rivas, *Nature of the high-pressure tricritical point in MnSi,* Physical Review B **79**, 060401 (2009).

[29] A. O. Leonov and K. Inoue, *Homogeneous and heterogeneous nucleation of skyrmions in thin layers of cubic helimagnets,* Physical Review B **98**, 054404 (2018).

[30] P. J. Ackerman and I. I. Smalyukh, *Diversity of Knot Solitons in Liquid Crystals Manifested by Linking of Preimages in Torons and Hopfions,* Physical Review X **7**, 2256 (2017).

[31] P. J. Ackerman and I. I. Smalyukh, *Static three-dimensional topological solitons in fluid chiral ferromagnets and colloids,* Nature Materials **16**, 426 (2016).

[32] I. I. Smalyukh, Y. Lansac, N. A. Clark, and R. P. Trivedi, *Three-dimensional structure and multistable optical switching of triple-twisted particle-like excitations in anisotropic fluids,* Nature Materials **9**, 139 (2009).

8

REORIENTATIONS, RELAXATIONS, METASTABILITIES, AND MULTIDOMAINS OF SKYRMION LATTICES

Magnetic skyrmions are nano-sized topologically protected spin textures with particle-like properties. They can form lattices perpendicular to the magnetic field and the orientation of these skyrmion lattices with respect to the crystallographic lattice is governed by spin-orbit coupling. By performing small angle neutron scattering measurements, we investigate the coupling between the crystallographic and skyrmion lattices in both Cu_2OSeO_3 and the archetype chiral magnet MnSi. The results reveal that the orientation of the skyrmion lattice is primarily determined by the magnetic field direction with respect to the crystallographic lattice. In addition, it is also influenced by the magnetic history of the sample which can induce metastable lattices. Kinetic measurements show that these metastable skyrmion lattices may or may not relax to their equilibrium positions under macroscopic relaxation times. Furthermore, multidomain lattices may form when two or more equivalent crystallographic directions are favored by spin-orbit coupling and oriented perpendicular to the magnetic field.

8.1. INTRODUCTION

Magnetic skyrmions are nano-sized topologically protected spin textures with particle-like properties which may form lattices oriented perpendicular to the magnetic field [2–8]. These Skyrmion Lattices (SkL) were first identified in cubic chiral magnets by Small Angle Neutron Scattering (SANS) inside the A-phase, which is a pocket in the magnetic field (B) - temperature (T) phase diagram just below the critical temperature T_C. Soon

This chapter has been published in Physical Review B **96**(18), 184416 (2017) [1].

after their first observation in MnSi [2], skyrmion lattices were found in other cubic chiral magnets including $Fe_{1-x}Co_xSi$ [9], FeGe [10], Cu_2OSeO_3 [11–13] and Co-Zn-Mn alloys [14, 15]. More recently, skyrmions and their lattices have been observed in polar magnets [16], in thin films [17, 18], and at surfaces and interfaces of different atomic layers [19]. Skyrmions are topologically stable and can be controlled with extremely small electric currents which frees the path for successful applications in novel spintronic and information storage devices [3, 4, 20, 21].

In chiral magnets, the Dzyaloshinskii-Moriya interaction [22, 23] plays a crucial role in stabilizing the helimagnetic order and skyrmion lattices [24]. However, this interaction in itself cannot explain the thermodynamic stability of skyrmion lattices, which has been attributed to additional terms including thermal fluctuations [2, 8, 25], spin exchange stiffness and/or uniaxial anisotropy [26–30]. The specific orientation of the skyrmion lattice with respect to the crystallographic lattice can be accounted for by higher order spin-orbit coupling terms [2]. In order to describe this orientation dependence, it is convenient to consider the skyrmion lattice as a single domain, long-range ordered state resulting from the superposition of three helical vectors $\vec{\tau}_i$ separated by 60° [13, 31]. These helices propagate in the plane perpendicular to the magnetic field and lead to the characteristic six-fold symmetric SANS patterns [2]. In MnSi one of the three helices preferentially aligns along the ⟨110⟩ crystallographic direction. For Cu_2OSeO_3 this orientational preference is along ⟨100⟩ [13, 32, 33], although some SANS measurements seem to indicate that for specific fields and temperatures the ⟨110⟩ direction is preferred [12, 34].

Besides this orientational preference, patterns with twelve or more peaks have been observed by SANS and resonant x-ray scattering on Cu_2OSeO_3 [32–35]. These patterns indicate the coexistence of multiple skyrmion lattice domains with different orientations. In fact, such multidomain states have also been seen by Lorentz transmission electron microscopy in thin films of MnSi and Cu_2OSeO_3 [36, 37] and by SANS in single crystals of $Fe_{1-x}Co_xSi$ [9, 38]. The occurrence of these multidomain states appears for bulk Cu_2OSeO_3 to be related to the thermal history [34, 39]. In addition, it was proposed that multidomains are stabilized by magnetic fields applied along directions deviating from the major cubic axes [32, 33]. However, none of these previous studies provides a holistic view on the interrelation between the orientation of skyrmion lattices and the crystallographic lattice, the occurrence of multidomain lattices and the influence of meta-stabilities induced by different magnetic field histories for all cubic chiral magnets.

In the following we fill this gap by studying the skyrmion lattice orientation with respect to the crystallographic lattice and the occurrence of multidomain lattices in both the insulator Cu_2OSeO_3 and the archetype chiral magnet MnSi. For this purpose, we performed SANS measurements in a way so far not considered. As schematically shown in Fig. 8.1, the measurements were performed by rotating the sample around its vertical axis, and thus having the magnetic field applied along different crystallographic directions. By rotating the sample both in zero and under field, we study the effect of the magnetic field history on the orientation of the skyrmion lattice with respect to the crystallographic lattice. The results show unambiguously that the orientation of the skyrmion lattice and the occurrence of multidomain states is primarily governed by the

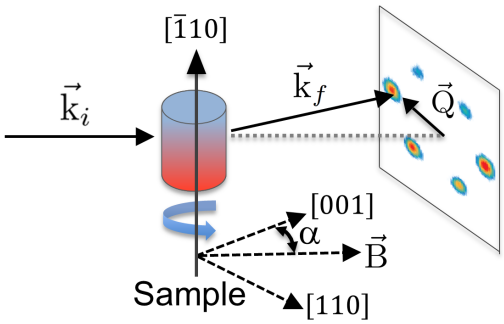

Figure 8.1: Schematic representation of the experimental set-up. SANS measurements were performed with the magnetic field applied parallel to the incoming neutron beam with wave vector $\vec{k}_i$. The sample was aligned with the [1̄10] crystallographic direction vertical and rotated around its vertical axis such that the magnetic field is applied along different crystallographic directions. The angle α is defined as the angle between the magnetic field and the [001] crystallographic direction in the horizontal plane, implying that $\alpha = 0°$ corresponds to $\vec{B}$ || [001] and $\alpha = 90°$ corresponds to $\vec{B}$ || [1$\bar{1}$0]. The wave-vector $\vec{k}_f$ of the scattered neutron beam and the scattering vector $\vec{Q}$ are also indicated.

magnetic field direction with respect to the crystallographic lattice. The orientation of the skyrmion lattice with respect to the crystallographic lattice is also influenced by the magnetic history of the sample. The latter can induce metastable orientations of the skyrmion lattice with respect to the crystallographic one that may or may not relax to their equilibrium orientation under macroscopic relaxation times. Furthermore, multidomain lattices may form when two or more equivalent crystallographic directions are favored by spin-orbit coupling and oriented perpendicular to the magnetic field.

8.2. EXPERIMENTAL

The SANS measurements on Cu_2OSeO_3 were performed on a single crystal with dimensions of about $5 \times 3 \times 3$ mm^3 grown by chemical vapor transport. The sample was aligned with the [1$\bar{1}$0] crystallographic direction vertical within 3°. The monochromatic SANS instrument PA20 of the Laboratoire Léon Brillouin was used with a wavelength of λ = 0.6 nm, $\Delta\lambda/\lambda = 0.12$ and the detector placed 12.7 m from the sample. The ^{3}He XY multidetector is made of 128×128 pixels of 5×5 mm^2. The magnetic field was applied parallel to the incoming neutron beam designated by its wave-vector $\vec{k}_i$ using an Oxford Instruments horizontal field cryomagnet.

The MnSi sample is a cubic single crystal with dimensions of about $5 \times 5 \times 5$ mm^3 and was already used in a previous experiment [40]. The MnSi sample was also aligned with the [1$\bar{1}$0] crystallographic direction vertical within 5°. The SANS measurements were performed at the time-of-flight instrument LARMOR of the ISIS neutron source using neutrons with wavelengths of $0.09 \leq \lambda \leq 1.25$ nm. The sample was placed 4.4 m from the detector that consists of eighty 8 mm wide ^{3}He tubes. The magnetic field was applied with a three-dimensional (3D) 2T vector cryomagnet along the incoming neutron

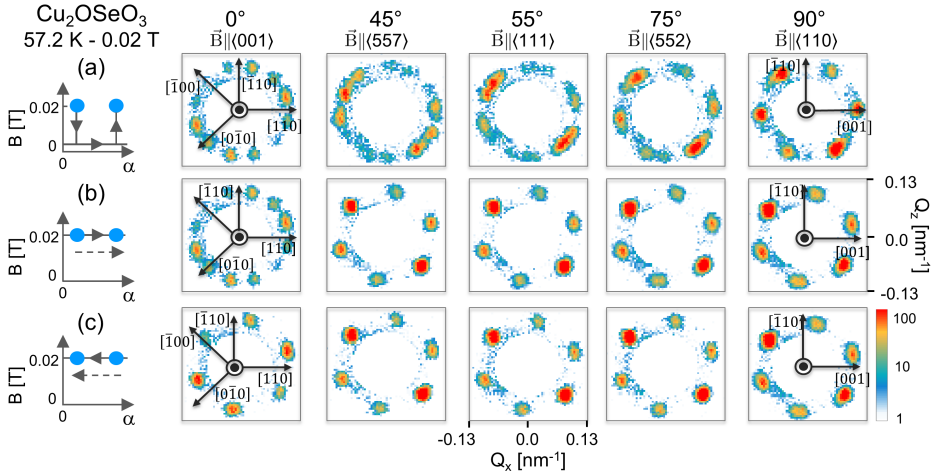

Figure 8.2: SANS patterns showing how the skyrmion lattice orients with respect to the crystallographic lattice for different magnetic field orientation for Cu_2OSeO_3 at T = 57.2 K and B = 0.02 T. The field was applied along different crystallographic directions by rotating the sample in steps of 5° from α = 0° ($\vec{B}$ || [001]) to α = 90° ($\vec{B}$ || [1$\bar{1}$0]) with (a) the field switched off during rotations, (b) the field continuously on, and (c) rotating the sample backwards in steps of -5° from α = 90° to 0° under field.

beam.[1] In particular, we eliminated the residual field of the cryomagnet by warming up the entire cryomagnet before the experiment.[2]

All SANS patterns are normalized to standard monitor counts and background corrected using a high temperature measurement at 60 K for MnSi and 70 K for Cu_2OSeO_3.

8.3. RESULTS

8.3.1. Cu_2OSeO_3

We first consider the case of Cu_2OSeO_3 and display in Fig. 8.2(a) and Supplemental Movie 1[41] a series of SANS patterns measured at T = 57.4 K and B = 0.02 T. The field was applied during the measurements and switched off when the sample was rotated in steps of 5° from α = 0° to 90°. The angle α is defined as the angle between the magnetic field and the [001] crystallographic axis in the horizontal plane, implying that α = 0° corresponds to $\vec{B}$ || [001] and α = 90° corresponds to $\vec{B}$ || [1$\bar{1}$0].

At α = 0°, twelve Bragg peaks are found corresponding to two six-peak patterns rotated 30° from each other. This indicates the stabilization of two distinct skyrmion lattice domains with different orientations with respect to the crystallographic lattice. One of

[1] The field homogeneity of the 3D cryomagnet, defined as 'the maximum field error over a 10 mm diameter spherical volume', is determined by the manufacturer as 0.11 % of the applied magnetic field.

[2] We mounted a field probe on the window of the cryostat to check directly the residual field taking into account its decay with distance. This field probe confirmed the absence of a sizeable residual field. In addition, we made magnetic field scans from negative to positive fields to evaluate the residual field. As the plot of the integrated scattered intensity vs magnetic field was symmetric and centered around zero, a sizable residual field was absent.

these domains has one set of two peaks aligned along [100] while the other domain has two peaks along the [010] direction. The intensity differences between the peaks are most likely due to a small misalignment of the single crystal and/or demagnetization effects that could also cause small differences in domain populations.

When the sample is rotated and α increases, the [100] and [010] directions are no longer perpendicular to the field and the skyrmion lattices can no longer orient along either of these directions. For small values of α, the twelve-peak patterns persist implying that the coexistence of the two skyrmion domains remains energetically favorable. For larger values of α around 45°, the patterns seem to indicate 18 peaks. Unfortunately, the resolution of the measurement is not sufficient to unambiguously confirm the existence of these 18 peaks, which would suggest the coexistence of three skyrmion lattice domains as reported elsewhere [32].

When α is further increased, the third [001] direction approaches the direction perpendicular to the field and the domains gradually merge into one. At $\alpha = 90°$ only six peaks are visible and among them two are aligned along the [001] direction. At this position, the lattice has rotated by 15° with respect to each of the two lattices seen at $\alpha = 0°$.[3]

A similar rotation scan was performed but this time with the field on during the rotation of the sample. The results, displayed in Fig. 8.2(b) and Supplemental Movie 2 [41], show two important differences with respect to the previous case. During this rotation, the scattering from one of the two skyrmion lattice domains is suppressed, whereas the other one is enhanced. Furthermore, the SkL does not reorient for any of the field directions including at $\alpha = 90°$. At this angle the favorable [001] direction is perpendicular to the field, but the skyrmion lattice is oriented 15° away from it and is pinned by the field to the position it had at $\alpha = 0°$. This six fold symmetry persists when the sample is rotated back from $\alpha = 90°$ to 0° under magnetic field. As shown in Fig. 8.2(c), the twelve fold symmetry is still not recovered at $\alpha = 0°$ where only one skyrmion lattice domain is found. These measurements show that the orientation of skyrmion lattices and the stabilization of multiple domains are strongly influenced by the history of the applied magnetic field direction within the equilibrium skyrmion phase.

8.3.2. MnSi

We now consider the case of MnSi and display in Fig. 8.3(a) a series of SANS patterns measured at $T = 28.4$ K and $B = 0.2$ T after zero-field cooling. For $\alpha = 0°$, i.e. for $\vec{B} \,||\, [001]$, two $\langle 110 \rangle$ directions ([110] and $[\bar{1}10]$), which are in MnSi preferred by spin-orbit coupling, are perpendicular to the magnetic field. In contrast to Cu_2OSeO_3 we do not observe twelve peaks, but only six, originating from a single SkL orientation along [110]. Six peaks are also seen for $\alpha > 0°$ but this time the SkL aligns along the $[\bar{1}10]$ direction. This orientation, which we name SkL 1, has a scattering pattern that is 30° rotated with respect to the one at $\alpha = 0°$ which we name SkL 2.

The MnSi sample was also rotated from $\alpha = 0°$ to 90° with a magnetic field of 0.2 T on during the measurements and the rotation of the sample. The SANS patterns were recorded every 2° and are presented in Supplemental Movie 3 [41] with a selection given

[3] The scattering patterns of this rotation scan are equivalent to those obtained after zero field cooling the sample.

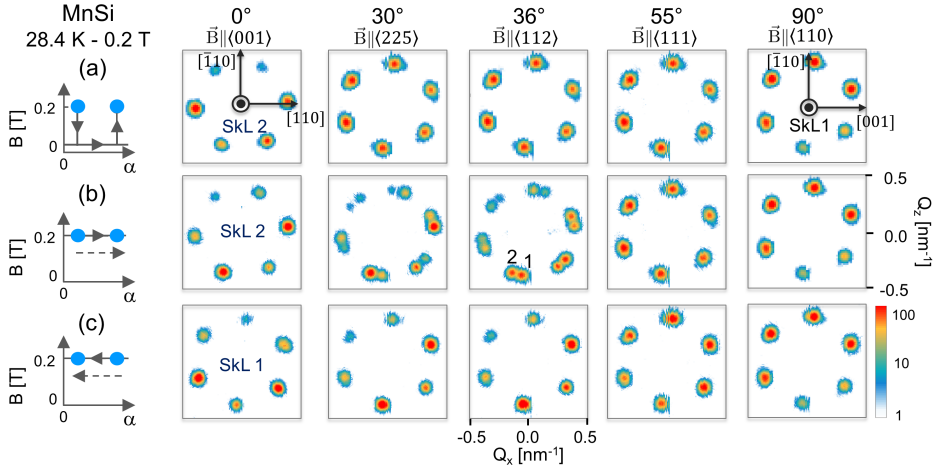

Figure 8.3: SANS patterns showing how the skyrmion lattice orients with respect to the crystallographic lattice for different magnetic field orientation for MnSi at $T = 28.4$ K and $B = 0.2$ T. The field was applied along different crystallographic directions (a) after zero field cooling, (b) by rotating the sample in steps of 2° from $\alpha = 0°$ ($\vec{B}$ || [001]) to $\alpha = 90°$ ($\vec{B}$ || [1$\bar{1}$0]) while keeping the field on during the rotations and (c) by rotating the sample backwards under field from $\alpha = 90°$ in steps of -2° to $\alpha = 0°$.

in Fig. 8.3(b). For $0 < \alpha \leq 28°$, the patterns correspond to SkL 2. The patterns qualitatively change for $\alpha > 28°$ and show a superposition of SkL 2 and SkL 1. By further increasing α, SkL 2 decreases in intensity and totally vanishes at $\alpha \approx 45°$, while at the same time SkL 1 becomes more prominent. As for Cu_2OSeO_3, the patterns remain the same when the sample is rotated under field back to $\alpha = 0°$. SkL 2 is still not recovered after waiting 30 min at $\alpha = 0°$. These results indicate that in both Cu_2OSeO_3 and MnSi the orientation of the SkL is determined by the magnetic field orientation with respect to crystallographic lattice as well as by the history of the magnetic field (direction) of the sample. They also demonstrate that it is possible to induce metastable skyrmion states in both Cu_2OSeO_3 and MnSi within the thermodynamic equilibrium skyrmion phase.

In order to follow the re-orientation from SkL 2 to SkL 1 as a function of time, we performed fast rotations from $\alpha = 0°$ ($\vec{B}$ || ⟨100⟩) to $\alpha = 55°$ ($\vec{B}$ || ⟨111⟩) while keeping the field on. The SANS patterns where recorded continuously using event mode data acquisition. Subsequently, they were processed such that a pattern was obtained for every 3 s. All patterns are displayed in Supplemental Movie 4 [41] and a selection of them is shown in Fig. 8.4(a). During the first 3 seconds, SkL 1 forms and coexists with SkL 2. Afterwards, the intensity of SkL 2 drops gradually whereas the intensity of SkL 1 increases. After $t \approx$ 25 s, the rate at which the intensity of SkL 2 decreases slows down considerably, and it takes almost ten minutes for SkL 2 to completely disappear.

A quantitative analysis of this reorientation is provided by considering the time dependence of the total intensity of all six Bragg peaks of SkL 2. The results are displayed in Fig. 8.4(b) and show a fast decrease in intensity within the first 25 seconds followed by a slow decay. Therefore, we fitted the data to a superposition of two exponentials:

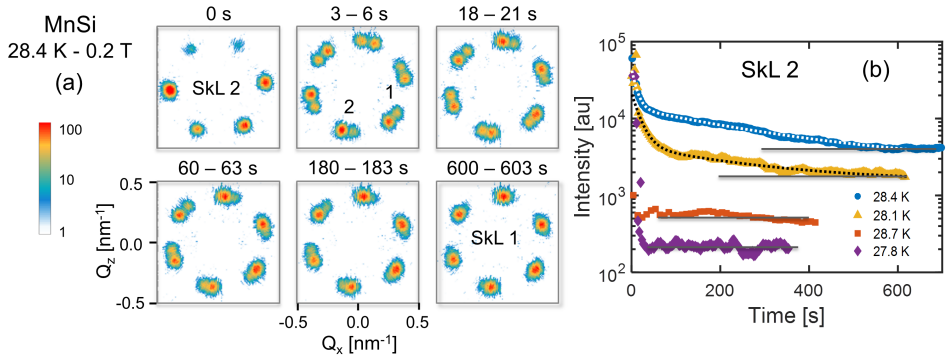

Figure 8.4: Time-dependent relaxation of the skyrmion lattice in MnSi when the sample was rotated within 5 s from $\alpha = 0^\circ$ ($\vec{B} \,||\, \langle 100 \rangle$) to $\alpha = 55^\circ$ ($\vec{B} \,||\, \langle 111 \rangle$) at $B = 0.2$ T. (a) Selection of SANS patterns obtained as a function of time at $T = 28.4$ K. All SANS patterns can be found in Supplementary Movie 4 [41] (b) The total intensity of SkL 2 as a function of time for several temperatures indicated. The dotted white line for $T = 28.1$ K and the dotted black line for $T = 28.4$ K indicate fits of Eq. 8.1 to the data. The horizontal grey-lines serve as guides to the eyes and represent the actual baseline intensity.

$$I(t) = a\exp(-t/t_1) + b\exp(-t/t_2) + c. \tag{8.1}$$

The fit at $T = 28.4$ K provides $a = 3.1 \pm 0.1 \times 10^4$, $b = 1.1 \pm 0.1 \times 10^4$, $c = 2.5 \pm 0.2 \times 10^4$ and the two time constants $t_1 = 11.2 \pm 0.6$ s and $t_2 = 3.0 \pm 0.3 \times 10^2$ s. As such, it shows that the relaxation is governed by two separate processes occurring on the seconds and minutes time-scales, respectively. These processes possibly reflect the movement of (topological) domain walls and/or their pinning to defects of the crystallographic lattice [37]. Slow relaxations that originate from multiple processes have also been observed around the A-phase by ac magnetic susceptibility measurements in $Fe_{1-x}Co_xSi$ [42].

The relaxation of skyrmion lattices does not change dramatically in the center of the A-phase. At a lower temperature of 28.1 K, the estimated values are $t_1 = 18.9 \pm 0.4$ s and $t_2 = 2.6 \pm 0.2 \times 10^2$ s. Thus, the characteristic time of the slow relaxation remains almost unchanged, whereas that of the faster process is almost doubled. The relaxation times are very different near the low- and high temperature borders as shown for 27.8 and 28.7 K in Fig. 8.4(b). The acceleration of the relaxation is not surprising for the high temperature border where it can be attributed to increased thermal fluctuations. The acceleration at the low temperature limit of $T = 27.8$ K may be due to the fact that at this temperature the SkL is stable only for $\vec{B} \,||\, \langle 001 \rangle$ [43]. Indeed, we observe that the skyrmion lattice relaxes to the conical phase at this temperature and the SkL is thus not stable for $\vec{B} \,||\, \langle 111 \rangle$. This highlights the importance of anisotropy terms.

8.4. DISCUSSION

The results presented above show that the skyrmion lattice orients along the crystallographic directions expected from spin-orbit coupling when the samples are zero field

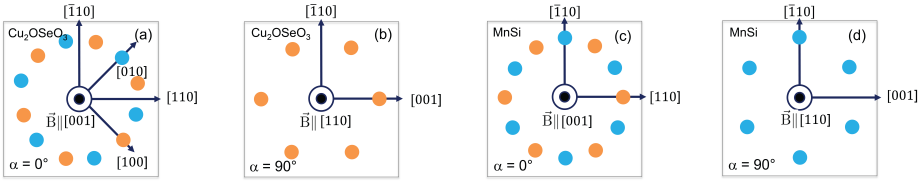

Figure 8.5: Schematic illustration of the skyrmion lattice orientations with the minimum energy for (a) and(b) Cu_2OSeO_3, where spin-orbit coupling prefers Bragg peaks along ⟨100⟩, and (c) and (d) MnSi, where it prefers peaks along ⟨110⟩. The illustrations correspond to the characteristic six Bragg peak scattering pattern of a skyrmion lattice domain seen by SANS. Different colors represent different domains of skyrmion lattices. The magnetic field is applied in the out of plane direction along (a) and (c) $\vec{B}\,||\,[001]$ ($\alpha = 0°$) and (b) and (d) $\vec{B}\,||\,[1\bar{1}0]$ ($\alpha = 90°$).

cooled. Indeed, based on a Ginzburg-Landau analysis [2, 9, 12], one expects from the relevant fourth and sixth order spin-orbit coupling terms $\sum_\tau(\tau_x^6+\tau_y^6+\tau_z^6)\,|\vec{m}_\tau|^2$ and $\sum_\tau(\tau_x^4\tau_y^2+\tau_y^4\tau_z^4+\tau_z^4\tau_x^4)\,|\vec{m}_\tau|^2$, with $\vec{m}_\tau$ being the Fourier transform of the local magnetization $\vec{M}(\vec{r})$, an alignment of the skyrmion lattice with one of the helical vectors $\vec{\tau}\,||\,\langle 100\rangle$ as for MnSi, or $\vec{\tau}\,||\,\langle 110\rangle$ as for Cu_2OSeO_3.

Multidomain lattices may form when several equivalent crystallographic directions, as preferred by spin-orbit coupling, are simultaneously perpendicular to the magnetic field. This is exemplified by the schematic drawings in Fig. 8.5. Figures 8.5(a) and 8.5(c) show that two domains of skyrmion lattices are expected for both Cu_2OSeO_3 and MnSi for $\alpha = 0°$ and $\vec{B}\,||\,\langle 100\rangle$, where there are two favorable ⟨100⟩ and ⟨110⟩ crystallographic directions perpendicular to the field. In the other configuration of $\alpha = 90°$ and $\vec{B}\,||\,\langle 110\rangle$ shown in Fig. 8.5(b) and 8.5(d), only one ⟨100⟩ and ⟨110⟩ crystallographic direction is perpendicular to the field, and hence, only one SkL domain is expected for both chiral magnets. A comparison with experiment shows, however, that multidomain SkLs are nucleated only in Cu_2OSeO_3. This is in agreement with the literature, where, to our knowledge, no stable multidomain lattice has been reported for bulk single-crystal MnSi so far.

This important difference between Cu_2OSeO_3 and MnSi may be attributed to substantial differences in the most relevant terms in the free energy Landau-Ginzburg functional that contains the Ferromagnetic exchange, Dzyaloshinskii-Moriya interaction, Zeeman energy and anisotropy/spin-orbit coupling terms [2]. The most obvious difference is in the coupling to the external field and the Zeeman energy, which is almost an order of magnitude stronger for MnSi than Cu_2OSeO_3. Indeed, the magnetic fields required to stabilize the skyrmion lattice phase are almost an order of magnitude stronger for MnSi than for Cu_2OSeO_3 although the volume magnetizations of both systems are very similar to each other [43, 44]. An additional more subtle but most relevant difference is in the spin-orbit coupling that pins the skyrmion lattice to the crystallographic one. The higher order spin-orbit coupling terms seem to be significantly stronger for MnSi than for Cu_2OSeO_3. In the later, both the fourth and sixth order terms responsible for this coupling are very weak as pointed out by a previous study [12]. Consequently, multidomain lattices are stabilized in Cu_2OSeO_3 for a wide range of field directions with respect

to the crystallographic lattice. A similar case has also been documented for $Fe_{1-x}Co_xSi$ where the coupling of the skyrmion lattice to the crystallographic lattice is likely even weaker [9, 38]. If the spin-orbit coupling is stronger, as is likely the case for MnSi, a different field orientation with respect to the crystallographic lattice has a larger impact on the energy levels of the energy minima. Thus, in MnSi both the stronger Zeeman and spin-orbit coupling terms in conjunction with even small sample misalignments, imperfections, or demagnetizing fields would raise the degeneracy between different and equivalent skyrmion lattice domains and thus favor a single domain configuration. We therefore conjecture that multidomain lattices should also exist in MnSi, but only within a very narrow region of field orientations with respect to the crystallographic lattice that has not been realized experimentally until now.

Our results also show that the specific history of the magnetic field (direction) has a significant impact on the SkL orientation. When rotations are performed under field, the multidomain SkL stabilized for $\vec{B} \,||\, \langle 100 \rangle$ in Cu_2OSeO_3 evolves to a single-domain SkL. Upon further rotation, this single domain does not reorient to its zero-field cooled configuration, which one may assume to be the most energetically favorable one. On the other hand, the skyrmion lattice may reorient under certain conditions for MnSi involving macroscopic relaxation times and metastable multidomain lattices. Thus, for both systems relatively large energy barriers prevent SkLs from reorienting to their thermodynamically most favorable state. The existence of such high energy barriers is not surprising as such a reorientation of the skyrmion lattice involves a rearrangement of the magnetic configuration over very large (macroscopic) volumes. These results thus show that it is possible to induce metastable skyrmion states in Cu_2OSeO_3 and MnSi within the thermodynamic equilibrium skyrmion phase.

The stabilization of the multidomain SkL in Cu_2OSeO_3 has previously been attributed to magnetic field directions deviating from the major cubic axes [32, 33] or to the thermal and magnetic history [12]. Our results show that specific magnetic field histories can indeed suppress multidomain lattices. However, in contrast to previous work [32, 33], we find that multidomain SkLs can also be stabilized when the field is applied along a major cubic axis such as the ⟨100⟩ crystallographic direction. The occurrence of multidomain lattices can thus be understood on the basis of symmetry arguments, as illustrated in Fig. 8.5.

8.5. CONCLUSION

In summary, the results presented above show that the orientation of the skyrmion lattice is governed primarily by the magnetic field direction with respect to the crystallographic lattice, but is also influenced by the magnetic history of the sample. Multidomain lattices may form when two or more equivalent crystallographic directions are favored by spin-orbit coupling and oriented perpendicular to the magnetic field. These results provide new insights into the factors that stabilize skyrmion lattices and influence their orientation. They shed new light on the puzzle of the occurrence of multiple skyrmion lattice domains, an issue that is of general relevance to chiral magnetism.

REFERENCES

[1] L. J. Bannenberg, F. Qian, R. M. Dalgliesh, N. Martin, G. Chaboussant, M. Schmidt, D. L. Schlagel, T. A. Lograsso, H. Wilhelm, and C. Pappas, *Reorientations, relaxations, metastabilities, and multidomains of skyrmion lattices,* Physical Review B **96**, 184416 (2017).

[2] S. Mühlbauer, B. Binz, F. Jonietz, C. Pfleiderer, A. Rosch, A. Neubauer, R. Georgii, and P. Böni, *Skyrmion lattice in a chiral magnet,* Science **323**, 915 (2009).

[3] A. Fert, V. Cros, and J. Sampaio, *Skyrmions on the track,* Nature Nanotechnology **8**, 152 (2013).

[4] N. Nagaosa and Y. Tokura, *Topological properties and dynamics of magnetic skyrmions,* Nature Nanotechnology **8**, 899 (2013).

[5] P. Milde, D. Köhler, J. Seidel, L. M. Eng, A. Bauer, A. Chacon, J. Kindervater, S. Mühlbauer, C. Pfleiderer, S. Buhrandt, *et al.*, *Unwinding of a skyrmion lattice by magnetic monopoles,* Science **340**, 1076 (2013).

[6] N. Romming, C. Hanneken, M. Menzel, J. E. Bickel, B. Wolter, K. von Bergmann, A. Kubetzka, and R. Wiesendanger, *Writing and deleting single magnetic skyrmions,* Science **341**, 636 (2013).

[7] S. Seki and M. Mochizuki, *Skyrmions in Magnetic Materials* (Springer, 2015).

[8] A. Bauer and C. Pfleiderer, *Generic aspects of skyrmion lattices in chiral magnets,* in *Topological Structures in Ferroic Materials* (Springer, 2016) pp. 1–28.

[9] W. Münzer, A. Neubauer, T. Adams, S. Mühlbauer, C. Franz, F. Jonietz, R. Georgii, P. Böni, B. Pedersen, M. Schmidt, *et al.*, *Skyrmion lattice in the doped semiconductor* $Fe_{1-x}Co_xSi$, Physical Review B **81**, 041203 (2010).

[10] H. Wilhelm, M. Baenitz, M. Schmidt, U. K. Rößler, A. A. Leonov, and A. N. Bogdanov, *Precursor Phenomena at the Magnetic Ordering of the Cubic Helimagnet FeGe,* Physical Review Letters **107**, 127203 (2011).

[11] S. Seki, X. Yu, S. Ishiwata, and Y. Tokura, *Observation of skyrmions in a multiferroic material,* Science **336**, 198 (2012).

[12] S. Seki, J.-H. Kim, D. S. Inosov, R. Georgii, B. Keimer, S. Ishiwata, and Y. Tokura, *Formation and rotation of skyrmion crystal in the chiral-lattice insulator* Cu_2OSeO_3, Physical Review B **85**, 220406 (2012).

[13] T. Adams, A. Chacon, M. Wagner, A. Bauer, G. Brandl, B. Pedersen, H. Berger, P. Lemmens, and C. Pfleiderer, *Long-wavelength helimagnetic order and skyrmion lattice phase in* Cu_2OSeO_3, Physical Review Letters **108**, 237204 (2012).

[14] Y. Tokunaga, X. Z. Yu, J. S. White, H. M. Rønnow, D. Morikawa, Y. Taguchi, and Y. Tokura, *A new class of chiral materials hosting magnetic skyrmions beyond room temperature,* Nature Communications **6** (2015).

[15] K. Karube, J. S. White, N. Reynolds, J. L. Gavilano, H. Oike, A. Kikkawa, F. Kagawa, Y. Tokunaga, H. M. Rønnow, Y. Tokura, *et al.*, *Robust metastable skyrmions and their triangular-square lattice structural transition in a high-temperature chiral magnet,* Nature Materials (2016).

[16] I. Kézsmárki, S. Bordács, P. Milde, E. Neuber, L. M. Eng, J. S. White, H. M. Rønnow, C. D. Dewhurst, M. Mochizuki, K. Yanai, *et al.*, *Néel-type skyrmion lattice with confined orientation in the polar magnetic semiconductor GaV_4S_8,* Nature Materials **14**, 1116 (2015).

[17] A. Tonomura, X. Yu, K. Yanagisawa, T. Matsuda, Y. Onose, N. Kanazawa, H. S. Park, and Y. Tokura, *Real-space observation of skyrmion lattice in helimagnet MnSi thin samples,* Nano Letters **12**, 1673 (2012).

[18] M. N. Wilson, A. B. Butenko, A. N. Bogdanov, and T. L. Monchesky, *Chiral skyrmions in cubic helimagnet films: The role of uniaxial anisotropy,* Physical Review B **89**, 094411 (2014).

[19] S. Heinze, K. Von Bergmann, M. Menzel, J. Brede, A. Kubetzka, R. Wiesendanger, G. Bihlmayer, and S. Blügel, *Spontaneous atomic-scale magnetic skyrmion lattice in two dimensions,* Nature Physics **7**, 713 (2011).

[20] X. Z. Yu, N. Kanazawa, W. Z. Zhang, T. Nagai, T. Hara, K. Kimoto, Y. Matsui, Y. Onose, and Y. Tokura, *Skyrmion flow near room temperature in an ultralow current density,* Nature Communications **3**, 988 (2012).

[21] J. White, K. Prša, P. Huang, A. A. Omrani, I. Živković, M. Bartkowiak, H. Berger, A. Magrez, J. Gavilano, G. Nagy, *et al.*, *Electric-field-induced skyrmion distortion and giant lattice rotation in the magnetoelectric insulator Cu_2OSeO_3,* Physical Review Letters **113**, 107203 (2014).

[22] I. E. Dzyaloshinskii, *A thermodynamic theory of "weak" ferromagnetism of antiferromagnetics,* Journal of Physics and Chemistry of Solids **4**, 241 (1958).

[23] T. Moriya, *Anisotropic Superexchange Interaction and Weak Ferromagnetism,* Physical Review **120**, 91 (1960).

[24] P. Bak and M. H. Jensen, *Theory of helical magnetic structures and phase transitions in MnSi and FeGe,* Journal of Physics C: Solid State Physics **13**, L881 (1980).

[25] S. Buhrandt and L. Fritz, *Skyrmion lattice phase in three-dimensional chiral magnets from Monte Carlo simulations,* Physical Review B **88**, 195137 (2013).

[26] A. N. Bogdanov and D. A. Yablonskii, *Thermodynamically stable 'vortices' in magnetically ordered crystals. the mixed state of magnets,* Zh. Eksp. Teor. Fiz **95**, 182 (1989).

[27] A. N. Bogdanov and A. Hubert, *Thermodynamically stable magnetic vortex states in magnetic crystals,* Journal of Magnetism and Magnetic Materials **138**, 255 (1994).

[28] U. K. Rößler, A. N. Bogdanov, and C. Pfleiderer, *Spontaneous skyrmion ground states in magnetic metals,* Nature **442**, 797 (2006).

[29] A. B. Butenko, A. A. Leonov, U. K. Rößler, and A. N. Bogdanov, *Stabilization of skyrmion textures by uniaxial distortions in noncentrosymmetric cubic helimagnets,* Physical Review B **82**, 052403 (2010).

[30] U. K. Rößler, A. A. Leonov, and A. N. Bogdanov, *Chiral skyrmionic matter in non-centrosymmetric magnets,* in *Journal of Physics: Conference Series*, Vol. 303 (IOP Publishing, 2011) p. 012105.

[31] T. Adams, S. Mühlbauer, C. Pfleiderer, F. Jonietz, A. Bauer, A. Neubauer, R. Georgii, P. Böni, U. Keiderling, K. Everschor, *et al.*, *Long-range crystalline nature of the skyrmion lattice in MnSi,* Physical Review Letters **107**, 217206 (2011).

[32] S. L. Zhang, A. Bauer, D. M. Burn, P. Milde, E. Neuber, L. M. Eng, H. Berger, C. Pfleiderer, G. V. V. van der Laan, and T. Hesjedal, *Multidomain Skyrmion Lattice State in Cu_2OSeO_3,* Nano Letters **16**, 3285 (2016).

[33] S. L. Zhang, A. Bauer, H. Berger, C. Pfleiderer, G. V. Van Der Laan, and T. Hesjedal, *Resonant elastic x-ray scattering from the skyrmion lattice in Cu_2OSeO_3,* Physical Review B **93**, 214420 (2016).

[34] K. Makino, J. D. Reim, D. Higashi, D. Okuyama, T. J. Sato, Y. Nambu, E. P. Gilbert, N. Booth, S. Seki, and Y. Tokura, *Thermal stability and irreversibility of skyrmion-lattice phases in Cu_2OSeO_3,* Physical Review B **95**, 134412 (2017).

[35] M. C. Langner, S. Roy, S. K. Mishra, J. C. T. Lee, X. W. Shi, M. Hossain, Y. D. Chuang, S. Seki, Y. Tokura, S. D. Kevan, *et al.*, *Coupled skyrmion sublattices in Cu_2OSeO_3,* Physical Review Letters **112**, 167202 (2014).

[36] M. Mochizuki, X. Z. Yu, S. Seki, N. Kanazawa, W. Koshibae, J. Zang, M. Mostovoy, Y. Tokura, and N. Nagaosa, *Thermally driven ratchet motion of a skyrmion microcrystal and topological magnon Hall effect,* Nature Materials **13**, 241 (2014).

[37] S. Pöllath, J. Wild, L. Heinen, T. N. Meier, M. Kronseder, L. Tutsch, A. Bauer, H. Berger, C. Pfleiderer, J. Zweck, *et al.*, *Dynamical defects in rotating magnetic skyrmion lattices,* Physical Review Letters **118**, 207205 (2017).

[38] L. J. Bannenberg, K. Kakurai, F. Qian, E. Lelièvre-Berna, C. D. Dewhurst, Y. Onose, Y. Endoh, Y. Tokura, and C. Pappas, *Extended skyrmion lattice scattering and long-time memory in the chiral magnet $Fe_{1-x}Co_xSi$,* Physical Review B **94**, 104406 (2016).

[39] J. D. Reim, K. Makino, D. Higashi, Y. Nambu, D. Okuyama, T. J. Sato, E. P. Gilbert, N. Booth, and S. Seki, *Impact of minute-time-scale kinetics on the stabilization of the skyrmion-lattice in Cu_2OSeO_3,* in *Journal of Physics: Conference Series*, Vol. 828 (IOP Publishing, 2017) p. 012004.

[40] C. Pappas, L. J. Bannenberg, E. Lelièvre-Berna, F. Qian, C. D. Dewhurst, R. M. Dalgliesh, D. Schlagel, T. A. Lograsso, and P. Falus, *Magnetic Fluctuations, Precursor Phenomena and Phase Transition in MnSi under Magnetic Field,* Physical Review Letters **119**, 047203 (2017).

[41] S. S. M. at http://link.aps.org/supplemental/10.1103/PhysRevB.96.184416 for the supplemental movies., .

[42] L. J. Bannenberg, A. J. E. Lefering, K. Kakurai, Y. Onose, Y. Endoh, Y. Tokura, and C. Pappas, *Magnetic relaxation phenomena in the chiral magnet $Fe_{1-x}Co_xSi$: An ac susceptibility study,* Physical Review B **94**, 134433 (2016).

[43] A. Bauer, A. Neubauer, C. Franz, W. Münzer, M. Garst, and C. Pfleiderer, *Quantum phase transitions in single-crystal $Mn_{1-x}Fe_xSi$ and $Mn_{1-x}Co_xSi$: Crystal growth, magnetization, ac susceptibility, and specific heat,* Physical Review B **82**, 064404 (2010).

[44] F. Qian, H. Wilhelm, A. Aqeel, T. T. M. Palstra, A. J. E. Lefering, E. H. Brück, and C. Pappas, *Phase diagram and magnetic relaxation phenomena in Cu_2OSeO_3,* Physical Review B **94**, 064418 (2016).

9

MULTIPLE LOW-TEMPERATURE SKYRMIONIC STATES IN A BULK CHIRAL MAGNET

Magnetic skyrmions are topologically protected spin textures with particle-like properties. In bulk cubic helimagnets, they appear under applied magnetic fields and condense spontaneously into a lattice in a narrow region of the phase diagram just below the magnetic ordering temperature, the so-called A-phase. Theory, however, predicts skyrmions to be locally stable in a wide range of magnetic fields and temperatures. Neutron diffraction measurements reveal the formation of skyrmion lattice states in large areas of the magnetic phase diagram, from the lowest temperatures up to the A-phase. Disappearing spiral states near critical lines catalyze topological charge changing processes leading to the formation and destruction of skyrmionic states at low temperatures, which are thermodynamically stable or metastable depending on the orientation and strength of the magnetic field. Skyrmions are surprisingly resistant to high magnetic fields: the memory of skyrmion lattice states persists in the field-polarized state, possibly in the form of torons or other topologically protected defects, even when the skyrmion lattice signal has disappeared. These findings highlight the paramount role of magnetic anisotropies in stabilizing novel skyrmionic states and open up new routes for manipulating these quasiparticles towards energy-efficient spintronics applications.

9.1. INTRODUCTION

The concept of a skyrmion, a topologically protected quasi-particle, was introduced by Tony Skyrme [2] in the early 1960s in his study of baryons as protons and neutrons. Since then, skyrmions being a topologically protected field configuration with particle-like properties, have been embraced by a multitude of scientific fields including condensed matter physics [3–6]. Since the recent observation of magnetic skyrmions [7, 8],

Parts of this chapter have been published in NPJ Quantum Materials **4**, 11 (2019) [1].

which are essentially swirling nanoscale spin structures, a new field of research emerged: skyrmionics. This field is driven both by the exploration of new topological phenomena and the perspective use of skyrmions in information storage and spintronics, which may result in more efficient and low-power computational solutions and high-density data storage [9–13].

In bulk cubic helimagnets, where magnetic skyrmions were first observed [7], lattices of skyrmions appear spontaneously in a small pocket of the temperature-magnetic field phase diagram, the so-called A-phase, just below the transition temperature T_C. The stability of these skyrmion latices (SkLs) is attributed to the competition between the ferromagnetic exchange, the Dzyaloshinskii-Moriya (DM) and Zeeman interactions in combination with additional small terms [14], such as thermal fluctuations [7, 15], dipolar interactions and the softening of the magnetization modulus [16, 17]. As the free energy imbalance between the skyrmion lattice phase and its main competitor, the conical state, is small, the boundaries of the A-phase can be changed substantially by applying pressure [18] or electric fields [12, 19–21]. On the other hand, theoretical models that are based on the Dzyaloshinskii approach [22, 23] and include magnetic stiffness or anisotropy, predict SkLs to occur in bulk cubic helimagnets over a wide range of magnetic fields and temperatures below T_C [14, 24–29].

Experimental efforts to find anisotropy-stabilized low temperature SkLs in bulk cubic helimagnets have been largely overshadowed by the search of skyrmion lattices and isolated skyrmions in thin films [8, 13, 30], where the main stabilization mechanism is the chiral surface twists [31–33]. Nevertheless, the importance of anisotropy in stabilizing novel states is underscored by the recent discovery of the tilted spiral state [34, 35], which results from the competition between the relatively strong anisotropic exchange and the cubic anisotropy in Cu_2OSeO_3. Furthermore, similar mechanisms possibly stabilize the low-temperature skyrmion lattice reported in the same material [35].

In the following, we present an experimental and theoretical study of skyrmionic states in the chiral magnetic insulator Cu_2OSeO_3 and discuss the stabilization and nucleation mechanisms thereof. Small angle neutron scattering (SANS) measurements were performed by carefully applying the magnetic field along the three major crystallographic directions, either after zero-field cooling (ZFC) or after fast-field cooling (FFC) through the A-phase [36–40]. In this way, extremely robust low-temperature skyrmionic states can be induced for all field directions and over large areas of the phase diagram, which are stable only for $\mathbf{H}||[001]$ where their stability is granted by competing cubic and exchange anisotropies. Emerging and disappearing spiral states near critical magnetic fields catalyze the change of topological charge required for the creation and destruction of these skrymions. In addition, these (metastable) skyrmions are surprisingly resistant to high magnetic fields: the memory of skyrmionic states persists, possibly in the form of isolated skyrmions or torons, in the field polarized state, even when the skyrmion lattice signal has disappeared. Our findings highlight the paramount role magnetic anisotropy plays in stabilizing skyrmionic states and opens new routes for the manipulation of skyrmions in view of potential spintronics applications.

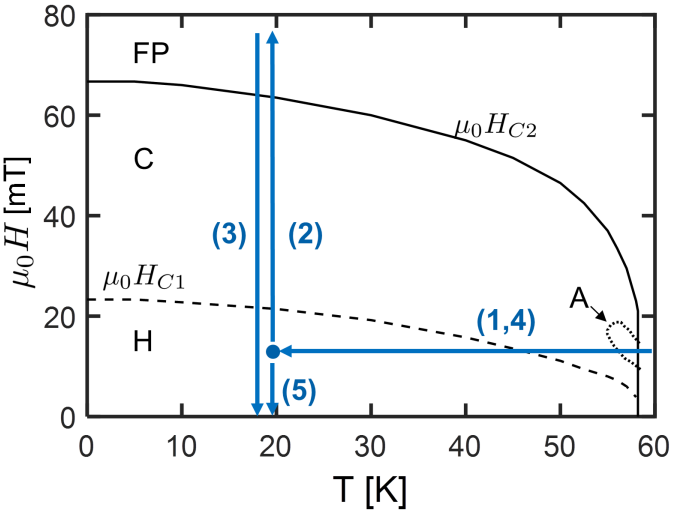

Figure 9.1: Schematic representation of the experimental procedure used for the Fast Field Cooled (FFC) measurements. For FFC sample was (1) first field cooled under a magnetic field of $\mu_0 H$= 14 mT to the temperature of interest with an average cooling rate of 10 K/s. Subsequently, (2) measurements were performed by stepwise increasing the magnetic field to $\mu_0 H$= 90 mT, well above the $\mu_0 H_{C2}$ line. Next, (3) measurements were performed by stepwise decreasing the magnetic field to $\mu_0 H$= 0 mT. In an additional step, the sample was brought to $T \gg T_C$, (4) field cooled again under $\mu_0 H$= 14 mT and (5) measurements were performed by stepwise decreasing the field to $\mu_0 H$= 0 mT. This figure also indicates the boundaries of the different helimagnetic phases generic to cubic helimagnets: the Helical phase (H) for magnetic fields $\mu_0 H < \mu_0 H_{C1}$, the Conical phase (C) for $\mu_0 H_{C1} < \mu_0 H < \mu_0 H_{C2}$, the Field Polarized state (FP) for $\mu_0 H > \mu_0 H_{C2}$ and the A-phase (A) close to T_C.

9.2. EXPERIMENTAL DETAILS

The experiments were performed at the SANS instrument D33 of the Institute Laue Langevin [41] with an incident wavelength of 0.8 nm, a sample-to-detector distance of 12.8 m and a wave-vector transfer resolution of $\Delta\lambda/\lambda$ = 10%. The 3×3×4 mm^3 Cu_2OSeO_3 single crystal was grown by chemical vapor transport and is the same sample as the one used in our previous work [34, 42]. It was glued to an aluminum cylinder with a diameter of 3 mm around which 1 m constantan wire was wound with a total resistance of 30 Ω. The wire was glued with GE low-temperature varnish and was used to generate large heat pulses.

The sample was placed inside an Oxford Instruments 7 T horizontal-field cryomagnet and the constantan heater was connected to an external power supply. Fast cooling was performed by first stabilizing the sample at the temperature of interest. Subsequently, a current of 0.3 A was applied for 1.5 s to the constantan heater, providing sufficiently heat to bring the sample to $T \gg T_C$. Switching off the current resulted in a rapid cooling with an average cooling rate of 10 K/s, as estimated from a comparison of the scattered intensity of the SANS patterns at zero magnetic field (recorded every 0.8 s) with the temperature dependent evolution of the scattered intensity of the helical Bragg peaks at zero magnetic field. All magnetic fields are corrected for demagnetization ef-

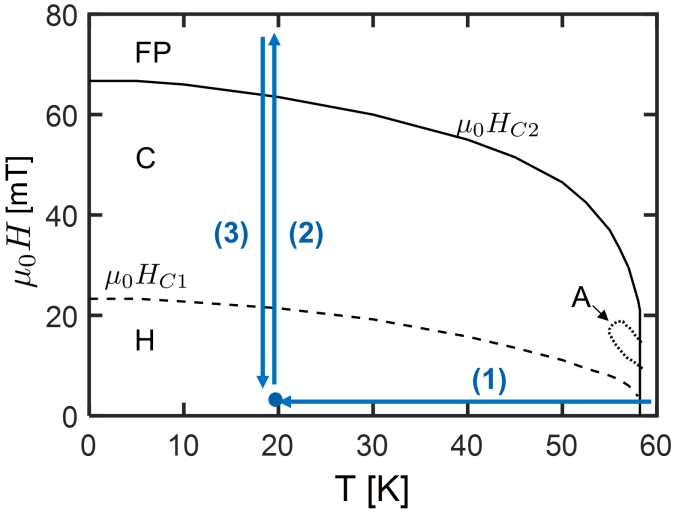

Figure 9.2: Schematic representation of the experimental procedure used for the Zero Field Cooled (ZFC) measurements. The sample was (1) first cooled at zero magnetic field to the temperature of interest. Subsequently, (2) measurements were performed by stepwise increasing the magnetic field to $\mu_0 H$= 90 mT, well above the $\mu_0 H_{C2}$ line. Next, (3) measurements were performed by stepwise decreasing the magnetic field to 0 mT.

fects assuming a demagnetization factor of 1/3.

Figure 9.1 schematically illustrates the FFC protocol followed, and also indicates the boundaries of the phases generic to cubic helimagnets. The FFC protocol starts with (1) cooling the sample from $T \gg T_C$ with a rate of ~10 Ks^{-1} to the temperature of interest under a magnetic field of $\mu_0 H$= 14 mT. Subsequently, in step (2), SANS patterns were collected at this temperature by stepwise increasing the magnetic field to $\mu_0 H$= 90 mT, i.e. well above the $\mu_0 H_{C2}$ transition line. In the next step (3), the temperature remained the same and the magnetic field was stepwise decreased to $\mu_0 H$= 0 mT. Subsequently, the sample (4) was fast cooled to the temperature of interest under exactly the same conditions as for step (1). Finally, (5) SANS patterns were collected by stepwise decreasing the magnetic field from $\mu_0 H$= 14 mT to 0 mT. The ZFC measurements were performed following the protocol schematically illustrated in Fig. 9.2 and commenced with (1) cooling the sample from $T \gg T_C$ to the temperature of interest at zero magnetic field. Subsequently, SANS patterns were collected at this temperature by stepwise (2) increasing the magnetic field to $\mu_0 H$= 90 mT and (3) decreasing the magnetic field to 0 mT.

The measurements were performed with the magnetic field applied both parallel (**H**||k$_i$) and perpendicular (**H**⊥k$_i$) to the incoming neutron beam which is designated by its wavevector k$_i$. The SANS patterns for **H**||k$_i$ were analyzed using the masks shown in Figure 9.3. These were introduced in order to distinguish between the scattered intensity arising from skyrmionic correlations and the Bragg peaks originating from the helical phase. For this reason, the masks are different for **H**||[111], **H**||[110] and **H**||[001].

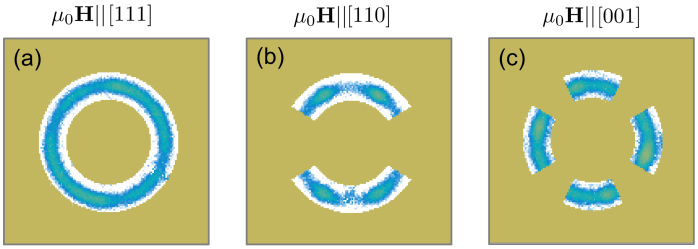

Figure 9.3: Masks used to evaluate the scattered intensity arising from skyrmionic correlations and discriminate it from the Bragg peaks of the helical phase. The calculated intensities are averages over the unmasked areas. The mask in Panel (a) was used for **H**||k_i||[111], in Panel (b) for **H**||k_i||[110] and in Panel (c) for **H**||k_i||[001].

9.3. RESULTS

Figure 9.4 shows a set of SANS patterns at T = 3 K after FFC, for **H**||[111]. A ring of scattering appears at $\mu_0 H$= 14 mT, which evolves with increasing magnetic field into a weak pattern with the six-fold symmetry characteristic of SkL scattering [7]. By further increasing the magnetic field, this scattering weakens and persists up to the $\mu_0 H_{C2}$ transition line. At higher magnetic fields, the scattering vanishes, implying that the SkLs have dissolved. Surprisingly, when the magnetic field is subsequently decreased from $\mu_0 H$= 90 to 0 mT, the scattering patterns with six-fold symmetry reappear for 65 mT> $\mu_0 H$>7 mT. This is a remarkable result because it implies that a memory of the SkL phase persists at magnetic fields high enough to suppress not only the SkL scattering but also any spiral modulations.

Additional measurements indicate that the SkL scattering reappears even after applying a field of 200 mT, i.e. more than twice as large as $\mu_0 H_{C2}$. Thus the memory of skyrmionic correlations is extremely robust and can only be erased by (relatively) high magnetic fields. This result is even more remarkable if one considers that these robust skyrmions are metastable, as they were induced by the FFC procedure. Indeed, this scattering disappears once the field has been reduced to zero, and it is not observed when the sample is zero field cooled (Fig. 9.4) or field cooled at much smaller cooling rates, or cooled down under magnetic fields exceeding the lower and upper boundaries of the A-phase. Skyrmions may survive due to the magnetic field inhomogeneity produced by stray fields, in particular near the sample edges, or in the form of magnetic defects such as torons [17, 43–45].

A similar behavior is found for **H**||[110], as evidenced by the SANS patterns shown in Fig. 9.5. After FFC at $\mu_0 H$= 14 mT, the scattering pattern mainly consists of two helical peaks along the [001] direction - a metastable spiral domain with the wave vector perpendicular to the field. This scattering is superimposed on a very weak additional signal, which evolves to a clear SkL pattern at $\mu_0 H$= 35 mT, i.e. a field where the helical peaks have almost completely disappeared. With increasing magnetic field, the SkL scattering weakens and finally disappears at $\mu_0 H$= 85 mT. When the magnetic field is subsequently decreased from $\mu_0 H$= 90 to 0 mT, the SkL scattering reappears around 50 mT, albeit with a much weaker intensity and within a smaller magnetic field interval than for **H**||[111].

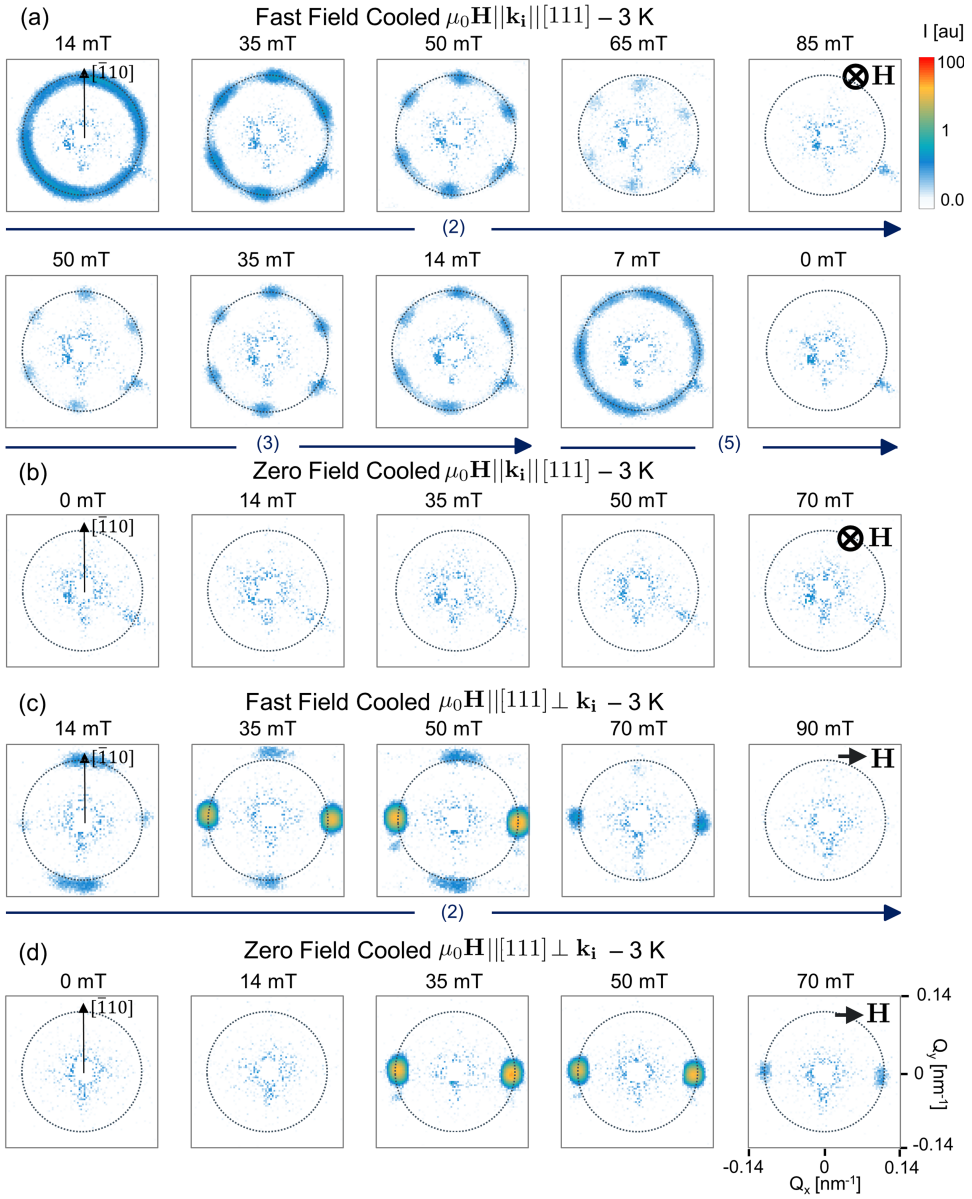

Figure 9.4: SANS patterns recorded at T = 3 K and with the magnetic field applied along the [111] crystallographic direction. The magnetic field was applied (a,b) parallel ($\mathbf{H}||\mathbf{k}_i$) and (c,d) perpendicular ($\mathbf{H}\perp\mathbf{k}_i$) to the incoming neutron beam following the (a,c) FFC and (b,d) ZFC protocols. The arrows and numbers below the SANS patterns indicate the step of the FFC protocol, as defined in Fig. 9.1, for which the measurements were performed.

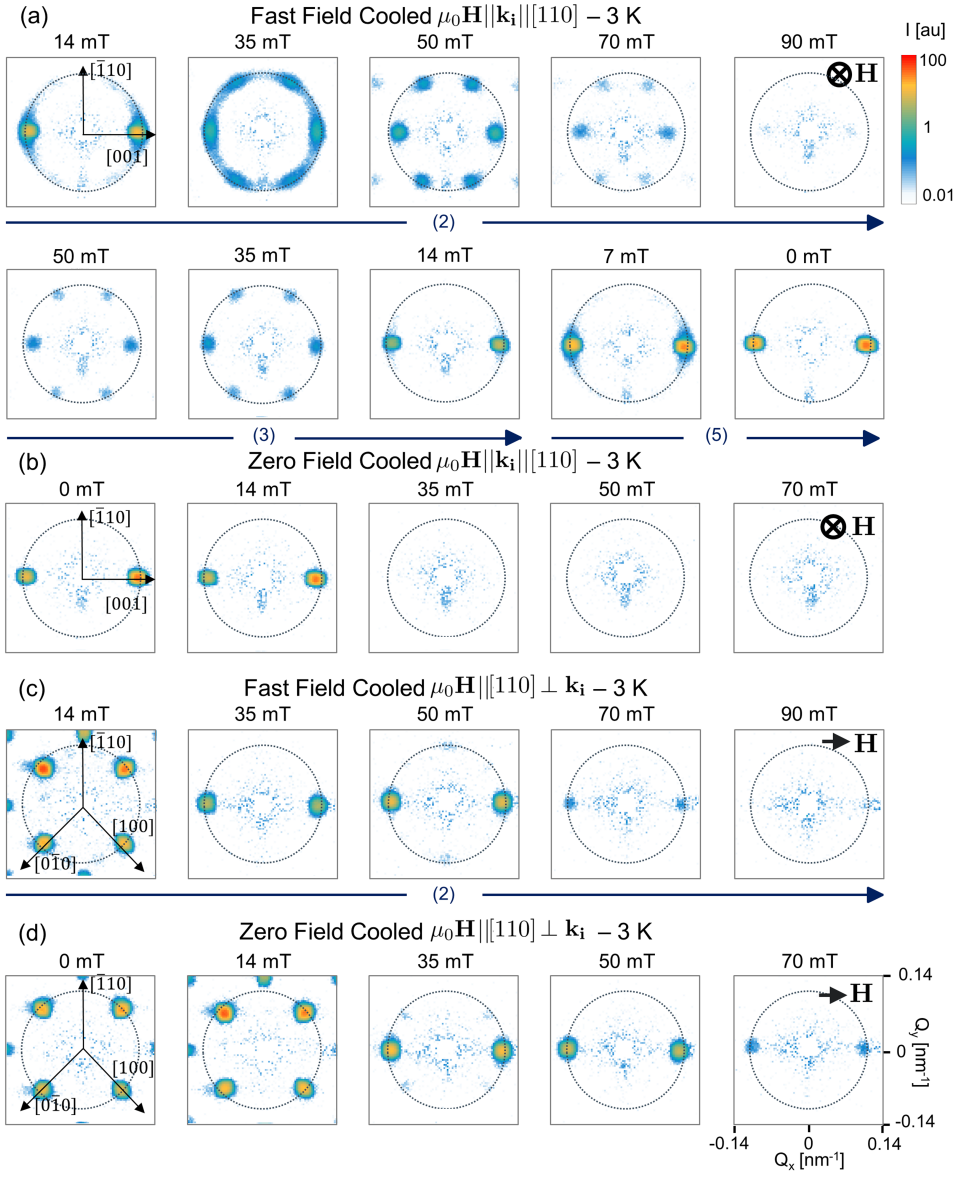

Figure 9.5: SANS patterns recorded at T = 3 K and with the magnetic field applied along the [110] crystallographic direction. The magnetic field was applied (a,b) parallel ($\mathbf{H}||\mathbf{k_i}$) and (c,d) perpendicular ($\mathbf{H}\perp\mathbf{k_i}$) to the incoming neutron beam following the (a,c) FFC and (b,d) ZFC protocols. The arrows and numbers below the SANS patterns indicate the step of the FFC protocol, as defined in Fig. 9.1, for which the measurements were performed.

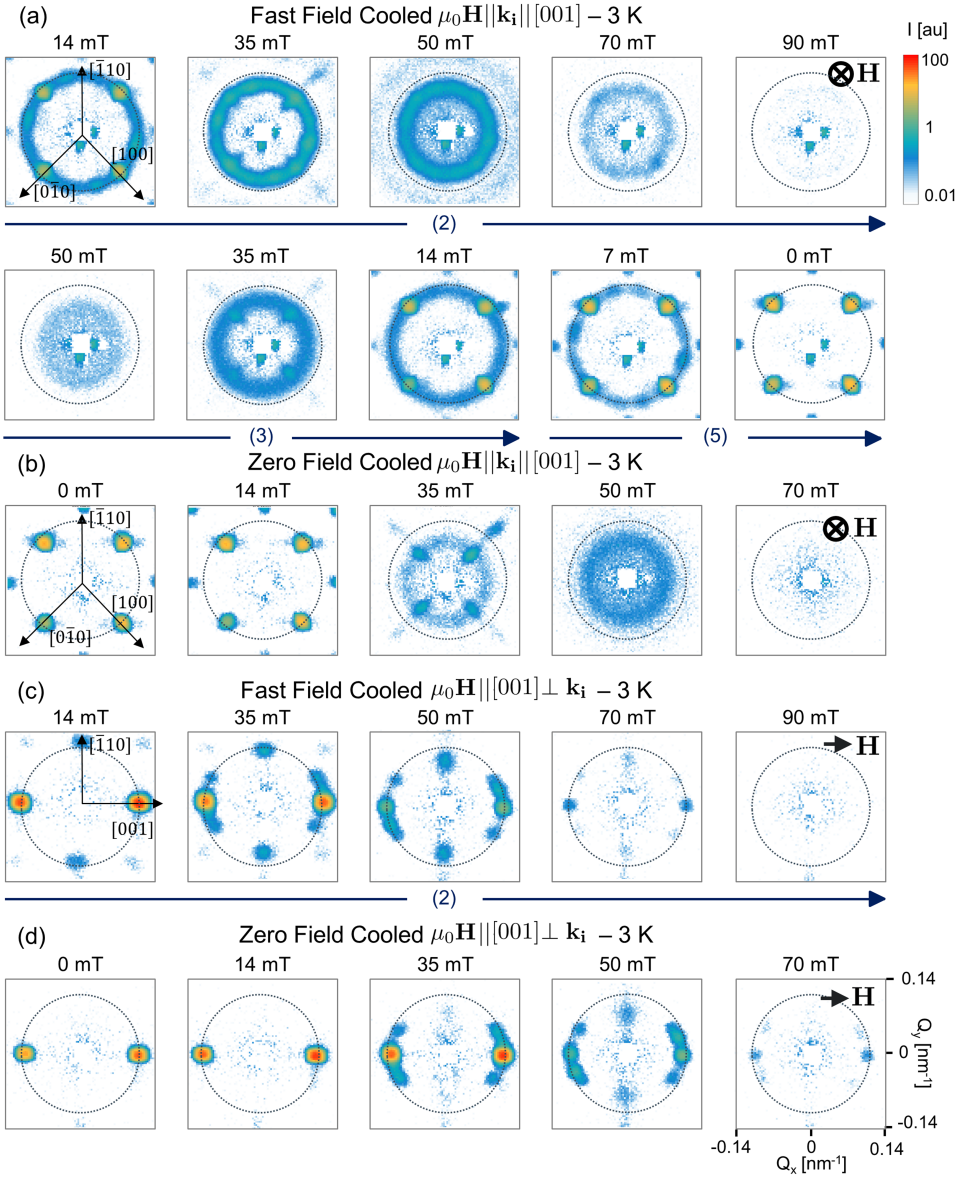

Figure 9.6: SANS patterns recorded at T = 3 K and with the magnetic field applied along the [001] crystallographic direction. The magnetic field was applied (a,b) parallel ($\mathbf{H}||\mathbf{k_i}$) and (c,d) perpendicular ($\mathbf{H}\perp\mathbf{k_i}$) to the incoming neutron beam following the (a,c) FFC and (b,d) ZFC protocols. The arrows and numbers below the SANS patterns indicate the step of the FFC protocol, as defined in Fig. 9.1, for which the measurements were performed.

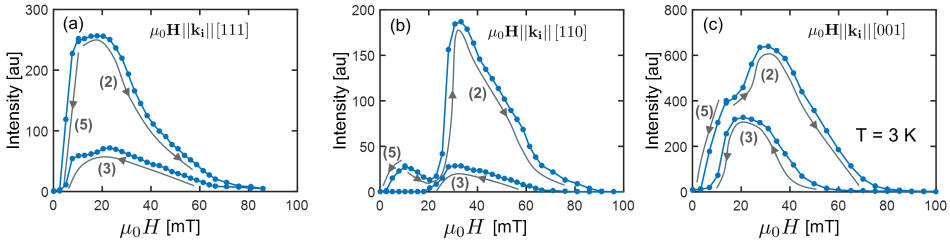

Figure 9.7: Scattered intensity at 3 K obtained by averaging over the detector after Fast Field Cooling (FFC) using the masks shown in Fig. 9.3. The numbers underneath the curves correspond to the experimental steps shown in Fig. 9.1 of the main text. The magnetic field was applied parallel to the incoming neutron beam ($\mathbf{H}||\mathrm{k_i}$) and along the (a) [111], (b) [110] and (c) [001] crystallographic directions.

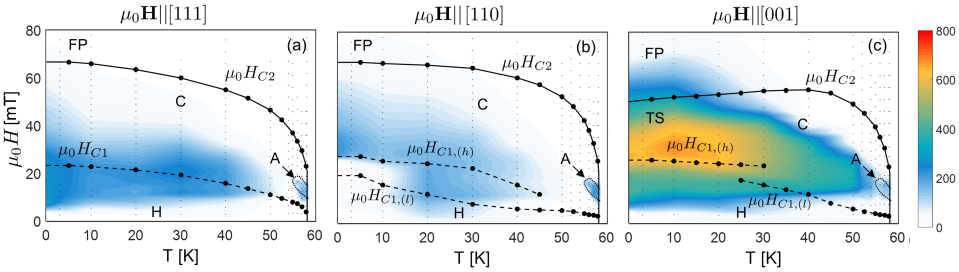

Figure 9.8: Phase diagrams indicating the extend and intensity of skyrmionic scattering after FFC through the A-phase. Contour plots of the total neutron scattering outside the helical peaks measured with the magnetic field applied parallel to the incoming neutron beam ($\mathbf{H}||\mathrm{k_i}$) and along the (a) [111], (b) [110] and (c) [001] crystallographic directions and averaged using the masks shown in Fig. 9.3 of the supplement. The lower ($\mu_0 H_{C1,(l)}$) and upper ($\mu_0 H_{C1,(h)}$) helical-to-conical, conical-to-field polarized ($\mu_0 H_{C2}$) transition lines as well as the boundaries of the A-phase just below T_C have been derived from susceptibility measurements [34]. The letters A, H, C,TS and FP stand for the A-, helical, conical, tilted spiral and field polarized phases respectively.

The most intriguing behavior is found for $\mathbf{H}||[001]$, the field direction for which the tilted conical phase appears close to $\mu_0 H_{C2}$ [34]. After FFC, the SANS pattern at 14 mT, shown in Fig. 9.6, reveals four Bragg peaks originating from the metastable spiral domains along [001] and [010] that are in the scattering plane. In addition, an intense ring of scattering with radius $\tau = 2\pi/\ell$ is visible, ℓ being the pitch of a helical modulation. One can distinguish 12 peaks originating from two SkL domains oriented along [001] and [010], as is also the case in the A-phase [42]. With increasing magnetic field, the helical peaks fade away whereas the ring of scattering gains intensity, broadens and its radii decreases considerably before it disappears above $\mu_0 H \approx 70$ mT. The broadening of the ring is even more pronounced when the SkL scattering reappears by decreasing the magnetic field from 90 to 0 mT. However, the radius and widths of the rings after FFC and ZFC are the same, which implies that they have the same origin. We thus conclude, that these rings arise from thermodynamically stable skyrmionic correlations, which coexist with the conical and tilted spiral phases.

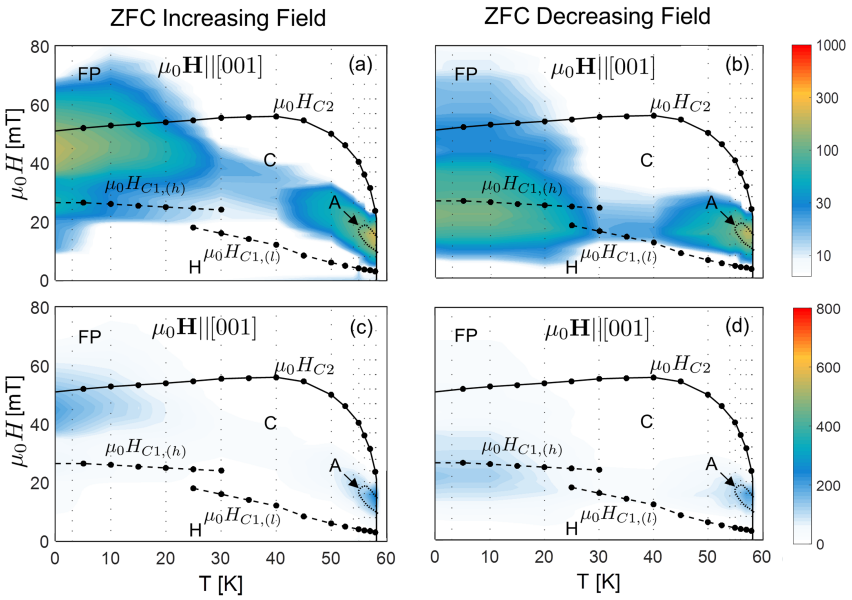

Figure 9.9: Phase diagrams indicating the extend and intensity of skyrmionic scattering after Zero Field Cooling (ZFC) for $\mathbf{H}||\mathrm{k_i}||[001]$. The measurements were performed upon increasing the magnetic field, step (2) in Fig. 9.2, (Panel (a) and (c)) and decreasing the magnetic field, step (3) in Fig. 9.2, (Panel (b) and (d)). The contour plots of Panels (a) and (b) use a logarithmic color scale, whereas those of Panels (c) and (d) a linear one.

9.4. DISCUSSION

The experimental results are summarized by Figs. 9.8 and 9.9, which display contour plots of the total scattering recorded after FFC (steps (2) and (5) in Fig. 9.1) and ZFC (steps (2) and (3) in Fig. 9.2), respectively. The intensity has been obtained by excluding the helical and conical peaks, and corresponds to the total scattering that can be attributed to skyrmionic correlations. This scattering appears over large areas, the extent of which strongly depends on the specific orientation of the magnetic field with respect to the crystallographic lattice. Indeed, thermodynamically stable skyrmions only appear at low temperatures for **H**||[001], which is also the crystallographic direction for which the skyrmionic scattering is the strongest after FFC.

In order to understand the large differences between the contour plots shown in Figs. 9.8 and 9.9 as well as the underlying skyrmion nucleation and stabilization mechanisms, we consider the Dzyaloshinskii model of cubic non-centrosymmetric ferromagnets [22, 23, 46]. This model includes the ferromagnetic exchange (with strength J), DM (with strength D) and Zeeman interaction energies, i.e. the principal interactions essential to stabilize modulated states:

$$f = \frac{-Ja^2}{2} \sum_{i=x,y,x} [\partial_i \hat{m} \cdot \partial_i \hat{m}] + aD\hat{m} \cdot \nabla \times \hat{m} - a^3 M \hat{m} \cdot \vec{B} + f_a, \tag{9.1}$$

with a the lattice constant, $\hat{m}$ the unit vector in the direction of the magnetization, and M the magnetization value. Different from other symmetry classes C_{nv} [47] and D_{2d} [48] where the DM interaction itself can stabilize skyrmions, additional terms are required in cubic helimagnets. We consider anisotropic contributions that include cubic anisotropy with $k_c > 0$ (easy ⟨001⟩ axes) and exchange anisotropy with $b_{EA} < 0$ (easy ⟨111⟩ axes):

$$f_a = k_c(m_x^2 m_y^2 + m_x^2 m_z^2 + m_y^2 m_z^2) + b_{EA}((\partial_x m_x)^2 + (\partial_y m_y)^2 + (\partial_z m_z)^2). \tag{9.2}$$

Different from other cubic helimagnets, both anisotropy terms are of similar strength in Cu_2OSeO_3 and the competition between them stabilizes a tilted spiral state, in which the propagation vector of the conical spiral is not along the magnetic field, but tilts away towards the ⟨111⟩ axes [34].

Computations performed by A.O. Leonov [1] show that skyrmion lattices with a lower energy than other modulated states can only be found for **H**||[001]. This explains why the skyrmionic correlations occur after ZFC only for **H**||[001] (Fig. 9.6) and why they are the strongest after FFC (Fig. 9.8(c)). However, for the other field directions considered, **H**||[110] and **H**||[111], the skyrmion lattice remains a metastable solution.

Our results also highlight how different mechanisms can generate and stabilize low temperature skyrmions besides quenching them by fast cooling through the A-phase as previously done in refs. [36, 37, 39, 40]. In fact, skyrmions may nucleate from metastable spiral domains. In the case of Cu_2OSeO_3, this may occur if $\mu_0 H_{C1}$ exceeds the field where it becomes energetically favorable for spirals to rupture [49, 50]. This is exactly what is observed for **H**||[001], where the spirals along [001] and [010] are metastable, and

where skyrmionic scattering emerges after ZFC or intensifies after FFC around $\mu_0 H$= 35 mT (Fig. 9.6). In addition, also for the other field directions, **H**||[110] and **H**||[111], the skyrmionic intensity is greatly enhanced around the critical lines. These results thus show that (dis)appearing spirals may catalyze the formation of topological charge, which is required in the nucleation process of skyrmions. Indeed, the nontrivial topology of magnetic skyrmions gives rise to energy barriers hindering their creation and destruction, and which makes transitions between states with a different topological number different from e.g. transitions between topological trivial states as ferromagnetic and helimagnetic states.

9.5. CONCLUSION

In conclusion, extremely robust low-temperature skyrmionic states can be induced for all field directions and over large areas of the phase diagram. These skyrmionic states are stabilized by competing cubic and exchange anisotropies, and are thermodynamically stable when the magnetic field is applied along the [001] axis. The formation and destruction of these skyrmionic states is enhanced by (dis)appearing spiral states near critical lines which catalyze topological charge changing processes. On the other hand, these skyrmions are surprisingly resilient to high magnetic fields and their memory persists, possibly in the form of isolated skyrmions or torons, even in the field polarized state. These findings underscore the paramount role of magnetic anisotropies in stabilizing novel skyrmionic states and provide valuable directions to manipulate and tune skyrmions for future applications, possibly with electric fields or strain.

REFERENCES

[1] L. J. Bannenberg, H. Wilhelm, R. Cubitt, A. Labh, M. Schmidt, E. Lelièvre-Berna, C. Pappas, M. Mostovoy, and A. O. Leonov, *Multiple low-temperature skyrmionic states in a bulk chiral magnet,* npj Quantum Materials **4**, 11 (2019).

[2] T. H. R. Skyrme, *A non-linear field theory,* Proceedings of the Royal Society Londen A **260**, 127 (1961).

[3] U. Al Khawaja and H. Stoof, *Skyrmions in a ferromagnetic Bose-Einstein condensate,* Nature **411**, 918 (2001).

[4] J.-i. Fukuda and S. Žumer, *Quasi-two-dimensional Skyrmion lattices in a chiral nematic liquid crystal,* Nature Communications **2**, 246 (2011).

[5] P. J. Ackerman, T. Boyle, and I. I. Smalyukh, *Squirming motion of baby skyrmions in nematic fluids,* Nature Communications **8**, 673 (2017).

[6] S. Tsesses, E. Ostrovsky, K. Cohen, B. Gjonaj, N. Lindner, and G. Bartal, *Optical skyrmion lattice in evanescent electromagnetic fields,* Science **15**, eaau0227 (2018).

[7] S. Mühlbauer, B. Binz, F. Jonietz, C. Pfleiderer, A. Rosch, A. Neubauer, R. Georgii, and P. Böni, *Skyrmion lattice in a chiral magnet,* Science **323**, 915 (2009).

[8] X. Z. Yu, Y. Onose, N. Kanazawa, J. H. Park, J. H. Han, Y. Matsui, N. Nagaosa, and Y. Tokura, *Real-space observation of a two-dimensional skyrmion crystal,* Nature **465**, 901 (2010).

[9] X. Z. Yu, N. Kanazawa, W. Z. Zhang, T. Nagai, T. Hara, K. Kimoto, Y. Matsui, Y. Onose, and Y. Tokura, *Skyrmion flow near room temperature in an ultralow current density,* Nature Communications **3**, 988 (2012).

[10] A. Fert, V. Cros, and J. Sampaio, *Skyrmions on the track,* Nature Nanotechnology **8**, 152 (2013).

[11] N. Nagaosa and Y. Tokura, *Topological properties and dynamics of magnetic skyrmions,* Nature Nanotechnology **8**, 899 (2013).

[12] J. S. White, K. Prša, P. Huang, A. A. Omrani, I. Živković, M. Bartkowiak, H. Berger, A. Magrez, J. Gavilano, G. Nagy, *et al.*, *Electric-field-induced skyrmion distortion and giant lattice rotation in the magnetoelectric insulator* Cu_2OSeO_3, Physical Review Letters **113**, 107203 (2014).

[13] A. Fert, N. Reyren, and V. Cros, *Magnetic skyrmions: Advances in Physics and Potential Applications,* Nature Materials **2**, 201731 (2017).

[14] M. N. Wilson, A. B. Butenko, A. N. Bogdanov, and T. L. Monchesky, *Chiral skyrmions in cubic helimagnet films: The role of uniaxial anisotropy,* Physical Review B **89**, 094411 (2014).

[15] S. Buhrandt and L. Fritz, *Skyrmion lattice phase in three-dimensional chiral magnets from Monte Carlo simulations,* Physical Review B **88**, 195137 (2013).

[16] H. Wilhelm, M. Baenitz, M. Schmidt, U. K. Rößler, A. A. Leonov, and A. N. Bogdanov, *Precursor Phenomena at the Magnetic Ordering of the Cubic Helimagnet FeGe,* Physical Review Letters **107**, 127203 (2011).

[17] A. O. Leonov and K. Inoue, *Homogeneous and heterogeneous nucleation of skyrmions in thin layers of cubic helimagnets,* Physical Review B **98**, 054404 (2018).

[18] I. Levatić, P. Popčević, V. Šurija, A. Kruchkov, H. Berger, A. Magrez, J. S. White, H. M. Rønnow, and I. Živković, *Dramatic pressure-driven enhancement of bulk skyrmion stability,* Scientific Reports **6**, 21347 (2016).

[19] Y. Okamura, F. Kagawa, S. Seki, and Y. Tokura, *Transition to and from the skyrmion lattice phase by electric fields in a magnetoelectric compound,* Nature Communications **7**, 12669 (2016).

[20] A. J. Kruchkov, J. S. White, M. Bartkowiak, I. Živković, A. Magrez, and H. M. Rønnow, *Direct electric field control of the skyrmion phase in a magnetoelectric insulator,* Scientific Reports **8**, 10466 (2018).

[21] J. S. White, I. Živković, A. Kruchkov, M. Bartkowiak, A. Magrez, and H. M. Rønnow, *Electric-Field-Driven Topological Phase Switching and Skyrmion-Lattice Metastability in Magnetoelectric* Cu_2OSeO_3, Physical Review Applied **10**, 014021 (2018).

[22] I. E. Dzyaloshinskii, *Theory of Helicoidal Structures in Antiferromagnets .1. Nonmetals,* Soviet Physics JETP **19**, 960 (1964).

[23] I. E. Dzyaloshinskii, *The theory of helicoidal structures in antiferromagnets. III. metals,* Soviet Physics JETP **20**, 665 (1965).

[24] A. N. Bogdanov and D. A. Yablonskii, *Thermodynamically stable 'vortices' in magnetically ordered crystals. the mixed state of magnets,* Zh. Eksp. Teor. Fiz **95**, 182 (1989).

[25] A. N. Bogdanov and D. A. Yablonskii, *Contribution to the theory of inhomogeneous states of magnets in the region of magnetic-field-induced phase transitions. Mixed state of antiferromagnets,* Journal of Experimental and Theoretical Physics **69**, 142 (1989).

[26] A. Bogdanov and A. Hubert, *The Stability of Vortex-Like Structures in Uniaxial Ferromagnets,* Journal of Magnetism and Magnetic Materials **195**, 182 (1999).

[27] U. K. Rößler, A. N. Bogdanov, and C. Pfleiderer, *Spontaneous skyrmion ground states in magnetic metals,* Nature **442**, 797 (2006).

[28] A. O. Leonov, *Twisted, localized, and modulated states described in the phenomenological theory of chiral and nanoscale ferromagnets*, Ph.D. thesis, Technical University of Dresden (2012).

[29] A. B. Butenko, A. A. Leonov, U. K. Rößler, and A. N. Bogdanov, *Stabilization of skyrmion textures by uniaxial distortions in noncentrosymmetric cubic helimagnets,* Physical Review B **82**, 052403 (2010).

[30] W. Jiang, G. Chen, K. Liu, J. Zang, S. G. E. te Velthuis, and A. Hoffmann, *Skyrmions in magnetic multilayers,* Physics Reports **704**, 1 (2017).

[31] A. O. Leonov, Y. Togawa, T. L. Monchesky, A. N. Bogdanov, J. Kishine, Y. Kousaka, M. Miyagawa, T. Koyama, J. Akimitsu, T. Koyama, *et al.*, *Chiral surface twists and skyrmion stability in nanolayers of cubic helimagnets,* Physical Review Letters **117**, 087202 (2016).

[32] D. McGrouther, R. J. Lamb, M. Krajnak, S. McFadzean, S. McVitie, R. L. Stamps, A. O. Leonov, A. N. Bogdanov, and Y. Togawa, *Internal structure of hexagonal skyrmion lattices in cubic helimagnets,* New Journal of Physics **18**, 095004 (2016).

[33] S. L. Zhang, G. van der Laan, W. W. Wang, A. A. Haghighirad, and T. Hesjedal, *Direct Observation of Twisted Surface skyrmions in Bulk Crystals,* Physical Review Letters **120**, 227202 (2018).

[34] F. Qian, L. J. Bannenberg, H. Wilhelm, G. Chaboussant, L. M. DeBeer-Schmitt, M. P. Schmidt, A. Aqeel, T. T. M. Palstra, E. H. Brück, A. J. E. Lefering, C. Pappas, M. Mostovoy, and A. O. Leonov, *New magnetic phase of the chiral skyrmion material Cu_2OSeO_3,* Science Advances **4**, eaat7323 (2018).

[35] A. Chacon, L. Heinen, M. Halder, A. Bauer, W. Simeth, S. Mühlbauer, H. Berger, M. Garst, A. Rosch, and C. Pfleiderer, *Observation of two independent skyrmion phases in a chiral magnetic material,* Nature Physics **14**, 936 (2018).

[36] H. Oike, A. Kikkawa, N. Kanazawa, Y. Taguchi, M. Kawasaki, Y. Tokura, and F. Kagawa, *Interplay between topological and thermodynamic stability in a metastable magnetic skyrmion lattice,* Nature Physics **12**, 62 (2016).

[37] L. J. Bannenberg, K. Kakurai, F. Qian, E. Lelièvre-Berna, C. D. Dewhurst, Y. Onose, Y. Endoh, Y. Tokura, and C. Pappas, *Extended skyrmion lattice scattering and long-time memory in the chiral magnet $Fe_{1-x}Co_xSi$,* Physical Review B **94**, 104406 (2016).

[38] L. J. Bannenberg, A. J. E. Lefering, K. Kakurai, Y. Onose, Y. Endoh, Y. Tokura, and C. Pappas, *Magnetic relaxation phenomena in the chiral magnet $Fe_{1-x}Co_xSi$: An ac susceptibility study,* Physical Review B **94**, 134433 (2016).

[39] K. Karube, J. S. White, N. Reynolds, J. L. Gavilano, H. Oike, A. Kikkawa, F. Kagawa, Y. Tokunaga, H. M. Rønnow, Y. Tokura, *et al., Robust metastable skyrmions and their triangular-square lattice structural transition in a high-temperature chiral magnet,* Nature Materials **15**, 3752 (2016).

[40] T. Nakajima, H. Oike, A. Kikkawa, E. P. Gilbert, N. Booth, K. Kakurai, Y. Taguchi, Y. Tokura, F. Kagawa, and T. Arima, *Skyrmion Lattice Structural Transition in MnSi,* Science Advances **3**, e1602562 (2017).

[41] C. D. Dewhurst, I. Grillo, D. Honecker, M. Bonnaud, M. Jacques, C. Amrouni, A. Perillo-Marcone, G. Manzin, and R. Cubitt, *The small-angle neutron scattering instrument D33 at the Institut Laue–Langevin,* Journal of Applied Crystallography **49**, 1 (2016).

[42] L. J. Bannenberg, F. Qian, R. M. Dalgliesh, N. Martin, G. Chaboussant, M. Schmidt, D. L. Schlagel, T. A. Lograsso, H. Wilhelm, and C. Pappas, *Reorientations, relaxations, metastabilities, and multidomains of skyrmion lattices,* Physical Review B **96**, 184416 (2017).

[43] P. J. Ackerman and I. I. Smalyukh, *Diversity of Knot Solitons in Liquid Crystals Manifested by Linking of Preimages in Torons and Hopfions,* Physical Review X **7**, 2256 (2017).

[44] P. J. Ackerman and I. I. Smalyukh, *Static three-dimensional topological solitons in fluid chiral ferromagnets and colloids,* Nature Materials **16**, 426 (2016).

[45] I. I. Smalyukh, Y. Lansac, N. A. Clark, and R. P. Trivedi, *Three-dimensional structure and multistable optical switching of triple-twisted particle-like excitations in anisotropic fluids,* Nature Materials **9**, 139 (2009).

[46] P. Bak and M. H. Jensen, *Theory of helical magnetic structures and phase transitions in MnSi and FeGe,* Journal of Physics C: Solid State Physics **13**, L881 (1980).

[47] S. Bordács, A. Butykai, B. Szigeti, J. S. White, R. Cubitt, A. O. Leonov, S. Widmann, D. Ehlers, H.-A. K. Nidda, V. Tsurkan, A. Loidl, and I. Kézsmárki, *Equilibrium Skyrmion Lattice Ground State in a Polar Easy-plane Magnet,* Scientific Reports **7**, 7584 (2017).

[48] A. K. Nayak, V. Kumar, T. Ma, P. Werner, E. Pippel, R. Sahoo, F. Damay, U. K. Rößler, C. Felser, and S. S. P. Parkin, *Magnetic Antiskyrmions Above Toom Temperature in Tetragonal Heusler Materials,* Nature **548**, 561 (2017).

[49] A. O. Leonov, A. N. Bogdanov, and K. Inoue, *Toggle-switch-like crossover between two types of isolated skyrmions within the conical phase of cubic helimagnets,* Physical Review B **98**, 1420 (2018).

[50] J. Müller, J. Rajeswari, P. Huang, Y. Murooka, H. M. Rønnow, F. Carbone, and A. Rosch, *Magnetic Skyrmions and Skyrmion Clusters in the Helical Phase of Cu_2OSeO_3,* Physical Review Letters **119**, 137201 (2017).

SUMMARY

Magnetic skyrmions are two-dimensional topologically protected spin textures with particle like properties which may crystallize in lattices that are typically oriented perpendicular to the magnetic field. Their first observation was in the archetype cubic helimagnet MnSi, where skyrmion lattices appear spontaneously in the A-phase located just below the transition temperature and under magnetic fields. As further discussed in Chapter 1, single crystal cubic helimagnets host, beside skyrmion lattices, a variety of helimagnetic phases that are stabilized by three hierarchically ordered interactions, being the strongest ferromagnetic, the weaker Dzyaloshinsky-Moriya which is non-zero due to the absence of inversion symmetry, and the weakest anisotropy interaction. The competition between these and the Zeeman interaction results in a relatively generic phase diagram for cubic helimagnets. Albeit this relative generic phase diagram, each of these systems have their own particularities. This thesis mainly presents results of magnetization, ac susceptibility and neutron scattering studies of four cubic helimagnets: MnSi, $Mn_{1-x}Fe_xSi$, $Fe_{1-x}Co_xSi$ and Cu_2OSeO_3.

The semiconductor $Fe_{0.7}Co_{0.3}Si$ is the subject of Chapters 2-4. $Fe_{0.7}Co_{0.3}Si$, is part of the $Fe_{1-x}Co_xSi$ family which shows helimagnetic order over a wide composition range of $0.05 \lesssim x \lesssim 0.8$. Chapter 2 provides an ac susceptibility study covering four orders of magnitude in frequencies from 0.1 Hz to 1 kHz, with particular emphasis on the pronounced history dependence. It reveals that the distribution of relaxation frequencies around the A-phase is broad, asymmetric and originates from multiple coexisting relaxation processes with characteristic relaxation times ranging from a few milliseconds to tens of seconds. Chapter 3 confirms the pronounced effect of the magnetic history and cooling rates on the magnetic phase diagram. Small angle neutron scattering shows that metastable skyrmion lattices can be induced outside the A-phase by cooling down the sample under magnetic fields. These skyrmion lattices appear in a wide region of the phase diagram, coexist with conical spirals and can be enhanced by increasing the cooling rate. Chapter 4 studies the helimagnetic transition in $Fe_{0.7}Co_{0.3}Si$ by means of neutron spin echo spectroscopy and small angle neutron scattering. In contrast to the sharp transition observed in the archetype chiral magnet MnSi, the transition in $Fe_{1-x}Co_xSi$ is gradual and long-range helimagnetic order coexists with short-range correlations over a wide temperature range. Together with an analysis of the hierarchy of the relevant length scales, these results show that the helimagnetic transition in $Fe_{1-x}Co_xSi$ differs substantially from the transition in MnSi, questioning the validity of a universal approach to the helimagnetic transition in chiral magnets.

Another non-stochiometric cubic chiral magnet, $Mn_{1-x}Fe_xSi$, is the subject of Chapters 5 and 6. Chapter 5 presents a comprehensive and systematic magnetization and ac susceptibility study of this compound for an extensive Fe concentrations range of $x = 0$ - 0.32. It shows that Fe substitution decreases the critical temperature, which vanishes at $x_C = 0.17$ where also the average magnetic interactions change sign. No signatures

of long-range magnetic order is found down to the lowest temperature for $x > x_C$, indicating a possible significant role for quantum fluctuations in these systems. In addition, Chapter 5 shows, together with the small angle neutron scattering results of Chapter 6, that the long-range helimagnetic order and the first-order phase transition, as seen in the archetype chiral magnet MnSi, persists only up to $x^* \approx 0.11$. In the intermediate regime of $x^* < x < x_C$, disordered isotropic helimagnetic correlations with finite correlation lengths are stabilized. The structure of these correlations bear similarities with the ones found in the precursor phase of MnSi, however, they appear completely frozen on the nanosecond timescale. Magnetic fields only gradually suppress and partly align these short-ranged helimagnetic correlations along their direction through a complex magnetization process.

Another way to tune the helimagnetic order of MnSi is by applying hydrostatic pressure, which is considered in Chapter 7. Previous studies indicate the emergence of a non-Fermi liquid behavior which exists in conjunction with a topological Hall signal and partial magnetic order. The small angle neutron scattering results show that the helimagnetic order persists at zero magnetic field up to the critical pressure. Nevertheless, under magnetic field skyrmion lattices and conical spirals appear at low temperatures, even in the absence of any helimagnetic correlations at zero field. However, no one-to-one relation is found between the appearance of skyrmion lattices and conical spirals on one side, and the non-Fermi liquid and topological Hall effect behavior on the other side, as the latter extends over a much larger region of the phase diagram. A possible explanation for this paradox is that the phase, out of which a magnetic field induces long range order at low temperatures, is heterogeneous and consists of spirals, skyrmions and other topologically non-trivial magnetic textures.

The coupling between the crystallographic and skyrmion lattices in both MnSi and Cu_2OSeO_3 is investigated in Chapter 8. The small angle neutron scattering results reveal that the orientation of the skyrmion lattice is primarily determined by the magnetic field direction with respect to the crystallographic lattice, but also influenced by the magnetic history of the sample. Furthermore, it shows that multidomain skyrmion lattices may form when two or more equivalent crystallographic directions are favored by spin-orbit coupling and oriented perpendicular to the magnetic field.

Cu_2OSeO_3 is further studied by small angle neutron scattering in Chapter 9. It reveals that skyrmion lattice states can be formed in large areas of the magnetic phase diagram, from the lowest temperatures up to the A-phase. Disappearing spiral states near critical lines catalyze topological charge changing processes leading to the formation and destruction of skyrmionic states at low temperatures, which are thermodynamically stable or metastable depending on the orientation and strength of the magnetic field. These results, together with the earlier reported tilted conical spiral phase, indicate substantial deviations from the generic magnetic phase diagram of cubic helimagnets and highlight the paramount role of magnetic anisotropies in Cu_2OSeO_3.

As a general conclusion, the experimental study of various cubic helimagnets by a variety of techniques reveals that despite their generic phase diagram, each system has their own particular behavior. Investigating the differences between these systems not only increases our understanding of these individual system, but also improves our fundamental knowledge about chiral magnetism as a whole.

SAMENVATTING

Magnetische skyrmionen zijn tweedimensionale topologisch beschermde spin texturen met deeltjesachtige eigenschappen. Deze skyrmionen kunnen kristalliseren in roosters die typisch loodrecht georiënteerd zijn ten opzichte van het magnetisch veld. De eerste waarneming van skyrmionen was in de archetype chirale magneet MnSi, waar skyrmionroosterformaties spontaan verschijnen in de A-fase. Deze A-fase treedt op in een magnetisch veld en voor temperaturen dicht onder de overganstemperatuur. Zoals uitgebreid besproken in Hoofdstuk 1 zijn er in kubische helimagneten naast een skyrmionroosterfase een variëteit aan helimagnetische fases die door drie hiërarchisch geordende interacties gestabiliseerd worden. Deze interacties zijn de sterke ferromagnetische interactie, de zwakkere Dzyaloshinsky-Moriya interactie die niet-nul is door de afwezigheid van inversie symmetrie, en de zwakste, de anistropische interacties. De competitie tussen deze drie en de Zeeman interactie resulteert in een relatief generiek fasediagram. Alhoewel het fasediagram van kubische helimagneten relatief generiek is, heeft elke kubische helimagneet zijn bijzonderheden. Dit proefschrift presenteert resultaten van magnetisatie, ac susceptibiliteit en neutronenverstrooiingsexperimenten van vier kubische helimagneten: MnSi, $Mn_{1-x}Fe_xSi$, $Fe_{1-x}Co_xSi$ en Cu_2OSeO_3.

De halfgeleider $Fe_{0.7}Co_{0.3}Si$ wordt behandeld in Hoofdstukken 2-4. $Fe_{0.7}Co_{0.3}Si$ is onderdeel van de $Fe_{1-x}Co_xSi$ familie waarin helimagnetische ordening voorkomt voor een groot concentratiebereik van $0.05 \lesssim x \lesssim 0.8$. Hoofdstuk 2 presenteert een ac susceptibiliteitstudie die vier ordes van grootte in frequenties omvat, van 0.1 Hz tot 1 kHz met de nadruk op de geschiedenisafhankelijkheid van het fasediagram. De metingen laten zien dat de verdelingen van relaxatiefrequenties rondom de A-fase breed en asymmetrisch is, wat haar oorsprong vindt in meerdere gelijktijdige relaxatieprocessen met karakteristieke relaxatietijden van enkele milliseconden tot tientallen seconden. Hoofdstuk 3 bevestigt het nadrukkelijke effect van de magnetische geschiedenis en de koelsnelheden op het magnetisch fasediagram. Kleine hoek neutronenverstrooiingsmetingen laten zien dat metastabiele skyrmionroosters geïnduceerd kunnen worden buiten de A-fase door het koelen van het monster in magnetische velden. Deze skyrmionroosters komen in een groot gebied van het fasediagram voor, waar ze coëxisteren met conische spiralen. De intensiteit van deze skyrmionroosters kan worden vergroot door de koelsnelheid te vergroten. Hoofdstuk 4 beschrijft de helimagnetische overgang in $Fe_{0.7}Co_{0.3}Si$ met neutronen spinechospectroscopie en kleine hoek neutronenverstrooiing. In tegenstelling tot de scherpe overgang in de archetype chirale magneet MnSi is de overgang in $Fe_{1-x}Co_xSi$ geleidelijk waarbij langedracht helimagnetische ordening coëxisteert met kortedracht magnetische correlaties over een breed temperatuurgebied. Samen met de analyse van de hiërarchie van de relevante lengteschalen laten deze resultaten zien dat de helimagnetische overgang in $Fe_{1-x}Co_xSi$ substantieel anders is dan die van MnSi, wat de validiteit van een universele aanpak van de helimagnetische overgang in chirale magneten in twijfel trekt.

Een andere niet-stoichiometrische kubische chirale magneet, $Mn_{1-x}Fe_xSi$, is het onderwerp van Hoofdstukken 5 en 6. Hoofdstuk 5 presenteert een veelomvattende en systematische magnetisatie en ac susceptibiliteitstudie van $Mn_{1-x}Fe_xSi$ voor een groot bereik in Fe concentratie van $x = 0$ tot $x = 0.32$. De studie laat zien dat Fe substitutie de overgangstemperatuur verlaagt en uiteindelijk verdwijnt bij $x_C = 0.17$, waar ook het teken van de gemiddelde magnetische interacties wisselt. Geen enkel teken van langedracht magnetische ordening voor $x > x_C$ is aanwezig, wat erop duidt dat er wellicht een significante rol is van kwantumfluctuaties in deze systemen. Verder laat Hoofdstuk 5 tezamen met de resultaten van kleine hoek neutronenverstrooiingsmetingen in Hoofdstuk 6 zien dat de langedracht helimagnetische ordening en de eerste-orde faseovergang, zoals ook gezien in MnSi, alleen bestaat voor $x^* \lessapprox 0.11$. In het tussenliggende concentratiegebied van $x^* < x < x_C$ bevinden zich wanordelijke isotropische helimagnetische correlaties met eindige correlatielengtes. De structuur van deze correlaties vertoont overeenkomsten met de correlaties in de precursorfase van MnSi. Deze correlaties blijken echter compleet bevroren te zijn op de nanoseconden schaal. Magnetische velden kunnen deze kortedracht correlaties alleen geleidelijk onderdrukken en langs het veld richten door middel van een complex magnetisatieproces.

Een andere manier om de helimagnetische ordening in MnSi te veranderen is door middel van hydrostatische druk. Zoals verder besproken in Hoofdstuk 7 laten eerdere studies zien dat niet-Fermi vloeistofgedrag voorkomt tezamen met een topologisch Hall signaal en een partiële magnetische ordening. De kleine hoek neutronenverstrooiingsmetingen laten zien dat de helimagnetische ordening in de afwezigheid van een magnetisch veld bestaat tot de kritische druk. Desalniettemin kunnen magnetische velden skyrmionroosters en conische spiralen stabiliseren bij lage temperatuur, dus zelfs in de afwezigheid van alle helimagnetische correlaties bij nul magnetisch veld. Desondanks is er geen een-op-een relatie tussen het voorkomen van skyrmionroosters en conische spiralen aan de ene kant, en het niet-Fermi vloeistof en topologische Hall effect gedrag aan de andere kant, omdat dit laatste een veel groter gebied van het fasediagram bestrijkt. Een mogelijke verklaring voor deze paradox is dat de fase van waaruit een magnetisch veld bij lage temperaturen skyrmionroosters en conische spiralen kan induceren heterogeen is en bestaat uit spiralen, skyrmionen en andere topologisch niet-triviale magnetische texturen.

De koppeling tussen het kristallografische en skyrmionrooster wordt in Hoofdstuk 8 onderzocht in zowel MnSi als Cu_2OSeO_3. De kleine hoek neutronenverstrooiingsmetingen laten zien dat de oriëntatie van het skyrmionrooster primair bepaald wordt door de richting van het magnetisch veld ten opzichte van het kristalrooster, maar ook wordt beïnvloed door de magnetische geschiedenis van het monster. Verder laten de resultaten zien dat multidomein skyrmionroosters gevormd kunnen worden wanneer twee of meerdere equivalente kristallografische richtingen energetisch gunstig zijn in het licht van de spin-orbitaal koppeling en loodrecht staan ten opzichte van het magnetisch veld.

Cu_2OSeO_3 wordt verder bestudeerd door middel van kleine hoek neutronenverstrooiingsmetingen in Hoofdstuk 9. Het laat zien dat skyrmionroosters gevormd kunnen worden in grote gebieden van het fasediagram, van de laagste temperaturen tot en met de A-fase. Verdwijnende helimagnetische toestanden nabij kritische lijnen kunnen processen katalyseren die de topologische lading veranderen, wat leidt tot de vorming of het

verdwijnen van skyrmionische toestanden, die afhankelijk van de richting en grootte van het magnetisch veld thermodynamisch stabiel of instabiel zijn. Deze resultaten laten, tezamen met de eerder gerapporteerde afbuigende conische fase, vergaande afwijkingen zien van het generieke fasediagram en onderstrepen de beslissende rol van magnetische anisotropieën in Cu_2OSeO_3.

De algemene conclusie gebaseerd op de experimentele studies van de verschillende kubische helimagneten met behulp van een variëteit aan technieken is dat elk systeem een individueel gedrag vertoont ondanks het generieke fasediagram. Het onderzoeken van deze verschillen tussen de systemen vergroot niet alleen het begrip van de individuele systemen, maar verbetert ook de fundamentele kennis van chiraalmagnetisme als geheel.

CONTRIBUTIONS TO THE LARMOR PROJECT

This appendix outlines the contributions made within this PhD project to the Larmor project. Larmor is a versatile neutron scattering instrument located at the ISIS Neutron and Muon Source, Oxfordshire, United Kingdom with (polarized) small angle neutron scattering (SANS), simultaneous diffraction and SANS experiments, spin echo small angle neutron scattering (SESANS) capabilities, as well as other experimental techniques using the Larmor precession of neutrons to encode their direction or energy. The Larmor instrument was constructed and financed as a SANS instrument by ISIS, while the additional capabilities were developed and constructed at and by Delft University of Technology as part of the NWO Groot Project 721.012.102 'Larmor'.

- Performed the first (published) experiments on Larmor demonstrating the capabilities of Larmor in condensed matter research.
- Testing and first-time operation of the ISISstat and Scientific Magnetics 3D vector field cryomagnet, including a rotating center stick, now available to all users. This includes the co-development and testing of programming code to control the cryomagnet.
- (Co-)development and testing software to process and analyze the SANS data for condensed matter research. This includes the use of event-mode data. In event-mode data acquisition, each detected neutron is time-stamped. After the experiments, the user has the flexibility to bin the neutrons in any way wanted, allowing e.g. kinetic measurements (see, e.g., Chapter 8).
- First-time use of event-mode data acquisition to perform e.g. magnetic field and rotation scans. This allows a significant reduction of the measurement times as it decreases the overhead time when starting and ending a measurements. In addition, it increases the flexibility to users.
- Performed the first high-pressure experiment at Larmor (up to 1.5 GPa at low temperatures) using a double-wall clamp cell mounted in the 3D vector cryomagnet.
- Performed Larmor diffraction measurements at TRISP, FRMII, Munich, Germany to explore the option to add Larmor diffraction capabilities to the Larmor instrument.

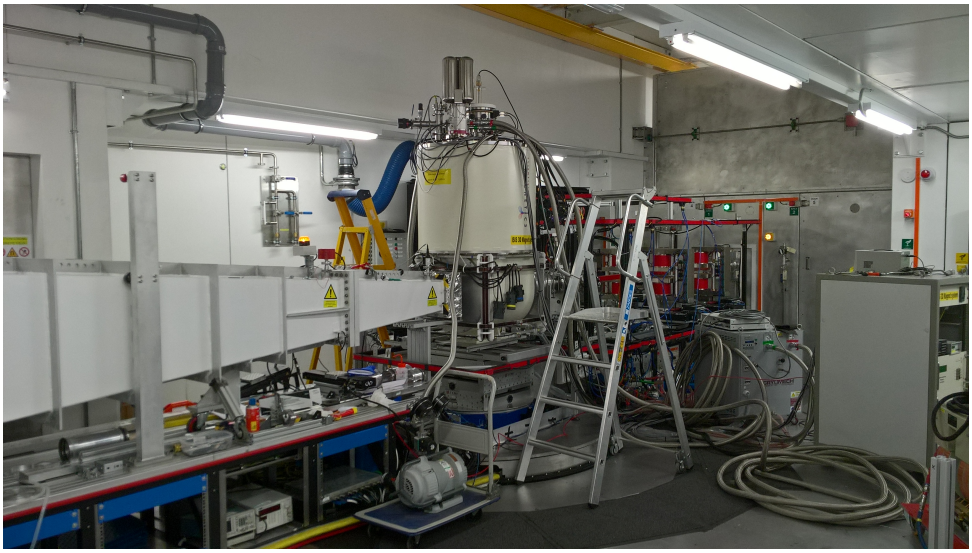

Figure 9.10: Photograph of the Larmor insturment at the ISIS Neutron and Muon Source, Oxfordshire, United Kingdom. The 3D vector field cryomagnet is positioned at the sample position.

ACKNOWLEDGMENTS

If I would have devoted my PhD time proportional to the popularity of the pages of my thesis, then I should probably have allotted three years on writing the acknowledgment. Although I certainly did not do so, that by no means reflect how grateful I am for all the help I received during the past years.

First of all, I would like to thank my promoter, Catherine (Katia) Pappas. Our intensive collaboration combined with your, at times, unconventional approach and critical attitude but most of all your impressive dedication and broad knowledge resulted in quite a few publications, manuscripts, and most importantly, the completion of this thesis. I am particularly grateful for the confidence you showed in me, but probably most of all, for offering me lots of scientific and travel opportunities and the freedom to perform (research) activities outside the scope of my thesis project. Ad van Well, besides being a great master thesis supervisor you were a fantastic co-promoter. Although our discussion were typically not related to chiral magnetism, and frequently not even to science, you have been a great support during the past years. Your warmhearted personality, broad interest, and hospitality were all a big stimulus during my PhD time. Besides the promoter and co-promoter, I would also like to thank all the other doctoral committee members for attending my thesis defense: Ekkes Brück, Frank Weber, Marnix Wagemaker, Maxim Mostovoy, Nicolas Martin, and Rob Dalgliesh.

A major share of the research presented in this thesis was performed at foreign laboratories, and I am very grateful to all the welcoming scientists I worked with during my frequent stays abroad. Whether it was in the UK with Rob Dalgliesh, Nina-Juliane Steinke, Adam Washington, Jos Cooper, Sarah Rogers, Najet Mahmoudi, Diego Alba-Venero, Christy Kinane, Chris Goodway, Ravil Sadykov or Heribert Wilhelm, at the Institut Laue-Langevin in Grenoble with Eddy Lelièvre-Berna, Peter Falus, Peter Fouquet, Robert Cubitt, Eric Bourgeat-Lami or Paul Steffens, in Saclay with Grégory Chaboussant, Isabelle Mirebeau and Nicolas Martin, in Karlsruhe with Frank Weber, in Garching with Thomas Keller, in Tokai with Kazuhisa Kakurai or in Oak Ridge with Lisa DeBeer-Schmitt and Ryan Desautels, I very much appreciate your great devotion to our common experiments and projects as well as the fantastic time spent together. Rob, your pragmatism, innovative ideas and solutions, and devotion to a successful experiment are probably as impressive as your knowledge about beer and chillies. Probably even more impressive is the confidence that both you and Nina had in Herman and me when we showed up at the beamline as inexperienced users with a bunch of equipment about four years ago, which remains greatly appreciated. Nina, the discussions on science related and unrelated matters all around the globe but mostly in the orange cabin were always useful and entertaining. Nicolas, thank you very much for the memorable moments in France, Korea and Russia and your kind invitation to join a real French family dinner. Eddy, besides your impressive knowledge about neutron scattering and cryogenics, your lessons about French cuisine and Champagne will certainly be of use after my PhD time. Ravil, your

step-by-step method and enormous enthusiasm helped us to reach even higher pressures than I could have ever imagined. Frank, working with you felt always at ease and I am grateful for all your valuable input and for introducing me to triple axis spectroscopy. Furthermore, I am indebted to Greame Blake, Andrey Leonov and Maxim Mostovoy, all at some point based in Groningen. Greame, thank you for all your help with the alignment of the single crystals and for traveling with me to Munich. Andrey and Maxim, the numerous enlightening, stimulating and valuable discussions we had together are very much appreciated and proofed to be very helpful in increasing my understanding of chiral magnetism.

Completing a PhD in Experimental Physics is impossible without fantastic colleagues, technical assistance and secretarial support. In this respect, I would like to thank all colleagues within the RID: Ankit Labh, Ashutosh Pati, Bei Tian, Bowei Huang, Chris Duif, Chrysoula Ioannidou, Ekkes Brück, Erik Kelder, Evgenii Velichko, Fengjiao Qian, Fengqi Zhang, Frederiki Naziris, Haixing Fang, Hanan Al-Kutubi, Henk Schut, Ivan Batashev, Jiawei Lai, Jeroen Plomp, Jun Liu, Jouke Heringa, Jurrian Bakker, Lambert van Eijck, Marnix Wagemaker, Menno Blaauw, Michael Maschek, Niels van Dijk, Peter-Paul Harks, Remco van der Jagt, Shasha Lyu, Shibabrata Basak, Stephan Eijt, Steven Parnell, Swapna Ganapathy, Tammo Schwietert, Theo Rekveldt, Tomas Verhallen, Van Thang Nguyen, Violetta Arszelewska, Viviam Marques Pereira, Wenqin Shi, Wim Bouwman, Xinmin You, Xuefei Miao, Yibole, Yifan Fu, Zhaolong Li, and Zhou Zhou. Anton Lefering, Frans Ooms, Fred Naastepad, Kees Goubitz, Kees de Vroege, Martijn de Boer, Michel Steenvoorden, Michel Thijs and Piet van der Ende, thank you for the numerous times you offered your technical assistance and advice. Erwin Jansen and Jörg Haberlah, without the liquid helium and gas provided by you my thesis would have been a lot thinner. Ilse van der Kraaij and Nicole Banga, besides for processing all the numerous receipts and travel requests I thank you for the great company during the last years and for becoming my favorite secretaries. Anton, without your perseverance, numerous repairs of the SQUID, your original approach and dedication all the susceptibility measurements in the thesis would not have been possible. Bei and Evgenii, thank you for the great company during the past period of time and for all our numerous science (un)related discussion and chats. Fengjiao, Jeroen, Michel, Steven, Wim thank you for accompanying me during lunch and at various trips and for all stimulating discussions, talks and drinks. Lambert, I very much appreciate your decisive, pragmatic yet philosophical approach and the numerous drinks, discussions and dinners we shared together. Henk van Doorn and Koos van Kammen, thank you for all your help with all Health Physics related issues, but most importantly and certainly most memorable, I am grateful to you and Robin de Kruijff for facilitating the drinks and events in 't Koepeltje and broadening my scope of beers.

Although not presented in this thesis, I would certainly like to thank Bernard Dam, Ben Norder, Christiaan Boelsma, Herman Schreuders and Trang Thu Tring for working together with me on thin film metal hydrides. In this respect, I am also grateful to Christoph Langhammer and Ferry Nugroho from Chalmers University: besides that it was very pleasant to work with you, I have learned an awful lot from our interactions. Bernard, working together with you has always been a great pleasure and your open-minded, pragmatic yet diplomatic and at times philosophical approach, as well as your comprehensive knowledge about physics, chemistry and beyond will remain a

great inspiration to me. Herman, accompanying each other on our first beamline experiment was the first in a long series of memorable moments we shared together. I am very grateful for your efficient, pragmatic and down-to-earth approach and for sharing your knowledge, experience, and enthusiasm with me. Joost Middelkoop, thank you for drawing beautiful skyrmions. The hospitality and the great company by Herman, Joost, Ruben Abellón and all other members of the MECS group during coffee breaks, lunches and drinks are very much appreciated. In addition, I would like to express my gratitude towards Nico van der Sar for his infinite enthusiasm, encouragements, guidance and for all the stimulating discussions. Your enthusiasm about Finance in general and IPOs in particular turned out to be infectious and I am very thankful that you offered me the possibility to continue our work in the field of Finance.

Last but certainly not least I would like to express my gratitude towards my family and friends. I am deeply aware that I am fortunate with such a large number of fantastic people around me. Words are not sufficient to express all my appreciation for your unconditional loyalty, generosity and hospitality that indirectly greatly contributed to the completion of this thesis.

LIST OF PUBLICATIONS

17. **Lars J. Bannenberg**, Ravil Sadykov, Robert M. Dalgliesh, Christopher Goodway, Deborah L. Schlagel, Thomas A. Lograsso, Eddy Lelièvre-Berna, and Catherine Pappas. *Skyrmions and Spirals in MnSi under hydrostatic pressure*, Submitted.

16. **Lars J. Bannenberg**, Ferry A.A. Nugroho, Herman Schreuders, Ben Norder, Trang T. Trinh, Nina-Juliane Steinke, Ad A. van Well, Christoph Langhammer, and Bernard Dam. *Direct comparison of PdAu thin films and nanoparticles on hydrogen exposure*, Accepted in ACS Applied Materials & Interfaces.

15. **Lars J. Bannenberg** Heribert Wilhelm, Robert Cubitt, Ankit Labh, Marcus Schmidt, Eddy Lelière-Berna, Catherine Pappas, Maxim Mostovoy, and Andrey O. Leonov. *Multiple low temperature skyrmionic states in a bulk chiral magnet*, NPJ Quantum Materials **4**, 11 (2019).

14. Ferry A. A. Nugroho, Iwan Darmadi, Lucy Cusinato, Arturo Susarrey-Arce, Herman Schreuders, **Lars J. Bannenberg**, Alice Bastos da Silva Fanta, Shima Kadkhodazadeh, Jakob B. Wagner, Tomasz J. Antosiewicz, Anders Hellman, Vladimir P. Zhdanov, Bernard Dam, and Christoph Langhammer. *Plasmonic Metal - Polymer Hybrid Nanomaterials for Ultrafast Hydrogen Detection*, Accepted in Nature Materials.

13. **Lars J. Bannenberg**, Christiaan Boelsma, Herman Scheuders, Sara Francke, Nina-Juliane Steinke, Ad A Van Well, and Bernard Dam. *Optical hydrogen sensing beyond palladium: hafnium and tantalum as effective sensing materials*, Sensors and Actuators B: Chemical **283**, 538-548 (2019) .

12. **Lars J. Bannenberg**, Robert M. Dalgliesh, Thomas Wolf, Frank Weber, and Catherine Pappas. *Evolution of helimagnetic correlations in $Mn_{1-x}Fe_xSi$ with doping: A small-angle neutron scattering study*, Physical Review B **98**(18), 184431 (2018) *Editors' Suggestion*.

11. **Lars J. Bannenberg**, Frank Weber, Anton J. E. Lefering, Nicolas Martin, Grégory Chaboussant, Thomas Wolf, and Catherine Pappas. *Magnetization and ac susceptibility study of the cubic chiral magnet $Mn_{1-x}Fe_xSi$*, Physical Review B **98**(18), 184430 (2018).

10. Fengjiao Qian, **Lars J. Bannenberg**, Heribert Wilhelm, Grégory Chaboussant, Lisa M. DeBeer-Schmitt, Marcus P. Schmidt, Aisha Aqeel, Thomas T. M. Palstra, Ekkes Brück, Anton J. E. Lefering, Catherine Pappas, Maxim Mostovoy, and Andrey O. Leonov. *New magnetic phase of the chiral skyrmion material Cu_2OSeO_3*, Science Advances **4**(9), aat7323 (2018).

9. Ravil Sadykov, Catherine Pappas, **Lars J. Bannenberg**, Robert M. Dalgliesh, Peter Falus, Christopher Goodway, and Eddy Lelièvre-Berna. *1.5 GPa compact double-wall clamp cell for SANS and NSE studies at low temperatures and high magnetic fields*, Journal of Neutron Research **20**(1-2), 25-33 (2018).

8. Isabelle Mirebeau, Nicolas Martin, Maxime Deutsch, **Lars J. Bannenberg**, Catherine Pappas, Grégory Chaboussant, Robert Cubitt, Claudia Decorse, and Andrey O. Leonov. *Spin textures induced by quenched disorder in a reentrant spin glass: Vortices versus 'frustrated' skyrmions*, Physical Review B **98**(1), 014420 (2018).

7. **Lars J. Bannenberg**, Fengjiao Qian, Robert M. Dalgliesh, Nicolas Martin, Grégory Chaboussant, Marcus Schmidt, Deborah L. Schlagel, Thomas A. Lograsso, Heribert Wilhelm, and Catherine Pappas. *Reorientations, relaxations, metastabilities, and multidomains of skyrmion lattices*, Physical Review B **96**(18), 184416 (2017).

6. Catherine Pappas, **Lars J. Bannenberg**, Eddy Lelièvre-Berna, Fengjiao Qian, Robert M. Dalgliesh, Deborah L. Schlagel, Thomas A. Lograsso, and Peter Falus. *Magnetic Fluctuations, Precursor Phenomena, and Phase Transition in MnSi under a Magnetic Field*, Physical Review Letters **119**(4), 047203 (2017).

5. Christiaan Boelsma, **Lars J. Bannenberg**, Michiel J. van Setten, Nina-Juliane Steinke, Ad A. van Well, and Bernard Dam. *Hafnium—an optical hydrogen sensor spanning six orders in pressure*, Nature Communications **18**, 15718 (2017).

4. **Lars J. Bannenberg**, Kazuhisa Kakurai, Peter Falus, Eddy Lelièvre-Berna, Robert M. Dalgliesh, Charles D. Dewhurst, Fengjiao Qian, Yoshinori Onose, Yasuo Endoh, Yoshinori Tokura, and Catherine Pappas. *Universality of the helimagnetic transition in cubic chiral magnets: Small angle neutron scattering and neutron spin echo spectroscopy studies of FeCoSi*, Physical Review B **95**(14), 144433 (2017) *Editors' Suggestion*.

3. **Lars J. Bannenberg**, Anton J. E. Lefering, Kazuhisa Kakurai, Yoshinori Onose, Yasuo Endoh, Yoshinori Tokura, and Catherine Pappas. *Magnetic relaxation phenomena in the chiral magnet $Fe_{1-x}Co_xSi$: An ac susceptibility study*, Physical Review B **94**(13), 134433 (2016).

2. **Lars J. Bannenberg**, Kazuhisa Kakurai, Fengjiao Qian, Eddy Lelièvre-Berna, Charles D. Dewhurst, Yoshinori Onose, Yasuo Endoh, Yoshinori Tokura, and Catherine Pappas. *Extended skyrmion lattice scattering and long-time memory in the chiral magnet $Fe_{1-x}Co_xSi$*, Physical Review B **94**(10), 104406 (2016).

1. **Lars J. Bannenberg**, Herman Schreuders, Lambert van Eijck, Jouke R. Heringa, Nina-Juliane Steinke, Robert M. Dalgliesh, Bernard Dam, Fokko M. Mulder, and Ad A. van Well. *Impact of Nanostructuring on the Phase Behavior of Insertion Materials: The Hydrogenation Kinetics of a Magnesium Thin Film*, The Journal of Physical Chemistry C **120**(19), 10185-10191 (2016).

CURRICULUM VITÆ

Lars Johannes BANNENBERG

14-09-1992	Born in Apeldoorn, the Netherlands.
2004–2010	Tweetalig Voorbereidend Wetenschappelijk Onderwijs (TVWO) (bilingual pre-university secondary education) Koninklijke Scholen Gemeenschap, Apeldoorn
2010–2013	Bachelor of Science in Applied Physics (Cum Laude) Delft University of Technology
2011–2014	Bachelor of Science in Economics and Business Economics (Cum Laude) Erasmus University Rotterdam
2013–2015	Master of Science in Applied Physics (Cum Laude) Delft University of Technology
2014–2015	Master of Science in Financial Economics (Summa Cum Laude) Erasmus University Rotterdam